

EFFECTIVE PASSIVATION OF BLACK SILICON SURFACES BY CONFORMAL THERMAL ALD DEPOSITED Al_2O_3 LAYERS

Dissertation

zur Erlangung des

Doktorgrades der Naturwissenschaften (Dr. rer. nat.)

der

Naturwissenschaftlichen Fakultät II
Chemie, Physik und Mathematik
der Martin-Luther-Universität
Halle-Wittenberg

vorgelegt

von Herrn Dipl.-Phys. Martin Otto
geboren am 20.05.1981 in Kassel

Gutachter

Prof. Dr. Ralf B. Wehrspohn, Martin-Luther-Universität Halle-Wittenberg, Deutschland
Prof. Dr. Roland Scheer, Martin-Luther-Universität Halle-Wittenberg, Deutschland
Prof. Dr. Mato Knez, Ikerbasque, San Sebastian, Spanien

Eingereicht in Halle (Saale) am 30.10.2014

Verteidigt in Halle (Saale) am 01.04.2015

Meinen Eltern

Contents

| | |
|---|------------|
| Table of Contents | v |
| List of Figures | xiii |
| List of Tables | xv |
| Nomenclature | xix |
| 1 Introduction | 1 |
| 1.1 Motivation: Limiting Effects in Crystalline Silicon Solar Cells | 3 |
| 1.2 Advantages and Challenges of Black Silicon | 5 |
| 2 Theory | 7 |
| 2.1 Light Trapping Concepts in Solar Cells | 7 |
| 2.1.1 Geometric Light Trapping | 8 |
| 2.1.2 Randomizing Structures and the Yablonovitch Limit | 9 |
| 2.1.3 Black Silicon Optics | 10 |
| 2.1.4 Other Photon Management Concepts | 10 |
| 2.2 Recombination of Charge Carriers in Crystalline Silicon | 11 |
| 2.2.1 Generation and Recombination | 11 |
| 2.2.2 Bulk Recombination Mechanisms | 13 |
| 2.2.3 Surface Recombination Velocity | 16 |
| 2.3 Surface Passivation of Black Silicon | 19 |
| 2.3.1 Requirements for Black Silicon Passivation | 20 |
| 2.3.2 Possible Passivation Schemes | 20 |

| | | |
|----------|---|-----------|
| 3 | Sample Preparation | 21 |
| 3.1 | Black Silicon Fabrication Methods | 21 |
| 3.1.1 | Inductive Coupled Plasma Reactive Ion Etching (ICP-RIE) | 22 |
| 3.1.2 | Wet Chemically Etched b-Si | 25 |
| 3.1.3 | KOH Reference and the Superstructure | 29 |
| 3.1.4 | Applicability of the Investigated Black Etching Methods | 29 |
| 3.2 | Surface Cleaning Prior to Atomic Layer Deposition | 30 |
| 3.2.1 | The RCA Standard Clean | 30 |
| 3.3 | Thermal Atomic Layer Deposition | 31 |
| 3.3.1 | ALD Cycle | 32 |
| 3.3.2 | Growth Per Cycle | 32 |
| 3.3.3 | Step Coverage and Film Conformality | 36 |
| 3.4 | Post-Deposition Annealing Treatments | 37 |
| 4 | Sample Analysis | 39 |
| 4.1 | Lifetime Spectroscopy by means of the Quasi-Steady-State Photoconductance Method | 39 |
| 4.2 | Microstructure Analysis | 40 |
| 4.2.1 | Scanning Electron Microscopy | 40 |
| 4.2.2 | Focused Ion Beam (FIB) | 41 |
| 4.2.3 | HR-TEM, EELS and EDX | 42 |
| 4.2.4 | ToF/SIMS | 42 |
| 4.3 | Optical Characterization of Thin Films | 43 |
| 4.3.1 | Setup for Reflectance and Transmission Spectroscopy | 43 |
| 4.3.2 | Ellipsometry | 44 |
| 5 | Microstructure and Optical Properties of Conformally Coated Black Silicon | 47 |
| 5.1 | Geometric Surface Morphology of ICP-RIE Etched b-Si | 47 |
| 5.1.1 | 3D Reconstruction of Real ICP-RIE Etched Black Silicon Surfaces | 49 |
| 5.1.2 | ALD-Al ₂ O ₃ Growth on b-Si Surfaces | 50 |
| 5.1.3 | CVD SiN _x Passivation Layers as an Alternative to ALD-Al ₂ O ₃ | 52 |
| 5.1.4 | Microstructure and Elemental Analysis of b-Si/Al ₂ O ₃ -Interfaces | 52 |

| | | |
|----------|---|-----------|
| 5.2 | Morphology and Al ₂ O ₃ Growth on Other Black Silicon Types | 55 |
| 5.2.1 | KOH Reference and ICP Superstructure | 55 |
| 5.2.2 | MACE Structured b-Si | 56 |
| 5.2.3 | Macroporous Silicon | 56 |
| 5.3 | Optics of Black Silicon | 58 |
| 5.3.1 | Dry Etched b-Si | 58 |
| 5.3.2 | Optical Performance of the Different Black Silicon Nanostructures | 60 |
| 6 | Black Silicon Surface Passivation by ALD Deposited Al₂O₃ | 63 |
| 6.1 | Al ₂ O ₃ Passivation Performance on Unstructured Si Surfaces | 64 |
| 6.1.1 | Effects of ALD Parameters on the Carrier Life Time | 64 |
| 6.1.2 | Post-Deposition Annealing | 67 |
| 6.1.3 | Surface Pre-Cleaning Treatments | 69 |
| 6.2 | Surface Passivation of Dry Etched Black Silicon | 71 |
| 6.2.1 | Transfer of ALD-Al ₂ O ₃ Passivation to Black Silicon | 71 |
| 6.2.2 | Black Silicon Nanostructure Geometry and Related Passivation Quality | 72 |
| 6.2.3 | Influence of ICP-RIE Etching Parameters on the SRV | 73 |
| 6.3 | Comparison of Dry and Wet Etched Black Silicon Types | 74 |
| 6.3.1 | Comparison of the Black Etching Methods Concerning Passivation Quality | 75 |
| 7 | Discussion | 77 |
| 7.1 | Surface Passivation Quality of ALD-Al ₂ O ₃ on Black Silicon | 77 |
| 7.1.1 | Requirements for Surface Passivation of Black Silicon | 78 |
| 7.1.2 | Passivation of Dry Etched Black Silicon | 84 |
| 7.1.3 | Comparison of the Different Black Etching Methods | 85 |
| 7.1.4 | Microstructure of b-Si/Al ₂ O ₃ -Interfaces and the Passivation Mechanism | 87 |
| 7.2 | Recombination in Black Silicon | 92 |
| 7.2.1 | A Model to Distinguish Surface Enhancement from Damage | 92 |
| 7.2.2 | Analysis of the Origin of Recombination-Active Surface Defects in b-Si | 94 |
| 7.3 | Optics of Conformally Coated Black Silicon Nanostructures | 96 |
| 7.3.1 | Anti-Reflection Properties | 96 |
| 7.3.2 | Light Trapping Properties | 98 |

| | |
|--|---------------|
| 8 Summary and Conclusions | 103 |
| 8.1 Summary and Conclusions | 103 |
| 8.2 Outlook | 106 |
| References | cxviii |
| Bibliography | cxviii |
| List of the Author's Publications | cxix |
| A Appendix | cxxiii |
| A.1 The AM1.5G Spectrum | cxxiii |
| A.2 Growth Per Cycle | cxxiv |
| A.3 ICP-RIE b-Si Etching Parameters | cxxiv |
| A.4 ALD Film Homogeneity and Wafer Cleavage Scheme | cxxv |
| A.5 ALD-Al ₂ O ₃ on Ag MACE NW b-Si Structures | cxxv |
| A.6 Supplm. Info. on the Analysis of the Carrier Lifetime with Respect to the Homogeneity of the Interfacial SiO _x and ALD Films | cxxvi |
| A.6.1 Intefacial SiO _x | cxxvi |
| A.6.2 Influence of the Al ₂ O ₃ | cxxvi |
| A.7 Chemical Analysis of Etching Residues on b-Si Surfaces by ICPMS | cxxix |
| A.7.1 ALD Precursor Purity Investigated by ICPMS | cxxix |
| A.8 Discussion of Error Sources | cxxix |
| A.8.1 Optics - Focused <i>vs.</i> Unfocused Beam Setup | cxxix |
| A.8.2 Discussion of Error Sources for the Lifetime Measured on b-Si Wafers | cxixii |
| A.8.3 ICP-RIE Process Stability | cxixiii |
| Acknowledgements / Danksagung | cxixv |
| Curriculum Vitae | cxixix |

List of Figures

| | | |
|-----|---|----|
| 1.1 | According to the estimation of Green [51] the plot shows for which approximate surface recombination velocities a solar cell would be limited. | 3 |
| 1.2 | Simulations calculated with PC1D for a 25 μm thick p-type Si solar cell with a diffused, high P-doped front emitter and a perfect rear-side mirror under one sun illumination. | 5 |
| 2.1 | Semi-logarithmic plot of the absorption coefficient of intrinsic c-Si. | 8 |
| 2.2 | Different non-resonant light trapping schemes. In the upper row the slabs are bifacially structured, whereas the lower row shows single-side structured wafers with a back-side mirror. | 8 |
| 2.3 | Recombination mechanisms in c-Si. | 14 |
| 3.1 | ICP-RIE process and the plasma process chamber | 23 |
| 3.2 | Schematic depiction of the b-Si nanostructuring methods: ICP-RIE, MACE, and MacP-Si | 25 |
| 3.3 | Schematic of a typical ALD cycle. | 33 |
| 3.4 | Growth per cycle of ALD- Al_2O_3 on $-\text{OH}$ -terminated Si | 34 |
| 3.5 | The ALD window is defined as the temperature range of a constant gpc. Mechanisms causing gpc changes are also indicated. (Adapted from [45]) | 35 |
| 3.6 | gpc as calculated from 1000 cyc. Al_2O_3 on polished Cz Si wafers with native SiO_2 for symmetric pulse and purge times. NV: needle valve. | 35 |
| 3.7 | gpc in dependence of the purge time after the H_2O pulse. | 36 |
| 3.8 | A thin film deposited onto rod-like features by the diffusion limited PVD technique (a) and the reaction-limited ALD method (b). | 37 |
| 3.9 | Step coverage b/a , conformality c/b , and bottom coverage d/a of films deposited on a structured substrates. | 37 |
| 4.1 | Measurement setup for quasi-steady-state photoconductance determination of the charge carrier lifetime. | 40 |

| | | |
|------|---|----|
| 4.2 | A variety of different electron-matter interactions occurring in scanning and transmission electron microscopy measurements. | 43 |
| 4.3 | Schematic of an ellipsometry measurement setup. | 45 |
| 5.1 | cross-sectional SEM micrographs of the three ICP-RIE model structures. The images were recorded by Thomas Käsebier and are courtesy of the IAP, FSU Jena. | 48 |
| 5.2 | SEM top-view of the shallow and deep ICP-RIE b-Si. | 48 |
| 5.3 | FIB slicing of a deep b-Si structure (a) and the 3D surface reconstruction of an intermediate b-Si (b). | 49 |
| 5.4 | SEM images of FIB cut cross sections of the three ICP nanostructures prepared on Cz material coated with 1000 ALD cycles of Al_2O_3 . The dielectric layer conformally covers perfectly all rough surfaces. | 51 |
| 5.5 | SEM micrographs of the three ICP-RIE model structures coated with 300 cyc of Al_2O_3 , corresponding to a film thickness of $\approx 33.2 \pm 5.9$ nm. The dielectric is highly conformal and extremely homogeneous. | 52 |
| 5.6 | FIB cut b-Si surfaces (dark gray) passivated with 52 nm of SiN_x (light gray) deposited by PECVD. Film homogeneity and step coverage are good on the shallow but rather poor on the deep structured b-Si surface. | 53 |
| 5.7 | TEM images of an unstructured (a) and an ICP-RIE structured intermediate b-Si/ Al_2O_3 -interface (b). | 53 |
| 5.8 | Micrographs and elemental analysis maps measured by scanning TEM EDX of ICP-RIE nanostructured intermediate b-Si/ Al_2O_3 -interfaces. | 54 |
| 5.9 | (a) The industrial standard KOH random pyramid texture. (b) ICP etching leads to the superstructure: shallow b-Si on KOH pyramids. | 55 |
| 5.10 | Black Si nanostructures prepared by MACE with Ag (a,b,c) and Au (d,e) catalysts. The thin ALD- Al_2O_3 passivation layer covers all b-Si surfaces perfectly conformal. Image (f) shows the macP-Si surface passivated with 300 cyc Al_2O_3 | 57 |
| 5.11 | Reflection ($R(\lambda)$, dashed) and absorption ($A(\lambda)$, solid) spectra of a polished reference and the three single side structured ICP-RIE b-Si surfaces as measured with the unfocussed beam setup. All samples are uncoated. For comparison, simulated spectra of a hypothetical perfect anti-reflection coating without (dotted) and with Lambertian light-trapping (dash-dotted) are also shown. | 59 |
| 5.12 | Angular dependence of the total integrated absorption of a shallow and a deep b-Si structure as tilted against the incident light beam. | 59 |
| 5.13 | Total integrated absorption of an out-of-box reference and single side ICP-RIE structured Cz b-Si wafers coated with varying numbers of Al_2O_3 ALD cycles. | 60 |

| | | |
|------|--|----|
| 5.14 | Hemispherical absorption spectra of bifacially processed ICP-RIE structured FZ b-Si wafers passivated with 300 cyc Al_2O_3 | 61 |
| 5.15 | Absorption of identically passivated wet chemically processed bifacial b-Si in comparison to KOH pyramids, the oob reference, and the theoretical limits in the UV/VIS (a) and NIR (b) spectral region. | 62 |
| 5.16 | Total integrated optical absorption, $\langle A \rangle$, of the presented b-Si samples in the wavelength range between 300 nm and 1180 nm. | 62 |
| 6.1 | (a) Schematic of the processing steps in the performed passivation experiments. (b) Typical minority charge carrier lifetime evolution during a passivation procedure. . . . | 64 |
| 6.2 | Impact of the ALD deposition temperature on the lifetime after passivation with 150 ALD cycles and subsequent PDA for 30 minutes at 400 °C in low pressure Ar atmosphere. | 65 |
| 6.3 | Lifetime of Al_2O_3 passivated samples deposited with different purge times following the water pulse, $t_{\text{H}_2\text{O,purge}}$ | 66 |
| 6.4 | Lifetime evolution during optimization of the ALD parameters plotted against the number of deposited Al_2O_3 ALD cycles on shiny-etched p-type FZ Si. | 66 |
| 6.5 | Passivation efficiency of ultra-thin Al_2O_3 layers after PDA. | 67 |
| 6.6 | (a) Oxide thickness of a 300 cyc thick Al_2O_3 film on an RCA cleaned wafer as measured by ellipsometry. (b) shows the according lifetime map of the same wafer determined by calibrated PL spectroscopy at an injection level close to $\Delta n = 10^{15} \text{ cm}^{-3}$. The lifetime appears to be high, where the oxide is thin. | 68 |
| 6.7 | (a) Lifetime homogeneity and reproducibility of p-type FZ oob wafers passivated with 2000 cyc of Al_2O_3 . The highest lifetimes in the middle of the wafers are approximately $\tau_{\text{eff}} \approx 5 \text{ ms}$ and therefore extremely close to the Auger limit for this doping level and wafer thickness as estimated by Richter <i>et al.</i> [131] (b) This results in a SRV of $S_{\text{eff}} < 2.3 \text{ cm/s}$ in the case of the best samples. | 68 |
| 6.8 | Impact of PDA temperature (a) and PDA duration (b) on the lifetime in two out-of-box wafers passivated with 150 ALD cycles Al_2O_3 | 69 |
| 6.9 | HF dipped samples rinsed under water of different sources before Al_2O_3 passivation leads to a more severe lifetime degradation with increasing contamination level. | 70 |
| 6.10 | Lifetime in FZ Si after application of the different indicated handling/cleaning sequences. The RCA sequence based on “supra” grade solution yields a more homogeneous lifetime distribution on unstructured Si and enables the desired cleaning effect required for b-Si surfaces prior to passivation. | 70 |
| 6.11 | PDA temperature optimization of 300 cyc thick Al_2O_3 passivation layers on the intermediate structure. | 71 |

| | | |
|------|--|---------|
| 6.12 | Al ₂ O ₃ passivation layer thickness series on intermediate b-Si annealed at $T_{\text{PDA}} = 370$ °C. | 71 |
| 6.13 | The highest lifetimes and lowest SRVs of ICP-RIE processed b-Si on Cz (a) and FZ (b) wafers, respectively demonstrated the feasibility to effectively passivate b-Si for the first time [119]. | 72 |
| 6.14 | SiN _x passivated shallow and deep b-Si surfaces in comparison to their according reference and Al ₂ O ₃ passivated samples. | 73 |
| 6.15 | Best and average lifetime in Al ₂ O ₃ passivated ICP-RIE processed b-Si Cz wafers that were etched for the indicated time. | 74 |
| 6.16 | Minority carrier lifetime <i>vs.</i> the ICP-RIE CCP power. | 74 |
| 6.17 | Measured lifetime of the wet-chemically (MACE and macP-Si) structured b-Si surfaces and their according reference samples fabricated without the black etching step. | 76 |
| 6.18 | Overview of the effective lifetimes of Al ₂ O ₃ passivated b-Si surfaces in comparison to the unstructured and KOH textured references. | 76 |
| 7.1 | Schematic comparison of fictive lifetimes in oob and b-Si wafers and their evolution during RCA cleaning. | 83 |
| 7.2 | The plot shows an overview of measured lifetimes in correlation to the total absorptance integrated over the indicated spectral width. | 86 |
| 7.3 | Ellipsometry and lifetime mappings of the oxide (SiO _x) thickness grown during a 10 min RCA SC2 cleaning step. | 88 |
| 7.4 | Depth profiles of the Si fraction, f , of some b-Si structures as extracted from FIB cross sections. | 97 |
| 7.5 | Average b-Si absorption in the light-trapping regime <i>vs.</i> the correlation length L_c (a) and the peak-to-valley height H (b). | 99 |
| A.1 | The AM1.5G spectrum. See text for further explanation. | cxxiii |
| A.2 | Thickness and average gpc of Al ₂ O ₃ on polished oob and HF-dipped Cz Si substrates. | cxxiv |
| A.3 | Wafer cleavage schemes for (a) 7, and (b) 21 pieces. | cxxv |
| A.4 | FIB cut cross sections of the Al ₂ O ₃ passivated long b-Si NWs (Ag-MACE). The coating completely covers the surface of the nanostructures. | cxxv |
| A.5 | Ellipsometry and lifetime mappings of the oxide (SiO _x) thickness grown during a 20 min RCA SC2 cleaning step. | cxxvii |
| A.6 | PL lifetime maps of wafers after RCA cleaning for 10 min and 20 min. | cxxviii |
| A.7 | Ellipsometry mapping of the "native" oxide thickness on an oob wafer. It appears clear that the oxide is symmetrically thicker on a diagonal line. | cxxviii |

A.8 Elemental concentrations of the indicated metals at the surface (a), in the SiO_x layer (b), and in the near-surface Si bulk (c) as measured by ICPMS in ICP-RIE b-Si. . . . cxxxix

A.9 Reflectance data measured with the unfocused light spot *vs.* data measured with the focused beam setup. cxxxii

A.10 Overview of the three highest available lifetime values from each processed sample set in the big b-Si passivation experiment series by chronological order. cxxxiii

List of Tables

| | | |
|-----|--|-------|
| 3.1 | Parameters of the different b-Si samples prepared by MACE. | 28 |
| 3.2 | Summary of the standard conditions used for surface passivation. | 37 |
| 4.1 | Optical constants as used for QSSPC measurements. | 40 |
| 5.1 | Process parameters of the three ICP-RIE processed standard structures. | 48 |
| 6.1 | Summary of the lifetime and SRV in Al ₂ O ₃ passivated b-Si wafers. | 76 |
| 7.1 | Overview of the passivated b-Si samples and references of the comparison series. Shown are the passivation quality (τ_{eff} , S_{eff}), and the surface enhancement and defect density enhancement factors γ and δ , respectively. Furthermore, the geometric surface parameters and optical performance indicators of the b-Si samples are listed with their overall optical absorption, the relative UV/VIS absorption, and the LT performance (absolute $\langle A_{\text{LT}} \rangle$, and relative to the Lambertian scatterer $\langle A_{\text{LLT}} \rangle$). | 101 |
| A.1 | Maximum short circuit current (I_{sc}) contained in the AM1.5G one sun solar spectrum. | cxxiv |
| A.2 | Typical ICP-RIE etching parameters of the 'standard' b-Si processes (IAP, FSU Jena). | cxxiv |
| A.3 | Summary of ICPMS analyzed b-Si samples. | cxxx |

Nomenclature

SYMBOLS:

| | |
|--------------------|---|
| $:=$ | definition |
| ["] | inches |
| α | optical absorption coefficient |
| ΔG | change in Gibbs free energy |
| Δn | <i>excess</i> minority charge carrier density / “injection level” |
| Δ | rotation of the polarization angle (ellipsometry) |
| δ | relative defect density in b-Si ($D_{S,nano}/D_{S,ref}$) |
| η | efficiency |
| γ | surface area enhancement factor (A_{nano}/A_{ref}) |
| $\mu_{n,p}$ | mobility electrons and holes, respectively |
| φ | phase shift |
| Ψ | amplitude change of the reflected light (ellipsometry) |
| σ_L | photoconductance |
| $\sigma_{n,p}$ | capture cross section of electrons and holes, respectively |
| τ_A | Auger lifetime |
| τ_b | carrier lifetime in the Si bulk |
| τ_{eff}, τ | effective carrier lifetime |
| τ_{rad} | carrier lifetime concerning radiative decays |
| τ_{SRH} | Shockley-Read-Hall impurity lifetime |
| τ_s | carrier lifetime at the surface |
| $A(\lambda)$ | absorptance |
| B | probability for spontaneous radiative recombination |
| d | film thickness |
| D, D_n, D_p | diffusivity, electron and hole diffusion constants |
| D_{it} | interface density of states |
| E_c | conduction band edge energy |
| E_F | Fermi energy |
| E_g | band gap energy (for Si: $E_g=1.12$ eV) |
| E_v | valence band edge energy |
| G | generation rate of charge carriers |
| h | Planck’s constant |
| I_{SC} | short circuit current |

| | |
|---|---|
| k_B | Boltzmann's constant |
| n | electron density in non-equilibrium, number of (ALD) cycles ("cyc"), refractive index |
| n_0 | electron density in thermal equilibrium |
| N_A, N_D | concentration of dopand atoms, acceptors (A) and donors (D), respectively |
| N_C, N_V | effective density of states in the CB and VB, respectively |
| n_i | intrinsic carrier concentration |
| N_t | trap state density |
| N_{it} | interface trap state density |
| p | hole density in non-equilibrium |
| p_0 | hole density in thermal equilibrium |
| q | elementary charge |
| R | total recombination rate of charge carriers |
| $R(\lambda)$ | reflectance |
| $S, S_{\text{eff}}, S_{\text{max}}$ | surface recombination velocity (SRV), effective SRV, maximal SRV, respectively |
| t | time |
| $T(\lambda)$ | transmittance |
| $t_{\text{H}_2\text{O,purge}}$ | purge time after the H ₂ O pulse |
| T_{ALD} | ALD deposition temperature |
| T_{PDA} | post-deposition annealing temperature |
| $t_{\text{TMA,purge}}$ | purge time after the TMA pulse |
| U_A | Auger recombination rate |
| U_b | recombination rate in the Si bulk |
| U_{rad} | radiative recombination rate |
| U_{SRH} | Shockley-Read-Hall recombination rate |
| U_s | surface recombination rate |
| V_{OC} | open circuit voltage |
| v_{th} | thermal velocity (of charge carriers) |
| W | wafer thickness |

ABBREVIATIONS:

| | |
|------------------------|----------------------------------|
| $\mu\text{c-Si}$ | micro-crystalline silicon |
| a-Si:H | hydrogenated amorphous silicon |
| ALD | atomic layer deposition |
| AR | anti reflection; anti reflective |
| ARC | anti reflection coating |
| b-Si | black silicon |
| c-Si | mono-crystalline silicon |
| CB | conduction band |
| CCP | capacitive coupled plasma |
| Cz | Czochralski (Si) |

| | |
|------------|---|
| DEZ | diethylzinc, $\text{Zn}(\text{C}_2\text{H}_5)_2$ |
| DI | de-ionized (water) |
| EDX | energy dispersive x-ray spectrometry |
| EELS | electron energy loss spectroscopy |
| EF-TEM | energy filtered transmission electron microscopy |
| FIB | focused ion beam |
| FZ | float zone (Si) |
| gpc | growth per (ALD) cycle |
| ICP-RIE | inductive coupled plasma reactive ion etching |
| ICPMS | inductive coupled plasma mass-spectrometry |
| IPA | isopropyl alcohol |
| IQE | internal quantum efficiency |
| MACE | metal assisted wet-chemical etching |
| mc-Si | multi-crystalline silicon |
| PC1D | a free solar cell device simulation software [22] |
| PDA | post-deposition annealing |
| PECVD, CVD | plasma enhanced chemical vapor deposition, chemical vapor deposition |
| QSSPC | quasi-steady-state photoconductance |
| RCA | standard cleaning procedure defined by the Radio Cooperation of America |
| RT | room temperature (≈ 300 K) |
| S | chemical element sulfur. ¹ Other elements are not listed |
| S-TEM | scanning transmission electron microscopy |
| SEM | scanning electron microscopy |
| SRH | Shockley-Read-Hall |
| SRV | surface recombination velocity |
| TEM | transmission electron microscopy |
| TMA | trimethylaluminium, $\text{Al}(\text{CH}_3)_3$ |
| VB | valence band |

¹Not to be confused with $S = S_{\text{eff}}$.

Chapter 1

Introduction

On our way into a future of greatly growing demands for high amounts of energy, a sustainable supply management will require solar power generation as a key technology. Specifically, clean electric power generation by photovoltaic (PV) light conversion will be valuable for the industry as well as for worldwide off-grid applications in developing countries. Within the PV sector, the lion share of solar cell systems has been based on crystalline silicon (c-Si) absorbers throughout the last decades and this trend is expected to go on [141]. The same prognosis aims for increasing solar cell efficiencies and simultaneously decreasing absorber thickness (i.e. higher material efficiency), for which the main driving factor is simply a reduced cost per watt peak.¹ However, c-Si comes with the drawback of low optical absorption, which quickly becomes a limiting factor in thin wafers. Therefore, innovative light trapping concepts are necessary allowing for effective light absorption in thin c-Si slabs while guaranteeing a high electrical output. As will be shown, optimal light trapping as given by a Lambertian scatterer requires a rough surface, whereas the electronic surface properties tend to be better in the case of smooth surfaces because generated (excited) charge carriers recombine, i.e. decay to the ground state, preferably at rough interfaces/surfaces. The reduction of this recombination is called passivation. The two demands of good light trapping and high electrical surface quality are competing with each other and the recombination losses likely overcompensate the optical gain. Hence, it is a challenging task to find a solution tackling both, which has been a subject of investigations for decades. Finding an easy-to-apply solution will pave the road to a whole new generation of cost effective PV systems.

Micro- and nanostructured silicon surfaces are widely known to have a high potential for various applications in terms of optical benefits or concerning the large surface area enhancement. Water-splitting by photo-electrochemical catalysis [98, 111] for regenerative fuel production, highly sensitive optical and chemical detection devices [46, 58], photo-diodes [151], and terahertz-emitters [69], MEMS [76] and the usage as hydrophilic bactericidal substrates [74] are just some of the fields of interest besides photovoltaic crystalline silicon solar cells [112, 128]. Some of these were already mentioned in the paper called “the black silicon method” by Jansen *et al.* [76]. However, the mentioned disadvantage of

¹Colloquially, the nominal power of a solar module is expressed in kWp (*read: kilo watt peak*), meaning the maximum output power of the module under standard conditions, i.e. illumination with the AM1.5G spectrum (see footnote 7 and section A.1 in the appendix) and an intensity of 1000 W/m² at a cell temperature of $T_{\text{cell}} = 25$ °C.

high surface recombination losses in solar cells based on optically advantageous black silicon absorbers has not yet been resolved. To overcome this decisive drawback, an effective surface passivation scheme for black silicon is required.

This first chapter (1) of this thesis starts with a motivation why surface passivation is so important for solar cells in general and especially if nanostructured absorbers are used. In chapter 2 the theoretical groundwork will be presented by introducing the fundamental optical and electronic properties necessary for the understanding of black silicon surfaces and recombination processes. chapter 3 explains the sample preparation in some detail, followed by important analysis tools in chapter 4. The results are organized in two chapters, which deal with the micro-structural and optical properties of black silicon surfaces (chapter 5) followed by the most important findings of this work on black silicon surface passivation in chapter 6. The heart-piece of this work is the discussion in chapter 7. The monograph closes with the summary, conclusions and an outlook given in chapter 8.

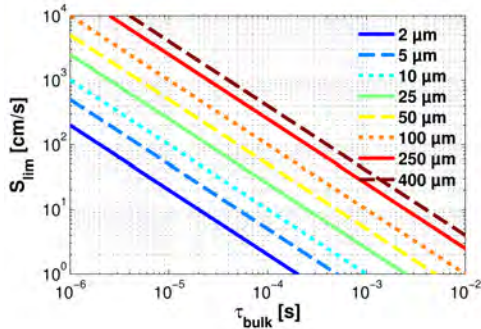


Figure 1.1: According to the estimation of Green [51] the plot shows for which approximate surface recombination velocities $S_{\text{lim}} \approx \frac{W}{\tau_{\text{bulk}}}$ a solar cell would be limited. Lower SRV values ($S < S_{\text{lim}}$) are acceptable. The parameter variation indicates the trend for a variety of wafer thicknesses W . It can be deduced that for thinner wafers as well as higher bulk lifetimes a higher degree of surface passivation (i.e. lower S) is needed.

1.1 Motivation: Limiting Effects in Crystalline Silicon Solar Cells

According to Shockley and Queisser the maximum efficiency of a single junction solar cell depends mainly on the band gap energy, E_g , of the semiconductor material used for light conversion [143]. In their paper on the detailed balance limit of efficiencies this maximum for c-Si with a band gap of $E_g = 1.12$ eV was calculated to be $\eta \approx 29\%$ [143]. Fundamental physical processes required by thermodynamics and quantum mechanics dictate the major limitations. The ultimate efficiency was calculated under the assumption that each photon with an energy $E_{\text{ph}} \geq E_g$ elevates one electron from the valence to the conduction band generating an electron-hole pair with a voltage of $V_g = \frac{E_g}{q}$ independent of the photon's actual energy [143]. This assumption is motivated by “thermalization” processes in which the excess energy of the charge carriers is passed to the crystal-lattice by collisions with phonons (i.e. converted into heat). However, this limit can only be reached if a number of idealizations are made, e.g. an absorption of unity combined with the described perfect IQE,² as well as no further charge carrier loss mechanisms³ besides intrinsic radiative and Auger recombination. The latter represents the most severe intrinsic bound to PV solar power conversion in c-Si [51]. Hence, the most important question is: Which loss mechanism actually limits the solar cell efficiency?

The first limitation to a semiconductor with a high refractive index like c-Si ($n \approx 3.5$) is of an optical nature. A polished Si surface on average reflects more than 30% of incident light. Hence, very effective anti-reflection (AR) measures are required for maximum light injection. In addition, the indirect semiconductor Si only weakly absorbs light close to the band gap energy. Therefore, effective light trapping (LT) is important to reach maximum absorption, i.e. structures that guide the weakly absorbed near-infrared (NIR) light through the cell multiple times until it is eventually absorbed. When the optical absorption is maximized, loss mechanisms reducing the carrier concentration become limiting to the current. Besides the mentioned intrinsic limits, crystal-defect related charge carrier recombination in the bulk becomes an issue. However, in high quality substrates and especially with decreasing wafer thickness [51,156] losses in the bulk linearly decrease, but recombination at the front and rear surfaces gain importance.

After Green [51] c-Si solar cells are intrinsically limited by Auger recombination. The highest possible efficiency including this limitation may be reached as long as the surface recombination velocity (SRV) is lower than the ratio of $\frac{W}{\tau_b}$, where W is the thickness of the wafer and τ_b its bulk lifetime [51].

²The internal quantum efficiency (IQE) is the fraction of absorbed photons that will contribute to the output current, i.e. Shockley and Quisser assumed an ideal IQE.

³The different recombination mechanisms will be introduced in sec. 2.2.1.

Figure 1.1 depicts the limiting S -values for a variety of wafer thicknesses over a range of bulk lifetimes. It is obvious, that the SRV must already be rather small ($S \approx 4$ cm/s) for thick wafers (400 μm) with high bulk lifetimes (10 ms) to reach the condition of non-limiting SRV. However, on thinner wafers, the surface to volume ratio and therefore the impact of S becomes even larger. It is important to note that the effective carrier lifetime,⁴ τ_{eff} , (only) needs to be high enough for the charge carriers to diffuse to the junction interface, such that the diffusion length is $L = \sqrt{D \cdot \tau_{\text{eff}}} \geq W$, where D is the diffusivity⁵ of the carriers within the bulk. Thus, for a thin wafer ($W \approx 25$ μm) effective carrier lifetimes in the range of 20–100 μs are sufficient and would require SRVs below 125–25 cm/s, respectively.

Figure 1.2 shows simulated surface plots of a solar cell based on a 25 μm thin wafer with a bulk lifetime of $\tau_b = 100$ μs . It has a 500 nm P-doped (n-type) front emitter with a sheet resistance⁶ of 250 Ω/\square and a perfect rear-side mirror and is illuminated by the air mass 1.5 global (AM1.5G [4])⁷ one sun spectrum with 0.1 W/cm^2 . The device was calculated based on a very simple model implemented with the simulation software PC1D assuming absorption up to unity, which, as will be shown, is not realistic in the case of a 25 μm wafer.⁸ The qualitative trends with respect to the SRV and the optical absorption, however, are demonstrated for the open circuit voltage, V_{oc} , and the short circuit current, I_{sc} . The open-circuit voltage in fig. 1.2(a) depends logarithmically on recombination within the active areas of the cells [185] and therefore shows a rather strong dependency on the surface recombination velocity if $S_{\text{eff}} \gtrsim 10$ cm/s, meanwhile it is almost completely independent of the optical absorption of the device. In contrast, the short circuit current shows a strong dependency on the optical absorption and is constant as long as $S_{\text{eff}} \lesssim 10^3$ cm/s. For a reduced S_{eff} , the optical absorption becomes limiting to the thin solar cell device. These trends are more obvious in fig. 1.2(c). The product of $V_{\text{oc}} \cdot I_{\text{sc}}$, depicts a maximum efficiency⁹ (not shown) indicating that no significant efficiency gain is expected for SRVs below 20 cm/s. This phenomenon may be explained as follows: For low S_{eff} Auger recombination in the emitter region becomes equal or greater than surface recombination losses. The Auger effect only depends on the charge carrier concentration due to doping or carrier generation and thus constitutes a hard intrinsic physical limit which cannot be overcome. Hence, further reduction of the surface recombination velocity is not necessary and the absorption in the slab has to be maximized while a low S_{eff} is maintained.

To date, the optical absorption of mono-crystalline (c-Si) wafers is improved by anisotropic alkaline etching of the diamond-cubic Si crystal lattice, which results in structures of intersecting (111) crystallographic planes [18]. The geometric light trapping of such structures represents the state of the art for industrial solar cells [18], but the residual surface reflection is still about 10% [89]. Hence, for good light injection in the UV and VIS spectral range an additional anti-reflection coating (ARC) is necessary, which may reduce the reflectance to a few percent. However, due to the $\lambda/2$ -condition for destructively interfering waves, such ARCs work efficiently only for a narrow range of wavelengths.

⁴The effective carrier lifetime is governed by the “shortest path” to recombination, and will be introduced in 2.2.

⁵typically $D_n \approx 30$ cm^2/s for electrons and $D_p \approx 12$ cm^2/s for holes.

⁶The unit of the sheet resistance is Ω/\square , read: *Ohm per square*.

⁷The Air Mass 1.5 Global spectrum defined by the “American Society for Testing and Materials (ASTM)” is the “Terrestrial Reference Spectra for Photovoltaic Performance Evaluation” [4]. See appendix A.1 for more details.

⁸see footnote 21 of sec. 7.1.3.

⁹for a fill-factor of unity

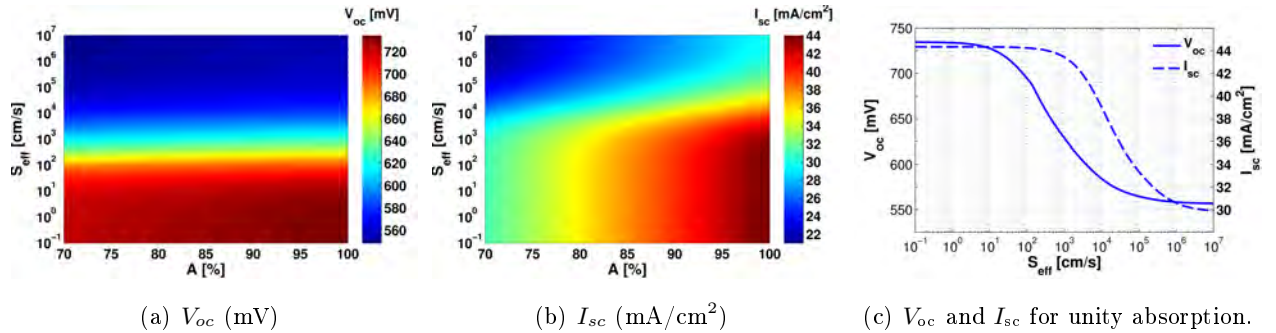


Figure 1.2: Simulations calculated with PC1D for a $25 \mu\text{m}$ thick p-type Si solar cell with a diffused, high P-doped front emitter and a perfect rear-side mirror under one sun illumination. (a) shows the hypothetical open circuit voltage, V_{oc} , for a large range of SRV and absorptance. In (b) the short circuit current, I_{sc} , is plotted for the same set of parameters. (c) represents a cut through the surface plots (a) and (b) for unity absorption.

To apply even better AR measures, stacks of multiple coatings with different refractive indices are necessary [36, 185] and quite costly. In addition, the best available geometric structures [17, 18] (e.g. inverted pyramids) require lithography, that, with respect to the strongly demanded cost reduction in silicon PV, cannot be used for solar cell fabrication. Furthermore, alkaline textures have the disadvantage to work only on (100) oriented wafer surfaces and hence are not applicable to any low cost multi-crystalline silicon (mc-Si) materials.

1.2 Advantages and Challenges of Black Silicon

A simple solution to overcome the mentioned optical drawbacks of alkaline textures is to apply micro- or nanostructures, which offer broad-band and quasi-omnidirectional anti-reflection properties [70] and make the Si surface appear macroscopically black.

In this work the term **Black Silicon** (b-Si) will be used for all randomly structured silicon interfaces with lateral feature sizes in the sub-micron range that exhibit a significantly reduced optical reflectance in the ultraviolet (UV), visible (VIS) and near infrared (NIR) spectral range without additional ARC and have a homogenous black visual appearance.¹⁰

We will learn that due to a b-Si surface, light coupling into the solar cell and the absorption of near band edge photons are improved. Higher optical absorption increases the short circuit current and on a logarithmic scale also the open circuit voltage. Alternatively, light trapping in b-Si slabs might allow to reduce the solar cell thickness while preserving a high absorptance. In that case, non-radiative bulk recombination losses are reduced, leading to an increased open circuit voltage [51, 156]. On the one hand, reducing the thickness increases the material efficiency and therefore helps to reduce the production cost, which is a holy grail in c-Si solar cell production [61]. On the other hand, in thinner wafers, the surface to bulk ratio increases, which raises the demand for increased surface passivation performance. Hence, b-Si can help to approach the limiting efficiency of c-Si solar cells and improves the material efficiency if the surfaces may be effectively passivated.

Experimentally, different implementations have been proposed to modify the optical properties of c-Si absorbers by mask-less (lithography-free) nanostructuring processes. The four most com-

¹⁰Definition in accordance to [113].

monly used methods for demonstrating the potential applicability of b-Si in solar cells are dry reactive ion etching (RIE) [23, 48, 70, 73, 76, 139, 173, 180, 181, 184], metal-assisted chemical etching (MACE) [12, 57, 85, 97, 109, 111, 158, 183], electrochemical structuring of macroporous silicon (macP-Si) [5, 13, 38, 46, 96, 120, 152], and femto-second (fs) laser structuring (L-Si) [47, 58, 84, 133, 172, 182]. Many of these methods allow the characteristic size distribution of randomly emerging sharp silicon needles to be tailored for high optical absorption efficiency. As an example, inductive coupled plasma reactive ion etching (ICP-RIE, short ICP) works on all Si crystal orientations (c-Si and mc-Si) [139] and even on micro-crystalline (μ c-Si) and amorphous (a-Si) thin films and makes additional ARCs unnecessary.

Nevertheless, all these nanostructures with good optical properties exhibit the drawback of rather low electronic surface quality leading to strong surface recombination which is limiting the device performance already in thick absorbers [139, 181, 184]. The effect will critically exacerbate in thin devices which suffer from surface recombination even more severely than thick cells [52]. Yet, no convenient passivation scheme is available for b-Si to overcome this drawback. The most commonly applied passivation layers in the PV industry are SiN_x and a-Si:H, which are deposited on industrial scale by plasma-enhanced chemical vapor deposition (PE-CVD). Unfortunately, the processes can not be transferred to b-Si because the steep sidewalls of complex structured Si surfaces are not appropriately coated for passivation [38]. In the recent years, Al_2O_3 deposited by atomic layer deposition (ALD) gained a lot of interest due to its outstanding passivation performance on both n-type and p-type Si surfaces of almost any doping level [31, and references within]. The material offers an extremely high level of chemical passivation, i.e. saturation of electronic states at the Si surface. In addition, the strongest known field effect passivation was observed in Al_2O_3 coated Si, arising from a uniquely high density of fixed negative charges at the Si/ Al_2O_3 -interface ($Q_{\text{fix}} \sim 10^{12} \text{cm}^{-2}$). However, it remains unclear if ALD- Al_2O_3 is suitable for b-Si surface passivation since it had not been applied as a passivation approach prior to this work.

Conclusively, if no effective passivation can be provided in addition to the good optical properties, no profitable yield can be drawn from b-Si absorbers in solar cells. This work aims to develop a new state of the art passivation scheme that is powerful enough to effectively passivate b-Si, which would open the road to fully exploit the optical and structural benefits in many device classes.

Chapter 2

Theory

2.1 Light Trapping Concepts in Solar Cells

To achieve maximum solar cell efficiency in c-Si photon management is necessary to push the optical absorption to the limit. Silicon is a semiconductor with a high refractive index of $n \approx 3.5$, which in the case of a flat surface, gives rise to a high specular reflection¹ ($R > 30\%$) for any angle of incidence [70]. There are two types of anti-reflection (AR) schemes. The first type uses interference of light waves with wavelength λ . Given that the phase shift, φ , of the incident and reflected part is π , the waves interfere destructively and no energy is reflected. This can be done by an anti-reflection coating (ARC) with an optical thickness of $\lambda/4$ leading to an optical path difference of $\lambda/2$ at the air to ARC interface² ($\Rightarrow \varphi = \pi$). The approach is limited to a narrow range of wavelengths and angles of incidence. The range of operation may be extended by application of multilayer ARC stacks. However, in practice the cost for multilayer ARCs increases unproportionally rapid as compared to the optical gain. The second concept aims to reduce the step in the refractive index function at the air-to-Si interface. This may be achieved by formation of porous silicon layers with smoothly decreasing porosity from air to silicon, called a density-graded index profile [48, 146, 152]. It will be experimentally demonstrated, that such profiles can be produced by silicon nanostructures with diverse morphologies.³

Low broad-band¹ reflection leads to a high injection of light into the Si bulk. Silicon absorption is mathematically expressed by the imaginary part of the complex index of refraction, which is rather high for photons of short wavelengths. The absorption coefficient of Si exhibits two strong rising slopes at $\lambda = 370$ nm ($E_{\text{ph}} = 3.4$ eV) and $\lambda = 300$ nm ($E_{\text{ph}} = 4.2$ eV) indicating direct band-to-band transitions. The peaks can be interpreted as a characteristic for high optical crystal quality [3, 6]. The penetration depth of long wavelength photons ($\lambda \geq 800$ nm), however, is vastly larger. This becomes obvious from fig. 2.1 where the absorption coefficient is plotted. With increasing wavelength the absorption strength quickly drops over a few orders of magnitude. Therefore, the optical path

¹In the spectral range of $300 \leq \lambda \leq 1180$ nm, corresponding to the whole active absorption bandwidth of Si.

²if $n_1 < n_2 < n_3$; Furthermore, for optimal AR behavior the refractive indices must obey the relation $n_2 = \sqrt{n_1 n_3}$, which is the case for SiN_x ($n_2 \approx 1.9$) between air ($n_1 \approx 1$) and Si ($n_3 \approx 3.5$). For the coupling from quartz glass ($n_1 \approx 1.46$) to Si the optimal refractive index of SiN_x is slightly higher ($n_2 \approx 2.26$).

³see sec. 5.3.2.

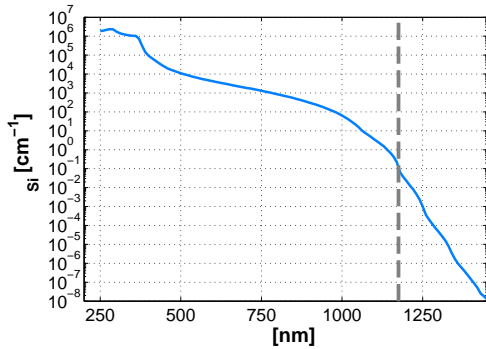


Figure 2.1: Semi-logarithmic plot of the absorption coefficient of intrinsic c-Si after Green [54]. The optical absorption edge is indicated by the dashed gray line.

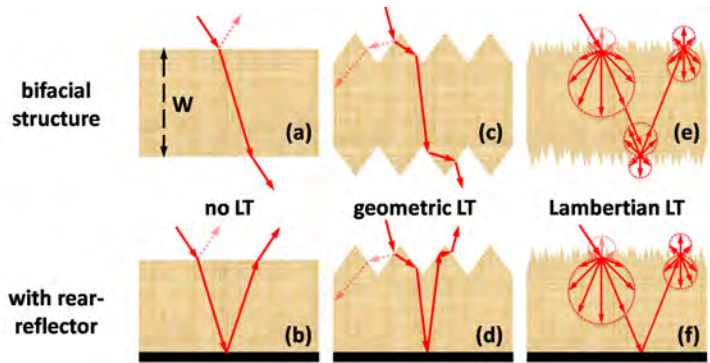


Figure 2.2: Different non-resonant light trapping schemes. In the upper row the slabs are bifacially structured, whereas the lower row shows single-side structured wafers with a back-side mirror. Structures are not to scale.

length of weakly absorbed photons ($E_{\text{ph}} \approx E_g$) in the absorber has to be increased to maximize absorption. The thicker the wafer appears to the traversing light, the higher becomes its absorption probability. With increasing absorption, and simultaneously high IQE, the resulting short circuit current increases. This way either a higher conversion efficiency can be attained in a solar cell with the same wafer thickness, or the absorber thickness can be reduced while I_{sc} is maintained, allowing for a higher material efficiency [126]. Additionally, decreasing cell thickness helps to reduce bulk recombination, which may in turn increase the open circuit voltage as long as the cell is not limited by surface recombination [51]. Effective light trapping⁴ (LT) is accomplished by surface structures which guide the light through the absorber slab multiple times.

2.1.1 Geometric Light Trapping

Conventionally used artificial LT schemes rely on structures that lead to (total) internal reflection and can be derived by ray optics [17, 18, 174, 177]. The light trapping concepts used in this work are depicted in fig. 2.2. The simplest enhancement is obtained by application of a rear-reflector which eliminates the escape possibility at the back-side of the cell and increases the path length by a factor of two (fig. 2.2 (b)) as compared to a single pass through the cell (fig. 2.2 (a)).⁵ Even without a rear-reflector for internal angles of incidence larger than $\theta_c \approx 16.6^\circ$ total (internal) reflection is reached at the polished Si/air-interface.⁶ Hence, a rear reflector only operates in the “loss-cone” ($\theta < \theta_c$).

Inverted pyramids with a rear-reflector (2.2 (d)) and double-layer ARC are used in the world-record high-efficiency single-junction silicon solar cells with conversion efficiencies over 24% [185] and are state-of-the-art. In addition to the LT effect, initially reflected light from the surface gets a second chance to enter the absorber as indicated by the semi-transparent (dashed) rays. However, even in the case of the PERC solar cell with a 110 nm SiO_2 single layer ARC introduced by Blakers *et al.* a more effective reduction of the front surface reflectance was expected to improve I_{sc} [10]. The pyramid

⁴LT is the artificial “thickening” of absorbing material by prolongation of the light path inside it.

⁵Note, that metallic back reflectors may lead to parasitic absorption.

⁶The critical angle depends on the refractive indices $\theta_c = \arcsin\left(\frac{n_2}{n_1}\right)$, with $n_1 \approx 3.5$ for Si and $n_2 \approx 1$ for air. However, due to symmetry reasons, incident light never leaves the loss-cone if no LT structures are applied.

geometry has to be carefully optimized to fit the wafer thickness, W . Otherwise, the light may be very effectively coupled out of the device if a back reflected ray hits a perpendicular facet [18]. Therefore, the best geometric LT designs for such high-efficiency solar cells require many lithography steps. In addition, the deposition of ARCs is necessary. Furthermore, the structures are angular selective [179]. Randomly oriented pyramids offer better LT because of their randomizing effect. They are easier to apply and represent the industrial standard. However, even with an optimized SiN_x coating their AR effect is weaker as not every reflected ray will hit another pyramid facet.

Note, that bifacial application of (random) pyramid structures (2.2 (c)) would lead to ideal LT only if a perfect back-side mirror were present [18]. In this work however, the main research topic is to investigate the minority charge carrier lifetime as a function of the surface morphology to be used as an indicator for the electronic surface quality, which requires bifacially identical wafer surfaces without any metals. Thus, structures with rear-reflectors have not been produced.

2.1.2 Randomizing Structures and the Yablonovitch Limit

The most effective LT concept for Si is to fully randomize the incident light rays. Thereby, the whole available optical phase space is filled [174]. The highest degree of randomization is achieved by the introduction of a Lambertian scatterer at one (or both) surface(s) leading to a cosine-distribution as depicted in fig. 2.2 (e) and (f). A true Lambertian scatterer operates fully independent of the angle of incidence, which requires multiple scattering events in the scattering layer. It is, however, challenging to implement such a behavior in a thin sheet of b-Si.

The Lambertian approach yields the so-called “ergodic” or “Yablonovitch” path length enhancement limit of $4n^2$ in the case of a bifacially structured slab with perfectly white backing [174]. For Si an intensity enhancement of approximately 50 was first calculated by Yablonovitch over thirty years ago in 1982. An assumption in this first publication was that this might only be the case for vanishing absorption, but the formalism was later generalized to apply for arbitrary absorption coefficients by Green [53].

The full $4n^2$ limit is however only reached for structures with a rear-reflectance of unity [26] as depicted in fig. 2.2 (f). Since no back-side mirror is present in our structures, an intensity or path enhancement of $2n^2$ represents the theoretical limit.

In general, randomizing – i.e. strongly scattering – structures lead to very effective broad-band LT with very wide angles of acceptance. A very high scattering probability is obtained for structures in the range of the wavelength of light, i.e. in the case of Mie scattering⁷ [110]. Furthermore, in terms of AR behavior surfaces with a high nano-roughness are also favorable, because they may represent the desirable graded refractive index for efficient in-coupling of light.

⁷Actually, the Mie theory exactly solves the Maxwell's equations for light scattered at (opaque and transparent) spherical objects of smaller, equal, and larger sizes than the wavelength. Mie scattering is colloquially understood as scattering of waves at particles of dimensions roughly equal to the wavelength.

2.1.3 Black Silicon Optics

This section shall give a brief overview of the optical properties of nanostructured surfaces from a theoretical point of view. Many papers on black silicon focus on optimizing the anti-reflection behavior of the surface while the possibility of enhancing LT is in many cases disregarded [70]. Short wavelength light up to $\lambda \lesssim 800$ nm penetrates c-Si only shallowly and is absorbed well. Hence, even in a rather thin wafer (≤ 50 μm), the absorption in this wavelength range only depends on surface reflections, so the spectral region will later be treated in terms of AR effects.

As mentioned for the Yablonovitch limit, however, the light intensity in the Si bulk can be vastly enhanced by LT which becomes especially important in thin wafers [90] and for wavelengths with absorption lengths greater than the wafer thickness ($\lambda \geq 800$ nm). Considering the available short circuit current resulting from the NIR spectral region, a significant portion of 28.4% ($I_{\text{sc,NIR}} = 19.56$ mA/cm²) of the total spectral energy is contained in photons requiring LT.⁸ This means that the geometrical features of the Si surface need to be adjusted to comply both, the demands for AR and LT effects. The optical properties of b-Si will be presented in sec. 5.3 with a focus on sharp Si needle-like features as obtained by dry plasma etching. The corresponding b-Si fabrication methods will be introduced in some detail in sec. 3.1.

2.1.4 Other Photon Management Concepts

This work deals only with the described non-resonant light trapping concepts of geometric and randomizing structures. There is, however, a large amount of ongoing research on how to get past the $4n^2$ limit by resonant, or angular- and energy-selective approaches [165, and refs. within]. If the absorber slab becomes thin enough ($\sim \lambda$), under certain conditions the light can be coupled into guided modes of the slab, leading to much higher path length enhancements. The trapping limits of such approaches are up to almost four orders of magnitude greater than $4n^2$. However, a serious drawback of these concepts is that higher optical path enhancement usually comes with strong constraints concerning the spectral and/or angular acceptance of the optical system. In addition, the experimental implementations require quite advanced technologies, which are not available or too expensive for industrial production. The limits of various available LT concepts are discussed in reference [165]. Since the ultimate Shockley-Queisser limit was defined for a single junction solar cell, the use of multiple materials building more than one junction may allow harvesting energy from the whole spectral range of the sun's spectrum. For those concepts however, electric interconnection of monolithic structures or their spacial distribution are rather challenging [160] and therefore very costly to apply. The starting point of this work is the search for a highly effective approach to boost the absorption in a moderately thin (~ 20 μm) absorber that is simple to implement and fully relying on mask-less processes applicable independent of crystal orientation (e.g. to mc-Si). Ideally, the implementation should not be far away from industrial standard tools.

⁸The spectral sub-regions referred to in this work are defined in fig. A.1 and tab. A.1 of appendix A.1. NIR light covers the spectral width of $780 \text{ nm} \leq \lambda \leq 1180 \text{ nm}$. The energy portion of 28.4% of the solar spectrum is referenced to the total sun spectrum including NIR and IR photons. The total absorbing range of Si covers 66.4% (see tab. A.1).

2.2 Recombination of Charge Carriers in Crystalline Silicon

In this section the theoretical mechanisms of electric charge carrier generation and recombination will be briefly introduced. The considerations are based on [127, 137] and [161].

Silicon (Si) is a single-element semiconductor which solidifies in a diamond cubic lattice. The periodic potential results in an electronic band structure wherein the Fermi energy, E_F , lies in a forbidden zone for all crystal directions. Therefore, Si has a full band gap. The gap energy in semiconductors is defined in thermal equilibrium (at $T = 0$ K) as the minimal difference between the (completely filled) valence band (VB) and the (completely empty) conduction band (CB)

$$E_g = E_c - E_v \quad (2.1)$$

which in Si corresponds to $E_g = 1.17$ eV (≈ 1.12 eV at room temperature (RT: $T = 300$ K)). Si has an indirect band gap because the CB minimum and the VB maximum are not located at the same position in k-space. Since physical processes necessarily require the conservation of energy *and* momentum,⁹ to complete a band-to-band transition the charge carrier has to exchange the momentum in addition to the gap energy, e.g. with the crystal lattice. A direct transition, i.e. without additional momentum, requires higher energy.

2.2.1 Generation and Recombination

In thermal equilibrium, the product of the electron and hole concentrations is constant and can be defined as the material constant “intrinsic carrier concentration” [144]

$$n_i^2 := n_0 \cdot p_0 \quad (2.2)$$

If sufficient energy is provided an electron can be transferred from the valence band into the conduction band. This process is called *generation* and may occur upon absorption of photons with $E_{ph} \geq E_{gap}$ or collisions with high energetic particles. Simultaneously, an unoccupied state in the valence band (called defect electron or *hole*) is produced, which possesses a (quasi-) positive charge. Both, electrons and holes, may freely diffuse through the bulk with diffusion constants in the range of $D_n \sim 30$ cm²/s and $D_p \sim 11$ cm²/s, respectively [137, 148]. Due to the excitation of charge carriers, i.e. generation of electron hole pairs, the system is no longer in equilibrium and equation 2.2 has to be rewritten as

$$n_i^2 < n \cdot p \quad (2.3)$$

where n and p are the non-equilibrium electron and hole concentrations, respectively. Since the system will relax into an equilibrium state, the electron-hole pairs have to undergo the opposite process to generation. The relaxation or decay of an electron from the CB to the VB, is called *recombination* and can only occur if a convenient hole is present in the VB. For reasons of energy conservation, the gap energy is then either released by (spontaneous) emission of a photon (*radiative* recombination) or indirectly transferred into the Si lattice (*non-radiative* recombination). However, due to its indirect

⁹among others

band gap all recombination processes in Si require the participation of a third body for momentum conservation. Most commonly such particles are phonons or charge carriers¹⁰.

Due to this fact recombination processes in semiconductors with indirect band gap require a certain time which is specific to the material's properties. The average time between a charge carrier's generation and recombination is called its lifetime, τ . We will see later that this characteristic lifetime very sensitively depends on possible recombination channels given by extrinsic factors. In terms of measuring the lifetime we have to look at statistical processes involving many recombination reactions. Thus, after generation has occurred the excess charge carrier densities of electrons and holes

$$\Delta n = n - n_0 \quad (2.4a)$$

$$\Delta p = p - p_0 \quad (2.4b)$$

will decay over time. Assuming charge neutrality and the absence of trap states, i.e. $\Delta n = \Delta p$, we only need to consider one charge carrier type. In this work only boron-doped p-type c-Si wafers without any diffused n-type regions were used. Hence, electrons are the minority charge carriers in all experiments and, therefore, later formulas will be given for the case of p-type doped material. However, the net recombination rate of excess minority charge carriers is a general magnitude which can be defined as [127, 144]

$$U(\Delta n(t), n_0, p_0) := -\frac{\partial \Delta n(t)}{\partial t} \quad (2.5)$$

in the case of spatially homogeneous generation. This rate depends on the excess charge carrier density and the intrinsic concentrations of electrons and holes, i.e. the doping level.¹¹ In thermal equilibrium the total generation and recombination rates of free charge carriers is balanced and thus $U_{(\Delta n=0)} = 0$. If the net recombination rate is only directly proportional to the excess carrier density, Δn decays exponentially over time. The characteristic time constant of the decay is the minority charge carrier recombination lifetime (short: lifetime) and can be defined more generally as the ratio [127, 144]

$$\tau(\Delta n, n_0, p_0) := \frac{\Delta n}{U(\Delta n, n_0, p_0)} \quad (2.6)$$

In the mentioned case ($U \sim \Delta n$) the resulting lifetime will be constant over Δn , i.e. independent of the injection level.¹² In general though, τ very strongly depends on the injection level. It will be shown in the next section that different recombination mechanisms dominate the charge carrier recombination in c-Si for different injection levels. In addition, τ also depends on the intrinsic carrier density related to the doping level,¹¹ which will be discussed thereafter. The different recombination processes occur in parallel, whereas the effective minority carrier lifetime will be determined by the "fastest" recombination channel. Hence, the shortest lifetime limits the effective lifetime. Thus, in

¹⁰Electrons and holes, which are not involved in the actual decay reaction.

¹¹In doped Si the intrinsic carrier concentration is governed by the majority carrier species, which in turn depends on the energy level of the defect type introduced by the dopant. In p-type material acceptor-like defects form close to the VB edge, E_V . In the case of full acceptor ionization this leads to an equivalently high number of holes such that $n_0 \ll p_0 \approx N_A$, the acceptor density. In n-type material the situation is vice-versa (donor-like defects close to E_C).

¹²The terms "injection level" and "excess charge carrier density", Δn , are used as synonyms, as the latter is a result of light injection and subsequent optical absorption followed by charge carrier generation.

analogy to the summation of parallel resistors the recombination channels add up as

$$\frac{1}{\tau_{\text{eff}}} = \sum_{i=1}^m \frac{1}{\tau_i} \quad (2.7)$$

where the τ_i denote the specific lifetimes of each of the m available recombination channels.

2.2.2 Bulk Recombination Mechanisms

As already mentioned, recombination processes can be classified by their underlying physics into categories of radiative and non-radiative decay. It is also very useful to further distinguish between recombination processes that would even occur in a perfect crystal lattice (*intrinsic* band-to-band recombination) and processes supported by electronic states inside the gap region (*extrinsic* or defect-assisted recombination). Electronically active defect states may form as a result of crystal disorder like crystal imperfections or impurity atoms in the Si lattice.¹³ Defect related extrinsic recombination may at least in theory be completely suppressed by assuming a perfect crystal, whereas intrinsic effects like radiative recombination and Auger-recombination will always be present and lead to physical upper lifetime limits.

Radiative Recombination

The spontaneously occurring electron decay from the CB into a hole in the VB under emission of a photon with the corresponding energy¹⁴ ($E_{\text{ph}} \approx E_{\text{g}}$) is called radiative recombination (see fig. 2.3(a)). The net recombination rate $U_{\text{rad}} = B(np - n_i^2)$ depends on the number of free electrons and holes, where B is the transition probability¹⁵ [127]. Following equation (2.6), the radiative lifetime, τ_{rad} , depends on the inverse of the charge carrier density. For low injection levels ($\Delta n \ll n_0 + p_0$), it depends only on the doping concentration, whereas for high injection ($\Delta n \gg n_0 + p_0$) it decreases with increasing Δn [137]

$$\tau_{\text{rad,li}} = (B \cdot p_0)^{-1} \quad (\text{p-type Si}) \quad (2.8a)$$

$$\tau_{\text{rad,hi}} = (B \cdot \Delta n)^{-1} \quad (2.8b)$$

Counterintuitively, this process does not necessarily limit the lifetime for direct semiconductors because the possible re-absorption strongly depends on the optical absorption coefficient close to the band gap [35].¹⁴ Therefore, τ_{rad} should have a severely limiting effect in semiconductors with a low absorption coefficient at the band gap region. Theoretically, thin Si wafers (with bad LT) are affected,¹⁶ but in fact τ_{rad} is rather long ($\tau_{\text{rad,li}} \approx 10$ ms in 1 Ωcm p-type Si). Nevertheless, the process cannot be suppressed and dictates an upper physical limit to the charge carrier lifetime in any semiconductor of nearly ideal crystallinity.

¹³The strongest lattice disorder in this sense is present at the surface, which will be discussed in section 2.2.3

¹⁴It may be that $E_{\text{ph}} \lesssim E_{\text{g}}$ if the participating phonon “steals” some energy. In this case the re-absorption probability may be severely lowered and the photon may escape more likely. The opposite ($E_{\text{ph}} \gtrsim E_{\text{g}}$) may also be the case.

¹⁵The indirect transition in Si requires a high momentum transfer. Thus, at RT $B = 4.73 \cdot 10^{-15} \frac{1}{\text{cm}^3\text{s}}$ is very small [157].

¹⁶According to Yablonoitch randomizing structures are most effective to minimize these losses as in turn the absorber slab may be substantially thinner [175].

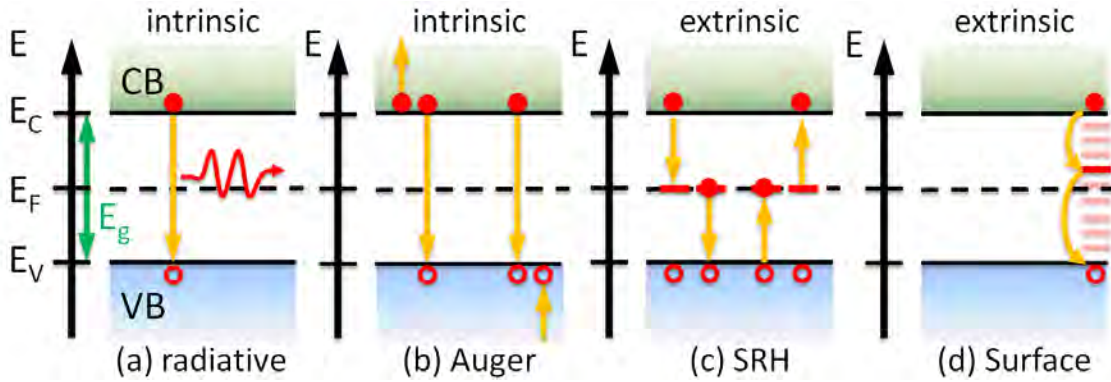


Figure 2.3: Recombination mechanisms. The direct band-to-band decays are *intrinsic* processes, whereas the *extrinsic* Shockley-Read-Hall (SRH) recombination and surface recombination are assisted by a defect level in the band gap. The arrows indicate the transition direction of electrons (full circles). Alternatively the holes (hollow circles) travel against the arrow direction. (a) schematic of spontaneous radiative recombination. A reversed arrow would describe photon absorption. (b) depicts the (eeh) and (ehh) Auger-processes. (c) shows the four fundamental transitions that may occur during SRH recombination. (d) represents surface recombination through a single gap state in a homogeneous defect density D_{it} .

Auger Recombination

For high charge carrier concentrations three body processes dominate the recombination rate. Here, energy and momentum conservation are preserved by an additional electron or hole, which can carry the excess amounts in the recombination reaction. These intrinsic processes are called electron-electron-hole (eeh), or electron-hole-hole (ehh) Auger recombination. Both situations are schematically drawn in fig. 2.3(b). Descriptively, the energy is transferred during a scattering collision, or by exchange of a “virtual boson”¹⁷ between the fermionic charge carriers. Just like in any other thermalization process the remaining (excited) charge carrier then passes its excess energy on to the crystal lattice by subsequent collisions, e.g. with phonons. The Auger recombination rate increases with increasing carrier concentration [127]

$$U_A = C_n(n^2p - n_0^2p_0) + C_p(np^2 - n_0p_0^2) \quad (2.9)$$

Herein, C_n and C_p are the Auger coefficients for the eeh and ehh processes, respectively. High carrier concentrations are either reached in the case of high doping levels like in diffused solar cell emitters, or for high light injection (e.g. under solar light concentration). Again, following equation (2.6) the lifetimes for low and high injection levels can be derived

$$\tau_{A,li} = (C_p \cdot p_0^2)^{-1} \quad (\text{p-type Si}) \quad (2.10a)$$

$$\tau_{A,hi} = ((C_n + C_p) \cdot \Delta n^2)^{-1} \quad (2.10b)$$

Hence, Auger recombination is stronger than radiative recombination in p-doped c-Si or in both low and high injection.¹⁸ This makes it the most severe physical limitation to the charge carrier lifetime in

¹⁷ e.g. a “virtual photon”

¹⁸ Ideally, $\tau_{A,hi} \sim \Delta n^{-2}$, whereas $\tau_{rad,hi} \sim \Delta n^{-1}$, hence, $\tau_{A,hi} < \tau_{rad,hi}$. The same is true in low doped ($p_0 \leq 2 \cdot 10^{16} \text{ cm}^{-3}$) Si and for low injection ($\Delta n \ll n_0 + p_0$), where instead the recombination rates scale with p_0^{-2} and p_0^{-1} , respectively.

c-Si and thus to solar cell efficiency [51]. The Auger recombination process is additionally enhanced¹⁹ by coulomb interactions between the charges, which leads to an even lower Auger lifetime in low doped p-type Si [137]. The current understanding of the Auger-limit in c-Si solar cells is nicely elaborated in [131]. In general, the intrinsic bulk lifetime of ideal crystals is limited by the doping level in low injection, whereas in high injection τ dynamically decreases with Δn^{-2} .

Shockley-Read-Hall Recombination

Besides the two intrinsic recombination channels that theoretically depict physical upper limits to the lifetime, practically, a more severe limitation in PV Si solar cell absorbers is given by impurity related recombination. All kinds of crystal defects may lead to discrete electronic states inside the forbidden band. Vacancies, stacking faults and extrinsic atoms induce so-called “traps” that capture electrons and holes (s. left of fig. 2.3(c)). From there the carriers can further decay. Usually, excess energy and momentum are again transferred to the crystal lattice by phonon scattering. However, defect-assisted Auger and radiative recombination are also possible. In the latter case, the sub-band gap photon can easily escape the crystal and the energy is lost. In reverse, however, a trap may also emit carriers (right of fig. 2.3(c)), an effect, which can actually be measured optically in heavily damaged crystals (optically active band of traps [24]).

Shockley, Read [144] and Hall [59] theoretically described impurity recombination in 1952, due to which the mechanism was named after them. The original Shockley-Read-Hall (SRH) model assumes only one type of defect state in (the middle of) the gap, i.e. “at midgap”, but in general, τ_{SRH} depends on the trap state energy, E_t . The characteristic time until (free) electrons and holes are captured by a trap depends on the trap concentration, N_t , and the corresponding capture cross sections, σ_n and σ_p , respectively²⁰

$$\tau_{n_0, p_0} = \frac{1}{\sigma_{n,p} v_{th} N_t} \quad (2.11)$$

with v_{th} the thermal carrier velocity. The full SRH lifetime further depends on the equilibrium- and excess carrier concentrations and the density of carriers in the traps (n_1, p_1)

$$\tau_{\text{SRH}} = \frac{\tau_{p_0}(n_0 + n_1 + \Delta n) + \tau_{n_0}(p_0 + p_1 + \Delta n)}{p_0 + n_0 + \Delta n} \quad (2.12)$$

where the defect populations are given by

$$n_1 = n_i \cdot e^{\frac{-(E_t - E_F)}{kT}} \quad (2.13a)$$

$$p_1 = n_i \cdot e^{\frac{-(E_F - E_t)}{kT}} \quad (2.13b)$$

Assumptions for (2.12) are charge neutrality ($\Delta n = \Delta p$) and thermal equilibrium of the carriers in their respective bands, separately. For high injection, equation (2.12) can be written as

$$\tau_{\text{SRH,hi}} = \tau_{p_0} + \tau_{n_0} \quad (2.14)$$

¹⁹Coulomb enhancement factors g_{eeh} and g_{ehh} are not included in eqn. (2.9)

²⁰A typical value for Si is $\sigma_{n,p} \approx 10^{-15} \text{ cm}^2$ [176]. In [176] the thermal carrier velocity $v_{th} \approx 10^7 \text{ cm/s}$ is also given.

Thus, defect recombination at high injection is limited by the slower capture rate. However, concerning the higher Auger recombination rates, this case is only of marginal interest and we shall consider low injection conditions in p-type material ($p_0 \gg n_0$)

$$\tau_{\text{SRH,li}} = \tau_{p_0} \left(\frac{n_1}{p_0} \right) + \tau_{n_0} \left(1 + \frac{p_1}{p_0} \right) \quad (2.15)$$

If further, the trap level coincides with the Fermi energy in the middle of the band gap²¹ the concentrations of trapped carriers are equal ($n_1 = p_1 = n_i$ (2.13)) such that the ratios in (2.15) vanish

$$\tau_{\text{SRH,li}} = \tau_{n_0} \quad (\text{for p-type}) \quad (2.16)$$

Thus, the recombination lifetime in low doped p-type Si bulk ($p_0 \approx 10^{16} \text{ cm}^{-3}$) and in low injection equals the defect lifetime. Finally, according to equation (2.7) all bulk recombination processes can be summed up to an effective *bulk lifetime*

$$\frac{1}{\tau_b} := \frac{1}{\tau_{\text{rad}}} + \frac{1}{\tau_A} + \frac{1}{\tau_{\text{SRH}}} \quad (2.17)$$

For low injection levels in low doped p-type Si the SRH lifetime should dominate the effective recombination lifetime. However, in an ideal Si crystal the effects of Auger- and even radiative recombination can not be totally neglected. As mentioned in the motivation, all bulk recombination channels can be reduced by reducing the wafer thickness, W , because in high-quality material τ_b scales with $\frac{1}{W}$ [51, 156, 175]. However, for increasing surface to bulk ratio, surface recombination becomes more and more important. Furthermore, if damage is introduced into the near surface bulk, e.g. by a black etching step, recombination processes will be dominated by the surface regions even more.

2.2.3 Surface Recombination Velocity

In section 1.1 the concept of surface recombination velocity (SRV) was already mentioned. From a theoretical point of view the phenomenon may be understood as the recombination rate of charge carriers in a surface-near sheet ($x = 0$, or $x = W$), that decay with a characteristic surface lifetime, τ_s . Thus, the surface contributes to the effective lifetime in the sample as

$$\frac{1}{\tau_{\text{eff}}} = \frac{1}{\tau_b} + \frac{1}{\tau_s} \quad (2.18)$$

The surface²² of an ideal semiconductor represents a high degree of crystal disorder giving rise to a large number of SRH-like recombination centers (interface traps). Thus, the recombination at such “dangling bonds”, i.e. unbound electronic states of Si atoms, can be described by the SRH-formalism. However, this type of defect density has to be defined as the number of defects per unit

²¹Traps close to E_F are referred to as “deep” level defects because their distances from the edges of the CB and VB are simultaneously maximized. Due to their symmetrically high population probability (2.13) they exhibit the highest recombination activity, which, depending on the doping level, is orders of magnitude higher than that of “shallow” donor- and acceptor-like defects close to the band edges [137].

²²Usually, the Si surface is terminated either by -OH groups making the surface hydrophilic (e.g. a native oxide), or by -H atoms making it hydrophobic (after an HF dip). Hence, the crystal surface always represents an interface. However, the expressions “surface” and “interface” are used synonymous.

area. Additionally, in contrast to energetically sharp localized bulk defects, surface defect states are distributed continuously over the band gap, so their density, D_{it} , is given per unit area and energy interval. This implies that the density of carriers at defect sites ($n_1 \equiv n_1(E)$ and $p_1 \equiv p_1(E)$) also depend on the energy level. The same holds for the capture cross sections $\sigma_{n,p}(E)$. Assuming that the SRH recombination processes are only assisted by a single defect (not multiple; s. fig. 2.3(d)) anywhere in the gap and following the definition for volume recombination (2.5), by applying the new quantities we find the total surface recombination rate by integrating over all energy levels in the gap [127]:

$$U_s = (n_s p_s - n_i^2) \int_{E_v}^{E_c} \frac{v_{th} D_{it}(E) \cdot dE}{\frac{n_s + n_1(E)}{\sigma_p(E)} + \frac{p_s + p_1(E)}{\sigma_n(E)}} \quad (2.19)$$

Note that, since D_{it} is a defect density per unit area and energy interval, U_s becomes a recombination rate per area and depends on the carrier concentration close to the surfaces.²³ In contrast to the approach in equation (2.6), i.e. instead of defining a surface lifetime due to the resulting unit [cm/s] the surface recombination velocity is defined as:

$$S(\Delta n, n_0, p_0) := \frac{U_s(\Delta n, n_0, p_0)}{\Delta n} \quad (2.20)$$

The full expression for S is derived by plugging in (2.19)

$$S(\Delta n, n_0, p_0) = (n_0 + p_0 + \Delta n) \int_{E_v}^{E_c} \frac{v_{th} D_{it} \cdot dE}{\frac{n_0 + n_1 + \Delta n}{\sigma_p} + \frac{p_0 + p_1 + \Delta n}{\sigma_n}} \quad (2.21)$$

The integral in (2.19) may only be solved numerically. However, in most cases it is sufficient to estimate an upper limit of S for the cases of low and high injection. Therefore, energetically constant capture cross sections are assumed.²⁰ In addition, the distribution of surface defect states D_{it} shall be homogeneous over the band gap (fig. 2.3(d)). Then, the remaining integral $\int_{E_g} D_{it} dE$ can be replaced by an equivalent effective density of interface traps per unit area, N_{it} , and in accordance to the capture lifetime in eqn. (2.11) we obtain:

$$S_{n_0, p_0} = \sigma_{n,p} v_{th} N_{it} \quad (2.22)$$

Similar to the case of SRH recombination (comp. eqn. (2.16)), this expression is a good estimate for the (maximum) recombination velocity for low injection ($S_{li, \max} \approx S_{n_0}$, in p-type Si), indicating that the recombination is governed by minority carrier capture processes. This estimate represents an upper limit because a defect close to the Fermi level is implied, which possesses the highest recombination activity due to maximum occupation of states ($n_1 = p_1$, comp. eqns. (2.13)). Since we assumed a homogeneous distribution, the actual SRV must be lower. However, S also depends slightly on σ_p and N_A . The former is noted in high injection $S_{hi, \max} = S_{n_0} (1 + \sigma_n / \sigma_p)^{-1}$. The latter can be neglected for this work as all wafers had doping levels of $2 \cdot 10^{15} \leq N_A \leq 2 \cdot 10^{16} \text{ cm}^{-3}$ and the surface recombination in high injection is again weaker than Auger-recombination.

Band bending close to the Si surface induced by charges present at the Si/dielectric interface is another phenomenon that strongly influences surface recombination. Charges may either get trapped in SRH-like recombination centers, or are fixed at the interface or in the bulk of the dielectric. As

²³The carrier densities are still given per unit volume (e.g. $n_s = n|_{(x \approx 0, x \approx W)}$ [cm⁻³]).

a result, a corresponding electric field is induced, which can be understood as a deformation of the electronic band structure acting on free charge carriers. Such band bending was implicitly considered during the derivation of S and is contained in the assumed charge neutrality ($\Delta n = \Delta p$). Therefore, eqn. (2.20) actually already defined the (maximum) effective surface recombination velocity.

$$S_{\text{eff}} := \frac{U_s}{\Delta n} \quad (2.23)$$

The exact origin of fixed charges is still under discussion in the literature [34, 75, 107, 166, among many others] and will be discussed in sec. 7.1.4.

Finally, we go back to eqn. (2.18) and connect the surface lifetime with the SRV. According to Sproul [149] τ_s may be approximated by

$$\tau_s = \left(\frac{W}{2 \cdot S} \right) + \frac{1}{D} \cdot \left(\frac{W}{\pi} \right)^2 \quad (2.24)$$

where W again is the wafer thickness and D the minority carrier diffusion constant.²⁴ It is assumed that the generation profile is constant over the wafer volume and that both surfaces contribute with equal recombination velocities $S_{x=0} = S_{x=W} = S$. In the case of a sufficiently low surface recombination velocity²⁵ ($S < \frac{D}{4W}$), the right term of eqn. (2.24) representing the effect of charge carrier diffusion becomes negligible to the recombination reactions. Therefore, eqn. (2.18) can be written as

$$\frac{1}{\tau_{\text{eff}}} = \frac{1}{\tau_{\text{bulk}}} + \frac{2S}{W} \quad (2.25)$$

Now, if the intrinsic bulk lifetime is very high,²⁶ it is appropriate to assume that the term $\frac{1}{\tau_{\text{bulk}}}$ becomes negligible leaving us with a simple expression for S_{eff} based on the measured effective charge carrier lifetime τ_{eff}

$$S_{\text{eff}} = \frac{W}{2\tau_{\text{eff}}} \quad (2.26)$$

By this expression, the total extrinsic recombination is attributed to the surface (and its close vicinity) still leading to an overestimation of the upper limit of S .

²⁴The derivation of this approximation may be found in [149]. Values for D can be derived from [148].

²⁵A typical value is $S < \frac{D}{4W} = 300$ cm/s in a wafer with a thickness of $W = 250$ μm . (The opposite is the case for unpassivated and abraded surfaces. Under such conditions the surface recombination velocity is prevailed by diffusion processes [148].)

²⁶Richter *et al.* reported “conservative values” of intrinsic bulk lifetimes in n- and p-type FZ Si of $\tau_{\text{bulk}} \sim 47$ ms [131].

2.3 Surface Passivation of Black Silicon

In general, passivation is the deactivation of electronic defects (traps) with an influence on the charge carrier lifetime. High quality FZ Si wafers are virtually free of crystal imperfections, but recombination active surface/interface states arise from the strong “lattice disorder” at the surface due to the broken crystal symmetry by missing neighboring atoms. From eqns. (2.21) and (2.22) two important conclusions can be drawn.

1. The SRV can be decreased by reducing the interface density of traps D_{it} , or by decreasing the according capture cross section $\sigma_{n,p}$ of the traps, to which S is directly linked. D_{it} can be reduced by saturating a maximum number of dangling bonds (*chemical passivation*).
2. The other possibility to reduce surface recombination is to reduce the charge carrier density of one type at the interface since the carriers can only recombine in pairs of electrons and holes. Such an asymmetric reduction of one carrier type can be achieved by inducing a band bending toward the surface. The zone of high recombination is then shifted into the bulk, where potentially fewer recombination centers are present. Band bending can be induced in two ways in p-type Silicon:
 - (a) High doping of Si with donor-like atoms forming an emitter or with acceptor-like atoms forming a so-called back surface field (BSF) both lead to asymmetric carrier concentrations due to a shift of the work function and according band bending toward the surface. However, increasing the carrier density by doping also increases Auger recombination and may simultaneously enhance SRH recombination at crystal defects.²⁷
 - (b) A more effective way is to introduce fixed charges that repel one type of free charge carriers (*field effect passivation*). To effectively implement a field effect passivation, preferably, the minority charge carrier density should be reduced. Otherwise, first a shift to higher recombination rates will be observed [64,67], because Δn and Δp must pass a cross-over point. By formation of negative charges on a p-type Si surface, the minority carriers (electrons) will be repelled from the defect-rich interface leading to a reduction of the recombination rate.

As shown with the simulation in sec. 1.1 the cell efficiency, and especially the open circuit voltage become limited by surface recombination as soon as the SRV is equal or greater than W/τ_b . Hence, for bulk lifetimes of the order of a few sets of ten microseconds, moderate surface recombination velocities of the order of $S \approx 100$ cm/s are necessary to become non-limiting to the solar cell efficiency in wafers with $W \approx 25 - 100$ μm . Hence, in order to take advantage of the optical benefits of b-Si, an efficient passivation of surface defects is crucial. However, this task is very challenging, as the extreme surface geometry of b-Si nanostructures can not be easily treated with standard tools and/or processes established in the solar cell industry.

²⁷Therefore, diffused n⁺p solar cells with an Al-BSF rear side with $S_{\text{rear}} = 10^4$ cm/s are usually limited to efficiencies lower than $\eta \lesssim 20\%$, whereas state-of-the-art PERC (passivated emitter and rear cells) with $S_{\text{rear}} = 20$ cm/s may yield efficiencies above $\eta \gtrsim 20\%$ [137, p. 42]. The “Rear-side recombination current values below 200 fA/cm² cannot be attained with an Al Back Surface Field (BSF).” [141]

2.3.1 Requirements for Black Silicon Passivation

If a nanostructured surface shall be effectively passivated, a number of prerequisites are needed:

- (i) The dielectric must be ideally suited to passivate a Si surface of preferably any crystal orientation (and doping level). High chemical passivation quality and strong field effect passivation appear to be desirable.
- (ii) Extremely rough structures must be coated in a highly conformal way to avoid recombination at “hot spots” like inclusions, voids or pin-holes.
- (iii) The coating should not significantly change the optical response of the black silicon surface.
- (iv) The highest process temperature should be kept rather low to avoid possible diffusion of eventually remaining contaminants from the black silicon etching step into the Si bulk.
- (v) The Si surface has to be kept as clean/pure as possible.
- (vi) Damage caused by the black silicon etching process itself has to be minimized [113, 119].

2.3.2 Possible Passivation Schemes

Different dielectrics are available for Si surface passivation, i.e. satisfying requirement (i): SiO₂ (thermally grown, CVD, ALD), SiN_x (PECVD), a-Si:H (PECVD), and Al₂O₃ (ALD). To satisfy requirement (ii) the material should be conformally grown on the surface, which is possible by ALD (Al₂O₃, SiO₂) or thermal oxidation (SiO₂). It might also be possible to synthesize conformal films by CVD. It has however been reported, that it is challenging to effectively passivate plasma etched b-Si by PECVD a-Si:H [106]. Requirement (iii) can be met if the optical properties of the film can be adjusted in the window of effective passivation and the films are highly transparent, which is not the case for a-Si:H, only. Furthermore, film conformality may constitute an issue again. It is ruled out by requirement (iv) that processes with high thermal budgets like thermally grown SiO₂ and high-temperature CVD processing will be useful. Therefore, ALD deposited Al₂O₃ is the passivating dielectric of choice for this work. Of the mentioned materials only ALD films of Al₂O₃ and SiO₂ fulfill all four requirements to the passivation layer. However, it was demonstrated that the passivation performance of Al₂O₃ on p-type Si is stronger than that of SiO₂ on polished [66] and nanostructured Si surfaces [129]. Finally, to also fulfill requirements (v) and (vi), an adequate b-Si structure with outstanding optical properties has to offer a high surface quality that needs to be thoroughly cleaned before passivation layer deposition. Hence, the charge carrier lifetime may be used to identify a low-damage blackening process. The combination of a b-Si fabrication method together with a highly effective passivation scheme will pave the road to a new generation of crystalline Si devices, such as solar cells.

Chapter 3

Sample Preparation

Substrate Material: The vast majority of crystalline silicon solar cell applications are built on p-type Si wafers with a specific resistivity in the range of 1 – 5 Ωcm . These doping levels correspond to boron concentrations of about $2.8 \cdot 10^{15}$ – $1.5 \cdot 10^{16}$ cm^{-3} in reversed order, respectively. Due to their extreme purity¹ float-zone (FZ) wafers usually have a higher bulk lifetime and are much more homogeneous concerning their doping distributions than Czochralski (Cz) grown² material.

Unless stated otherwise, experiments within this work were carried out on 6" FZ wafers with (100)-orientation, a p-type boron doping level of 1.00 ± 0.25 Ωcm and a thickness of ≈ 250 μm . These 'shiny etched' out-of-box (oob) wafers were used for black silicon (b-Si) etching and served as untreated/unstructured process references. For a few experiments Cz 6" (100) p-type Si material with a resistivity of 1 – 5 Ωcm was used. These data will be labeled 'Cz'.

3.1 Black Silicon Fabrication Methods

The reflection of light from a Si wafer strongly depends on its surface morphology as was described in section 2.1. Various methods are available to effectively nanostructure Si surfaces, reducing its reflection down to a very small percentage of the total. To permit a comprehensive comparison of different b-Si nanostructures, four of the most commonly used blackening methods were chosen and applied, namely, dry reactive ion etching in an inductive coupled plasma (ICP-RIE) [42, 89, 90, 119], metal assisted wet-chemical etching (MACE) with Ag [12, 99, 112] and Au [3, 85] catalysts, and electrochemical anodization that leads to the formation of macroporous silicon (macP-Si) [46]. These b-Si techniques will be briefly explained throughout this section with a strong focus on dry reactive ion etching, which was used as the model system.

¹Electronic grade FZ Si comes in a purity of 11N; meaning a purity of 'eleven nines' (99.999 999 999%). Solar grade Si only has a purity of 99.99%.

²In Cz growth, Si atoms nucleate at a seed crystal that is slowly withdrawn from a Si melt containing the desired doping content. In contrast, for production of FZ material purified chemical vapor precursors are used to build a high-purity high-ohmic Si rod. The resulting rods are then pushed through a RF-heating coil providing energy to locally melt the Si material. At this position, the desired doping level is introduced by adding a P or B precursor from the surrounding gas atmosphere. Like in Cz growth, the melt is then crystallized on a seed crystal.

The goal of comparing the lifetime after passivation is to identify b-Si methods that may simultaneously facilitate excellent optical properties and high lifetimes. Such b-Si substrates would potentially serve as effective solar cell absorbers that do not limit the device performance.

3.1.1 Inductive Coupled Plasma Reactive Ion Etching (ICP-RIE)

In 1979 Gittleman showed that reactive sputter etching in a chlorine plasma could be used to fabricate c-Si wafers that are non-reflecting in the useful solar wavelength range [48]. Shortly after, Craighead *et al.* announced “textured thin-film Si solar selective absorbers using reactive ion etching” and demonstrated the practical use of nanostructured black a-Si thin films for PV applications [23]. Over a decade later, Jansen *et al.* published the so-called “black silicon method” [76], wherein they actually describe a method to get rid of “nano-grass”-formation which was a major problem in dry-etching processes based on SF₆, O₂, and CHF₃ before. Hence, the phenomenon of b-Si formation actually occurred as a side effect in plasma etching of Si at cryogenic temperatures for applications in micro-electronics and MEMS.³

Jansen *et al.* explained that each plasma gas has its specific function [76]. The etching mechanism is schematically depicted in fig. 3.1(a). SF₆ forms F^{*}-radicals, which aggressively attack and dissolve the Si lattice under formation of volatile SiF₄. Cracked O₂ molecules supply O^{*}-radicals which passivate the Si surface forming SiO₂ and SiO_xF_y. Both Si-compounds chemically inhibit F^{*} etching, creating a situation of continuously competing reactions of surface etching and passivation. Then, CHF₃ may be added to provide CF_x⁺-ions that effectively remove the SiO_xF_y-layer and hence the growth of nanostructures is omitted. For this work, no CHF₃ was added to intentionally form b-Si. SiO_xF_y-debris leads to local micro-masking of the surface, while the Si etch rate around them is rather high. Hence, the remaining Si underneath starts to form needle-like structures as a result of overlapping pores. However, the needle-like tips may also be attacked again. This phenomenon can be explained by the physical etching component of e.g. impinging SF_x⁺ ions which enable sputtering of the passivation layer. Hence, the sidewalls of the emerging nanostructures are preferably passivated whereas the pore bottoms are quickly etched and the tips remain somewhat protected.

Pure SF₆ plasma etches Si isotropically. To find the black etching regime, the initial SF₆ flow rate can be fixed. Then O₂ is added until the Si surface becomes macroscopically black. Thus, the SF₆ to O₂ gas flow ratio determines the b-Si fabrication window, which in the absence of CHF₃ may be rather large. Jansen *et al.* recommended to etch only ~ 1 μm of Si to obtain b-Si needles, which indicates that very little Si must be removed if the etching process is optimized for minimal material consumption [76].

Influence of ICP-RIE Parameters on the b-Si Surface Morphology

Most of the investigations of this work are based on dry etched b-Si structures. Thus, a brief overview on the available etching parameters and their principal influence on the resulting surface morphologies shall be given in this section. For b-Si fabrication a cryogenic plasma etch system ‘SI-500 C’ from Sentech Instruments Berlin was used. The setup is located at the Institute of Applied Physics (IAP)

³Micro-Electro-Mechanical Systems

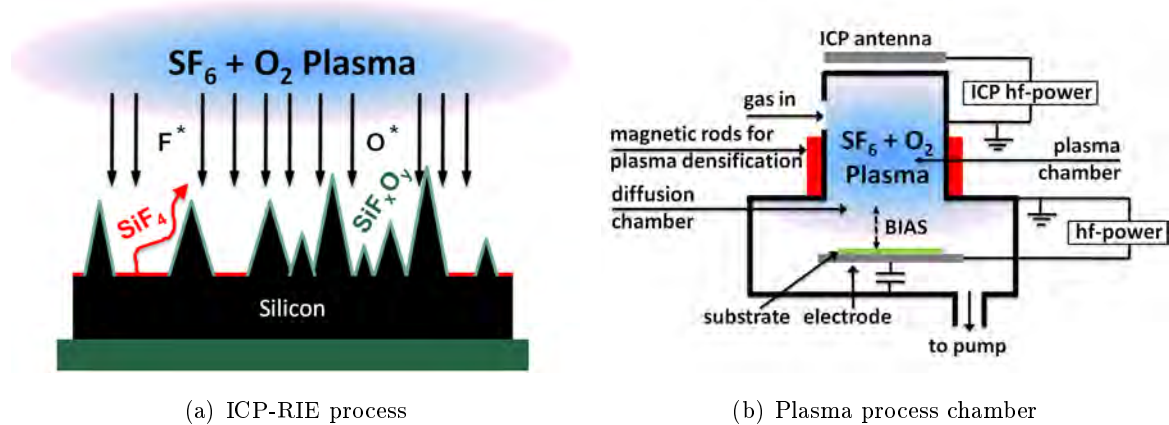


Figure 3.1: (a) Schematic of the ICP-RIE process for b-Si fabrication based on SF_6 and O_2 . (b) Diagram of the used process chamber.

of the Friedrich-Schiller-University (FSU) Jena and consists of a high-vacuum chamber with an ICP source on top and a plate electrode holding the wafer as shown in fig. 3.1(b).

Depending on the ICP-RIE etching parameters various surface geometries can be produced and in turn physical parameters like the optical absorption behavior can be tailored and/or the electronic surface quality may be influenced. Basically, the available parameters can be classified into two categories concerning the regimes of physical and chemical etching, and finally, the result obviously may depend on the etching time.

Etching Time: Roughly during the first 2 min. after plasma ignition no significant change in surface morphology can be observed (e.g. a polished wafer stays flat). This inhibition of b-Si formation could have two possible causes. (i) Either no material is consumed during this time because the native oxide on the wafer acts as an initial etch stop or (ii) micro-masking is only enabled if the concentration of SiF_4 is high enough to form SiO_2/SiO_xF_y micro-particles.

After this initial phase, randomly small etch pits start to form rapidly ($t_{ICP-RIE} \approx 3$ min.) on the surface. These pits then quickly grow deeper because the etch rate of exposed Si is much greater than the etch rate of SiO_2 or SiO_xF_y . Then the etch rate stays constant, and hence, the pore depth increases linearly with etching time. Simultaneously, the pores widen laterally until they overlap, which leads to the formation of sharp needle-like surface features. However, at a certain pore depth the competing reactions of micro-masking by oxide-particles and etching by F^* -radicals level out and the b-Si etch rate decreases to zero. Thus, the final pore depth (or according needle height) saturates after approximately 5–10 min. However, if the etching process is further continued the dynamically altering surface front is driven through the wafer consuming more bulk Si, while the characteristic morphology (structure depths, angular distribution, and lateral pore distances) is basically maintained. Thus, the etching time determines the depth of the nanostructures only after the initial inhibition until the depth becomes limited by reaction kinetics. SEM images of this etch evolution are published in [43]. The author of this work⁴ speculates that the initial time and correlated material consumption could be minimized by directly providing SiF_4 in the plasma to directly form micro-masking oxide particles. However, SiF_4 was not available in the used equipment.

⁴together with the authors of [43]

Chemical Etching Regime: As already mentioned, the gas flows of SF_6 and O_2 have a rather strong influence on the surface morphology. While the micro-masking effect increases with increasing O_2 concentration, the isotropic chemical etch rate will increase with increasing amounts of SF_6 . Hence, the resulting pore depth and structure size depend on the ratio of $\text{SF}_6:\text{O}_2$. For large ratios (2.15 : 1) the surface becomes more frayed, whereas low ratios (3 : 4) may lead to etching inhibition and more shallow structures and the sidewalls appear smoother. For the three standard structures⁵ this ratio is 1 : 1. The abrasiveness of the reaction kinetics slightly depends on the total amount of SF_6 provided to produce F^* -radicals and on the substrate temperature T_s .

Usually, ICP-RIE processes are conducted at low temperatures in the range of $-40\text{ }^\circ\text{C} \leq T_s \leq 0\text{ }^\circ\text{C}$. At $T_s \approx -30\text{ }^\circ\text{C}$ the emerging sidewalls are rather smooth. With higher temperature the reactions become more and more chemistry dominated and the effect of physical sputter etching monotonically decreases. Thus, at higher temperatures the surfaces have a higher porosity and the tips look much more frayed. With increasing substrate temperature the characteristic pore depth exponentially decreases. However, the depth stays constant for T_s in the range of $0\text{ }^\circ\text{C} \leq T_s \leq +20\text{ }^\circ\text{C}$. Thus, the shift from chemically to physically dominated etching kinetics is controlled by the temperature.

Physical Etching Regime: In our dry etching process the substrate surface is directly exposed to the plasma cloud (comp. fig. 3.1(b)). Hence, charged and neutral particles as well as energetic radiation generated in the plasma⁶ impinge on the sample surface. The particle's energies may be high enough to engage sputtering, while the radiation might harm the near surface bulk. Actually, physical etching has to be divided into two components concerning the ion's *direction* and *density*. Physical etching is influenced by the ICP-power, P_{ICP} , the Capacitive Coupled Plasma (CCP) power, P_{CCP} (which is applied between sample-electrode⁷ and electrically grounded plasma chamber), and the process pressure, $p_{\text{ICP-RIE}}$.

The ICP-power determines the plasma density, i.e. the number of ions and radicals per unit volume. These, in turn, influence the size and depth of the nanostructures as well as their sidewall angles. For our lifetime experiments, the ICP-power was fixed to $P_{\text{ICP}} = 750\text{ W}$. With lower ICP-power ($P_{\text{ICP}} = 450\text{ W}$) the plasma density decreases and therefore the b-Si pore depth decreases by about a factor of two. However, with higher ICP-power ($P_{\text{ICP}} = 900\text{ W}$) the structure depth does not exceed the one obtained under standard conditions indicating a constant plasma density. The Si needles only become slightly more frayed at the tips. Hence, the process is mainly gas flow limited.

Independently, the CCP-power, P_{CCP} , influences the so-called bias voltage, V_{BIAS} , which is freely floating and can not be directly controlled. V_{BIAS} builds up between the plasma cloud and the substrate electrode and leads to an extraction of charged particles from the plasma. Thus, it determines the ion energy distribution impinging on the sample and therefore the physical etching component (direction of ions). In the present work the CCP-power was varied between $0\text{ W} \leq P_{\text{CCP}} \leq 6\text{ W}$. However, P_{CCP} has only a very weak influence on the surface morphology in the tested range. Even for $P_{\text{CCP}} = 0\text{ W}$ a minimal bias voltage⁸ remains, because the plasma cloud, due to the loss of positive ions, always charges up with respect to the capacitive coupled substrate electrode (fig. 3.1(b)).

⁵will be defined in the following (see p. 25).

⁶Ions, electrons, radicals, vacuum ultraviolet (VUV) and UV-light

⁷The sample is located on a capacitive coupled plate electrode as depicted in 3.1(b).

⁸typical values are $-25\text{ V} \leq V_{\text{BIAS}} \leq -10\text{ V}$.

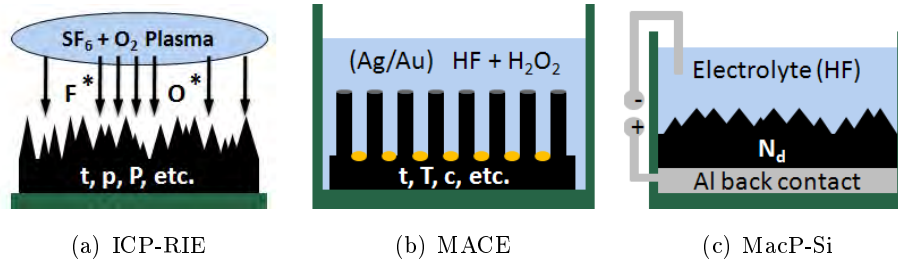


Figure 3.2: Schematic depiction of the alternative b-Si nanostructuring methods (b) and (c) in comparison to the ICP-RIE method (a). Note that neither the structures, nor the experimental details are to scale.

Finally, by changing the process pressure from $1 \text{ Pa} \leq p_{\text{ICP-RIE}} \leq 9 \text{ Pa}$ the nanostructure depth can be adjusted. At lower pressures the physical etching rate is low because the density of impinging ions is low. Therefore, masking particles can persist longer on the surface, even though the plasma species have longer mean free path lengths and may impact with higher energy. For $p_{\text{ICP-RIE}} = 2 \text{ Pa}$ ($\approx 2 \mu\text{m}$) deep nanostructures are obtained. With increasing pressure, the physical etching component increases along with a decreasing mean free path length and the nanostructures become more shallow ($< 1 \mu\text{m}$) because the masking layer is physically etched at a higher rate. However, for pressures above $p_{\text{ICP-RIE}} \geq 4.5 \text{ Pa}$ the pore depths do not significantly decrease further.

The three Standard ICP-RIE b-Si Structures

As described above, by variation of the etching parameters different nanostructure morphologies can be etched in the ICP-RIE process. Three b-Si surfaces with characteristic heights of approximately 500, 600, and 1700 nm were selected as the “standard structures”. These ICP-RIE fabricated surface geometries will be called “shallow”, “intermediate” and “deep” b-Si according to their pore depths and have aspect ratios of roughly 3, 4, and 10, respectively. SEM images are shown in fig. 5.1 of section 5.1. The corresponding process parameters are listed in table 5.1. To isolate the parameter influences on the electronic surface properties (i.e. SRV) of the resulting b-Si, samples with additional parameter variations were produced that differ from these standard etching conditions. The parameter variations will be described along with the results.

3.1.2 Wet Chemically Etched b-Si

Metal Assisted Chemical Etching (MACE)

Si can be etched in aqueous solutions of oxidizing agents like H_2O_2 (or HNO_3)⁹ if HF is supplied to dissolve the oxidized Si. It was observed that this reaction occurs much faster in the vicinity of Al [27] and many other metals¹⁰ [97]. The MACE process is predicated on the catalytic function of a (noble) metal, which physically reduces the surface potential of Si and facilitates the exchange of electronic holes from the etching solution to the Si at the crystal/liquid interface. Due to the nature

⁹ HNO_3 was not used in this work

¹⁰(Al, Cu, Fe, Pt, Pd, Au, Ag, etc.)

of this catalytic mechanism and the fact that holes originate from the oxidant decomposition (H_2O_2), the etching mechanism functions for a wide range of doping levels in n- and p-type Si [97] and can be applied to Si substrates with different crystallinity like c-Si, mc-Si, $\mu\text{c-Si}$, and a-Si:H [85–87]. If the Si surface is partly coated with an ultra-thin metal film or nanometer-sized particles, the Si atoms underneath the metal fraction are oxidized and etched, while the “off-metal-fraction” remains unetched (comp. fig. 3.2(b)). This way, straight nanopores (NP) or nanowires (NW) can be obtained on p-type wafers depending on the metal surface coverage without application of any electrical potential (“electroless”) in the dark [97]. Therefore, MACE quickly gained popularity and various opto-electronic applications were proposed [97, and refs. within].

Different models can be found in the literature describing the reaction kinetics of metal assisted chemical etching of Si. A rather comprehensive review of the method is given in reference [71]. Therein, Huang *et al.* suggested that the local dissolution of c-Si in aqueous HF/ H_2O_2 catalyzed by a noble metal may in general be understood as follows: (i) the oxidant is preferentially reduced at the metal/liquid interface due to the catalytic function of the metal. (ii) The electronic hole diffuses through the metal film and is injected into the Si at the metal/Si contact. (iii) The Si is oxidized by capturing holes and can subsequently be selectively dissolved by the HF in the solution. Due to the high concentration of holes in the vicinity of the metal (film/particle) the Si substrate is dissolved much more aggressively there than elsewhere, resulting in a channel (pore) along the etching direction [71]. However, since the holes are injected into the c-Si lattice, they may diffuse through the crystal and can lead to Si etching at the Si/liquid interface within their reach. This may cause micro-morphous structures with pore sizes down to a few nanometers and leads to fibrous sub-nanometer Si structures in the off-metal-region [3, 71, 99].¹¹ Nevertheless, the resulting surface morphology strongly depends on the initial metal film distribution (nanoparticle density and lateral distribution on the wafer surface) and the H_2O_2 concentration [71]. The etching direction is dominated by the crystal orientation and typically proceeds along the [100] direction of Si [12]. As a result, vertical nanopores are formed on a (100) Si wafer with pore diameters slightly larger than that of the metal nanoparticles as depicted in fig. 3.2(b). If the pores overlap, vertically aligned NWs emerge on the substrate. The Si etching rate mainly depends on the process temperature and the content of the oxidant source. In contrast, the reaction is hardly ever limited by HF dissolution of the SiO_x , because very low HF concentrations are sufficient for immediate etching of the SiO_x .

The preparation of b-Si by the MACE method usually requires three steps: (i) metal catalyst deposition, (ii) black etching, and (iii) removal of the metal catalyst. The metal can be deposited as an ultra-thin film ($\lesssim 2$ nm) either by sputtering [3, 85], by electrochemical or electroless deposition [99, 112] to form nanoparticles before black etching. Alternatively, *in-situ* deposition of the metal catalyst is also possible if a nanoparticle solution is intermixed with the etching solution [12, 183]. This allows a combination of preparation steps (1) and (2). For this work, three different MACE processes were applied for b-Si etching on both sides of full 6" p-type FZ wafers in HF: H_2O_2 : H_2O solutions. Laboratories around the world¹² where the MACE methods are commonly used, were

¹¹A similar phenomenon was earlier reported for electrochemical etching of Si [95] which will be discussed in the following section.

¹²National Renewable Energy Laboratory (NREL), Walter Schottky Institute (WSI), and Martin Luther University Halle-Wittenberg (MLU)

asked to prepare b-Si on the mentioned standard substrates. These samples could then be used for a comparison of the surface quality concerning optical absorption and the feasibility of passivation by ALD- Al_2O_3 [113].

Black Silicon Nanowires (NW): Two b-Si nanowire samples were prepared at the MLU [98]. After removal of the native oxide in 5% HF for 3 minutes, Ag-nanoparticles were deposited by electroless plating for a duration of 1 minute from an aqueous HF silver-nitride solution.¹³ Black etching of the Ag plated Si wafers was done in aqueous HF(8.5%): H_2O_2 (0.9%) and lead to NW formation and a homogeneously black surface. The NW-length was controlled by the etching time for constant temperature and HF: H_2O_2 : H_2O concentrations [98, 113]. The two nanostructures obtained after 5 min. and 10 min. will be referred to as the “short” and “long” NW sample, respectively. After black etching, the wafers were cleaned in concentrated HNO_3 for Ag removal. To completely remove the Ag nanoparticles, the cleaning procedure was repeated two times. Finally, the samples were rinsed in deionized (DI) water and dried with a N_2 pressure gun. These experimental steps were performed at RT inside a fume hood.

Black Silicon Nanopores (NP): Two nanostructuring processes were performed at the NREL in Golden, Colorado (USA), using Ag and Au nanoparticles as catalysts [12, 112, 183]. The Ag deposition is very similar to the one performed at the MLU. Ag nanoparticles were first electrolessly deposited on a Si wafer using 0.001 mol/l AgNO_3 in 0.5 % HF for 90 s at RT. Subsequently, MACE was performed by immersing the Ag nanoparticle-decorated Si wafer in a mixed solution of 12.5% HF and 3 % H_2O_2 for 20 s at RT in a sonication bath leading to defined separated nanopores (“Ag-MACE NP”). Thereafter, the Ag nanoparticles at the bottom of the NPs were removed by treating the wafer in concentrated HNO_3 for 3 minutes. Between the fabrication steps, the wafer was carefully rinsed with DI water for at least 3 minutes [112].

For the Au-catalyzed MACE nanostructures, a Si wafer was immersed in a solution of $4 \cdot 10^{-4}$ mol/l HAuCl_4 . The small (5 nm) nanoparticles with a density of $5 \cdot 10^{13}$ cm^{-3} start to form Au-nanoparticle-clusters of about 20 to 100 nm in diameter [12]. An equal volume of a mixed HF: H_2O_2 : H_2O solution with a 1 : 5 : 2 ratio was added while the reaction container was kept in a sonication bath. Hence, Au nanoparticle formation and black etching were performed in the same step. Black etching was performed for a duration of 3 minutes leading to nanopores (“Au-MACE NP”) comparable to the ones catalyzed in the Ag-MACE NP process. Afterwards, the b-Si wafer was rinsed with DI water and the remaining Au nanoparticles at the bottom of the pores were removed by an I_2/KI solution as described in detail in [12, 183].

Black Silicon Nanococones (NC): For the MACE method developed at the WSI of the Technical University of Munich (TUM), Au is used as the catalyst. A previously optimized nanostructure type [3] was fabricated there. Wafer pieces were pre-cleaned in acetone and isopropyl alcohol (IPA), followed by a dip in HF(5%) to remove the native oxide. A thin Au film with a nominal thickness of 1 nm served as a nanoparticle seed layer. The metal was deposited onto the Si surface by thermal evaporation at a base pressure of $\approx 10^{-6}$ mbar. This leads to a discontinuous film of spatially separated

¹³5 mol/l HF, 0.01 mol/l AgNO_3 in H_2O

Table 3.1: Parameters of the different b-Si samples prepared by MACE.

| | HF [s],(%) | (i) Deposition [s],(mmol/l) | (ii) MACE [s], (%) | (iii) Removal [s] |
|------------|-------------------|--|---|--|
| NW (short) | 180, (5) | 60, HF(8.3%):AgNO ₃ (10) | 300, HF(8.3):H ₂ O ₂ (0.9) | 2×HNO ₃ |
| NW (long) | 180, (5) | 60, HF(8.3%):AgNO ₃ (10) | 600, HF(8.3):H ₂ O ₂ (0.9) | 2×HNO ₃ |
| NP (Ag)* | 90, (0.5) | 20, HF(5%):AgNO ₃ (1) | 20, HF(12.5):H ₂ O ₂ (3) | HNO ₃ |
| NP (Au)* | 90, (0.5) | 20, HF(5%):HAuCl ₄ (0.4) + 180, HF(12.5):H ₂ O ₂ (3):H ₂ O 1 : 5 : 2 | | I ₂ :KI:H ₂ O |
| NC (Au) | Ace., IPA** HF | therm. evap. (10 ⁻⁶ mbar) | 70, HF(50):H ₂ O ₂ (30):H ₂ O ratio 1 : 5 : 10 (by vol) | 120, I ₂ :KI:H ₂ O 1 : 4 : 40 (by wt) |

*MACE process in sonication bath with 3 min. DI water rinsing after each process step.

**Acetone and isopropyl alcohol (IPA)

Au-clusters with several nanometers in diameter. Black etching took place in an aqueous solution of HF(50%):H₂O₂(30%):H₂O with a volume ratio of 1 : 5 : 10 at RT for 70 s, leading to nanocone-like hillocks. Simultaneously, an evolution of fibrous Si takes place at the top of the nanocones (NC) [3]. Therefore, an additional post-etching treatment is necessary to remove the unwanted fibrous Si network. As previously shown in Ref [3], the “standard clean one” (SC1) from the common RCA cleaning sequence (see sec. 3.2.1) is sufficient to remove the fibrous Si fraction [3]. In the case of the b-Si samples used in this work, the SC1 post-etching treatment of the RCA clean [80] prior to the passivation procedure was exploited for the removal of the fibrous Si. Au residues were removed from the as-prepared sample by etching in an aqueous I₂/KI solution with a ratio of 1 : 4 : 40 by weight at RT.

Macroporous Silicon

In the 1990’s an (opto-)electrochemical etching process was introduced for Si in aqueous HF [94]. Shortly after Lehmann and Gösele presented their model showing how –H terminated Si surfaces can be etched under application of a positive bias voltage¹⁴ [95]. Si-H is almost completely inert to F⁻ ion etching from the HF solution as long as no electronic holes are available. They explained that if a hole reaches the Si-electrolyte interface a Si-H bond can be broken and replaced by Si-F. Due to the polarity of the new bond another F⁻ ion may replace another H atom while H₂ is released. Subsequently, the neighboring Si-Si bonds are weakened by the presence of the fluorine groups and can either be attacked by HF or H₂O [95]. Hence, Si can be dissolved where the hole concentration is high. This electrochemical etching reaction (anodization) of Si can be triggered via an externally applied electric current (see. fig. 3.2(c)). If the described dissolution of a single Si atom would occur from an atomically flat surface and an applied potential, the electric field distribution would lead to a rising hole concentration at this spot and hence surface inhomogeneities are amplified [95]. The so-called macroporous Si (“macP-Si”) process has been described in detail by Lehmann for both n-type Si [93] and p-type material [96]. To process n-type Si an additional light source is needed for the generation of electronic holes, which then, similar to the MACE process, lead to an oxidation of Si atoms at the Si-electrolyte interface. By lithographically structuring the substrate defined micrometer-sized pores can be etched. In p-type Si holes are the majority carriers such that the minimum carrier concentration is fixed to the doping level. Charge carrier injection by light absorption is possible, but

¹⁴Si is the anode.

not needed. With larger electronic hole concentrations, the pore density increases as the space charge region at the surface becomes thinner [96]. For constant current and HF concentration at sufficiently low hole concentrations, the pore depth may be controlled by the etching time and temperature. Depending on the electrolyte solution and the galvanic current density etch rates of the order of 0.1 – 10 $\mu\text{m}/\text{min}$ may be reached in 1 Ωcm p-type (100) Si [96]. Thus, short etching times ($\sim\text{min}$) are sufficient for electrochemical black etching.

The pore diameter can be controlled by the induced current through the wafer back-contact to the counter-electrode in the electrolyte, the illumination intensity and the applied voltage. This way the 3D-pore shape can be freely modulated as device design requires [9, 103, 135], which allows tailoring the optical surface properties within the available parameter range. Under certain conditions, this method can be used for kerf-free wafering¹⁵ of n-type Si and *in-situ* black-etching in a one-step-process [13]. However, if no lithography is applied to pre-define the pore positions, randomly emerging (“wild”) pores in p-type Si tend to overlap. Hence, the doping level which defines the average pore distance sets a limit to the achievable feature size. A comprehensive description of the macP-Si process and various applications may be found in [91].

For this work, one 6" FZ wafer with a resistivity of 1 Ωcm was fabricated without applying any lithography. The back contact of the wafer was realized by electron beam deposition of about 100 nm Al in an UHV chamber. Etching was carried out in the dark in equipment of the company *Smart Membranes*¹⁶ located near the MLU in Halle.

3.1.3 KOH Reference and the Superstructure

To compare the opto-electronic performance of the diverse b-Si surfaces to state of the art industrial processes, random pyramid textures were produced on the same wafers by alkaline etching in KOH:IPA (isopropyl alcohol) solution. For good comparability of the data and experimental simplicity, the bifacial KOH textured wafers were passivated by the same RCA + ALD- Al_2O_3 + PDA as the black etched samples. Therefore, the optical performance of the KOH texture was not optimized by an according ARC in this work, because greater interest was put to the electronic surface properties like the modification of interface properties during the blackening processes.

Finally, KOH reference structures were used to build a combined “superstructure” by imposing an ICP-RIE shallow b-Si nanostructure on the alkaline textured random pyramids. This way, an additional anti-reflection layer as well as light-trapping scheme is incorporated in a two step structuring process.

3.1.4 Applicability of the Investigated Black Etching Methods¹⁷

The range of applicability is quite large for most of the presented blackening methods. There are no restrictions concerning crystal orientations and doping level of the substrate wafers. In the case of the ICP-RIE process this also includes multi-crystalline (mc-) [129], micro-crystalline ($\mu\text{c-Si}$) and even amorphous silicon (a-Si) [23], which can mainly be explained by the high isotropy of the fluorine

¹⁵Waste-free wafering methods that do not require cutting by wire saws are generally referred to as “kerf-free” [61].

¹⁶www.smartmembranes.de

¹⁷This paragraph was published in [113].

etching reaction and the purely physical decomposition of the passivating SiO_xF_y layer. Chemically dominated processes may be somewhat more restricted to crystallographic planes. However, MACE also works on mc-Si, $\mu\text{c-Si}$ and a-Si as shown by Koynov *et al.* [86]. An exception is the macroporous Si technique, which may only be used for pore fabrication on mono-crystalline Si substrates in a certain range of doping levels ($\geq 10 \text{ } \Omega\text{cm}$). Nevertheless, this technique is very attractive since the pore-diameter-modulation offers the possibility for under-etched facets [5] and in-situ wafering [39]. All presented methods can be applied selectively on a single wafer side. However, in this work only lifetime samples with bifacially macroscopic identical wafer sides were investigated. MACE is the only method that allows simultaneous blackening of both sides if needed.

3.2 Surface Cleaning Prior to Atomic Layer Deposition

According to the SRH recombination model (2.2.2), any unsaturated surface sites or impurity atoms may give rise to active recombination centers. Hence, the adjacent layer to the Si interface should not only saturate dangling bonds to a maximum degree, but it also needs to be as pure as possible. Usually, a Si surface is terminated by a very thin native SiO_x layer, which forms if the material is exposed to air or water. The out-of-box (oob) FZ wafer substrates used in this work were terminated by a clean SiO_2 grown by the manufacturer with a typical thickness of $2.0 \pm 0.3 \text{ nm}$ as determined by ellipsometry (comp. fig. A.7). However, during black etching the well defined SiO_2 is removed. In addition, several handling steps are necessary which may leave contaminations on the wafer surfaces. Hence, an appropriate cleaning procedure is essential to provide a solid starting point for ALD deposition after black etching.

3.2.1 The RCA Standard Clean

The used cleaning method rather closely follows the procedure published by the Radio Cooperation of America (RCA) [80].¹⁸ The sequence consists of a first step in hot oxidizing alkaline solution (“standard clean one” (SC1)) and a second step in hot oxidizing acidic solution (“standard clean two” (SC2)). The oxide grown in SC1 may be removed in an intermittent HF dip before SC2. Depending on the desired surface termination (hydrophilic or hydrophobic) a final HF may be applied [79]. According to Kern the NH_4OH solution in SC1 removes organic contaminants and many metals, whereas the HCl containing SC2 further removes metals (e.g. Au, Fe), alkali ions, and other residues that are insoluble in SC1 [79]. The wafers are rinsed in deionized (DI) water after every step.

Herein, SC1 and SC2 were carried out in (5:1:1) solutions of $\text{H}_2\text{O}:\text{NH}_4\text{OH}:\text{H}_2\text{O}_2$ and $\text{H}_2\text{O}:\text{HCl}:\text{H}_2\text{O}_2$ at $80 \text{ } ^\circ\text{C}$ for 10 min, respectively. Between the two cleaning steps the samples were dipped in 1% HF at room temperature for 60 s. After SC2, the clean $-\text{OH}$ terminated (hydrophilic) wafers are directly transferred to the ALD reactor, where the Al_2O_3 deposition is carried out. A summary of the used cleaning parameters is given in table 3.2.

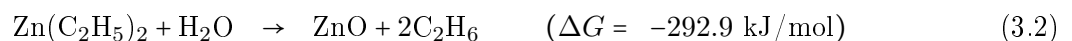
¹⁸The RCA developed the H_2O_2 solution based procedure for surface cleaning of wafers in integrated circuit technology and gave the method its name.

3.3 Thermal Atomic Layer Deposition

Atomic layer deposition (ALD) is a method to deposit thin films¹⁹ based on sequentially separated and self-terminating chemical vapor-solid reactions. It is important to note that the reaction terminates upon saturation of surface sites while an excess amount of precursor is supplied. However, there is no commonly accepted precise definition of ALD itself, as there exist various similar methods that may depend on the precursor material and/or the source of energy to catalyze the reaction (e.g. heat, plasma [67], or UV/VIS light [178]). Specifically, ALD is a sub-class of chemical vapor deposition (CVD) methods, dividing the reaction of the precursor and the reactant material into two half-reactions²⁰ that are repeated until the desired film thickness is reached. The reaction steps may either be separated in time [124] or in space [122, 153] and can only occur at the sample's (and chamber's) surface until saturation is reached and the reaction stops. Thus, during one reaction cycle a maximum of one monolayer of the desired compound is deposited, which should not be expected when compounds (ML_n, where M is metal and L is ligand) are used as reactants [124]. This way, the method provides extremely precise thickness control, down to the (sub-)nanometer range and facilitates control of the composition gradient in multinary layered systems during deposition.

ALD was developed in two different groups in the 1960s and 1970s. It was first called '*molecular layering*' (ML) by Aleskovskii *et al.* who deposited films from various catalysts they elaborated²¹ [124]. More broadly recognized, in 1974 Suntola and Antson used their independently discovered method of '*atomic layer epitaxy*' (ALE) in Finland for the deposition of thin ZnS films for large-scale electroluminescent displays [124]²² and declared the first patent on ALD [153]²³. Since then ALD has increasingly gained attention in the fields of various applications [83, and references within]. Especially in micro-electronics, high-k dielectrics deposited by ALD are exploited for their superior electrical properties over the classical solution of thermally grown SiO₂.

For this work, aluminum oxide (Al₂O₃) and zinc oxide (ZnO) as well as aluminum doped zinc oxide (ZnO:Al, short: AZO) films have been deposited in a thermal ALD reactor ("TFS-200")²⁴ from *Beneg* using the precursor materials trimethylaluminium (TMA, Al(CH₃)₃) and diethyl zinc (DEZ, Zn(C₂H₅)₂) in combination with water (H₂O) as the oxygen source. The basic chemical net-reactions are [45]:



¹⁹In most cases binary (or multinary) compounds are deposited, but the deposition of pure elements is also possible in some cases [124].

²⁰As Puurunen points out in reference [124, footnote 72]: "The term 'half reaction' in ALD should not be confused with the conceptual half reactions in electrochemistry. In ALD, the half reactions are real reactions."

²¹Aleskovskii showed deposition of TiO₂, GeO₂, VO_x, and Al₂O₃ amongst others mainly for precursor development.

²²According to [124] Suntola *et al.* also fabricated compounds of GaP, Ta₂O₃ and Al₂O₃, amongst others.

²³Interestingly, this first patent by Suntola and Antson [153] presented both, the "spatial" ALD method which can be much faster than the simultaneously introduced "temporal" ALD. However, the latter was established as the classical method whereas the spatial-ALD technique has only been re-discovered after more than 30 years and is now exploited for implementation in industrial applications [121].

²⁴Thin Film System for single wafer with a max. size of 203 mm $\hat{=}$ 8".

where ΔG is the Gibbs free energy for the according exothermal²⁵ reactions at 0 °C [45]. The extremely large (negative) reaction enthalpy indicates the high robustness of the ALD reactions. Here it becomes clear that the reactions may be conducted at fairly low temperatures which can be exploited to coat temperature sensitive substrates [159, 160].

3.3.1 ALD Cycle

In order to profit from the exceptional thickness control of ALD and to facilitate the preparation of pinhole free thin films, it is necessary to study ALD film growth. Fortunately, Al₂O₃ formation from TMA and H₂O is the ALD process, which is understood in most detail concerning the surface chemistry. As done in some review articles [45, 124] general ALD deposition shall be explained using this exemplary reaction.

A typical deposition cycle in time-separated (or “temporal”) ALD is depicted in fig. 3.3 for the reaction of TMA and water. The deposition is started on Si-OH (fig. 3.3(0)). In the first step, precursor one (TMA) is introduced into the reactor. It reacts with active sites (e.g. -OH groups) all along the surface, including the walls of the reaction chamber (fig. 3.3(1a)). Once the surface is saturated by the precursor, the excess precursor molecules do not find any more partners for chemisorption and the reaction stops (fig. 3.3(1b)). This effect of self-termination makes ALD a non-continuous deposition method, which is a unique feature and enables precise thickness control of the deposited film down to the atomic level. In the second step, the excess precursor and reaction by-products are purged out of the reactor (fig. 3.3(2)). If the purge time is adjusted adequately, no gaseous precursor of type one is present when in step three the second precursor enters the reactor volume (fig. 3.3(3a)). Again, the precursor molecules of type two (H₂O) only react with active surface sites (-CH₃ groups) completing the (sub-)monolayer formation (fig. 3.3(3b)). In the last step, the excess reactant as well as reaction by-products are purged out leading back to an -OH terminated surface similar to the initial state (fig. 3.3(4)). This reaction cycle may be repeated until the desired film thickness is reached.

3.3.2 Growth Per Cycle

ALD film growth is specified as the material amount deposited per full reaction cycle, called the ‘*growth per cycle*’ (gpc), in contrast to continuous deposition methods like CVD or PVD²⁶ where a deposition/growth rate (amount per time) is used. The gpc may be quantified in atoms deposited per unit surface area [nm⁻²] [125], or as the resulting change in layer thickness during each deposition cycle [nm/cyc] (in the literature often [Å/cyc]). For this work, the deposited film thickness was measured ex-situ by ellipsometry on unstructured surfaces or by SEM/TEM on (nano)structured ones. Therefore, the unit [nm/cyc] is used. It is rather simple to attain an average gpc for a given number of cycles by dividing the measured film thickness into this number. However, the real gpc is actually a differential quantity describing the thickness change during each individual cycle.

²⁵The reaction is exothermal if $\Delta G < 0$.

²⁶physical vapor deposition (PVD)

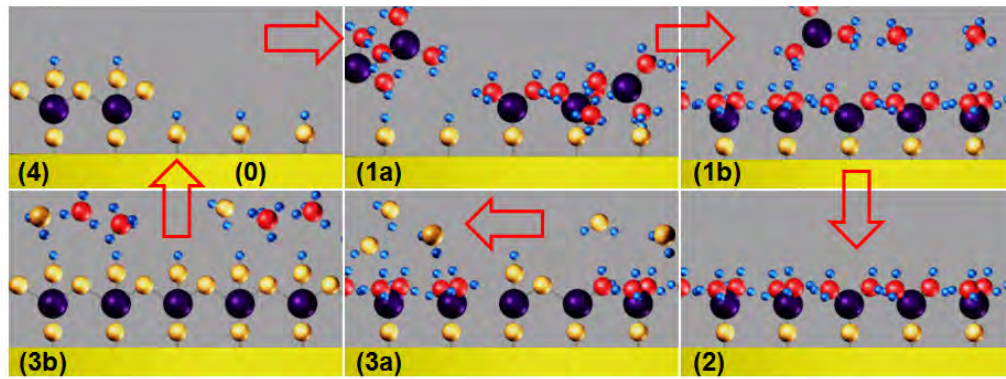


Figure 3.3: Schematic presentation of a typical ALD cycle. The initial surface (0) is exposed to the precursor in step one (1a). Here, TMA molecules react with the surface until it is saturated and the reaction stops (1b). In step two excess precursor and reaction by-products are purged out (2). The second precursor, here water, is pulsed into the chamber in step three (3) and likewise reacts with active surface sites. Finally, excess reactant and by-products are purged out leading back to the initial situation (4). The images were extracted and adapted from [15].

GPC Dependence on Surface Condition and Number of Cycles

According to Puurunen *et al.* the gpc is a function of the precursors (i.e. their deposition chemistry), the reaction temperature, and the surface condition [125, and references within]. Therefore, the value must not be constant if the (initial) surface condition changes while depositing the film. Both, TMA and DEZ, preferably react with $-OH$ groups. Thus, on a $-H$ terminated Si surface the reaction may not start until the H_2O pulses have slightly oxidized the surface [125]. This type of substrate-inhibited growth was reported for Al_2O_3 on HF dipped Si which leads to an island-like growth mode with the first monolayer being complete after ≈ 10 cycles [125]. After Puurunen *et al.* “the gpc is small in the beginning of the growth, increases with the number of ALD reaction cycles, goes through a maximum [≈ 20 cyc, M.O.], and settles finally to a constant, ‘steady’ value.” after deposition of about 40 cycles [125]. A similar behavior was observed in our experiments (see fig. A.2(b) of appendix A.2). In an accompanying study investigating the Si/ Al_2O_3 -interface as a function of the first deposited ALD cycles by means of XPS before and after thermal annealing [107] it was found that the first 1 – 2 Al_2O_3 monolayers close within the first 10 – 15 cyc on HF dipped substrates. The growing Al_2O_3 layers are found to be non-stoichiometric with a rather high excess of unbound $-O$ atoms in the vicinity of the interface. However, measured by means of optical ellipsometry, the average gpc on $-OH$ and $-H$ terminated Si surfaces were found to follow the trend observed by Puurunen *et al.* and could not be distinguished in the range of errors of the conducted ex-situ measurements of this work. In general, ALD film growth was observed to be more homogeneous on $-OH$ terminated Si surfaces which were therefore chosen as the standard surface condition because film homogeneity might have an influence on the charge carrier lifetime. In addition, usually a comparably high number of cycles ($\gg 50$) was deposited for optimal surface passivation so a constant gpc can be assumed.

The real gpc of Al_2O_3 on Si- OH was determined by depositions with a varying number of cycles, n . The resulting total oxide layer thickness, d , was measured by ellipsometry on three samples of each thickness. The thickness data and the accordingly calculated (average) gpc are plotted *vs.* n in fig. 3.4. Clearly, d linearly increases with the cycle number indicating a constant gpc (fig. 3.4(a)). However,

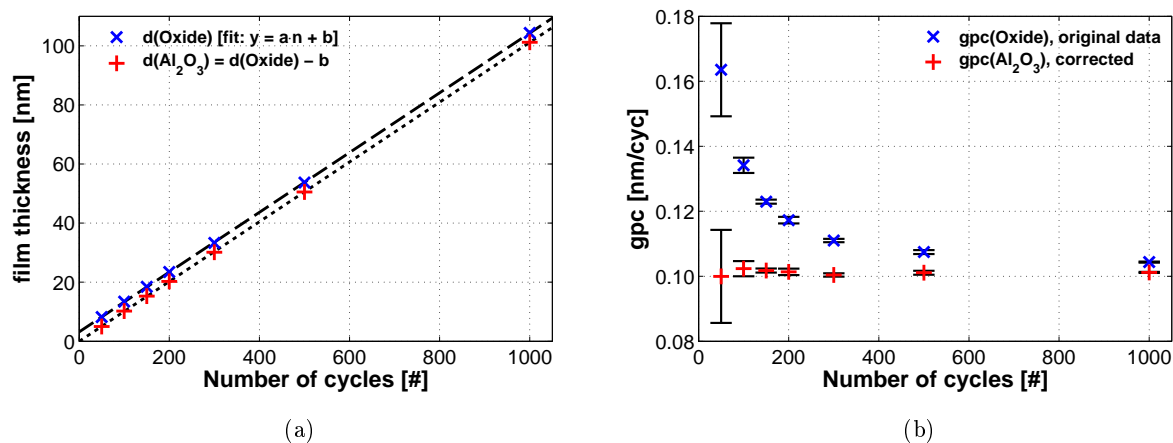


Figure 3.4: (a) The oxide layer thickness as measured by ellipsometry on Si samples with native oxide after ALD deposition of Al₂O₃ with increasing cycle number (x). The dashed line is a linear fit to the averaged thickness (three samples per cycle number) $y = a \cdot n + b$, with b representing the average thickness of the native SiO₂. The data were then corrected by the ordinate intersection (+, dotted line). (b) Calculated gpc in dependence of the number of ALD cycles for the as measured and corrected data, respectively.

the ratio of d/n seems to be decreasing with increasing cycle number (fig. 3.4(b)). This behavior can be explained by the thin underlying native SiO₂, which had an average thickness of about 3 nm in the case of this experiment. The linear fit allows one to subtract the average SiO₂ thickness, b , leading to the expected constant gpc of 0.101 ± 0.001 nm/cyc, which is in good agreement with similar experiments on other oob and HF-dipped substrates (comp. appendix A.2) and with values found in the literature. However, for thin Al₂O₃ layers the uncertainty is much larger than for thicker films because the relative SiO₂ thickness and the influence of its corresponding statistical spread is larger.

ALD Window

True ALD reactions have in common that the amount deposited per cycle is constant in a certain range of process parameters. The according phase space is called the ALD window. As an example a schematic of a temperature window is shown in fig. 3.5. If the temperature is too low the reaction is not activated leading to incomplete reactions and thus to growth inhibition. In other cases multilayer adsorption may occur due to precursor condensation. If the temperature is too high the precursors may decompose which can lead to accelerated reactions (e.g. the precursor may become self-reactive). Yet another possibility is diminishing growth due to re-evaporation, i.e. desorption of the surface species.

Due to the direct carbon-metal bond true metal-organic precursors with alkyl-ligands like TMA and DEZ are rather reactive if a group six element like oxygen is supplied (e.g. by adding H₂O) [124]. Therefore, these precursors often exhibit a rather high gpc. For the exemplary Al₂O₃ reaction (fig. 3.3) the gpc may vary in the range of 0.13 nm/cyc at 180 °C to 0.08 nm/cyc at 300 °C [123, fig. 1] corresponding to roughly 30 – 40% of a monolayer [45, 123–125].²⁷ Similarly, ZnO deposited from

²⁷Even though thermal ALD deposited Al₂O₃ is amorphous, a monolayer may be defined by the number of active surface atoms, i.e. the total number of accessible bonds for chemisorption of precursor molecules. However, it is

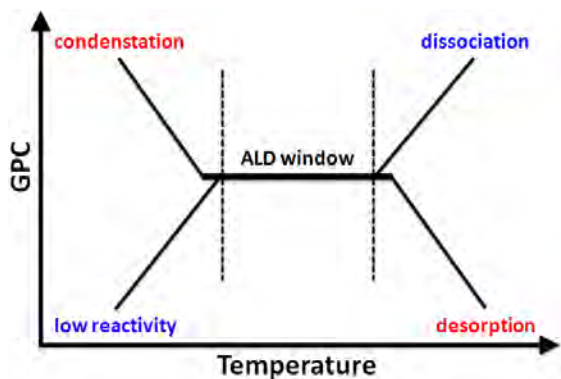


Figure 3.5: The ALD window is defined as the temperature range of a constant gpc. Mechanisms causing gpc changes are also indicated. (Adapted from [45])

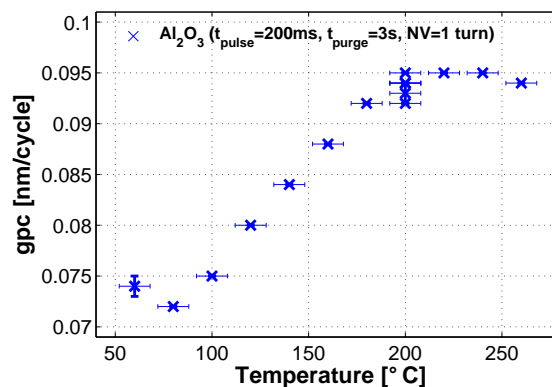


Figure 3.6: gpc as calculated from 1000 cyc. Al_2O_3 on polished Cz Si wafers with native SiO_2 for symmetric pulse and purge times. NV: needle valve.

DEZ and water at temperatures between 100 and 160 °C leads to a gpc between 0.22 nm/cyc and 0.25 nm/cyc [7, 45], respectively. Just to give an example, films deposited from other classes of precursors may have (much) smaller gpc values: A Y-complex in combination with O_3 forms YO_2 at a gpc of only 0.023 nm/cyc in a temperature range of $250\text{ °C} < T_{\text{ALD}} < 380\text{ °C}$ [123, fig. 2]).

Within this work, the gpc of Al_2O_3 was calculated for the range of $60\text{ °C} < T_{\text{ALD}} < 260\text{ °C}$ and for the parameters indicated in fig. 3.6.²⁸ Below 80 °C the film thickness is rather inhomogeneous while the gpc is relatively low. With higher T_{ALD} the gpc increases and within an error of reproducibility stabilizes on a plateau between 180 and 260 °C. As previously mentioned, for even higher temperatures the gpc should decrease again [123], which may be indicated by the slight drop at 260°C.

GPC Dependence on the Purge Time

For solar cell surface passivation a high sample throughput is necessary. Even in a batch reactor the cycle time should be kept as short as possible, and hence, the precursor dose should be kept low to minimize the purge time. On the other hand, for true (self-terminated) ALD reactions some excess precursor is needed. In turn, an adequate purge time is necessary to avoid “parasitic CVD” growth. The characteristic time of a full ALD cycle therefore depends on the precursor chemistry (viscosity, volatility, vapor pressures), the process temperature, total pressure, and even the reactor geometry, etc. Fig. 3.7 shows the deposited film thickness of Al_2O_3 for varying purge times. With increasing purge time, the film thickness decreases. For short purge times a parasitic CVD component can

important to note that there is a difference between a monolayer of adsorbed precursor molecules fully saturating the surface so the reaction is self-terminated, and a monolayer of the ALD deposited compound material. The first full compound monolayer may only be completed after a certain number of cycles. According to R. Puurunen one full monolayer of Al_2O_3 has an average thickness of $\bar{h}^{\text{ml}} = 0.289\text{ nm}$ [123], whereas George calculated a thickness of $\bar{h}^{\text{ml}} = 0.38\text{ nm}$ [45]. For more detailed thoughts on that matter please refer to the work published in [45, 123, 125] and [124, sec. III A., and V B.2.].

²⁸The NV is a manually adjusted valve to control the amount of precursor (pc) evaporated from the pc-container. The gpc error bars indicate the film homogeneity over single 3" wafers. Repeated experiments under similar conditions are plotted at $T_{\text{ALD}} = 220\text{ °C}$. The error bars on the T_{ALD} axis denote a possible systematic error concerning the measurement of an absolute temperature value in the deposition system.

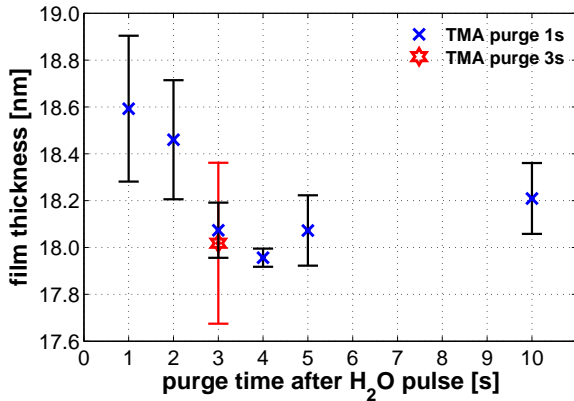


Figure 3.7: Film thickness of 150 ALD cycles Al₂O₃ on out-of-box Si/SiO₂ for increasing purge times after the H₂O pulse and constant TMA purge time of 1 s (x). An extra sample with symmetric purge times of 3 s is also shown (☆). The standard deviations were calculated from single measurements on three different samples.

not be excluded. However, depending on the desired film such a component may be exploited to manipulate physical properties and may be beneficial. Both, homogeneity and reproducibility may still be extremely high. The gpc of the shown ALD-Al₂O₃ process seems to stabilize for H₂O purge times longer than 3 s.

3.3.3 Step Coverage and Film Conformality

ALD film growth is limited by chemisorption, i.e. the chemical surface reaction of a gaseous precursor with the surface of a solid sample. The precursor and reactant molecules chemisorb along the surfaces of substrate (and reactor walls) forming a conformal solid film of the desired compound. In contrast, PVD or sputtering methods are working by the physical principal of ballistic transport. Therefore, the deposition of material at the surface is limited by shadowing and diffusion along the surface, and hence, conformal film growth is limited to deposition on flat surfaces or shallowly structured ones if the samples are rotated. Essentially, one has to distinguish between macroscopic textures and nanostructures. Standard KOH-texturing leads to pyramidal shaped surfaces, whereas b-Si is a very rough nanostructure. The surface coverage of both methods (PVD and ALD) is depicted schematically in fig. 3.8. ALD is the deposition method with the highest step coverage and enables the highest level of conformal and homogenous film growth on (and in) complex and porous 3D structures at low temperatures [8, 160], porous substrates [55, 83, 92], and even powders [163].

To characterize such films and/or the applicability of deposition methods to rough and deep structured surfaces, the following criteria can be defined as depicted in fig. 3.9:

- **Step coverage** is defined as the ratio b/a of the minimum film thickness, b , on the side of a (deep) step and the maximum film thickness, a , on the top of the structure. In the same way one may define *bottom coverage* d/a , with d , the film thickness on the bottom of a trench or pore.
- **Conformality** is defined by the ratio of c/b , with c , the bulge thickness sideways from the top of a step and the thinnest film thickness, b , on the side of the step.
- The **aspect ratio** is the height h of a structure divided by its width w .

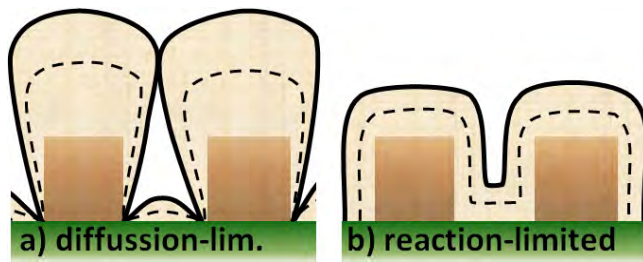


Figure 3.8: A thin film deposited onto rod-like features by the diffusion limited PVD technique (a) and the reaction-limited ALD method (b).

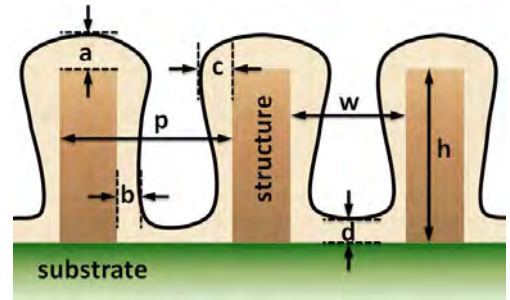


Figure 3.9: Step coverage b/a , conformality c/b , and bottom coverage d/a of films deposited on a structured substrates. The pores of period p have aspect ratios of h/w .

Table 3.2: Summary of the standard conditions used for surface passivation. The sequence was applied after the black etching step. According reference wafers were identically treated.

| RCA Clean | <i>Solution</i> | <i>c</i> [%vol] / <i>R</i> [MΩ] | <i>Mixture</i> | <i>Time</i> [min] |
|--------------------------|---|-----------------------------------|-----------------------------|------------------------------|
| HF-dip | HF | 1% (or 5%) | - | 1 |
| SC1 | NH ₄ OH : H ₂ O ₂ : H ₂ O | 25% : 30% : ($R \geq 15$) | 5 : 1 : 1 | 10 |
| HF-dip | HF | 1% (or 5%) | - | 1 |
| SC2 | HCl : H ₂ O ₂ : H ₂ O | 37% : 30% : ($R \geq 15$) | 5 : 1 : 1 | 10 |
| DI water rinse | H ₂ O | $R \geq 15$ | - | until <i>R</i> is reached |
| ALD | <i>Precursor</i> | <i>Duration</i> [ms] | <i>T_{ALD}</i> [°C] | |
| step 1 | TMA pulse | 200/250 | 180 | |
| step 2 | N ₂ -purge | 1000 | 180 | |
| step 3 | H ₂ O pulse | 200/250 | 180 | |
| step 4 | N ₂ -purge | 3000 | 180 | |
| PDA ²⁹ | <i>T_{PDA}</i> [°C] | <i>Ambient</i> (<i>p</i> [mbar]) | <i>Duration</i> [min] | |
| Muffle Furnace | 385 | Air ($p \sim 1013$) | 30 | |
| Vacuum Furnace | 385 | Ar ($p \leq 1$) | 30 | |

3.4 Post-Deposition Annealing Treatments

It is known from the literature that ALD deposited Al₂O₃ films only have a rather poor passivation performance in the as-deposited state [62, 65]. After annealing at moderate temperatures around 400 °C usually a much greater number of negative fixed charges can be measured at the Si/SiO_x/Al₂O₃-interface [2, 65]. At the same time, the interface density of states vastly decreases [28, 62, 64]. Hence, thermal activation of Al₂O₃ passivation layers was found to be essential for both the chemical and field effect passivation [31].

Various annealing conditions have been used in this work. Different annealing temperatures, durations and the ambient atmospheres were tested to optimize the lifetime of passivated out-of-box and b-Si wafers. The standard conditions are listed in 3.2 and were applied in all presented experiments if not indicated otherwise.

²⁹Post-Deposition Annealing

Chapter 4

Sample Analysis

4.1 Lifetime Spectroscopy by means of the Quasi-Steady-State Photoconductance Method

To determine the minority charge carrier lifetime in a semiconductor (as introduced in sec. 2.2) the excess carrier density has to be monitored over time. The lifetime can be determined in equilibrium and non-equilibrium. Under constant illumination – the so-called quasi-steady-state – thermal equilibrium dictates equal generation and recombination rates: $(G - G_0) - (R - R_0) = 0$, where $U = R - R_0$ is the net recombination rate and G_0 and R_0 are the generation and recombination rates in thermal equilibrium in the dark. Hence, if the generation rate is known, the lifetime may be calculated following eqn. (2.6) by replacing the recombination by the generation: $\tau_{\text{eff}} = \frac{\Delta n}{G - G_0}$. In contrast, if the generation is terminated abruptly, the excess carrier density changes only due to recombination. Hence, as for many other decaying physical quantities the characteristic decay time can be calculated from the slope of the decay curve, called the transient:¹ $\frac{dn}{dt} = -\frac{\Delta n}{\tau_{\text{eff}}}$.

In both cases the carrier density is needed in order to solve eqn. (2.6). If the sample thickness W and the mobilities for electrons and holes² $\mu_{n,p}$ are known, Δn can be determined through the conductance, σ_L , of the sample in the dark and under illumination by the relation [25, 145]:

$$\Delta n = \frac{\Delta \sigma_L}{qW(\mu_n + \mu_p)} \quad (4.1)$$

The conductance can be easily measured by probing the wafer inductively with a calibrated electromagnetic coil that is part of a resonant circuit. Upon illumination, generated charge carriers follow the field oscillations and thereby de-tune the resonance frequency. To combine the advantages of both methods, Sinton and Cuevas introduced the quasi-steady-state photoconductance (QSSPC)

¹After a short light pulse, the excess carrier density will decay to a fraction of $\frac{1}{e}$ during a characteristic period of time called “lifetime”.

²According to Sinton μ_n and μ_p are well known for Si including their dependence on doping level and excess carrier density and can be found in the literature [145, refs. 3 and 4 within] and [148]. Cuevas and Macdonald note, however, that “the mobilities are a function of themselves of the carrier density (both, via doping and excitation) and temperature (Arora *et al.* 1982). Because of this, Eq. (3) [eqn. (4.1), M.O.] needs to be iterated a few times to obtain self-consistent values of Δn and $\mu_n + \mu_p$.” [25].

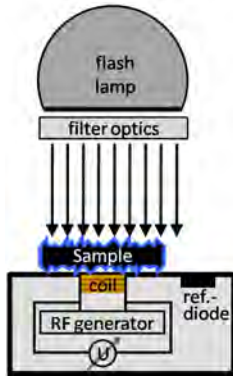


Figure 4.1: Measurement setup for quasi-steady-state photoconductance determination of the charge carrier lifetime.

Table 4.1: Optical constants as used for QSSPC measurements.

| surface/coating | optical constant |
|---|------------------|
| uncoated out-of-box wafer | 0.7 |
| Al ₂ O ₃ (30 nm) | 0.7 |
| Al ₂ O ₃ (100 nm) | 0.9 |
| b-Si* | 1.05 |

*All b-Si sample types independent of the coating's thickness were treated equally.³

method [145], following the idea that a broad range of injection levels can be scanned in a single light flash assuming momentarily constant illumination conditions and homogeneous generation across the bulk [25]. This assumption can be made if the flash light intensity varies very slowly with respect to the investigated lifetime [25, 145]. Spatially homogeneous injection was already assumed, all the while, when introducing τ_{eff} in eqn. (2.6). Experimentally, a homogeneous generation profile in the wafer is created by a (NIR) red-light flash. In the quasi-steady-state, an additional calibrated reference solar cell (or photodiode) is needed to measure the light intensity of the flash lamp, i.e. the generation rate. The specific front surface reflectance of the sample is then taken into account by an according optical constant.³ For transient measurements this optical constant is not needed, however, the lifetime should be larger than $\tau_{\text{eff}} \approx 50 \mu\text{s}$ in order to measure accurate values [145], which was the case for almost all of the presented samples. Hence, most measurements were made in transient mode. However, for unpassivated samples the described “generalized” method was used. The detectable lifetime is only limited by signal strength and may range down to the nanosecond scale [25, 145]. For “generalized” measurements, the optical constants were fixed to the values in table 4.1. The wafer thickness was directly measured by a micrometer gauge. All measurements were performed in a controlled clean room environment at RT in the dark.

4.2 Microstructure Analysis

4.2.1 Scanning Electron Microscopy

Due to the much smaller wavelengths of energetic electrons scanning electron microscopy offers a much higher magnification than optical microscopy. This versatile method can be applied to a very large class of samples including semiconductors, insulators and even biomaterials. However, one of the restrictive factors to the sample is the requirement of high vacuum conditions. Thus, no outgassing samples can be introduced into the chamber.

³The optical constant represents the photogeneration fraction compared to 38 mA/cm^2 . Hence, if the sample's absorption is higher than that of the reference cell, the value may surpass 1.00.

Electrons are either thermally evaporated from a filament, or can be directly extracted by field emission (FE). If a sufficiently high voltage is applied to a metal (e.g. W) tip with a very small radius of curvature, the electric field reaches intensities high enough to enable electron tunneling into the vacuum. The narrow spatial and energy (i.e. velocity) distributions allow for very high resolution imaging. The extracted electron beam ($1 \leq E_{\text{beam}} \leq 30$ keV) is then guided through a set of electromagnetic lenses where it is focused and scanned over the sample's surface. The image resolution (usually a few nm) primarily depends on the beam diameter.

Various image contrast mechanisms can be exploited to gain information about the sample (compare fig. 4.2 in sec. 4.2.3). The most common ones use secondary-electrons (SE; $E_{\text{SE}} \sim \text{eV}$) or back scattered electrons (BSE; $E_{\text{BSE}} \sim \text{keV}$) which are guided by a certain counter-voltage toward the detector. Due to their low energy, SE can only escape near surface regions and display the topography of the sample. The SE are sensed by the so-called SE and/or in-lens (IL) detectors. Surface facets inclined towards the detector and edges facilitate higher electron intensities and appear brighter than other zones. Another possibility is to record energy dispersive electron images (e.g. of BSE) to obtain information about the chemical composition of the sample. Heavy elements lead to a higher scattering probability and hence appear brighter than light materials. In detail, electron-matter interactions as well as their detection and contrast mechanisms are much more complicated and beyond the scope of this work. For this work, different FE-SEMs were used: A *Jeol - JSM 6700 F*, and a *Zeiss GEMINI®*. The latter represents the SEM column of the analysis systems presented in the following.

4.2.2 Focused Ion Beam (FIB)

To resolve the geometric surface morphology of the nanostructured black Si surfaces two *Zeiss CrossBeam®* focused ion beam (FIB) systems (the *NVision 40* and the *AURIGA™*) at the Fraunhofer Institute for Mechanics of Materials (IWM) were used. The systems allow for material modification and *in-situ* visualization. Analogue to in an SEM, a FIB column consists of an ion gun and corresponding electromagnetic beam optics to provide a confined energetic beam of e.g. Ga-ions. This way the FIB can be used to either cut into the surface or to locally deposit certain materials from gaseous precursors (e.g. Pt, C, etc.). To choose an adequate precursor, the resulting image/material contrast should be considered. Amongst numerous other FIB parameters the beam current and aperture can be adjusted for effective material removal with high precision. Craters of a few micrometer depth and width can be milled into a surface. This way transversal cross sections or thin lamellae of thicknesses below 100 nm can be prepared. The cross sections can be examined *in-situ* by SEM and the lamellae are used for subsequent TEM investigations.

If the surface has a complex 3D structure and/or is composed of materials of different density or atom species with different core-masses, the effective sputtering coefficients may locally differ. This phenomenon leads to the so-called “curtaining” effect. Due to the locally different surface abrasion, a prepared transversal cross section may become corrugated which then looks just like a theater curtain (for examples of curtaining please refer to figs. 5.5, 5.9(b) or 5.10(d)).

The ion beam intensity follows a spatial Gaussian distribution. Hence, a surrounding halo of energetic ions with a lower intensity is present around the beam core. To protect the nanostructures from halo-damage in the region of interest our samples underwent a standard preparation procedure before

geometric FIB analysis and/or TEM lamella preparation. On planar surfaces, sputter-deposited metal protection layers (e.g. Pt, Au, Ag, etc.) may be used. However, on complex structures like the random b-Si surfaces voids are formed due to the PVD-growth mode described in section 3.3.3 (comp. fig. 3.8). Thus, a protection layer of ALD ZnO or AZO was conformally deposited on top of the b-Si surfaces, which helps to avoid curtaining. The pores are completely filled by the ALD films until a more or less flat surface is obtained. Typically, a film thickness of ≥ 160 nm was used for either b-Si structure. In some cases sputtered Pt layers were used to protect the ZnO/AZO films which rapidly decompose under ion beam irradiation. In addition, the region of interest was usually protected by an additional Pt pillow which was directly deposited by FIB before ion-milling.

4.2.3 HR-TEM, EELS and EDX

Transmission electron microscopy [155] is a very reliable and precise method for structural analysis. In high resolution transmission electron microscopy (HRTEM) lateral resolutions down to the sub-nanometer scale can be achieved. As mentioned above, the exact measurement processes are rather complicated. A very comprehensive introduction on electron diffraction, imaging and spectrometry is given in [167].

Electrons, once extracted, are accelerated with several hundred kV onto the sample, passing different lenses and filters. Upon arrival at the sample, several electron-matter interactions are possible: the electrons may be back-scattered (SEM), provoke secondary electrons or Auger electrons, photons (cathodoluminescence), and x-rays (energy dispersive x-ray spectrometry, EDX), which can all be used for sample analysis (see fig. 4.2). Many methods and operational modes are possible. If the sample is thinned to ≤ 100 nm the electron energy is high enough to traverse the thin sample lamella. Some of the transmitted electrons (TEM) get scattered elastically and in-elastically (electron energy loss spectroscopy, EELS) and may then be detected below the target.

For this study only a few selected samples were subjected to lamella preparation and (HR)TEM imaging with the *FEI TITAN* at Fraunhofer IWMH [50], to get insight into the local microstructure of the coated b-Si interfaces. In combination with EELS and EDX spectroscopy some locally resolved elemental information of the sample's composition could be gained. Also, the thickness of ALD deposited films was in some cases estimated from these SEM or TEM images of cleaved edges or FIB cut cross sections. Of course, ellipsometry would be a more precise method to accurately determine the film thickness. However, nanostructured surfaces depolarize the light due to the randomizing scattering effect and simultaneously reduce the intensity of reflected light making ellipsometry measurements unfeasible for b-Si.

4.2.4 ToF/SIMS

Time of flight secondary ion mass spectrometry (ToF/SIMS) is an analysis method to resolve the elemental composition of thin films with a precision in the part-per-million (ppm) range. Hence, atomic contents as low as $\approx 5 \cdot 10^{16} \text{ cm}^{-3}$ can be detected in a sample volume. Two heavy ion beams with energies of a few keV are needed. The primary beam sputters surface species (secondary ions)

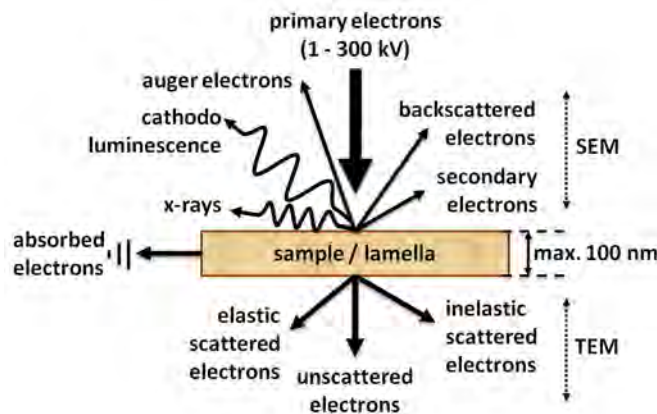


Figure 4.2: A variety of different electron-matter interactions occurring in scanning and transmission electron microscopy measurements.

that are analyzed by a time of flight spectrometer. By measuring energy and time, the secondary ion's mass can be calculated. Subsequently, an additional focused ion beam with a higher current is used to mill into the depth (similar to FIB preparation).

The milling crater may be $300 \times 300 \mu\text{m}^2$ wide, whereas the according region of interest only consists of the centered $100 \times 100 \mu\text{m}^2$. The inner crater is then probed by the primary ion beam with a resolution of 256×256 pixels. At each position a single pulse of the primary beam is deposited and subsequently a fraction of surface species is sputtered. These secondary atoms or molecules may actually be neutral, positively or negatively charged depending on their electronegativity. The primary ion beam must be of opposing electronegativity to obtain a good signal to noise ratio. Thus, for the detection of preferably positive secondary ions (e.g. H^+ , Al^+ , etc.) a beam of energetic O^+ -ions can be used. The initial beam is charged like the targeted species because the O^+ -ions will collect electrons during the sputtering process and easily become negative. In contrast, for the detection of negative ions (e.g. O^- , Zn^- , etc.) Cs^- can be used. To prevent charging effects, the surface is treated with a low energy electron beam ("flood gun") after milling into the depth, i.e. before probing the surface with the primary beam again.

4.3 Optical Characterization of Thin Films

4.3.1 Setup for Reflectance and Transmission Spectroscopy

For optical spectroscopy a *Lambda* 900 spectrometer (by *Perkin Elmer*) was used. The setup is located at the IAP in Jena and is equipped with a 150 mm diameter integrating sphere covering the full half-space of 2π .⁴ The sphere holds two detectors (Si and InGaAs⁵) for detection of UV/VIS and NIR light, respectively. This allows to capture the specular and diffuse components of reflected or transmitted light from a tungsten lamp, which was focused to a spot size of about $2 \times 4 \text{ mm}^2$ on the

⁴If the sample is mounted on the entrance/exit port, the sphere covers one half-space of 2π . It is also possible to mount the sample inside allowing to measure its absorption directly. In that case, the sphere covers almost the full space of 4π less the port openings.

⁵The band gap of $\text{In}_{1-x}\text{Ga}_x\text{As}$ increases with increasing $0 \leq x \leq 1$ from below 0.4 eV for InAs to over 1.4 eV for GaAs.

sample.⁶ The signal intensity was normalized to a *Labsphere Spectralon* reflectance standard.⁷ The wavelength resolution of the recorded spectra was typically 2.5 nm in the UV/VIS and 10 nm in the NIR ($\lambda > 860$ nm), respectively. The reflection was measured under an angle of incidence of 8° to capture the specular reflex, whereas transmission measurements could be performed at an angle of incidence of 0° . A special sample holder allowed to put samples into the sphere, which enabled direct measurements of the absorption for angles of incidence between 15° and 70° .⁴

4.3.2 Ellipsometry

By ellipsometry the complex dielectric function⁸ and the thickness of a material can be probed very precisely, if an appropriate model is used for data analysis. The measurement is based on the detection of the change in polarization of a light beam reflected from a surface (see fig. 4.3). Therefore, linear or circular polarized light is directed to the sample under a variety of angles. The polarization state of the specular reflex is detected by a second polarizer (analyzer) and the intensity is measured by a CCD detector. The (complex) amplitude ratio of the reflected p- and s- polarized components can be expressed by Ψ , and the rotation of the polarization angle, Δ , which depend on the thickness and the optical properties of the material [170]:

$$\frac{r_p}{r_s} = \tan(\Psi) \cdot e^{i\Delta} \quad (4.2)$$

The VIS and NIR spectral range was investigated with the automated *Woollam M-2000V* ellipsometer with mapping stage at the MLU.⁹ The data were fitted according to Fresnel's equations with a least-square method implemented in the *Woollam* software.¹⁰ A simple Cauchy model (no absorption) was assumed for the analysis of the transparent dielectric films (Al_2O_3), whereas conductive films (ZnO , AZO) required a more complex oscillator model including a Drude term to account for free carrier absorption. For brevity the models are not explained in detail here but may be reconstructed with help of the *Woollam* software [78, 170].

⁶A few samples were re-measured with an unfocused beam setup, which will be indicated in the results. These measurements appear to be more accurate than the ones measured with the focused beam setup. Unfortunately it was not possible to re-measured all presented samples.

⁷The integrating sphere is made of *Spectralon*.

⁸which (for $\mu_r \approx 1$) is equivalent to the complex index of refraction

⁹The setup is located at the Interdisciplinary Center of Materials Science (CMAT) and measures about 390 wavelengths in the range from 370 – 1000 nm simultaneously via a CCD chip [171].

¹⁰The program Variable Angle Spectroscopic Ellipsometry (VASE) was used. An overview on the features can be found in references [170] and [78].

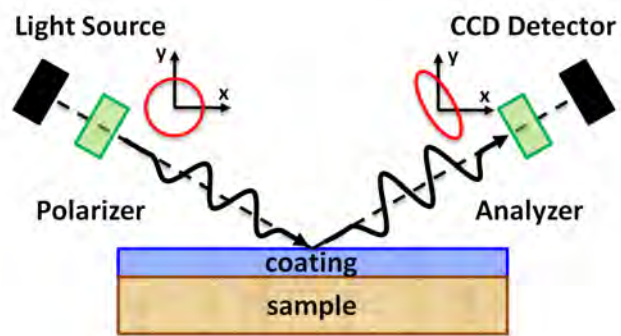


Figure 4.3: Schematic of an ellipsometry measurement setup and the beam propagation. Polarized light hits the coated sample surface under an angle and gets reflected. The analyzer and the CCD chip detect the polarization and light intensity, respectively.

Chapter 5

Microstructure and Optical Properties of Conformally Coated Black Silicon

This work focuses on the comparison of different nanostructured b-Si surfaces concerning their optoelectronic properties in terms of optical absorption and charge carrier lifetime for photovoltaic solar cell applications. This chapter first presents the different surface morphologies arising from the black etching treatments, which will allow to connect geometric and micro-structural features to the applied preparation parameters, starting with a detailed section on ICP-RIE structures. Selected pieces of passivated surface nanostructures were characterized by means of HRTEM (including chemical analysis by means of EELS/EDX). This way, also ALD film growth as well as, conformality and homogeneity could be investigated. In section 5.3 the optical response of the b-Si types is shown and the methods will be compared concerning their absorption.

5.1 Geometric Surface Morphology of ICP-RIE Etched b-Si

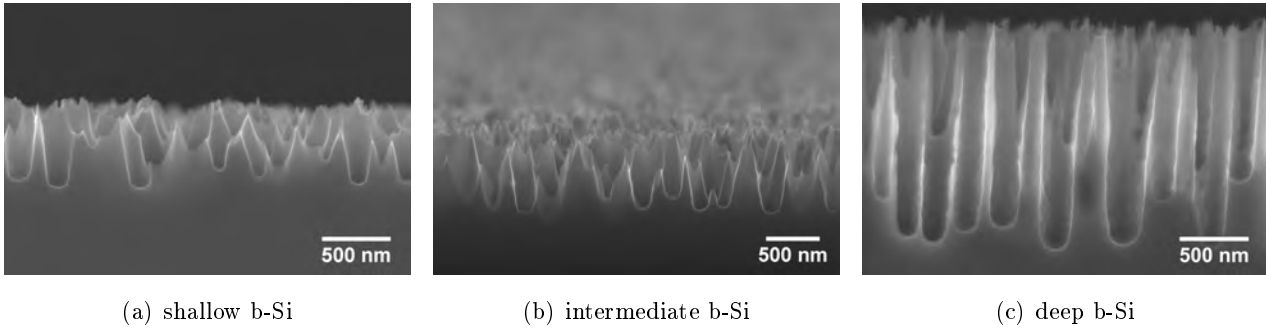
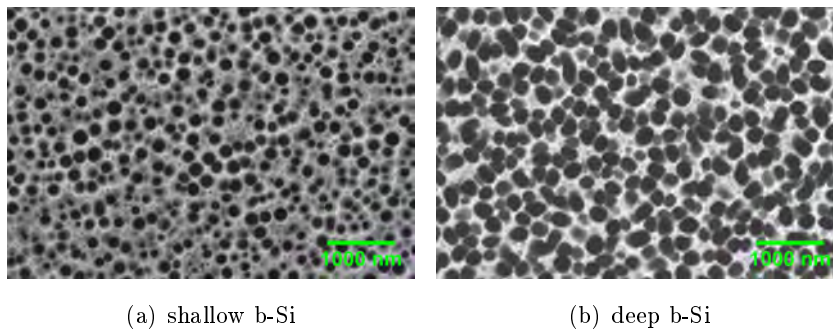
Upon inductive coupled plasma reactive ion etching under the conditions described in sec. 3.1.1 sharp needle-like features appear on the wafer surface. SEM images of the shallow, intermediate, and deep b-Si structures are shown in fig. 5.1(a)-(c), respectively. The shallow and intermediate structures were etched at a “high pressure” ($p_1 = 4$ Pa) for 10 min and 20 min, respectively, whereas the deep structure was processed during 10 min etching in “low pressure” ambient ($p_2 = 2$ Pa). The process conditions are listed in table 5.1.

All structures consist of overlapping pores of typical diameters of roughly 200 nm. The shallow b-Si structure has maximum depths of about 600 nm and sidewall angles around $13 \pm 8^\circ$ from the surface normal (fig. 5.1(a)). Basically, the morphology of the intermediate structure does not differ very much from the shallow one, but as will be discussed later, the electronic surface quality may be different. The deepest pores in 5.1(b) are approximately 750 nm deep with a very similar distribution of sidewall angles. Doubling the etching time drives the topography further into the wafer bulk, meanwhile the structure depth is limited by the process pressure. The deep structure, as the name suggests, has deeper pores of about 1700 nm with sidewall angles in the range of only $3 \pm 2^\circ$. Even though the Si

Table 5.1: Process parameters of the three ICP-RIE processed standard structures.

| $p_1 = 4 \text{ Pa} / P_{\text{hf}} = 6 \text{ W}$ $p_2 = 2 \text{ Pa} / P_{\text{hf}} = 2 \text{ W}$ | | |
|---|--------------|------|
| $t_1 = 10 \text{ min}$ | shallow | deep |
| $t_2 = 20 \text{ min}$ | intermediate | - |

A complete set of etching parameters is listed in table A.2.

**Figure 5.1:** cross-sectional SEM micrographs of the three ICP-RIE model structures. The images were recorded by Thomas Käsebier and are courtesy of the IAP, FSU Jena.**Figure 5.2:** SEM top-view of the shallow and deep ICP-RIE b-Si. Clearly, the structures consist of overlapping pores, which are larger in the case of the deep structure and appear more circular on the shallow etched surface.

needles have base widths of up to 400 nm and almost vertical sidewalls, the very tips in some cases have curvature radii below 10 nm. This deep b-Si surface is even slightly frayed. Little pits are visible at the pore bottom and sidewalls showing how aggressively the etch-passivating layer is attacked by the etching F^* radicals. Note, that the given dimensions in this section were extracted from these very pictures and may differ somewhat from run to run.

The top-view images in fig. 5.2(a) and 5.2(b) show the different lateral dimensions of the nanopores. The shallow pores are rather round and have average diameters of $\approx 145 \text{ nm}$. Again, the intermediate sample has shallow-like pore shapes and diameters. The deep b-Si structure exhibits average pores of $\approx 250 \text{ nm}$ which are more square-like shaped. Due to the statistical distribution the pore sizes scatter by $\pm 30\%$ in either case. Therefore, the characteristic size distributions of the shallow and intermediate can be considered equal, which is especially true if a possible run-to-run deviation is considered. Finally, distinct Si features may range from below 10 nm up to several hundred nanometers and pore sizes may also vary in this range.

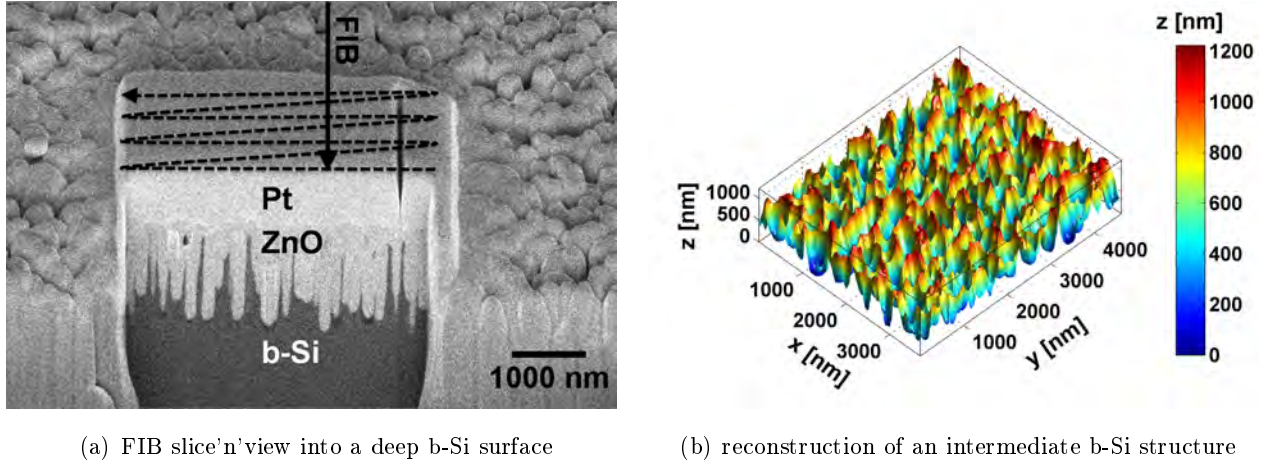


Figure 5.3: (a) FIB slicing of a deep b-Si structure. The surface is protected by a conformal ALD deposited ZnO coating and an additional FIB deposited Pt “pillow”. The material contrast allows for a good boundary detection by the software. The slit on top was cut as a position marker for drift detection. (b) shows the 3D surface reconstruction of an intermediate b-Si structure. The model was calculated as published by Kroll *et al.* in [89].

5.1.1 3D Reconstruction of Real ICP-RIE Etched Black Silicon Surfaces

ALD coated nanostructures were analyzed by means of FIB cutting in the so-called “slice’n’view” mode. Herein, the protected sample surface is cut away slice by slice and subsequently SEM images are recorded of the remaining cross sections. A typical SEM image of a deep b-Si structure is shown in fig. 5.3(a). The slices can have minimal thicknesses of ≈ 10 nm, while the pixel resolution in x and y direction is also ≈ 10 nm. In this manner, volumes of about $5 \times 5 \times 5 \mu\text{m}^3$ were examined with a high voxel resolution of all three standard ICP-RIE b-Si surfaces. From these volumes 3D reconstructions of the surface topography could be calculated by using a flood fill algorithm.¹ The real-life b-Si topographies were then used for the first time as a model for rigorous optical simulations and the results were published by Kroll *et al.* in reference [89]. This way, the geometric surface analysis helped to fundamentally understand the optical response of ICP-RIE nanostructured b-Si surfaces, upon which the discussion will be based. More details on the optical simulations can be found in [88–90].

Surface Enhancement Factor

It was claimed in many papers that the true surface area of b-Si nanostructures enhances the surface recombination and hence limits the lifetime in the b-Si nanostructures [57, 111, 139, 183, 184]. The exact surface area of a nanostructure is not known and can not easily be measured. The FIB slicings and subsequent surface reconstructions allow the estimation of the surface enhancement factor for the different b-Si model structures. Following Oh *et al.* [111], the surface enhancement factor can be calculated by relating the true surface area of the nanostructures, A_{nano} , with its planar footprint (projected area), A_{ref} :

$$\gamma := \frac{A_{\text{nano}}}{A_{\text{ref}}} \quad (5.1)$$

¹The algorithm was programmed by Matthias Kroll at the IAP (FSU Jena) and the method was published in [89].

Obviously, γ becomes unity for the reference sample itself. From the reconstructed surfaces, the surface enhancement factors for the shallow and deep b-Si structure were estimated to lie in ranges of $\gamma \approx 2-4$ and $\gamma \approx 5-10$, respectively [113]. The ranges include a possible structural deviation debited to a possible run-to-run variation of the ICP process. The γ -value of the intermediate structure again equals the one of the shallow b-Si structure. The γ value can also be estimated by measuring the anodic oxide formation [57]. By applying a voltage between the nanowire sample and an electrolyte, a largely enhanced current through the interface can be observed. The reaction saturates once a passivating anodic oxide layer inhibits further growth of the surface oxide. The anodic charge can then be related to the surface area. This way, the γ values of the NW samples were estimated. Yet, another possibility is to weigh the samples before and after removal of a thermally grown oxide as proposed in [112]. Finally, atomic force microscopy was used to estimate the surface area enhancement of a NC-like structure, which yielded a lower boundary of $\gamma_{\min} \leq 3$ [3]. The estimated γ values for the b-Si types investigated in this work are listed in the overview of tab. 7.1 on page 101.

5.1.2 ALD- Al_2O_3 Growth on b-Si Surfaces

Black Si surfaces prepared on polished Cz and FZ Si wafers received a RCA standard clean, were coated with 1000 and 300 ALD cycles of Al_2O_3 , respectively, and subsequently annealed. The sample surfaces were investigated by means of FIB cross sections. Figures 5.4 and 5.5 show the coated nanostructures, respectively. The perfectly conformal Al_2O_3 layer (black) is well visible between either ICP-RIE nanostructured Cz surface (gray) and the Pt protection layer (white/light gray). Protecting Pt films were deposited by sputtering over the whole shallow and deep b-Si surfaces (fig. 5.4(a),(c)) prior to FIB investigation. The additional Pt pillow was deposited by FIB and protects the surface from sputtering effects of the ion beam and its surrounding halo in the region of interest. The shallow structure has pore depths of up to 600 nm which are more or less completely filled with Al_2O_3 . In the left of image 5.4(a) the Si tips are conformally rebuilt by Al_2O_3 resulting in little bumps on a rather flat surface. Note, that the deep pore on the right is completely filled. The white line following the top of the dark Al_2O_3 coating indicates a homogeneously sputtered Pt film.

In the case of the intermediate structure (fig. 5.4(b)), the Al_2O_3 film looks inhomogeneous. However, no sputtered Pt layer was deposited before FIB deposition of the Pt pillow. Nevertheless, the b-Si surface with pore shapes and diameters similar to the shallow structure is completely covered by the dielectric coating. Clearly, a fine bright line is visible at the Si/ SiO_2 / Al_2O_3 -interface, which is rather blurry in the image of the shallow one.

The Al_2O_3 deposition on deep nanostructured b-Si with pore depths of up to 2 μm is shown in fig. 5.4(c). The coating appears to be very conformal and homogeneous on the nanostructure with aspect ratios of about 10. For the deposited film thickness of about 100 nm, the extremely conformal growth leads to partly filled pores which appear to be coated with a thicker film (narrow pore bottom in the lower left). From this image it becomes obvious, that the visible film thickness in FIB cross sections may not be exactly equal to the deposited one. The centered tip appears to have a much thicker coating to the right than to the left. However, to the right of that only Al_2O_3 -like contrast is visible without a Si needle. The ion beam must have removed the Si needle(s) from the cross section. Furthermore, the sputtered Pt layer (white “topping”) is much more inhomogeneous than

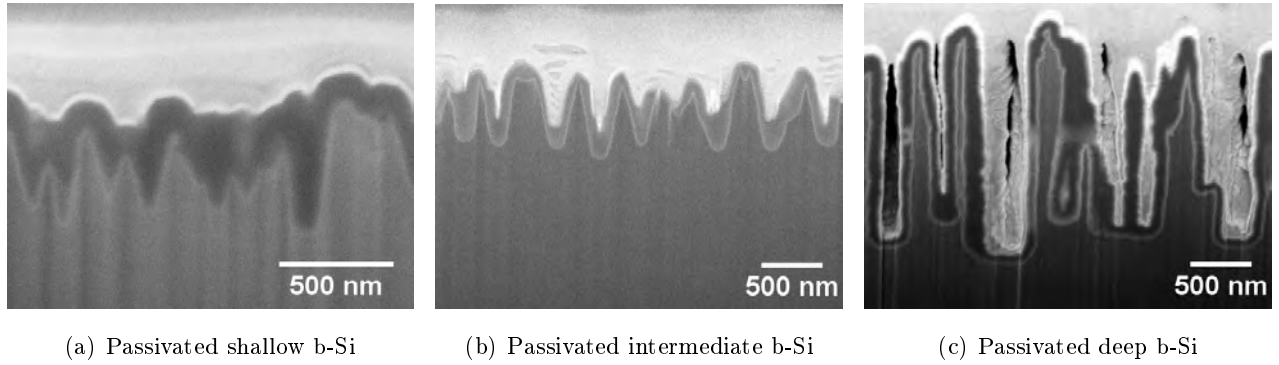


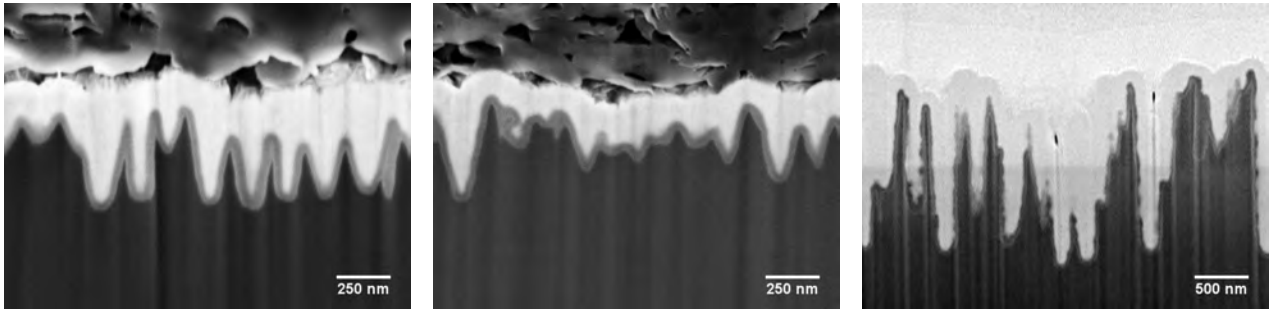
Figure 5.4: SEM images of FIB cut cross sections of the three ICP nanostructures prepared on Cz material coated with 1000 ALD cycles of Al_2O_3 . The dielectric layer conformally covers perfectly all rough surfaces.

on the shallow nanostructure. The top of the tips exhibit thick snow-like covers, whereas there is no white Pt contrast visible in the valleys (including rather wide ones of ≈ 500 nm). Neither did the FIB deposited Pt pillow protrude nor fill the gaps between Si needles.²

Figures 5.5(a)-(c) show the three ICP etched structures on shiny-etched FZ Si wafers after deposition of a 300 cyc thin Al_2O_3 passivation layer. The pores of the shallow and intermediate structures are only up to 450 nm deep and therefore a bit smaller than the ones described previously. The deep structure exhibits maximum peak-to-valley heights of about 1650 nm. Estimated from all three images, the Al_2O_3 coating has an approximate thickness of 33.2 ± 5.9 nm. Again, the coating is highly conformal and extremely homogeneous over all nanostructure types. The images were recorded with the detector for secondary electrons and the fine white line at the Si/SiO₂/Al₂O₃-interface is by far not as pronounced. These structures were additionally coated with a sacrificial ALD ZnO layer (white). The ZnO layer was somewhat damaged in a first attempt to examine the sample, just like the Al_2O_3 passivation in the previously described intermediate structure without a protective coating. The shallow and intermediate sample were then protected with conductive carbon paste (coarse porous/dark gray top layer) and the deep one directly received a FIB deposited Pt cover. In these images a slightly stronger “curtaining” effect is present (comp. sec. 4.2.2).

In general, no pinholes, voids nor inclusions were found on any ALD coated ICP b-Si/Al₂O₃-interface. The ALD films appear to be very homogeneous in thickness and exhibit a smooth monochrome shading in the micrograph. Increasing the etching time from 10 to 20 minutes results in almost identical geometry as the structure depth is limited by the process pressure and the larger etching time only causes a proportional transfer of the topography further into the wafer bulk. Lowering the process pressure from 4 to 2 Pa, the maximum pore depths increased by a factor of ≈ 3 and features with much steeper sidewalls emerged. Maximum depths of the Si features may vary by a few hundred nanometers. However, the needle length distributions are broader than that. Sidewall angles and lateral correlation lengths appear to be stable within the given error ranges. The bias voltage was more or less stable around 21 ± 5 V for all runs even though P_{hf} was varied. Very little “curtaining” is apparent in either of the presented images even though the deep structures exhibit voids that were not completely filled by Pt layers deposited prior to FIB cutting. If the samples were adequately

²comp. fig. 3.8.



(a) ALD- Al_2O_3 coated shallow b-Si (b) ALD- Al_2O_3 on intermediate b-Si (c) ALD- Al_2O_3 coated deep b-Si

Figure 5.5: SEM micrographs of the three ICP-RIE model structures coated with 300 cyc of Al_2O_3 , corresponding to a film thickness of $\approx 33.2 \pm 5.9$ nm. The dielectric is highly conformal and extremely homogeneous.

coated by a protecting (sacrificial) ALD ZnO and sputtered Pt layer, curtaining artifacts could be minimized.

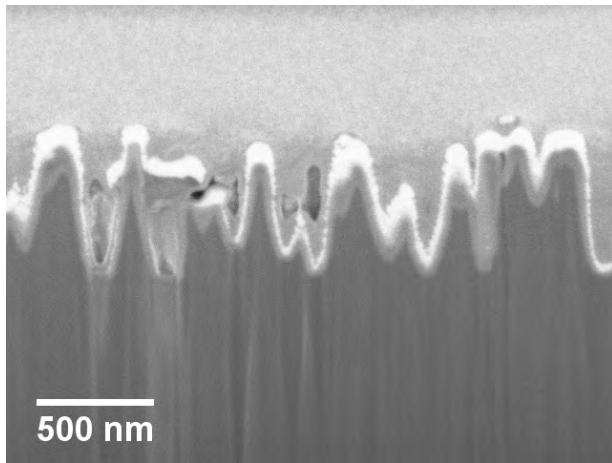
5.1.3 CVD SiN_x Passivation Layers as an Alternative to ALD- Al_2O_3

An attempt was made to passivate ICP-RIE b-Si nanostructures by means of PE-CVD SiN_x . After RCA cleaning, a shallow and a deep b-Si structure along with an unstructured reference were coated with a nominal thickness of 70 nm SiN_x . FIB cross sections of the nanostructures are shown in fig. 5.6. On the shallow structure (bottom black of fig. 5.6(a)) the passivating dielectric (gray) seems to cover the whole surface area. The SEM image reveals a rather good step and bottom coverage and high film homogeneity. However, with roughly 52 nm the film appears to be thinner than intended. The sputtered Pt layer (white) is less homogeneous than the CVD film. In contrast, the SiN_x step and bottom coverage on the deep structure is rather poor. On top of the tips a thick film was deposited, whereas almost no dielectric is present at the bottom of the pores. Also, the sputtered Pt layer only scarcely covers the inner pore surfaces. In comparison to the SiN_x layers, ALD- Al_2O_3 films exhibit more suitable deposition (i.e. growth) properties in terms of full coverage of all ICP-RIE b-Si surface geometries.

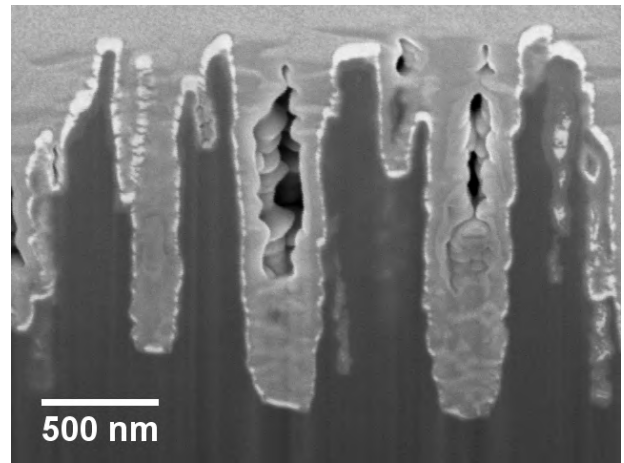
5.1.4 Microstructure and Elemental Analysis of b-Si/ Al_2O_3 -Interfaces

To further analyze the microstructure of b-Si/ Al_2O_3 -interfaces, transmission electron microscopy was used for high-resolution imaging of cross section lamellae. Two micrographs of an unstructured reference wafer and an ICP-RIE structured intermediate b-Si/ Al_2O_3 -interface are shown in fig. 5.7. Both samples are coated with 300 cyc of Al_2O_3 . The crystalline Si matrix is nicely visible on the bottom of either image, whereas the oxide layers appear to be fully amorphous.

Above the unstructured Si surface (fig. 5.7(a)), a narrow region of slightly darker contrast is visible between the Si crystal and the Al_2O_3 passivation layer. According to Hoex *et al.* this is an interfacial SiO_2 [65]. However, as will be shown in the following, the exact chemical fingerprint of this layer could not exactly be determined. The thickness of this layer is $d_{\text{SiO}_x, \text{TEM}} = 1.58 \pm 0.23$ nm. As measured from this TEM image, the ALD- Al_2O_3 coating on the unstructured surface has an approximate

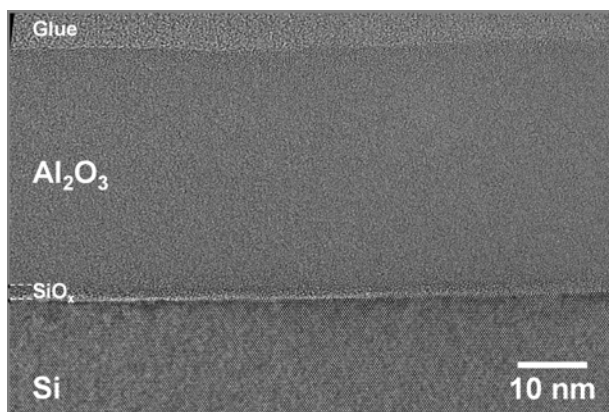


(a) SiN_x on shallow b-Si

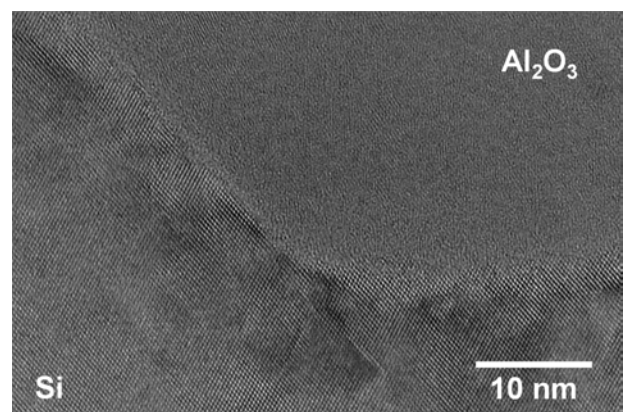


(b) SiN_x on deep b-Si

Figure 5.6: FIB cut b-Si surfaces (dark gray) passivated with 52 nm of SiN_x (light gray) deposited by PECVD. Film homogeneity and step coverage are good on the shallow but rather poor on the deep structured b-Si surface.



(a) Unstructured Si/ Al_2O_3 interface.



(b) Al_2O_3 on ICP-RIE intermediate b-Si.

Figure 5.7: TEM images of an unstructured (a) and an ICP-RIE structured intermediate b-Si/ Al_2O_3 -interface (b). The samples exhibited the highest charge carrier lifetime presented in fig. 6.13. The crystal structure of the Si substrate is well visible, whereas the SiO_x and Al_2O_3 appears to be amorphous.

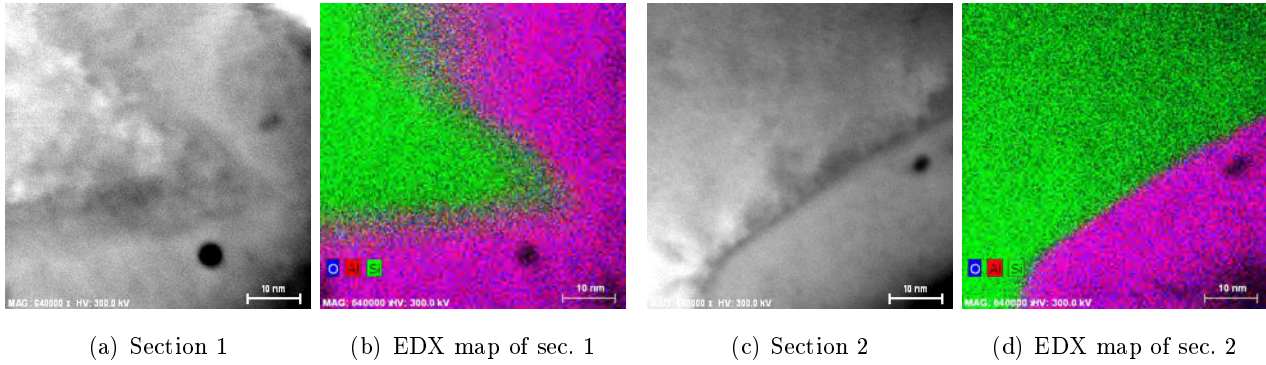


Figure 5.8: Micrographs and elemental analysis maps measured by scanning TEM EDX of ICP-RIE nanostructured intermediate b-Si/Al₂O₃-interfaces.

film thickness of $d_{\text{Al}_2\text{O}_3, \text{TEM}} = 34.05 \pm 0.31$ nm. The values of the interfacial SiO_x and Al₂O₃ layer thicknesses are in excellent agreement with accompanying ellipsometry measurements, in which the oxide layer on the 6" wafer was measured at 221 positions leading to an average film thickness of $d_{\text{E110}} = 34.97 \pm 0.14$ nm. For optical modeling of the ellipsometry data an initial SiO₂ thickness of 1.7 nm was assumed and a Cauchy model was used for data fitting. A film thickness map of these data is shown in fig. 6.6(a).

At the nanostructured b-Si/Al₂O₃-interface (fig. 5.7(b)), the image contrast is not as clear concerning a potential interfacial SiO_x layer. The Al₂O₃ region (upper right corner) appears equally smooth like on the unstructured reference. However, contrast inhomogeneities are visible in the near-surface bulk region of the underlying crystalline Si substrate. From other TEM images (not shown) the Al₂O₃ film thickness was determined to be $\approx 34.1 \pm 0.7$ nm. The according SiO_x thickness could be estimated to be $\approx 2.0 \pm 0.3$ nm.

An elemental analysis of nanostructured surfaces was carried out by means of EDX measurements in scanning mode (S-TEM). Herein, the focused electron beam is scanned over the lamella while EDX spectra are recorded at each position. Hence, elemental mapping of the lamella volume is possible. Two selected sections and their corresponding EDX maps are shown in fig. 5.8. The left half of the figure ((a), and (b)) shows a section of a b-Si tip, whereas the right half ((c), and (d)) exhibits a pore bottom of the same sample. The colored maps 5.8(b) and 5.8(d) contain overlaying information of the indicated elements showing Si: green, O: blue, and Al: red. Thus, pure element regions appear monochrome, e.g. crystalline or amorphous Si (green), whereas compound materials, like Al₂O₃, result as purple color (red+blue). SiO_x is a mixture of green and blue and should, hence, appear cyan. However, neither of the maps clearly shows a cyan-like coloring. Instead, at the tip where the interface region appears rather blurry, all of the signals overlap. In contrast, at the pore bottom the interface is pretty sharp. These effects of overlapping signals are also apparent in the TEM images to the left of the EDX maps. Around the tip (5.8(a)) a dark gray shadow is located between the b-Si and the Al₂O₃ layer. This interfacial effect is not as pronounced in the case of the pore bottom (5.8(b)). Here, the Si surface also appears a bit darker, but the interface to the Al₂O₃ layer is much sharper in both, the TEM image and the EDX map.

The electron beam (300 keV) may easily burn holes into the lamella, which was also the case if a low energy beam with 80 keV was used. The little black spots in fig. 5.8 originated from beam adjustment.

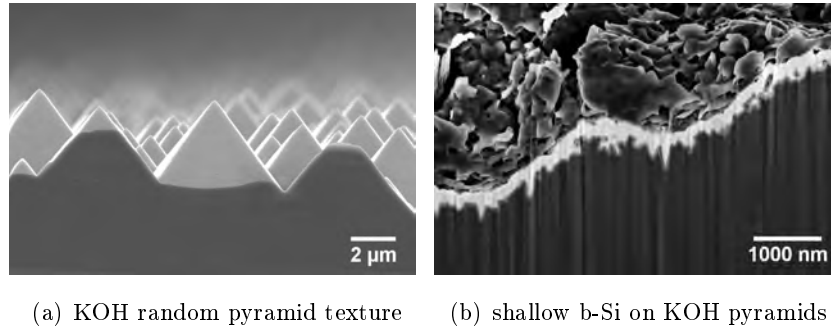


Figure 5.9: (a) The industrial standard KOH random pyramid texture (black) was used as a reference for passivation performance of the ALD-Al₂O₃ coating (white). (b) ICP etching leads to the superstructure: shallow b-Si on KOH pyramids (black). The passivation layer (dark gray) conformally covers the double-texture and is protected by a ZnO film (white).

Here, the electron beam was focused long enough (several seconds up to very few minutes) that the lamella completely evaporated.

5.2 Morphology and Al₂O₃ Growth on Other Black Silicon Types

To investigate the electronic surface quality of different blackening methods, bifacial lifetime samples with macroscopically identical surfaces were prepared and the minority charge carrier lifetime was evaluated after application of the standard passivation scheme (s. tab. 3.2). After RCA cleaning and ALD of 300 cyc Al₂O₃ the samples received a PDA at 385 °C. The lifetime results will be shown in section 6.3, the optics in sec. 5.3.2. The morphological differences arising from the etching step are subject to investigation in this section. Even though the wet-chemical methods include more than one preparation step, blackening was the only process variation of this experiment.

5.2.1 KOH Reference and ICP Superstructure

The KOH reference and a two-step process combination of the shallow b-Si process with a random pyramid texture are shown in fig. 5.9. Image (a) reveals the large pyramid etch pits with depths of approximately 4 μm and sidewall angles of 54.7° with respect to the Si (100) plane. After ICP etching the random pyramids slightly diminished. The shallow nanopores on the inclined Si (111) planes are vertically aligned like on the oob substrate. Furthermore, they have very similar dimensions on flat and textured surfaces, as can be seen from a comparison to the simultaneously passivated structures in fig. 5.5(a).

The alternatively processed b-Si structures presented in the following (fig. 5.10) were also passivated within this same batch.

5.2.2 MACE Structured b-Si

Black Silicon Nanowires (NW) emerge from the MACE process based on Ag catalyst films that were electrolessly deposited from AgNO_3 . The NW length was adjusted by the etching time. The “short” NWs in fig. 5.10(a) have lengths of $2.3 \pm 0.1 \mu\text{m}$ and were prepared during an etching time of 5 min. The “long” NWs have peak-to-valley heights of $6.0 \pm 0.2 \mu\text{m}$ and result from etching for 10 min. The passivated long NW surface is shown in fig. 5.10(b). The diameters of both NW structures diverge between 20 – 300 nm. The structures are vertically aligned along the [001] axis and have lateral gaps of roughly 50 – 300 nm. The ALD- Al_2O_3 thickness could not be accurately determined by FIB, because the cross-sectional plane could not be well aligned with the wires (comp. fig. A.4). However, the NW surface area is completely covered by the Al_2O_3 passivation layer. No voids were observed at the b-Si/ Al_2O_3 -interface.

Black Silicon Nanopores (NP) were fabricated by a reduced metal covered surface area fraction. Two density graded nanoporous structures emerged from Ag- and Au- catalyzed etching as described in the experimental section. A cross section of the Ag-MACE NP surface is shown in fig. 5.10(c). The Al_2O_3 coated surface exhibits a quite shallow roughness, with nanopores reaching up to $\approx 500 \text{ nm}$ into the Si surface with a rather large divergence in depths. Even in the case of very small pore features, the ALD passivation layer appears to cover the surface area with extreme conformality. In a few positions dark spots are visible. The Au catalyzed b-Si structure in fig. 5.10(d) also has maximum pore depths of $\approx 500 \text{ nm}$. However, the pores are slightly wider and have more gradual sidewall angles of $7 \pm 6^\circ$. The pore widths hardly exceed 70 nm, which is obvious because they are completely filled by the passivation layer. Nevertheless, the Si surface roughness is higher than in the case of the Ag-MACE NP surface, which is emphasized by the inhomogeneous appearance of the Al_2O_3 film. Underetched Si extensions are crossing the image plane through the conformal Al_2O_3 layer (right end of fig. 5.10(d)), which might also be the case at the Ag-NP surface.

Black Silicon Nanocones (NC) formed under an ultra-thin catalytic layer of thermally evaporated Au. The b-Si structure in fig. 5.10(e) significantly differs from the other examples above. The hillocks have maximum heights of 700 nm with small radii of curvature at the tips and thick base widths up to 500 nm. All NC features are leveled on a rather flat silicon surface ground. The sidewall angles are distributed around $14 \pm 7^\circ$. The Al_2O_3 film covers the surface very homogeneously.

5.2.3 Macroporous Silicon

The surface structure fabricated by the macroporous Si method is shown in fig. 5.10(f). MacP-Si etching in 1 Ωcm p-type FZ Si results in overlapping random (“wild”) pores with distances of about 700 nm and depths of roughly 500 nm with facet angles between 30° and 60° . Due to the high doping level, no actual pore formation is possible here [96]. The thin and very homogeneous Al_2O_3 passivation layer is visible on top of the surface.

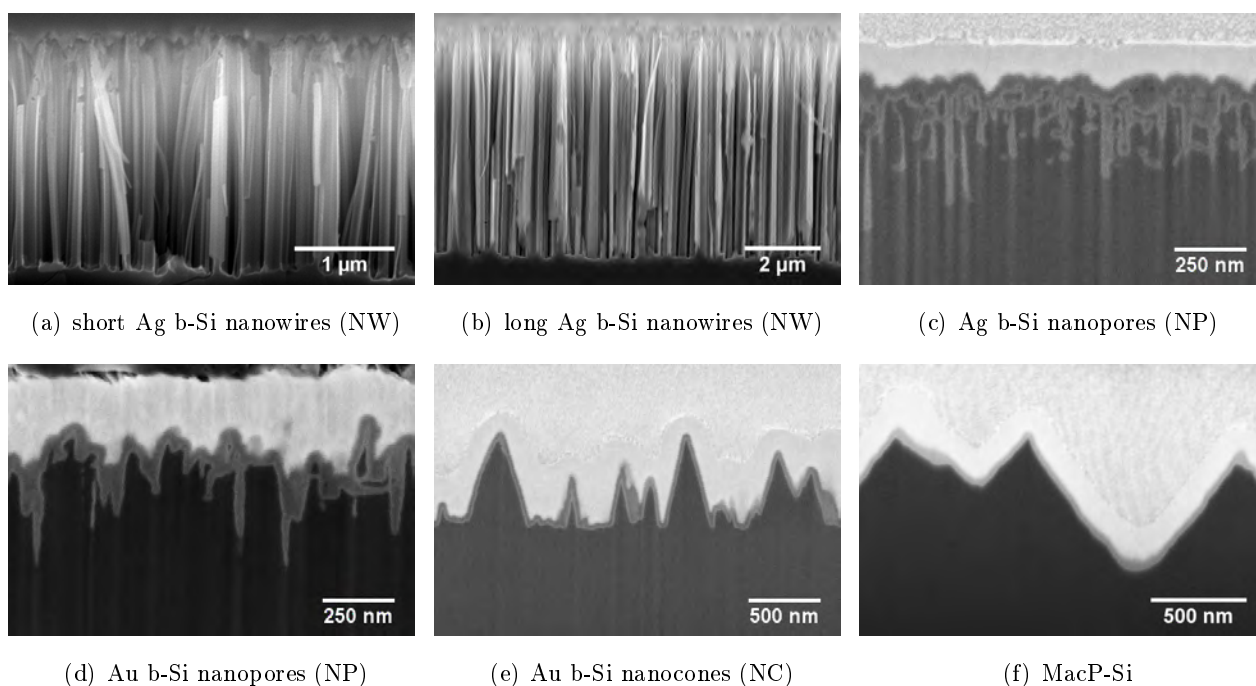


Figure 5.10: Black Si nanostructures prepared by metal assisted wet chemical etching with Ag (a,b,c) and Au (d,e) catalysts. Interconnecting Ag films lead to NW structures (a,b), whereas separate metal nanoparticles induce NP formation (c,d). The sputtered Au catalyst lead to nanocone-like hillocks (e). The thin ALD- Al_2O_3 passivation layer covers all b-Si surfaces perfectly conformal – not visible in (a) and (b) due to scale. Image (f) shows the macroporous Si surface cross section passivated with 300 ALD cycles of Al_2O_3 (gray) and the thicker ZnO protection layer (white).

5.3 Optics of Black Silicon

5.3.1 Dry Etched b-Si

Optical spectra of the three uncoated standard ICP-RIE processed b-Si samples are shown in figure 5.11. The spectrally resolved total absorptance, $A(\lambda)$, was calculated from the measured hemispherical reflectance, $R(\lambda)$, and transmittance, $T(\lambda)$, by $A(\lambda) = 1 - R(\lambda) - T(\lambda)$. To build a solid theoretical frame of reference, spectra of a hypothetical perfect anti-reflection coating with no light-trapping (LT) and with perfect Lambertian LT (LLT) were calculated.³ The spectra are plotted along with the data and continuously serve as a comparison for the presented measurements. Both simulations ignored the light-matter-interaction for the incident light at the front-side of the wafer. The dotted black line in fig. 5.11 represents the absorption of a polished Si wafer without any front reflection losses (perfect ARC, pARC). The dash-dotted black line represents the Yablonovitch limit [174] assuming a perfect ARC with additional light trapping due to a Lambertian scattering layer [119]. Incoherent light propagation through the Si bulk with a thickness⁴ of W and Fresnel reflection at the polished rear side were further assumed. The optical constants for silicon were taken from Green [54]. Later, in the case of bifacially structured samples, according spectra with a Lambertian backside will be presented without further indications.

Fig. 5.11 shows that the average reflectance of the deep b-Si structure is as low as 0.8% throughout the VIS range,⁵ while the shallow and intermediate sample reflect about 3% on average. In the UV region the surface reflection of all structures peaks close to 370 nm. However, a considerable improvement from $R \approx 60\%$ for the polished sample down to 7, 6 and 1.3% were reached for the shallow, intermediate and deep structure, respectively. The very low reflectance of the b-Si samples translates into their high absorptance in the UV/VIS. In the NIR, the effective absorption edge of the deep b-Si structure is red-shifted by about 90 nm as compared to the Si wafer with pARC but no LT. By dividing $A_{\text{deep}}/A_{\text{pARC}}$ an enhancement factor of about 4 can be estimated at a wavelength of 1100 nm, increasing to nearly 11 at 1150 nm. Lower absorption is observed for the shallow and intermediate structures, which behave very similarly - the shallow structure's absorption being slightly stronger. The transmittance, which is not shown here, is effectively zero in the range from 300 to 900 nm for any of the presented Si samples. Solely, for wavelength greater than 1000 nm it rises to a non-negligible level. Since R and T represent loss channels for a solar cell, the absorptance was chosen as the representative function of interest for this work, because it translates into generated charge carriers (injection level).

Angular Reflection Dependency

The angular dependence of the reflectance of shallow and deep b-Si could be investigated by directly measuring their absorption inside the integrating sphere. The samples were tilted against the incident

³The calculations were performed by Matthias Zilk, IAP, Jena and are used with his permission. The method is explained in detail in [89].

⁴ W was adjusted to the accordingly measured wafer thicknesses in each experiment.

⁵i.e. $380 \text{ nm} \leq \lambda \leq 780 \text{ nm}$

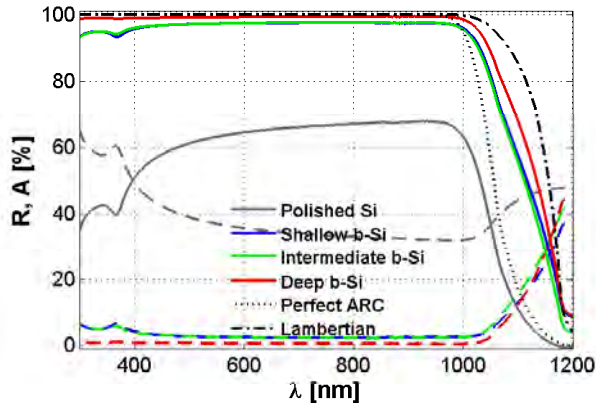


Figure 5.11: Reflection ($R(\lambda)$, dashed) and absorption ($A(\lambda)$, solid) spectra of a polished reference and the three single side structured ICP-RIE b-Si surfaces as measured with the unfocused beam setup. All samples are uncoated. For comparison, simulated spectra of a hypothetical perfect anti-reflection coating without (dotted) and with Lambertian light-trapping (dash-dotted) are also shown.

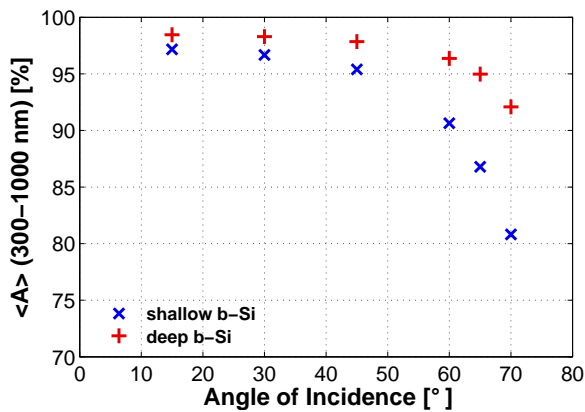


Figure 5.12: Angular dependence of the total integrated absorption of a shallow and a deep b-Si structure as tilted against the incident light beam. The spectra were integrated over the indicated wavelengths range. Deep b-Si exhibits a less pronounced absorption decrease for high angles of incidence than the shallow structure.

light beam. The hemispherical absorption spectra were integrated over the wavelength range from 300 to 1000 nm and plotted *vs.* the angle of incidence in fig. 5.12. Interestingly, the integrated absorption, $\langle A \rangle$, of both samples depends only a little on the angle of incidence up to 45° . Thereafter, $\langle A \rangle$ decreases slightly in case of the deep and stronger in case of the shallow structure. The former even exhibits a total absorption of 92% for incident light under an angle of 70° . Higher angles could not be measured because the spot on the sample becomes too large, whereas for smaller angles the specular reflex is lost from the integrating sphere. The spectral integration range was limited to the UV/VIS region due to non-unity reflection of transmitted light from the sample holder.

Effect of Passivation Layer Thickness

Up to this point, it is unclear what passivation layer thickness will be required for effective reduction of the surface recombination velocity. The influence of ALD- Al_2O_3 layers on the optical response function of b-Si was investigated for 300–2500 cyc on all three standard ICP structures and according polished Cz Si references ($W = 400 \mu\text{m}$). Assuming a gpc of $\approx 0.1 \text{ nm/cyc}$ the Al_2O_3 thickness varied from 30 nm to 250 nm. The resulting total integrated absorption is shown in fig. 5.13. The absorption of the polished sample rises with increasing layer thickness until it reaches a maximum around 100 nm and decreases somewhat for thicker films. In the case of b-Si $\langle A \rangle$ is maximized for 30 nm. Al_2O_3 thicknesses above 50 nm lead to a slight absorption decrease. Very thick films completely fill the nanopores (comp. fig. 5.4) leading to a rather flat Al_2O_3 /air-interface. Nevertheless, the deep b-Si structure performs at least as well as the pARC even with a coating of 250 nm Al_2O_3 . These results

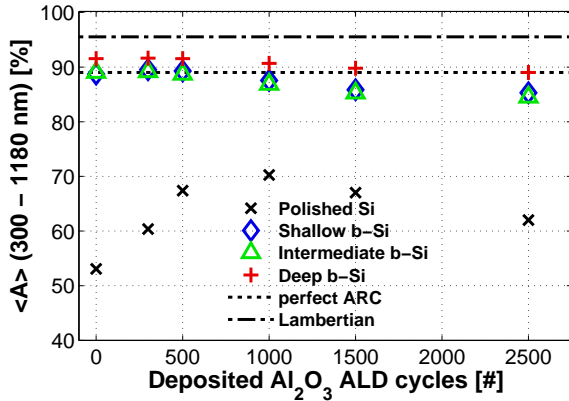


Figure 5.13: Total integrated absorption of an oob reference and single side ICP-RIE structured Cz b-Si wafers coated with varying numbers of Al_2O_3 ALD cycles. Coatings with less than 1000 cyc do not dramatically reduce the optical performance of b-Si. Calculated absorption values of the pARC and the Lambertian scatterer are included for orientation across the whole range of deposited cycle numbers.

indicate a process window for the passivation layer thickness up to 100 nm, wherein the optical influence of the Al_2O_3 layer is negligible for all three b-Si structures.

5.3.2 Optical Performance of the Different Black Silicon Nanostructures

KOH Reference, Dry Etched ICP-RIE b-Si and the Superstructure

Alkaline etched KOH random pyramid textures represent the standard LT scheme for industrial solar cells. Such textures⁶ were used to experimentally evaluate the opto-electronic competitiveness of the different b-Si types. The bifacially etched FZ b-Si wafers were passivated by Al_2O_3 along with KOH textured and unstructured reference wafers. To achieve a good charge carrier lifetime comparability on either structure, all samples were coated with the same Al_2O_3 layer thickness of $d \approx 35$ nm. Therefore, the optical performance of the KOH texture is non-optimized. The thin film with a refractive index of $n \approx 1.6$ only has a slight AR effect in the blue spectral range as previously shown.

The spectrally resolved absorptance data are plotted in fig. 5.14. The absorptance of KOH sample is about 92% between 450 nm and 950 nm. Above 1000 nm the texture also exhibits a high absorption with a strongly red-shifted absorption edge. The unstructured wafer was passivated to serve as an optimized oob reference for lifetime spectroscopy and is only included here for completeness. All ICP-RIE structures effectively reduce the reflection peak of Si around 370 nm resulting in a high UV absorption. Again, the shallow and intermediate structure both show very similar absorption behavior. However, here their absorptance drops with increasing wavelengths. The deep structured sample of this batch is the only one without the typical dip at 370 nm and exhibits a wide minimum around 500 nm. Its absorptance varies between 98.7% and 97% in the interval of 340 and 515 nm and rises to over 98% for wavelengths over 700 nm, respectively. Its NIR light absorptance is as good as the KOH texture under normal incident light, but the nanostructure profits from the better AR effect and reaches LT close to the $2n^2$ limit. The superstructure was fabricated by shallow ICP etching of an underlying KOH textured surface. The combination shows an improved absorption in the UV/VIS compared to the shallow and intermediate structure as well as to the KOH texture alone. Its absorption characteristic is very similar to the pure ICP-RIE nanostructured samples and

⁶Purchased from the “CiS Erfurt - Research Institute for Micro Sensors and Photovoltaics GmbH”.

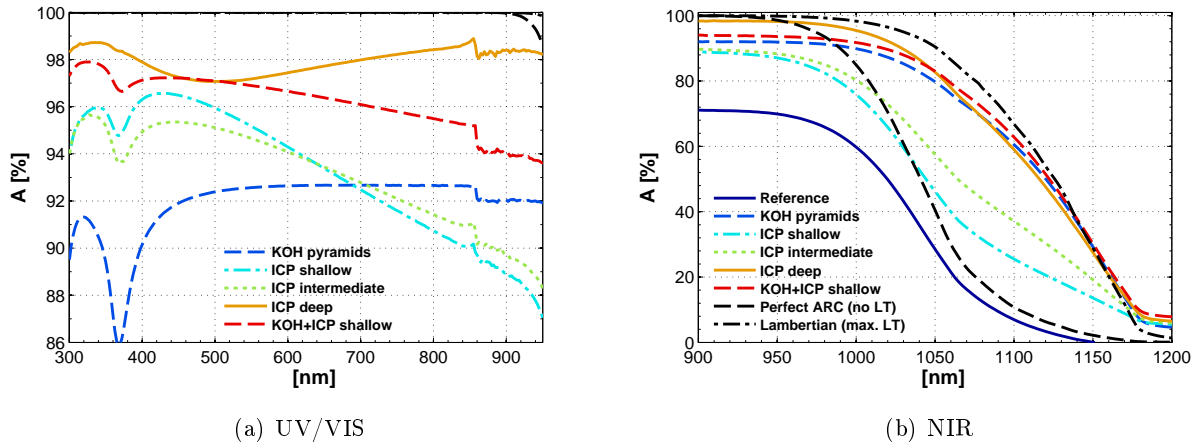


Figure 5.14: Hemispherical absorption spectra of bifacially processed ICP-RIE structured FZ b-Si wafers passivated with 300 cyc Al_2O_3 . The superstructure is a combination of shallow b-Si etched on the basis of KOH random pyramids (KOH + ICP shallow). A standard KOH texture and an unstructured reference sample are included along with the theoretical limits. (a) Zoom into the UV/VIS region. (b) Close-up of the absorption edge of Si.

moderately drops from 97.9% at 325 nm to about 94% at 900 nm. The superstructure exhibits the highest NIR light absorption in this scheme and is closest to the $2n^2$ limit. Like the deep b-Si sample, the superstructure profits from a low reflection at long wavelengths.

The kink in the absorbance data curves close to $\lambda \approx 860$ nm is due to switching the detectors in the integrating sphere.⁷ The phenomenon is present in almost all spectra and could not be abolished.

Wet Etched b-Si

Fig. 5.15 displays the absorbance of the wet chemically processed samples. Again, plot (a) only shows the upper 14% of the UV/VIS absorption scale to better distinguish the very closely located curves. The Au-catalyzed NCs and the short and long Ag-catalyzed NWs exhibit the highest absorbance between $99.3\% \leq A \leq 99.6\%$ over the whole UV/VIS spectral range. The typical absorption dip at 370 nm is effectively completely suppressed for the NC sample. For the NW samples the dip appears broader and red-shifted. The same is the case for the weaker absorbing Ag and Au catalyzed NP samples, which show a broadened absorption peak in the UV followed by a rather broad dip. The absorption coefficient of the Au-induced NPs slightly drops with increasing wavelengths. The Ag-etched sample's absorption runs about 1% lower in parallel. The macroporous Si sample has a pronounced absorption dip at 370 nm and a maximum absorption of 97.4% around 550 nm. Its absorption, which is 4 – 5% higher than that of the KOH sample decreases slightly with increasing wavelength.

In comparison to the KOH texture, the macP-Si exhibits a marginally stronger NIR absorbance ($(A_{\text{macP-Si}}(\lambda) - A_{\text{KOH}}(\lambda))|_{\lambda=1100 \text{ nm}} \approx 1.5\%$). The Au-MACE NCs and the long Ag-etched NWs show almost indistinguishable absorption behavior (fig. 5.15(b)), which is $\approx 3\%$ less effective than the KOH texture at 1100 nm. In all three cases, the LT performance is close to the theoretical $2n^2$ limit. In contrast, the short NWs exhibit $\approx 10\%$ weaker absorption at 1100 nm. Both NP-structures capture the NIR light rather weakly, whereas the rougher Au-etched NP sample is slightly stronger absorbing than the Ag-etched one.

⁷Detector switch from Si:UV/VIS to InGaAs:NIR.

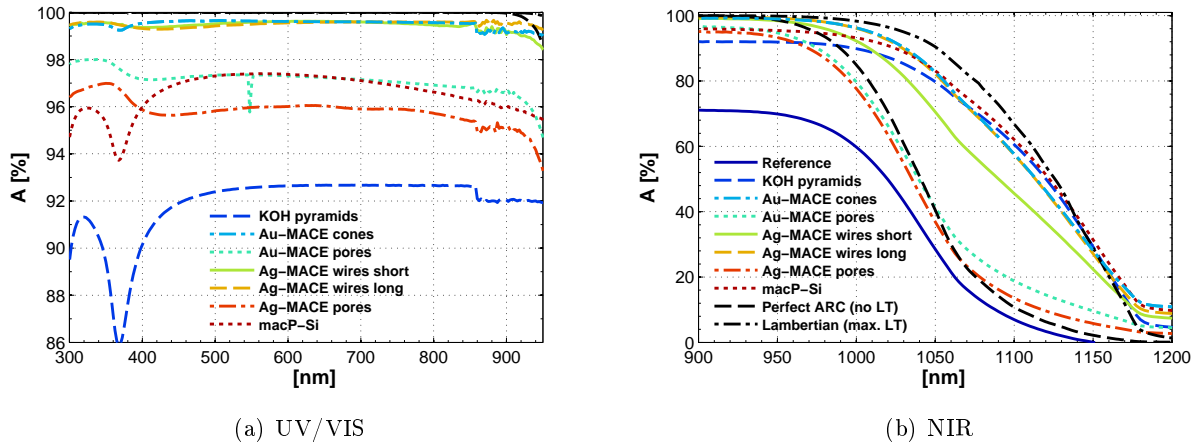


Figure 5.15: Absorption of identically passivated wet chemically processed bifacial b-Si in comparison to KOH pyramids, the oob reference, and the theoretical limits in the UV/VIS (a) and NIR (b) spectral region.

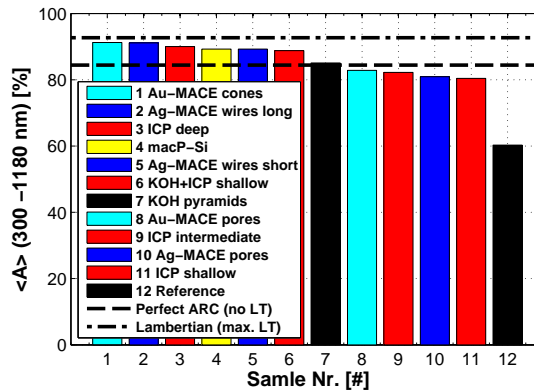


Figure 5.16: Comparison of the total integrated optical absorption efficiency of the presented b-Si samples passivated with 300 cyc nm Al_2O_3 in the wavelength range between 300 nm and 1180 nm. As references, the KOH textured and the shiny etched sample as well as the theoretical limits of a perfect anti-reflection coating with no light trapping (dashed line) and with Lambertian light trapping (dash-dotted line) are shown. The samples are sorted by absorption efficiency in descending order. Similar processes are grouped by color (Au-MACE: cyan); (Ag-MACE: blue); (ICP-RIE: red); (macP-Si: yellow); (References: black).

Average Optical Absorption

Finally, the integrated total absorption, $\langle A \rangle$, of the presented samples is shown in fig. 5.16. The overall absorption is highest for the Au-MACE NC and the long Ag-MACE NW samples with 91.3% and 91.1%, respectively. These values are only about 1.5% (abs.) below the Yablonovitch limit. The deep ICP b-Si, the macP-Si structure and the short Ag-MACE NWs as well as the ICP superstructure exhibit acceptable overall absorption values above the simulated perfect anti-reflection coating (pARC). For the spectral range of interest, the reflection losses of the alkaline KOH texture and its gain by light-trapping almost compensate one another such that its total absorption is just as high as for the pARC. The results are summarized in tab. 7.1.

Chapter 6

Black Silicon Surface Passivation by ALD Deposited Al_2O_3

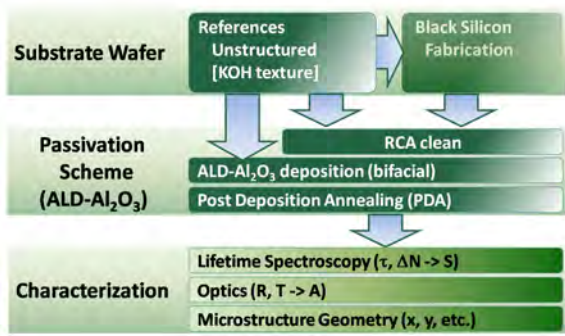
This chapter deals with the resulting minority carrier lifetimes in unstructured and b-Si wafers after application of pre-cleaning steps, Al_2O_3 deposition by thermal ALD and according post-deposition annealing (PDA) treatments.

The typical process flow and the according lifetime evolution in a wafer are depicted in fig. 6.1(a). Unstructured (out-of-box, oob) and KOH textured wafers served as references and for b-Si fabrication. The Al_2O_3 deposition process and the subsequent PDA were optimized on oob wafers to reach a maximized lifetime, i.e. a minimal surface recombination velocity (SRV, S_{eff}).

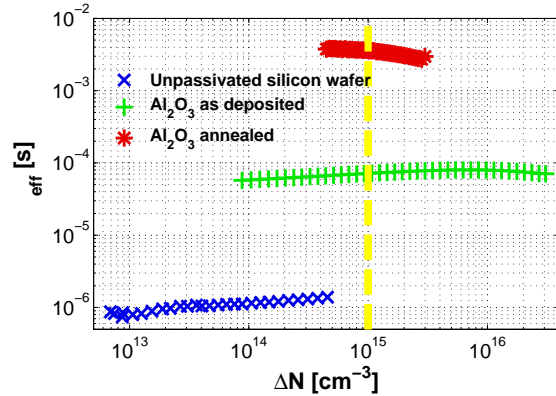
The codependent optimization of ALD and PDA parameters will be presented in section 6.1. The passivation of nanostructured surfaces necessarily includes wet chemical cleaning prior to ALD. An according cleaning procedure was developed in our laboratory to achieve the highest possible lifetimes on clean oob wafers. The resulting passivation scheme (RCA + ALD + PDA) was then transferred to b-Si substrates structured by ICP-RIE as described in section 6.2. A comprehensive comparison of the passivation quality on nanostructured surfaces resulting from alternative b-Si methods is presented in section 6.3.

Unpassivated wafers typically show a low lifetime of $\tau \approx 1 \mu\text{s}$ at an injection level of $\Delta n = 10^{14} \text{ cm}^{-3}$ (comp. fig. 6.1(b)). Higher injection ($\Delta n \geq 10^{15} \text{ cm}^{-3}$) may not be reached because the recombination processes are too fast to build up higher carrier densities. The process is limited by carrier diffusion to the surfaces.¹ After ALD of 1000 cyc Al_2O_3 ALD the lifetime rises to a level of $\tau \approx 70 \mu\text{s}$, and after subsequent annealing it reaches a maximum of $\tau = 3.6 \text{ ms}$, in this specific case. Note, that the lifetime is almost constant with the injection level.

¹On the other hand, very well passivated wafers tend to develop higher injection levels and for a given flash intensity low Δn values may not be accessible, which also depends on the optical absorption (AR, LT, and wafer thickness, W).



(a) Process flow chart



(b) Lifetime evolution during passivation

Figure 6.1: (a) Schematic of the processing steps in the performed passivation experiments. Oob wafers were either used for b-Si fabrication, or served as references for surface cleaning, deposition of Al_2O_3 , and subsequent post-deposition annealing (PDA) experiments. Finally, the samples were characterized by means of their lifetime, optical absorption, and microstructural properties. (b) Typical minority charge carrier lifetime evolution during a passivation procedure. The lifetime increases by more than one order of magnitude upon Al_2O_3 deposition and another order of magnitude upon PDA. The yellow vertical line indicates an injection level of $\Delta n = 10^{15} \text{ cm}^{-3}$ at which the lifetimes are usually compared, if not indicated otherwise.

6.1 Al_2O_3 Passivation Performance on Unstructured Si Surfaces

The shiny etched 6" FZ wafers with a thickness of $250 \mu\text{m}$ and a doping level of $1 \Omega\text{cm}$ as purchased from Silchem² have rather well defined surfaces that are rather homogeneously terminated with a clean SiO_2 . The oxide thickness was measured on an oob wafer by ellipsometry to be $1.9 \pm 0.2 \text{ nm}$ and $2.1 \pm 0.2 \text{ nm}$ on the rear, corresponding to a uniformity of $\approx 90\%$ in both cases. The thickness maps are plotted in the appendix (fig. A.7). This starting point enables to optimize the ALD deposition process and the subsequent post-deposition annealing parameters to minimize S_{eff} in the $-\text{OH}$ terminated Si wafers.

6.1.1 Effects of ALD Parameters on the Carrier Life Time

As indicated by the lifetime evolution in fig. 6.1(b) only a codependent optimization of ALD and PDA parameters is possible, because the maximum achievable lifetime is only obtained after both process steps. Therefore, single 6" wafers were broken into 21 pieces according to the scheme shown in appendix A.4 (fig. A.3(b)). To gain at least minimal statistics, i.e. to check for reproducibility of the results and eventually eliminate outliers, the samples were grouped to seven sets of three Si pieces each. To rule out that a “best spot” on the wafer would influence the results, the samples were selected from different regions across the wafer. Cleaving was carried out just before the process step undergoing the parameter variation, i.e. before Al_2O_3 deposition or annealing, respectively.

²www.silchem.de

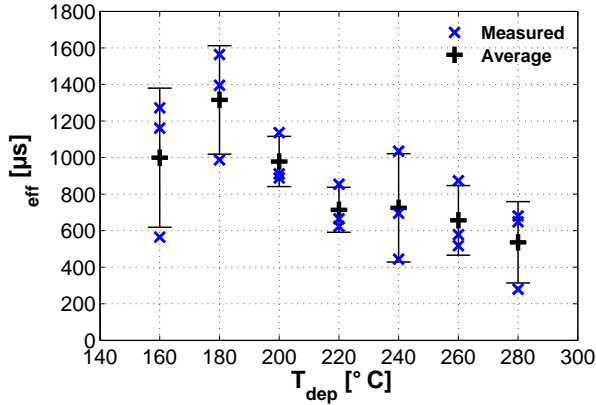


Figure 6.2: Impact of the ALD deposition temperature on the lifetime after passivation with 150 ALD cycles and subsequent PDA for 30 minutes at 400 °C in low pressure Ar atmosphere.

ALD Deposition Temperature

The ALD deposition temperature, T_{ALD} , was varied in steps of 20 °C in the range of 160 to 280 °C. Layers of 150 cyc Al₂O₃ were deposited corresponding to a nominal thickness of 15 nm. All samples were annealed at once at 400 °C for 30 min in low pressure Ar atmosphere and measured by QSSPC. The lifetimes at a fixed injection level of $\Delta n = 10^{15} \text{ cm}^{-3}$ are shown with the corresponding average values and standard deviations in fig. 6.2. The result indicates a maximum at a deposition temperature of $T_{\text{ALD}} = 180 \text{ °C}$. At this temperature the highest lifetime value as well as the highest average lifetime were obtained. Above 180 °C the lifetime monotonically decreases with increasing deposition temperature. The deposition at 160 °C also leads to shorter carrier lifetimes.

Purge Time

Up to this point ALD films were deposited with symmetrical purge times of 3 s after the H₂O and TMA pulses. Since the deposition time of a temporal ALD cycle is dominated by the purge time, shorter purges are desirable to enable a higher throughput in the lab, which would also be useful if a batch process on an industrial scale was targeted. On the other hand, true ALD deposition critically relies on sufficient precursor purging. H₂O and TMA have different partial pressures and viscosities. Therefore, asymmetric purge times may help to alter the physical properties of the films. The lifetime evolution for 150 ALD cycles with varying purge time is depicted in fig. 6.1.1. Shortening $t_{\text{TMA,purge}}$ from 3 s to 1 s improves the lifetime by more than half a millisecond. Both, the lifetime of a single sample as well as the average lifetime are maximized for $t_{\text{H}_2\text{O,purge}} = 2 \text{ s}$.

Al₂O₃ Layer Thickness

The dependence of the charge carrier lifetime with increasing number of deposited Al₂O₃ ALD cycles is shown in fig. 6.4. The plot in fig. 6.4(a) compares the normalized³ lifetime values to the literature data reported by Dingemans *et al.* [33]. All curves show a rather steep inclined lifetime increase with increasing number of cycles up to $\approx 300 \text{ cyc}$. For thicker films the lifetime approaches saturation.⁴

³Each data set was normalized to the highest lifetime value.

⁴Note, that the same behavior is apparent before the annealing step (not shown).

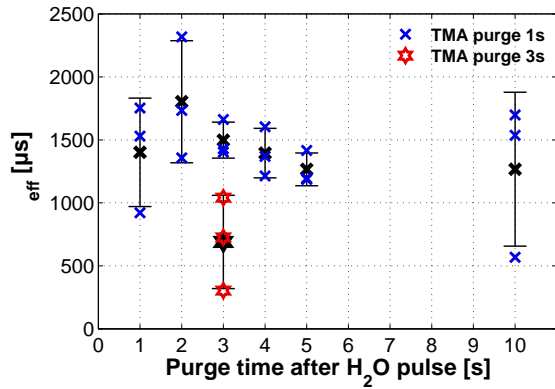
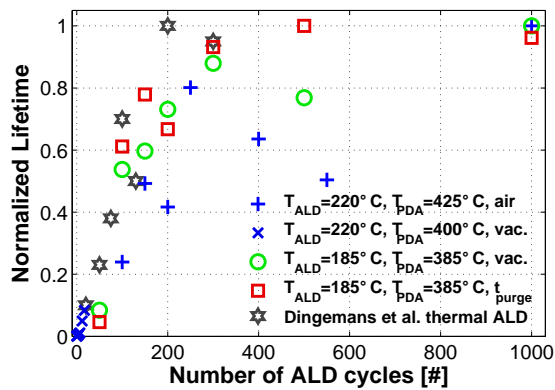
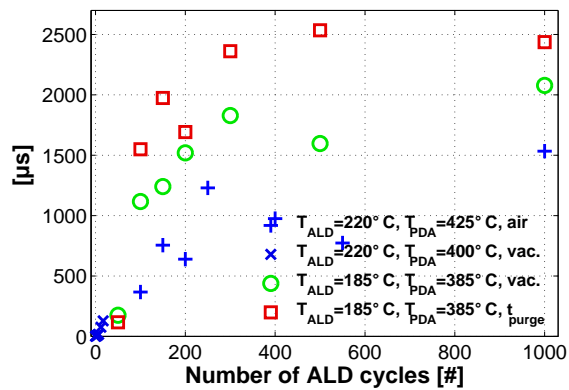


Figure 6.3: Lifetime of Al₂O₃ passivated samples deposited with different purge times following the water pulse, $t_{\text{H}_2\text{O,purge}}$. The purge time after the TMA pulse, $t_{\text{TMA,purge}}$, was kept constant at 1 s (\times). Additionally, in one experiment (\star) the TMA and water purge times were symmetric ($t_{\text{purge}} = 3$ s). The ALD and PDA temperatures were $T_{\text{ALD}} = 180$ °C, $T_{\text{PDA}} = 385$ °C.



(a) Normalized lifetime vs. number of ALD cycles



(b) Lifetime vs. number of ALD cycles

Figure 6.4: The plots show the lifetime evolution during optimization of the ALD parameters plotted against the number of deposited Al₂O₃ ALD cycles on shiny-etched p-type FZ Si. Graph (a) compares our results against some literature values from Dingemans *et al.* [33] (\star). Therefore, the lifetime values were normalized to the highest value in each series, respectively. A reduced deposition temperature (\circ) leads to a steeper lifetime increase between 50 and 300 cyc thick Al₂O₃ layers (a) as compared to the initial process ($+$). Deposition with optimized purge time (\square), again, increases the slope slightly. Both improvements also lead to higher absolute lifetime values (b).

Single values may not follow the trend, but the measurements for thick films confirm the saturation behavior reported previously by Dingemans *et al.* [33]. The non-normalized lifetime data in fig. 6.4(b) exhibits the two optimization steps (lower deposition temperature (\circ), and optimized purge times (\square). Both lead to higher absolute lifetime values compared to the initial process ($+$). The combination substantially increased the saturated lifetime by about 1 ms. However, a certain Al₂O₃ film thickness (≈ 300 cyc) seems to be necessary to reach this level of surface passivation.

Nevertheless, ultra-thin Al₂O₃ films resulting from the deposition of single ALD cycles already significantly increase the charge carrier lifetime over the whole range of injection by two orders of magnitude after annealing (fig. 6.5(a)). A comparison at a fixed injection level, exhibits a quadratic lifetime increase with the first 17 deposition cycles (fig. 6.5(b)).

Homogeneity and Reproducibility of Al₂O₃ Film Thickness and Carrier Lifetime

A 300 cyc thick Al₂O₃ passivation layer was deposited at 180 °C on RCA cleaned 1 Ω cm FZ Si and subsequently annealed at 385 °C for 30 min in low pressure Ar atmosphere. Fig. 6.6(a) shows

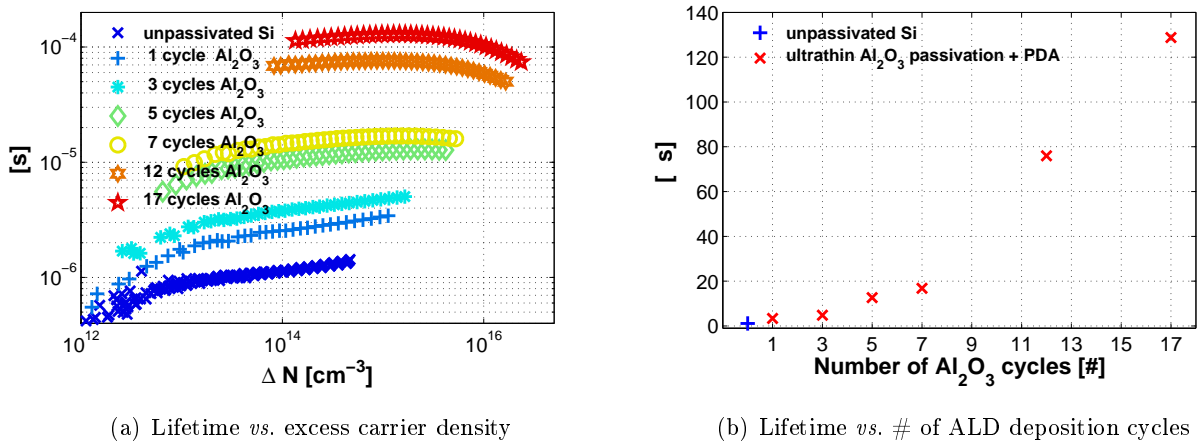


Figure 6.5: Passivation efficiency of ultra-thin Al₂O₃ layers after PDA. (a) shows the injection dependent lifetime. (b) Lifetime *vs.* the deposited number of cycles on a linear *y*-scale at an injection level close to $\Delta n = 10^{15}$ cm⁻³. The samples were RCA cleaned before Al₂O₃ deposition and subsequently annealed at 400 °C for 30 minutes in low pressure Ar atmosphere (×). Note, that the lifetime of the unpassivated sample (+) was taken at 5 positions on the same wafer before the passivation procedure was applied. The fit indicates a quadratic increase of the lifetime with increasing number of cycles in the presented range.

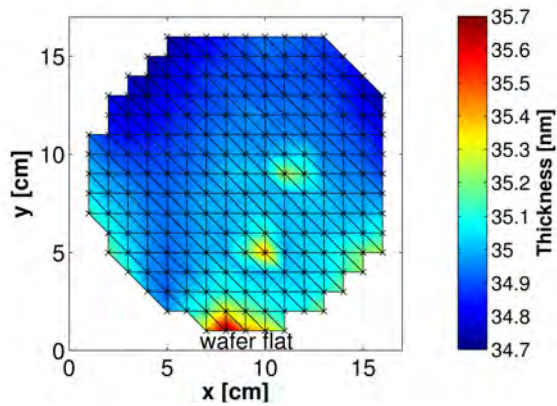
the spatially resolved film thickness as measured by ellipsometry at 221 positions on the 6" wafer. As mentioned in section 5.1.4 the average thickness is 34.97 ± 0.14 nm with a standard deviation of less than 0.4% and a total span of $d_{\max} - d_{\min} < 1.2$ nm. The according lifetime map measured by calibrated photo-luminescence (PL) spectroscopy on the same wafer is shown in fig. 6.6(b). The lifetime is homogeneously high in the center and upper half of the wafer. However, a certain lifetime gradient is visible toward the wafer flat. A comparison of the oxide thickness⁵ and the lifetime suggests that a slightly thinner oxide may lead to an increased lifetime even though local inhomogeneities (degraded spots) do not correlate directly. Note, that the resolution of the ellipsometry (221 pt) and PL (900 × 900 pt) images is rather different.

The run-to-run reproducibility of the lifetime homogeneity was demonstrated on out-of-box wafers and is shown in fig. 6.7. These 2000 cyc thick Al₂O₃ films offer the highest passivation level (up to 5 ms) measured within this work. On all four 6" FZ Si out-of-box wafers the lifetimes were measured by QSSPC at 21 positions on each wafer (fig. 6.7(a)). The lifetime values follow the same pattern and vary between 3 ms and 5 ms. At the center position (#11) of the wafers this results in an extremely low SRV of $S_{\text{eff}} < 2.3$ cm/s.

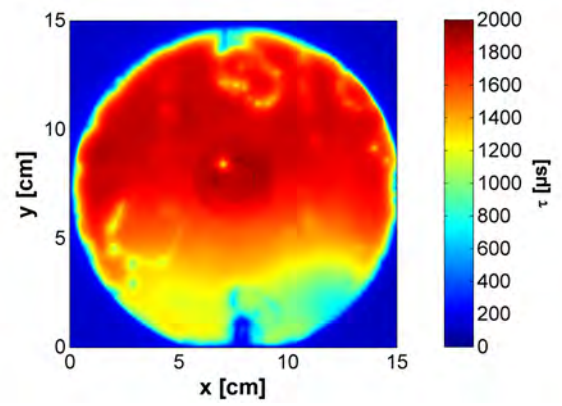
6.1.2 Post-Deposition Annealing

As mentioned earlier, a heat treatment is necessary to activate the passivation performance of the ALD-Al₂O₃ films to the full extent – a fact that is well known and reported many times in the literature [2,62,65, etc.]. However, as shown in fig. 6.1(b) the lifetime increase attained by an according PDA may account for more than one order of magnitude. Therefore, it is reasonable to move the process conditions into the right phase space window.

⁵Including the underlying Si oxide grown in the SC2 step of the applied RCA cleaning sequence.

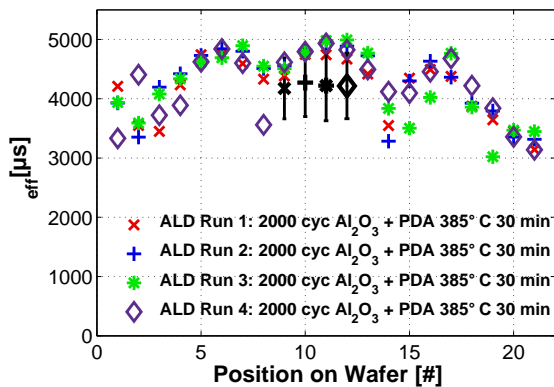


(a) Oxide layer thickness

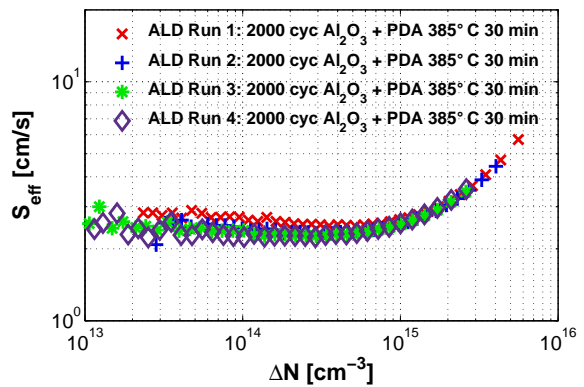


(b) PL lifetime map (wafer flat at bottom)

Figure 6.6: (a) Oxide thickness of a 300 cyc thick Al_2O_3 film on an RCA cleaned wafer as measured by ellipsometry. The average thickness is 34.97 ± 0.14 nm, corresponding to a standard deviation lower than 0.4% over the full 6" wafer area. The max. and min. film thickness are 35.91 nm and 34.72 nm, respectively, with a span of 1.19 nm. Note that the z-scale represents a total span of 1 nm. (b) shows the according lifetime map of the same wafer determined by calibrated PL spectroscopy at an injection level close to $\Delta n = 10^{15} \text{ cm}^{-3}$. The lifetime appears to be high, where the oxide is thin.



(a) Lifetime Homogeneity



(b) Surface Recombination Velocity

Figure 6.7: (a) Lifetime homogeneity and reproducibility of p-type FZ oob wafers passivated with 2000 cyc of Al_2O_3 deposited at $T_{\text{ALD}} = 180^\circ\text{C}$. The films were annealed at $T_{\text{PDA}} = 385^\circ\text{C}$ in low pressure Ar atmosphere for 30 min. The highest lifetimes in the middle of the wafers are approximately $\tau_{\text{eff}} \approx 5$ ms and therefore extremely close to the Auger limit for this doping level and wafer thickness as estimated by Richter *et al.* [131]. (b) This results in a SRV of $S_{\text{eff}} < 2.3$ cm/s in the case of the best samples.

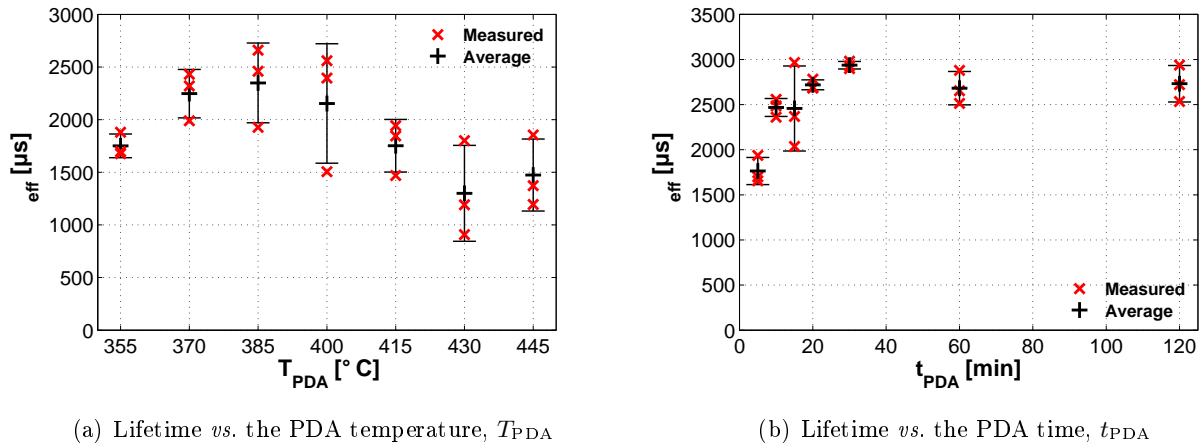
(a) Lifetime *vs.* the PDA temperature, T_{PDA} (b) Lifetime *vs.* the PDA time, t_{PDA}

Figure 6.8: Impact of PDA temperature (a) and PDA duration (b) on the lifetime in two out-of-box wafers passivated with 150 ALD cycles Al₂O₃ at a deposition temp of $T_{\text{ALD}} = 180$ °C. The samples in (a) were annealed in low pressure Ar atmosphere for 30 minutes at the indicated temperatures yielding a maximum around 385 °C. In (b) the lifetime rises respectively with increasing annealing time at 385 °C in air and saturates after 15 – 30 min.

The lifetime results obtained by varying the temperature during PDA carried out in low pressure Ar atmosphere for 30 min are plotted in fig. 6.8(a). Three identically treated samples passivated with 150 cyc thick Al₂O₃ films deposited at 180 °C were annealed at each temperature (×). The measured lifetimes were averaged (+) and plotted with their standard deviations, respectively. Initially, the charge carrier lifetime in the p-type FZ Si pieces rises with increasing PDA temperature. The highest values are reached in a window around $T_{\text{PDA}} \approx 385$ °C. For PDA temperatures above $T_{\text{PDA}} \approx 400$ °C the lifetime decreases again by more than 0.5 ms. Hence, optimized results are obtained in a temperature window $T_{\text{PDA}} \approx 385 \pm 15$ °C.

Varying the annealing time (fig. 6.8(b)) the lifetime rises during the first 15 to 30 min. For longer annealing times at $T_{\text{PDA}} = 385$ °C the lifetime saturates. Other combinations of temperature and duration may yield similar results (e.g. the activation may be achieved in a shorter time at higher temperature (not shown)). However, if at higher temperatures a certain annealing time is exceeded, a so-called over-annealing effect may be observed: After passing through a maximum similar to the case in fig. 6.8(a), the lifetime may drop by one order of magnitude within the first minute in the furnace for $T_{\text{PDA}} > 600$ °C [187].

6.1.3 Surface Pre-Cleaning Treatments

As the SRH recombination model implies, the chemical purity as well as the crystalline quality of the surface terminating layer is of utmost importance to a working passivation. Hence, after black etching a cleaning sequence is required to remove contaminants and provide proper surface conditioning before Al₂O₃ deposition. The cleaning procedure was dynamically developed throughout this PhD work and could be improved several times.⁶ To demonstrate the lifetime sensitivity of a shiny-etched Si surface

⁶Different sources for deionized (DI) water were available in the lab and clean room facility, and different chemical purities of acidic, alkaline, and oxidizing solutions were tested. For quality control of the liquids before and after wafer cleaning inductive coupled plasma mass spectrometry (ICPMS) analysis was used (not shown).

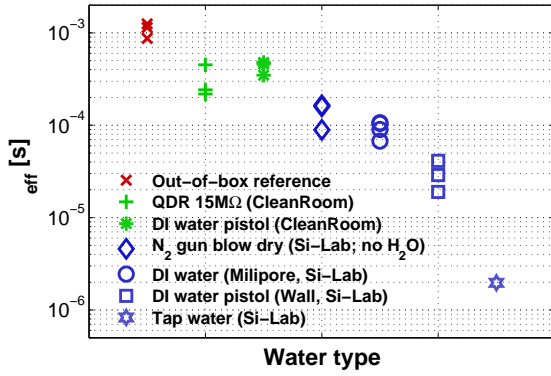


Figure 6.9: HF dipped samples were rinsed under water of different sources before Al₂O₃ passivation. The oob reference did not receive an HF dip. The N₂ blown dry sample did not get in contact with water after the HF dip. Note that the acid quality was of “technical grade” in the Si-Lab and of “very large scale integration” (VLSI) grade in the clean room. Later, electronic grade HF was used for RCA cleaning (comp. fig. 6.10).

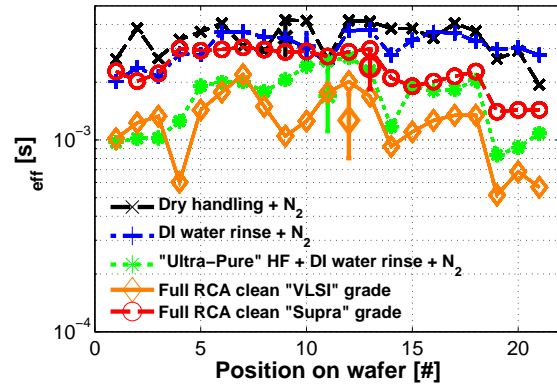


Figure 6.10: Lifetime in FZ Si after application of the different indicated handling/cleaning sequences as measured at 21 positions on each wafer. The oob reference exhibits the highest lifetimes. However, the RCA sequence based on “supra” grade solution yields a more homogeneous lifetime distribution on unstructured Si and enables the desired cleaning effect required for b-Si surfaces prior to passivation.

to different contamination levels, a FZ wafer was cleaved into 21 pieces, of which 18 were stripped off the SiO₂ by 5% HF during 1 minute and subsequently dried by N₂ after previously rinsing them with water from sources with different purity levels as indicated in fig. 6.9. After Al₂O₃ passivation, the out-of-box references with the protecting SiO₂ exhibit the highest lifetime. Dipping the samples in VLSI⁷ grade HF and rinsing with DI water in the clean room lead to a lifetime reduction of a factor of two. Technical grade HF acid in combination with N₂ drying and/or rinsing with H₂O from a small purification system in the lab, the house internal filtered H₂O system, or finally with water from the facility’s tap all substantially decreased the lifetime. Note, that the latter condition leads to lifetimes comparable to that of completely unpassivated wafers.

By inductive coupled plasma mass spectrometry (ICPMS) analysis of the chemical’s quality a certain level of potentially recombination-active species could be identified and eliminated (not shown). In general, higher purity acids lead to more robust average lifetime results, i.e. a higher absolute lifetime and improved homogeneity as shown in fig. 6.10. However, the water source feeding the chemical baths could not be influenced and eventually remained as the purity limiting factor. Nevertheless, the achieved passivation level based on the applied passivation is adequate for b-Si surface cleaning and conditioning. Nevertheless, wafer handling should be kept minimal at any time.

⁷Used chemical purity grades were: “Very Large Scale Integration” (VLSI), “Super Large Scale Integration” (SLSI or “supra pure”), and “ultra-pure” (UP). The purity level rises by at least one order of magnitude per class, i.e. the residual contamination levels decrease from the ppm (10⁻⁶)/ppb (10⁻⁹) region for VLSI to the ppt (10⁻¹²) level for UP solutions, respectively. As an example, the content of Fe in HF was: $c_{\text{Fe, HF}}^{(\text{VLSI})} < 50$ ppb [68]; $c_{\text{Fe, HF}}^{(\text{SLSI/supra})} < 1$ ppb [19, 68]; $c_{\text{Fe, HF}}^{(\text{ultra})} < 10$ ppt [20].

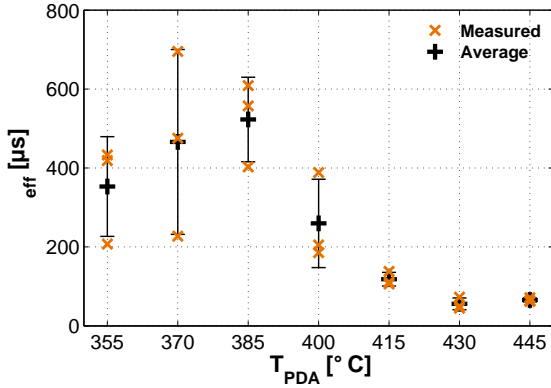


Figure 6.11: PDA temperature optimization of 300 cyc thick Al_2O_3 passivation layers on the intermediate structure.

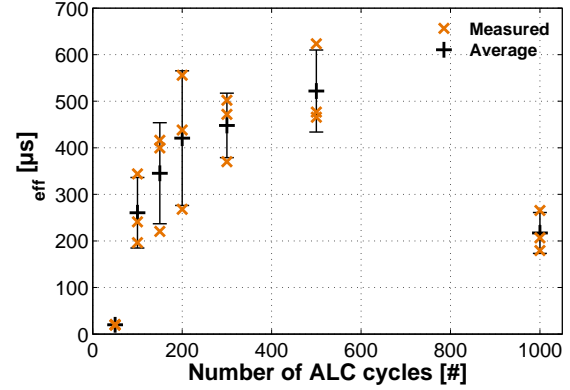


Figure 6.12: Al_2O_3 passivation layer thickness series on intermediate b-Si annealed at $T_{\text{PDA}} = 370^{\circ}\text{C}$.

6.2 Surface Passivation of Dry Etched Black Silicon

6.2.1 Transfer of ALD- Al_2O_3 Passivation to Black Silicon

Based on the results from sec. 5.1.2, we can assume that the black surfaces accept the ALD coating just as well as the unstructured references.⁸ Therefore, the presented passivation scheme as listed in table 3.2 is directly transferred to b-Si surfaces. In this section only ICP-RIE etched samples are treated.

It was suspected in sec. 2.3.2 (requirement (iv)) that the lifetime in black silicon might be more sensitive to high process temperatures due to residual contaminations from the black etching step. The PDA temperature was varied on the intermediate b-Si. The lifetime results in fig. 6.11 exhibit a similar trend to the one on unstructured material (see fig. 6.8(a)). However the highest lifetime was measured for $T_{\text{PDA}} = 370^{\circ}\text{C}$, whereas the best average result remained at $T_{\text{PDA}} = 385^{\circ}\text{C}$. Since the highest lifetime from each experiment demonstrates the feasibility to reach at least this passivation level $T_{\text{PDA}} = 370^{\circ}\text{C}$ is considered the optimal annealing temperature for Al_2O_3 deposited on b-Si at $T_{\text{ALD}} = 180^{\circ}\text{C}$. PDA treatments were conducted in low pressure Ar atmosphere, in normal pressure air inside a muffle furnace or on a hot plate. However, these conditions do not significantly influence the lifetime (not shown).

The lifetime dependency of the intermediate b-Si (Cz) structure on the Al_2O_3 film thickness is shown in fig. 6.12. Again, the trend may be recognized from the unstructured substrate (comp. fig. 6.4) as a saturation-like behavior is apparent between 200 and 500 ALD cycles. Nevertheless, the average lifetime slowly increases with increasing film thickness in this region. In the case of the thickest passivation layer (1000 cyc) the lifetime is strongly decreased.

⁸i.e. requirement (ii) of sec. 2.3.1 is fulfilled.

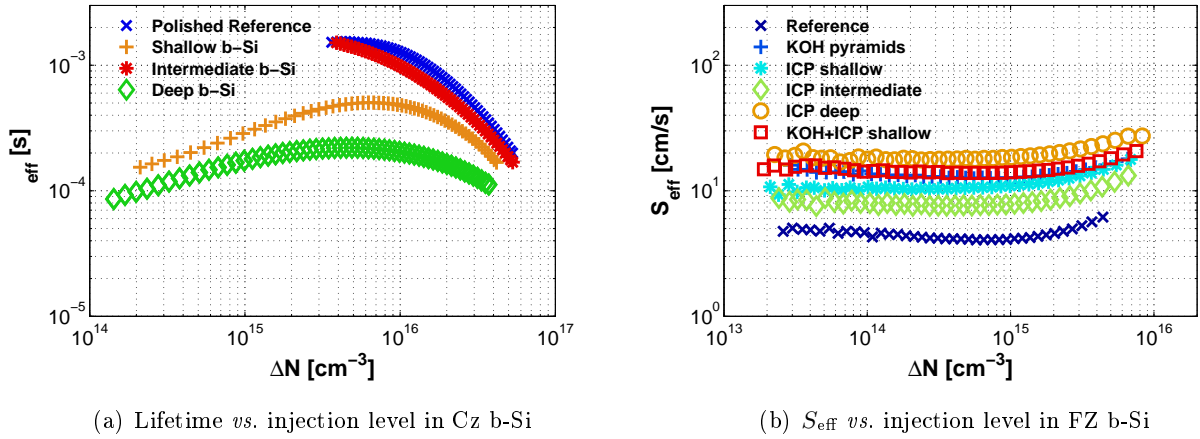
(a) Lifetime *vs.* injection level in Cz b-Si(b) S_{eff} *vs.* injection level in FZ b-Si

Figure 6.13: The highest lifetimes and lowest SRVs of ICP-RIE processed b-Si on Cz (a) and FZ (b) wafers, respectively demonstrated the feasibility to effectively passivate b-Si for the first time. The data were published in [119] (a), and as a progress report in [117] (b).

6.2.2 Black Silicon Nanostructure Geometry and Related Passivation Quality

Conformally coating the b-Si nanostructures with Al_2O_3 effectively reduces the SRV. Fig. 6.13 shows the injection level dependent lifetime and SRV of black etched Cz and FZ wafers, respectively, including according unstructured references. The Cz and FZ samples were RCA cleaned with VLSI and “supra” purity chemicals and coated with 1000 cyc and 300 cyc Al_2O_3 , respectively. Subsequently, all wafers received a PDA to activate the passivation.

Considering that the first batch of samples was prepared on Cz wafers (a), extremely high carrier lifetimes of over $\tau_{\text{eff}} = 1.4$ ms and $\tau_{\text{eff}} = 1.6$ ms were measured on the intermediate b-Si structure and the reference, respectively, at an injection level of $\Delta n = 5 \cdot 10^{15} \text{ cm}^{-3}$. The shallow and deep structure both exhibit significantly lower values of $\tau_{\text{eff}} = 500 \mu\text{s}$ and $\tau_{\text{eff}} = 230 \mu\text{s}$, respectively. For the polished reference and the intermediate b-Si structure, this results in SRVs of $S_{\text{eff}} < 12 \pm 2 \text{ cm/s}$ and $S_{\text{eff}} < 13 \pm 2 \text{ cm/s}$, respectively. The lifetime depends rather strongly on the injection level. Despite the large film thickness (1000 cyc), no blistering was observed after annealing on the OH-terminated Cz wafer surfaces.

In the case of thinner FZ wafers, the lifetime values are higher, and therefore result in even lower SRVs, which are plotted in fig. 6.13(b). Here, the SRV is virtually independent of the injection level over the whole investigated range. Furthermore, extremely low SRVs were measured on all b-Si geometries including the superstructure, which is just as well passivated as the KOH textured random pyramids without additional blackening. The shallow and intermediate b-Si samples even outperform the KOH reference.

Note that the intermediate b-Si structure, which was etched twice as long as the shallow one, outperforms the shallow b-Si in both experiments. The lifetimes and surface recombination velocities of the shown b-Si structures are summarized in table 6.1.

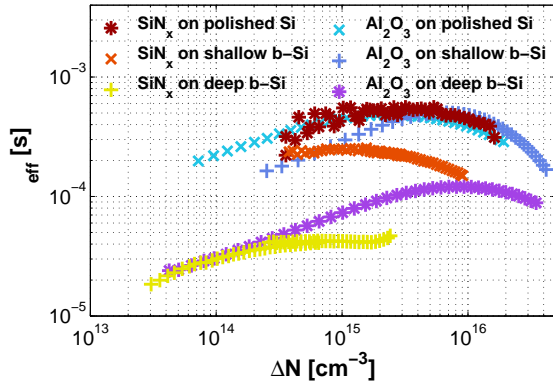


Figure 6.14: SiN_x passivated shallow and deep b-Si surfaces in comparison to their according reference and Al_2O_3 passivated samples. Al_2O_3 outperforms the SiN_x passivation on nanostructured surfaces, whereas comparable lifetimes were obtained on the polished samples. FIB cut cross sections of the SiN_x passivated b-Si samples are shown in fig. 5.6.

Alternative SiN_x Passivation Deposited by PECVD

As an alternative passivation approach SiN_x was bifacially deposited by PECVD on shallow and deep b-Si structured Cz wafers as well as on an according oob reference.⁹ The passivating layer was deposited from SiN_4 and NH_3 at 400 °C with a nominal thickness of 70 nm SiN_x . However, the actual thickness was smaller on the b-Si structures as determined by FIB/SEM and appeared to be somewhat inhomogeneous concerning step and bottom coverage, especially in the case of the deep structure (comp. fig. 5.6). The refractive index was measured to be $n = 2.42 \pm 0.03$. In fig. 6.14 the lifetimes are plotted *vs.* the injection level and are compared to samples passivated with 1000 cyc Al_2O_3 . At an injection level of $\Delta n = 10^{15} \text{ cm}^{-3}$, both references exhibit lifetimes around 450 μs . For the shallow b-Si structure, the SiN_x passivation yielded 250 μs and therefore inferior to the 300 μs measured on the Al_2O_3 passivated sample, whose lifetime at higher injection is competing with the reference samples. A similar trend is visible for the deep b-Si samples which exhibit one order of magnitude lower lifetimes with 73 μs and 42 μs in the case of Al_2O_3 and SiN_x passivation, respectively. Passivation of b-Si with SiN_x appears to be possible, however, the passivation strengths - as well as the deposited film quality - are superior in the case of ALD- Al_2O_3 . In addition, it is known from the literature, that Al_2O_3 passivation generally outperforms SiN_x independent of the wafer doping type and level. Usually for Al_2O_3 passivation, the lifetime is more independent of the injection level, which is not observed in this experiment.

6.2.3 Influence of ICP-RIE Etching Parameters on the SRV

ICP-RIE Etching Time

Fig. 6.15 shows the best and average lifetimes of ICP-RIE fabricated b-Si on Cz wafers. The samples were cleaned at imec, Leuven, Belgium, and passivated in our ALD reactor. The whole 6" wafers were ICP-RIE etched under standard conditions (s. table A.2) for the indicated times, subsequently cleaned, coated with 300 cyc Al_2O_3 , and annealed for 30 min in low pressure Ar atmosphere at 370 °C.

⁹Both, sample cleaning and SiN_x deposition were carried out at ISFH, Hameln, Germany. The samples passivated with Al_2O_3 were processed at the MLU, Halle, Germany.

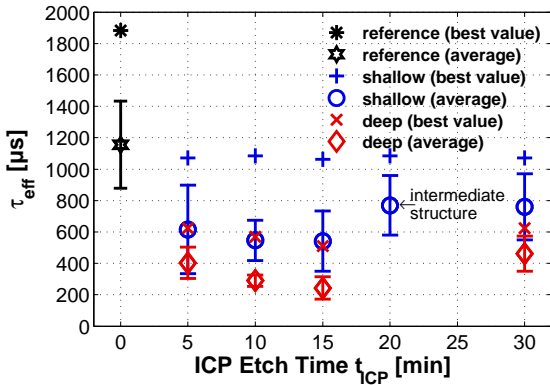


Figure 6.15: Best and average lifetime in Al₂O₃ passivated ICP-RIE processed b-Si Cz wafers that were etched for the indicated time.

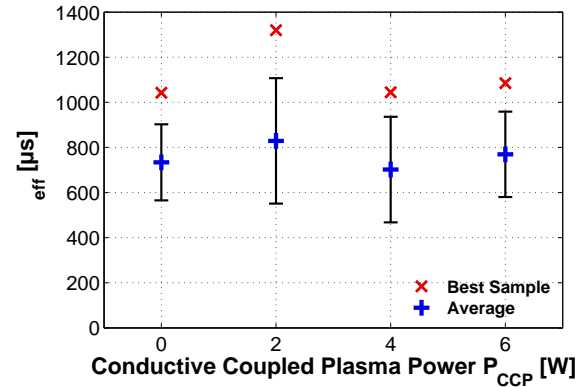


Figure 6.16: Minority carrier lifetime *vs.* the ICP-RIE CCP power.

For both b-Si structures (shallow (\circ) and deep (\diamond)), the average lifetime drops with increasing etching time up to 15 min. However, for $t_{ICP-RIE} \geq 20$ min it recovers to a stable value, higher than the one obtained for the shortest etching time. The best values follow the same trend in the case of the deep b-Si structure (\times), whereas they are rather constant in the case of the shallow one ($+$).

The effect of lifetime recovery after increased ICP-RIE processing time was observed in many experiments when the intermediate structure was introduced as an optimal compromise between high optical absorption and coatability in terms of sputter-deposited ITO.¹⁰ Due to this lifetime behavior, the “intermediate” b-Si structure became even more interesting for potential solar cell usage.

ICP-RIE CCP Power

Other ICP-RIE parameters were checked for their influence on the carrier lifetime. E.g. the capacitive coupled plasma forward power, P_{CCP} , was varied to further reduce the damage induced by plasma-species impinging on the surface. However, fig. 6.16 shows that the lifetime seems to be rather constant in the tested power regime with one elevated result for $P_{CCP} = 2$ W. This b-Si series was prepared based on the intermediate process and carried out on Cz wafers, which were cleaned at imec. The passivating layer of 300 cyc Al₂O₃ was deposited in Halle and activated by the according PDA treatment.

6.3 Comparison of Dry and Wet Etched Black Silicon Types

To prove the feasibility for effective passivation of different b-Si nanostructure types, the developed passivation scheme was applied to commonly available b-Si structures produced by the wet chemical etching methods described in sec. 3.1.2. The samples were identically treated and can be compared to the ICP-RIE standard structures.¹¹ Hence, the bifacially applied black-etching procedure represents

¹⁰Indium Tin Oxide ((In₂O₃)_{1-x}(SnO₂)_x, with $x \approx 0.1$) was used as TCO in the SIS solar cell concept for the PHIOBE project and was published in [41, 42, 44].

¹¹The full extent of this experiment including laser structured b-Si may be found in [113].

the only process variation in this experiment, even though for the wet-chemical methods more than one process step was necessary. After the black etching procedure, all samples were RCA¹² cleaned, coated with 300 cyc of ALD deposited Al₂O₃ and the passivation layer was activated by a PDA for 30 min at 385 °C in air (tab. 3.2). The non-black-etched references (unstructured oob and alkaline textured wafers) were subjected to the same passivation procedure.

To monitor the influence of different wet-chemical black etching step to the lifetime, an additional reference was fabricated for each method. The reference samples were treated identically along with the black etched wafers (metal deposition and removal), but did not receive the black etching step. The metal catalysts were removed from the control samples and the black etched ones with the same procedure. This way the direct influence of the black etching step to the sample's carrier lifetime could be investigated.

All lifetime data of the MACE etched samples, the macP-Si sample and the original references (unstructured and KOH) are shown in fig. 6.17. The MACE nanostructured samples with the longest carrier lifetimes are the Au-catalyzed nanocones (NC) with $\tau_{\text{eff}} = 111 \mu\text{s}$ and the Ag-etched nanopores (NP) with $\tau_{\text{eff}} = 102 \mu\text{s}$. Both show a similarly weak injection level dependency. In contrast to the results on these nanostructured samples, the lifetime values of the respective process references differ by almost a factor of three (Au-NC-Ref.: $\tau_{\text{eff}} = 775 \mu\text{s}$; Ag-NP-Ref.: $\tau_{\text{eff}} = 2 \text{ms}$). The reference for the Ag-MACE nanowire (NW) process (1.2 ms) exhibits a slightly stronger injection level dependency. The short NWs that were etched in an Ag-MACE process have a longer charge carrier lifetime than the long NWs produced with the similar method.¹³ No noticeable passivation could be achieved on the Au-catalyzed NP sample. The macP-Si sample exhibits a rather short lifetime of less than 10 μs . Common to all wet-chemically etched samples is a very weak injection level dependency of the carrier lifetime.

6.3.1 Comparison of the Black Etching Methods Concerning Passivation Quality

A comparison of the highest lifetimes from each b-Si method¹⁴ is presented in fig. 6.18. The unstructured reference has the highest lifetime followed by the group of ICP-RIE samples in the millisecond range, whereas the intermediate and shallow b-Si sample both outperform the KOH textured reference. It is important to note, that the superstructure (KOH + ICP shallow) also exhibits comparable lifetime performance to the KOH texture, followed by the deep b-Si sample. The group of MACE etched samples is spread over two orders of magnitude with the Au-MACE NCs and the Ag-MACE NPs of $\tau_{\text{eff}} > 100 \mu\text{s}$ on the high end. The NW samples show deteriorating lifetime with larger surface area, whereas the lifetime of the long NWs is comparable to the macP-Si. Finally, the Au-MACE NP sample exhibits almost no surface passivation at all. The lifetime values and SRVs of all samples are summarized in table 6.1.

¹²“supra” grade

¹³The NW samples were processed at the MLU, whereas the NP samples were produced at NREL.

¹⁴At $\Delta n = 10^{15} \text{cm}^{-3}$

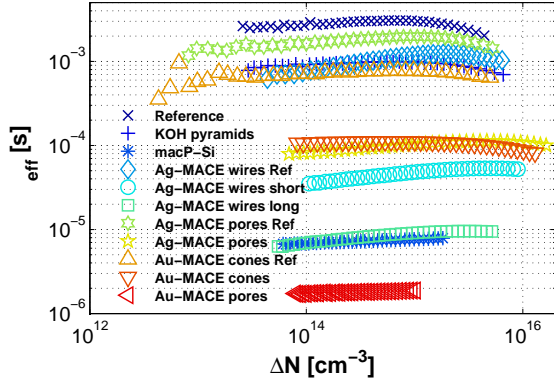


Figure 6.17: Measured lifetime of the wet-chemically (MACE and macP-Si) structured b-Si surfaces and their according reference samples fabricated without the black etching step. The lifetime is plotted *vs.* the injection level. For comparison, the unstructured sample as well as the KOH textured one are included.

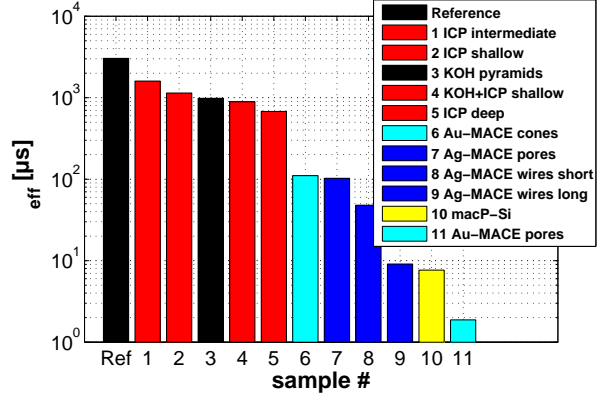


Figure 6.18: Overview of the achieved effective lifetimes of thermal ALD- Al_2O_3 passivated b-Si surfaces in comparison to the unstructured and KOH textured references at an injection level of $\Delta n = 10^{15} \text{ cm}^{-3}$. The colors group similar etching processes: References (black), ICP (red), Au-MACE (cyan), Ag-MACE (blue), macP-Si (yellow).

Table 6.1: Summary of the lifetime and SRV in Al_2O_3 passivated b-Si wafers.

| Structure | Material | $\tau_{\text{eff}} [\mu\text{s}]^*$ | $S_{\text{eff}} [\text{cm/s}]^*$ | published in |
|------------------------------|----------|-------------------------------------|----------------------------------|--------------|
| Polished Substrate | (Cz) | 1634 ± 245 | $\leq 12 \pm 2$ | |
| Shallow b-Si | (Cz) | 502 ± 76 | $\leq 45 \pm 7$ | [119] |
| Intermediate b-Si | (Cz) | 1475 ± 133 | $\leq 13 \pm 2$ | |
| Deep b-Si | (Cz) | 237 ± 36 | $\leq 80 \pm 6$ | |
| Out-of-box Reference | (FZ) | 3040 ± 567 | $\leq 4.1 \pm 0.9$ | |
| KOH Pyramids | (FZ) | 983 ± 102 | $\leq 12.7 \pm 1.9$ | |
| Shallow b-Si | (FZ) | 1142 ± 244 | $\leq 11.0 \pm 2.6$ | [113, 117] |
| Intermediate b-Si | (FZ) | 1597 ± 319 | $\leq 7.8 \pm 1.8$ | |
| Deep b-Si | (FZ) | 677 ± 82 | $\leq 18.5 \pm 2.9$ | |
| KOH Pyramids+Shallow b-Si | (FZ) | 891 ± 82 | $\leq 14.0 \pm 4.5$ | |
| Au-MACE Nanocones (NC) | (FZ) | 111 ± 33 | $\leq 113 \pm 36$ | |
| Ag-MACE Nanopores (NP-Ag) | (FZ) | 102 ± 31 | $\leq 122 \pm 39$ | |
| Au-MACE Nanopores (NP-Au) | (FZ) | 2 ± 1 | $\leq 6653 \pm 2100$ | [113] |
| Ag-MACE Nanowires (NW short) | (FZ) | 48 ± 15 | $\leq 260 \pm 83$ | |
| Ag-MACE Nanowires (NW long) | (FZ) | 9 ± 3 | $\leq 1374 \pm 435$ | |
| MacP-Si | (FZ) | 8 ± 3 | $\leq 1635 \pm 517$ | |

*The τ -error represents the standard deviation of the bifacially structured and passivated wafers. To estimate the error for S_{eff} , error propagation of the wafer thickness and lifetime were considered.

Chapter 7

Discussion

In this chapter the results of the electronic carrier lifetime measurements will be related to the microstructural characteristics of the different b-Si surfaces. The observed physical properties in the various b-Si types are discussed with a focus on ICP-RIE b-Si (sec. 7.1). A model for recombination in b-Si is elaborated (sec. 7.2). Finally, we will try to elucidate the relation between the different geometric features of the b-Si surfaces and the observed optical characteristics (sec. 7.3).

7.1 Surface Passivation Quality of ALD- Al_2O_3 on Black Silicon

In general, the effective minority charge carrier lifetime of a passivated c-Si sample serves as a strong indicator for the opto-electronic quality of the substrate material and its surfaces and for the potential open circuit voltage in a c-Si solar cell. Hence, it is a very important electronic property. Unfortunately, the lifetime can not be calculated from wafer parameters [25] (e.g. resistivity, thickness, etc.) because it may change with too many factors (e.g. high temperature processing, ARC/passivation coatings, light soaking, Si growth mode and according crystal quality/purity, etc.). Therefore, the lifetime has to be determined experimentally from wafer to wafer [25]. According to the recombination model from sec. 2.2, there are many factors that influence the lifetime in a negative way. The recombination channel with the highest recombination rate, i.e. the shortest lifetime limits the effective lifetime (comp. eqn. (2.7)). Hence, to achieve maximum lifetime all recombination processes must be suppressed to a maximum degree. However, only the extrinsic factors – such as bulk and surface recombination – may be eliminated if (nearly) perfect crystal and interface quality are provided in the Si sample. Therefore, the peak lifetime in each experiment demonstrates the experimentally achievable lifetime on the wafer by the applied passivation scheme. Low lifetime values may be disregarded, as the cause for degradation may be manifold. Nevertheless, highly homogeneous processes on full 6" wafers are desirable and the homogeneity issue must be addressed. It was shown that degraded spots are present in every sample and may originate e.g. from inhomogeneous processing or handling issues. The cleaning experiments (see fig. 6.9) demonstrated how sensitive wafers are to any low level of contamination if they are stripped from the defined SiO_2 layer, due to the higher chemical activity of the bare Si surface.

Nevertheless, it is appropriate to directly compare the lowest surface recombination velocities (SRVs) as calculated from the highest lifetime in the same batch of wafers. The SRV was estimated throughout this work by assuming infinite bulk lifetime (see eqn. 2.26). Hence, it was assumed that no other recombination channels (Auger, radiative, SRH) were active, which leads to an overestimation and therefore to an upper limit of S_{eff} . However, it was mentioned that for some cases of very high lifetime the Auger limit as parametrized by Richter *et al.* was very likely reached (see fig. 6.7). Hence, the contribution of the Auger recombination channel ($\frac{1}{\tau_{\text{Auger}}}$) is at least of the same order of magnitude as (or greater than) the losses due to surface recombination. Therefore, the SRV was again largely overestimated in such cases. Accordingly, the given S_{eff} values must be understood as an upper limit, $S_{\text{eff,max}} > S$, corresponding to a “worst case” of a high recombination rate near the surface. Nevertheless, if Auger recombination kicks in (i.e. $\tau_{\text{eff}} \rightarrow \tau_{\text{A}}$), the performance of a later solar cell would approach its theoretical limit [51] as calculated by Shockley and Quisser [143]. Hence, the SRV is not limiting anymore, which was initially mentioned as one of the main goals pursued by the PV industry. The demonstrated effective passivation scheme will be discussed for b-Si in this section.

7.1.1 Requirements for Surface Passivation of Black Silicon

For the effective surface passivation of b-Si nanostructures six requirements were defined in sec. 2.3.1 followed by a preliminary discussion in sec. 2.3.2. The hypothesis was put up, that ALD- Al_2O_3 should be ideally suited to passivate b-Si surfaces. In the following, the developed Al_2O_3 passivation scheme and the according b-Si structures are discussed and their potential for solar cell applications is evaluated according to the necessary prerequisites defined above.

Requirement (i) – Ideal Passivation Quality on c-Si Surfaces as a Prerequisite

Concerning requirement (i) demeaning for ideal passivation quality of Si surfaces of preferably any crystal orientation (and doping level) it can be stated that at the moment of writing, Al_2O_3 represents the state-of-the-art passivation scheme and offers the highest known level of surface passivation for p- and n-type c-Si surfaces in a broad range of doping levels throughout the literature [31].¹ In fact, the originally determined empirical limit for Auger recombination of Kerr and Cuevas [81] had to be adjusted [131] due to the high lifetime values that were measured since ALD- Al_2O_3 emerged in 2006. Our results on the surface passivation of unstructured (fig. 6.7(b)) and KOH textured surfaces (fig. 6.13(b)) by thermal ALD- Al_2O_3 show that lifetimes close to the Auger limit may be achieved with the elaborated passivation scheme (summarized in tab. 3.2) and concur with the reported literature values for similarly doped substrates [131]. On (100) cut c-Si surfaces, very high chemical passivation quality ($D_{\text{it}} \sim 4 \cdot 10^{10} \text{ cm}^{-2} \text{ eV}^{-1}$) and strong field effect passivation due to a high number of negative fixed charges ($Q_{\text{fix}} \sim -10^{13} \text{ cm}^{-2}$) were reported [2, 29, 62, 64, 65]. The latter condition is claimed to lead to a relaxation of the requirement for low interface defect densities. Therefore, Al_2O_3 generally appears to be ideally suited for the passivation of c-Si surfaces and is an excellent candidate for b-

¹A rather comprehensive review on that matter was published by Dingemans and Kessels in reference [31].

Si passivation.² However, the impact of superficial crystal orientation on the passivation quality of Al_2O_3 is rather poorly investigated – an issue that will be discussed in more detail along with the KOH textured reference and the superstructure in sec. 7.2.2.

Requirement (ii) – Deposition Conformality on b-Si Surfaces

From the highly conformal film deposition shown in sec. 5.1.2, the conclusion can be drawn that the need for high conformality of Al_2O_3 passivation layers, as defined in requirement (ii) of sec. 2.3.1, is considered fulfilled for all ICP-RIE structures. The FIB cut cross sections of sec. 5.2 indicate that the same is true for all other investigated (i.e. wet etched) b-Si nanostructures (fig. 5.10). Hence, ALD- Al_2O_3 has the advantage of almost perfect conformality on all investigated b-Si types. In addition, no hot-spots nor any kind of inclusions were found at any point of the investigated Si/ Al_2O_3 -interfaces. This observation is well in agreement with reports from the literature, where ALD- Al_2O_3 films are ascribed to be absolutely pin-hole free and contain no parasitic growth of particles [138].³ In contrast, for the PECVD deposited SiN_x films compromised homogeneity and conformality were observed in the case of the deep b-Si structure leading to rather poor passivation quality, whereas the shallow structure could be coated with an acceptable step coverage leading to a moderate level of passivation (see fig. 6.14). This industrial standard c-Si solar cell passivation process was directly transferred to the b-Si samples without adapting the deposition or cleaning parameters for the high nano-roughness. Probably, thicker SiN_x layers may lead to better passivation on the cost of deteriorated optical properties of b-Si. This behavior was reported for a-Si:H passivation layers on Au-Mace NC-like structures [105].⁴ It was also reported that passivation of ICP-RIE b-Si surfaces by thermal SiO_2 – a perfectly conformal growing layer – is outperformed by thermal ALD- Al_2O_3 thin films on p-type c- and mc-Si substrates [129]. Furthermore, in a solar cell concept, the lifetime of the Al_2O_3 passivated b-Si was higher than that of the KOH textured references passivated with optimized $\text{SiO}_2/\text{SiN}_x$ stacks [186]. Conclusively, even though the lifetime result for the PECVD SiN_x passivated shallow b-Si structure appears promising, the overall performance of Al_2O_3 is higher than that of SiN_x . Since the PECVD deposition did not conformally reproduce the rough surface which was the case for ALD- Al_2O_3 , the hypothesis of requirement (ii) is confirmed.

In high injection the Auger effect limits the lifetime and leads to strong decrease of the lifetime ($\Delta n \geq 10^{16} \text{ cm}^{-3}$). For almost all Al_2O_3 passivated samples a low (or *no*) injection level dependence is observed in the low injection range ($\Delta n \leq 10^{16} \text{ cm}^{-3}$). In general, this can be interpreted as a sign for extremely low SRH recombination [25]. In this experiment (fig. 6.14), however, a stronger lifetime decrease with decreasing injection level is apparent indicating an elevated SRH/surface recombination in the Al_2O_3 passivated samples including the reference. This is most probably caused by insufficient surface cleaning as well as non-optimal Al_2O_3 deposition and/or PDA conditions.⁵ The MACE NP

²A review on the passivation of b-Si by the most commonly used passivating dielectrics (SiN_x , SiO_2 , and Al_2O_3) was recently published in [101, sec. 4]. For a-Si:H passivation of b-Si see [105].

³The only exception is constituted by “blistering”, which may occur in thick ALD- Al_2O_3 films deposited at low temperatures during PDA [162]. However, blistering does not necessarily compromise the passivation quality [132].

⁴Note, that a-Si:H exhibits the disadvantage of high optical absorptance, which is not the case for SiN_x .

⁵Note, that the SiN_x passivated samples were RCA cleaned at the ISFH, which was optimized for solar cell processing – not for b-Si. In contrast, the Al_2O_3 passivation procedure was done at the MLU in Halle prior to the optimizations

samples surely require the highest deposition performance concerning conformal film growth, since the pores are extremely narrow. Nevertheless, the author speculates that the inner pore walls of the Ag-MACE NP surface are completely covered by the ALD passivation layer. The lifetime of over 100 μs is high enough to exclude a highly porous material layer. If previously present, such a layer was removed in the SC1 cleaning step [3]. The FIB cut cross-sectional images revealed that the b-Si/ Al_2O_3 -interface is redrawn by a bright line⁶ which possibly indicates the space charge region. In addition, the top of the surface is fully covered by Al_2O_3 , which is in good color contrast to the ZnO protection layer. Single dark spots are visible in the region of the Al_2O_3 film, that could either be interpreted as voids or remaining Si extensions crossing the image plane. The latter appears more plausible, since the lifetime on the Ag-MACE NP sample is of the same order of magnitude as measured for wafers with extremely thin Al_2O_3 passivation layers ($\approx 5 - 10$ nm; see fig. 6.4(b)). Therefore, it is concluded that a closed Al_2O_3 layer conceals the whole surface area of the inner pore walls, which may be thinner than the targeted passivation layer thickness and leads to a slightly elevated SRV.

Requirement (iii) – Unchanged Optical Response

Requirement (iii) claimed the need for a negligible impact of the passivating layer on the optical response function of b-Si. Clearly, thin Al_2O_3 layers (≤ 500 cyc, i.e. $d_{\text{oxide}} \lesssim 50$ nm) do not only fulfill this demand, but even improve the absorptance slightly in the blue spectral range. The same effect was observed for thin ZnO and ZnO:Al layers deposited by thermal ALD onto ICP-RIE processed b-Si structures earlier by the author of this work [114]. This behavior may be understood in terms of an additional AR effect leading to destructive interference in the short wavelength range. The AR effect is stronger on the shallow structure than on deep b-Si sample. The latter already offers very low reflectance in the short wavelength range, which is only improved very slightly (see fig. 5.13). Since the passivating effect of Al_2O_3 saturates for passivation layer thicknesses above 300 cyc (i.e. $d_{\text{oxide}} \gtrsim 30$ nm) for both, c-Si and b-Si (figs. 6.4 and 6.12), a positive process window exists to fulfill requirement (iii). The optical properties of the different b-Si structures and their related geometrical features will be discussed in some detail in sec. 7.3

Requirement (iv) – Necessity for Low Temperature Processing

The fourth requirement (iv) demanded that the highest process temperature should be kept as low as possible to avoid diffusion of the eventually remaining contaminants from the black silicon etching step into the Si bulk. For surface passivation by ALD- Al_2O_3 a PDA is essential to activate the passivating effect, which is usually carried out at temperatures around $T_{\text{PDA}} \approx 400$ °C. Fig. 6.11 showed that annealing at this temperature and above ($T_{\text{PDA}} \geq 400$ °C) already leads to a notable reduction of the lifetime in b-Si, whereas the same processes yields rather good lifetimes on unstructured samples (fig. 6.8(a)). Note that the lifetime degradation is more severe on the b-Si sample than in the case of the oob wafer, where the lifetime is preserved at a level of over 1 ms. The highest lifetimes in ICP-RIE

described in secs. 6.2.1 and 6.1.3.

⁶The phenomenon was described for the ICP-RIE structures recorded with the IL detector (see secs. 5.1.2 and 7.1.4).

processed (FZ) b-Si were obtained for a deposition temperature of $T_{\text{ALD}} = 180\text{ }^\circ\text{C}$ in combination with a low annealing temperature of $T_{\text{PDA}} = 385\text{ }^\circ\text{C}$ (tab. 6.1).

During the PDA treatment several processes occur that improve the passivation quality (in unstructured Si) while others may lead to lifetime deterioration in b-Si. First, the XPS study revealed that the PDA treatment of Al_2O_3 on polished HF-dipped samples leads to a strong improvement of the coordination of Si-O bonds, which is related to a reduction of interface defect states [107]. The higher oxidation state of the interfacial SiO_2 indicates a more complete reaction of Si bonds that were open prior to annealing (not shown). Similar densification of the SiO_x to a SiO_2 layer with a slightly increased thickness was also found by other authors [64,82]. The effect is simultaneously supported by hydrogenation of the Si surface and near-surface Si bulk [28,30,82].

Second, it is widely known that the formation of high densities of negative fixed charges induce a high field effect passivation, which leads to a higher tolerance of defects at the Si/ SiO_2 / Al_2O_3 -interface [64]. A more detailed discussion on the field effect passivation will be given in sec. 7.1.4.

Third, it appears probable that annealing of sub-surface damage in the Si bulk by recrystallization and/or hydrogenation takes place during PDA at the applied temperatures. It was reported that surface damage induced by SF_6/O_2 etching, like vacancies in the near-surface bulk could be annealed at temperatures around $350\text{ }^\circ\text{C}$ in forming gas [134]. Since ALD- Al_2O_3 provides high amounts of H_2 due to the precursor chemistry, similar hydrogenation was observed during PDA [28,30,82]. At the same time Al_2O_3 serves as a barrier against out-diffusion of H_2 [28]. The author believes that these effects essentially help to improve the lifetime in b-Si surfaces, without providing direct evidence.

Even though most diffusion processes actually require higher temperatures,⁷ in-diffusion⁸ of extrinsic defects is most probably supported by vacancies. Wittmer *et al.* observed strongly enhanced diffusion (of more than 4 orders of magnitudes higher) if elevated densities of vacancies were present in the near-surface bulk.⁹ Schaefer and Lüdemann reported vastly elevated densities of vacancies ($\sim 10^{-19}\text{ cm}^{-3}$) in the first 20 nm of SF_6/O_2 plasma treated Si surfaces [134], which, paired with the findings of Wittmer *et al.* probably promote in-diffusion of extrinsic defects. We observed high contamination contents on ICP-RIE treated samples prior to RCA cleaning, which is in concordance to [134] (see sec. A.7).¹⁰

In MACE prepared b-Si the situation may be somewhat different. However, due to the high injection of electronic holes during etching and the related removal of Si atoms by HF, which e.g. leads to the formation of a fibrous Si layer on the Au-MACE NC surfaces, I speculate that the effect of micro- and meso-porous Si formation can induce a high number of Si voids in MACE b-Si and macP-Si. Furthermore, the metal catalyst Au is rather recombination active, if incorporated into the Si bulk [102]. Therefore, it is necessary to keep the process temperature low for plasma etched b-Si as well as wet chemically produced b-Si surfaces. Nevertheless, the demonstrated lifetimes show that adequate passivation may be obtained for the optimized annealing scheme on dry and wet etched b-Si in compliance of requirement (iv).

⁷For example, emitter diffusion and firing (i.e. melting the metal contact through the passivating oxide) are carried out at temperatures of over $T \gtrsim 800\text{ }^\circ\text{C}$.

⁸*in-diffusion* is the process “in which the dopant atoms enter through the silicon surface and diffuse into the bulk” [40].

⁹In the vicinity of an advancing near-noble metal silicide interface dopant diffusion is largely enhanced due to vacancy formation as silicide formation extracts Si atoms from the bulk forming voids [169].

¹⁰More details concerning the dry etching process will be discussed in sec. 7.1.2

Requirement (v) – Purity of the b-Si/Al₂O₃-Interface

After requirement (v) the Si surface has to be kept as clean/pure as possible, which is implied by the SRH theory from section 2.2.2. On the one hand, a clean black etching process is required, aggravated by the mentioned possibility of largely elevated diffusion rates of extrinsic defects into the Si bulk. On the other hand, an efficient cleaning procedure must remove possible contaminants and enable the growth of a pure interfacial SiO_x layer with an optimized homogeneous thickness, which is essential to achieve high effective lifetimes. The latter requires high purity DI water and high purity chemicals,¹¹ which will be discussed in some detail in sec. 7.1.4. In this work higher purity grade chemicals led to elevated lifetimes (fig. 6.10). Therefore, the author suspects that the available DI water quality may have been a limiting factor.¹²

It is difficult to distinguish whether a surface was damaged by the structuring process, the cleaning procedure was insufficient and/or resulted in a suboptimal growth of the interfacial SiO_x. Therefore, clean oob substrates were used to optimize the cleaning and SiO_x growth during SC2. It was shown that very homogeneous and high lifetimes can be obtained by the passivation scheme if the developed cleaning procedure is applied (see tab. 3.2). Higher homogeneity is obtained for longer cleaning treatments. It will be shown, however, that the SiO_x thickness needs to be controlled precisely (sec. 7.1.4) to obtain optimized lifetimes.

The cleaning procedure has different effects on oob wafers and b-Si substrates. Fig. 7.1 depicts the lifetime evolution during RCA cleaning schematically. Whereas, the lifetime in a perfectly clean surface may suffer from the application of an insufficient cleaning procedure, the identical RCA treatment may have a vastly positive effect on damaged and/or contaminated b-Si surfaces. The final lifetime difference between the oob wafer and the b-Si sample most probably results from remaining sub-surface damage from black etching. However, it will be discussed that a slightly thicker SiO_x layer on the nanostructures, remaining cross contaminations from the black etching procedure and/or a surface enhancement effect could also contribute to the slightly lower lifetimes in b-Si.

The ICP-RIE processed wafers were not RCA cleaned prior to black etching. Therefore, initially present contaminants may be driven into the surface if they are non-volatile and not effected by the etching chemistry. Additionally, cross contamination from the plasma reactor probably led to a degradation of the lifetime in b-Si samples. Chemical analysis of the surface residues by means of ICP-MS¹³ after black etching in a dry reactive ion plasma demonstrated that the contamination levels of several metals (e.g. Cr, Fe, V, Mn) at the Si/SiO_x surface are rather high (see appendix A.7). If incorporated into the Si lattice, the metals lead to recombination active defect states inside the forbidden band of Si and deteriorate the lifetime in c-Si for the indicated surface contamination levels. An extremely elevated Cr concentration¹⁴ of up to four orders above the reference was found in the case of the shallow and deep b-Si structures, whereas it was lower on the intermediate b-Si surface. Cr can induce a deep donor defect state in Si at $E_V+0.74$ eV [60], or a shallow donor at $E_C-0.22$ eV with extremely large capture cross sections (of $\sim 10^{-13}$ cm²) for electrons and holes [102].

¹¹especially of the oxidizing agent H₂O₂

¹²DI water with a resistivity of 18 MΩ is usually used for industrial processing [72]. However, for the presented experiments only DI water with a resistivity of 15 MΩ was available.

¹³Inductive Coupled Plasma Mass-Spectrometry

¹⁴Cr most probably originates from hard-mask etching carried out in the ICP-RIE reactor.

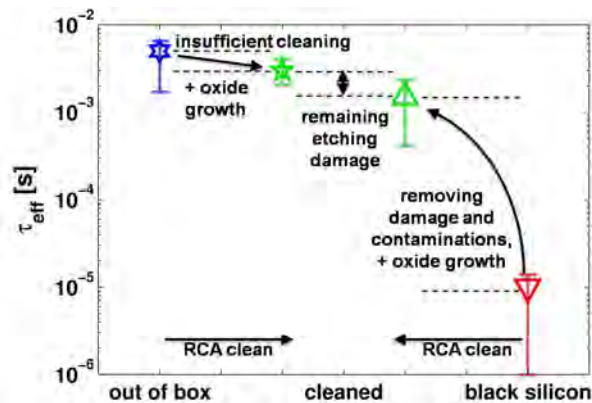


Figure 7.1: Schematic comparison of fictive lifetimes in oob and b-Si wafers and their evolution during RCA cleaning. The RCA sequence enables a lifetime increase of several orders of magnitude on the black surfaces due to removal of contaminations and superficial damage. It leaves the clean and homogeneous SiO_x , which is essential to enable high passivation performance of annealed Al_2O_3 . In contrast, the oob wafer's lifetime slightly decreases as it may suffer from minor concentrations of impurities in the chemical cleaning solutions, while its homogeneity (error bars) may improve.

If ionized – which can be assumed to be the case at RT – the state leads to an elevated recombination rate. This may allow the speculation that equal lifetimes on b-Si and the according reference may be achievable if the ultimate difference originated from this type of cross contamination, which could be easily avoided by designating a plasma reactor only to b-Si fabrication.

Finally, it is important to leave the surface geometry unaffected by the surface clean to comply with requirement (iii) for unchanged optics. In both RCA steps not more than 2 – 3 nm of Si are consumed [79]. Hence, even very small features remain after RCA cleaning of b-Si surfaces leaving the optical features in the absorbing range of Si unchanged. Note however, that in the case of the Au-MACE NC b-Si surface the cleaning step SC1 removes a superficial layer of highly recombination active fibrous Si [3] (not shown here). In contrast, damage removal etching (DRE) of the shallow and deep ICP-RIE b-Si surfaces did not significantly improve the lifetime, but led to significantly higher optical reflectance after removing approximately the top 75 nm (not shown).

It can be stated that requirement (v) is fulfilled in terms of the developed cleaning procedure, which can possibly be further optimized to meet the needs of a specific b-Si surface.¹⁵

Requirement (vi) – Minimized Damage Induced by Black Etching

Finally, requirement (vi) constitutes that damage caused by the b-Si etching process itself has to be minimized in order to achieve a high lifetime. This demand arises in part from requirements (iv) and (v) concerning the generation of defects and contamination. The issue of plasma induced damage will be discussed in the following section (7.1.2). It was found that ICP-RIE damage is minimized, or rather the lifetime is maximized for an optimized combination of pressure and etching time, while appropriate cleaning still appears to be necessary. Note, that the optical absorption is simultaneously maximized. In contrast, for MACE b-Si the removal of the metal catalyst is essential and additional cleaning steps are necessary. Especially Au is highly recombination active if introduced into the Si bulk. Some effects that occur in wet chemical black etching of Si are elucidated in sec. 7.1.3.

Conclusively, the first five requirements for the passivation of b-Si are fulfilled by the presented passivation scheme of RCA cleaning, subsequent deposition of 300 cyc Al_2O_3 by thermal ALD, and according PDA. However, requirements (v) and (vi) also demand high electronic surface quality resulting from the black etching process.

¹⁵see also sec. 7.1.3.

7.1.2 Passivation of Dry Etched Black Silicon

Concerning the opto-electronic properties of the three ICP-RIE processed b-Si standard structures, very high lifetimes in the millisecond range could be obtained as shown in fig. 6.13.¹⁶ The passivation performance of the Al₂O₃ films on nanostructured surfaces is comparable to the identically passivated planar references.

Etching Process *vs.* Surface Morphology

Outstanding within the group of dry etched b-Si types prepared on Cz and FZ wafers, is the intermediate b-Si structure with the highest lifetimes and accordingly lowest SRVs. FIB cross-sectional images (see figs. 5.4 and 5.5) of the b-Si/Al₂O₃-interfaces showed that the Al₂O₃ passivation layer was equally conformal on all three structures. The shallow and intermediate b-Si structures possess rather similar surface morphology concerning their statistical surface parameters like sidewall angles, pore depths, and accordingly their aspect ratios (fig. 5.1). Their optical absorption behavior is very similar (fig. 5.11) and the coverage of the passivating ALD-Al₂O₃ films appear to be identical (fig. 5.5). However, especially in the case of the experiment based on Cz grown wafers the electronic performance distinctly differs. The author speculates that the plasma-induced damage on the intermediate b-Si structure must be lower than on the shallow one, which would lead to an accordingly lower total recombination rate. This hypothesis is supported by the ICP etching time experiments for process conditions leading to shallow and deep type b-Si surfaces (fig. 6.15). After a notable initial drop in lifetime for both sets of process conditions, further degradation of the average (and peak) lifetime with increasing etching time was observed during the first 15 minutes. Thereafter, a step-like increase of the average lifetime was observed, indicating reduced sub-surface damage.¹⁷ For the process conditions leading to the shallow geometry, the “intermediate” structure is obtained after $t_{\text{ICP}} = 20$ min etch time. The lifetime and the pore depths of the intermediate structure are simultaneously increased as compared to the shallow one ($t_{\text{ICP}} = 10$ min). Therefore, a purely negative effect of surface enhancement can be excluded and the difference in lifetime has to originate from the etching process itself. Schaefer and Lüdemann reported that a prolonged plasma etching time in their parallel plate reactor led to a reduced plasma induced damage layer: $V_{\text{oc}}(t_{\text{etch}} = 3 \text{ min}) > V_{\text{oc}}(t_{\text{etch}} = 0.5 \text{ min})$ [134]. However, a reduced V_{oc} was observed for even longer etching times after $t_{\text{etch}} = 15$ min, which was not the case in our etching process for the investigated time range (fig. 6.15). A similar effect was observed by Afanas’ev *et al.*, who reported that low fluences of VUV¹⁸ irradiation ($\Phi_{\text{VUV}} < 10^{17} \text{ cm}^{-2}$) onto SiO₂/Si-interfaces¹⁹ led to the formation of two different electron-traps with capture cross sections of about $\sigma_{\text{e,I}} \geq 10^{-16} \text{ cm}^2$ and $\sigma_{\text{e,II}} \approx 2 \cdot 10^{-17} \text{ cm}^2$ [1]. According to Afanas’ev, both defects disappear for higher VUV fluences ($\Phi_{\text{VUV}} > 10^{17} \text{ cm}^{-2}$), and subsequently, a third defect emerges with a capture cross section of $\sigma_{\text{e,III}} \approx 5 \cdot 10^{-18} \text{ cm}^2$, whereas the capture cross sections for holes are much larger for

¹⁶For the summary of the lifetime data see tab. 6.1.

¹⁷Changing the CCP power has a negligible impact on structural changes and also leaves the lifetime basically unchanged in the tested parameter range (fig. 6.16). This is most likely explained by an unchanged bias voltage.

¹⁸Vacuum UV light (hard UV irradiation of $E_{\text{ph}} = 10 \text{ eV}$ in this case) is absorbed by air, and hence, only propagates through vacuum. Note, that the reflectance of c-Si is rather high ($R \approx 65\%$) for VUV photons [54].

¹⁹ $d_{\text{SiO}_2} \approx 66 \text{ nm}$ thick SiO₂ films on Si.

all three defect types ($\sigma_p \approx 3 \cdot 10^{-14} \text{ cm}^2$). In terms of charge carrier lifetimes the defects with higher cross sections lead to much higher recombination rates in p-type Si. Furthermore, Afanas'ev *et al.* observed an initial damage level that appeared to be irreversible by annealing. The trend in fig. 6.15 may result from such “VUV-like” defects with a similar behavior, if indeed such defects would result from ICP-RIE etching and endured the subsequent process steps in b-Si. Eventually, the O₂ plasma is responsible, because the effect of “in-situ annealing” or “back etching” of damaged material was not observed for a pure sulfur based ICP-RIE process (sec. A.7). However, there is no proof for this speculation and fairly different experimental conditions apply here as compared to Afanas'ev *et al.* The deep b-Si structure was fabricated at a lower pressure than the shallow and the intermediate ones, which leads to a stronger physical etching component of the plasma species. Even though the number of particles impinging on the surface decreases with decreasing pressure, the mean free path of the plasma particles simultaneously increases.²⁰ Therefore, the kinetic distribution of energetic particles shifts to higher energies, because the energy transfer due to particle collisions is reduced. It was speculated by the author that this might lead to increased plasma-damage of the silicon sub-surface layer and hence lower carrier lifetimes [119]. Conclusively, it appears obvious that optimizing the plasma-induced damage layer is equally as important as providing an effective surface passivation scheme [119]. The same was proposed in requirement (vi), demanding for the best possible reduction of initial plasma damage to the surface. Considering the surface enhancement factor of $\gamma_{\text{deep}} \approx 5 - 10$ (sec. 5.1.1) requirement (vi) appears to be satisfactorily fulfilled for the presented dry etching processes for b-Si fabrication.

7.1.3 Comparison of the Different Black Etching Methods

To identify black etching techniques that simultaneously offer excellent optical properties and high effective lifetimes, different b-Si nanostructures were produced and passivated on the same batch of wafers and the optical properties and lifetimes were determined as described previously (see secs. 5.3.2 and 6.3). Since all samples were produced on FZ wafers with nominally identical doping level and thickness, it is assumed that all observed differences concerning optical absorption and lifetime/SRV are related solely to the b-Si properties.

Passivation Feasibility *vs.* Optical Absorption Efficiency in b-Si

Figure 7.2 shows the determined surface recombination velocities of the b-Si samples fabricated by the different black etching methods at an injection level of $\Delta n = 10^{15} \text{ cm}^{-3}$ plotted against their integrated optical absorption between 300 nm and 1180 nm. Hence, samples in the lower right corner are most desirable for photovoltaic applications.

For the investigated black etching methods, there is no obvious correlation between the SRV and optical performance covering all nanostructure types. First, this may indicate that to a certain extent the electronic surface properties can be tailored independent of the optical absorption. Second, it

²⁰Note, that Schaefer and Lüdemann pointed out that the self-induced bias voltage increased with decreasing process pressure for their reactor geometry. However, according to our data this was not the case for the ICP-RIE processes and the range of pressures used for this work (comp. tab. A.2).

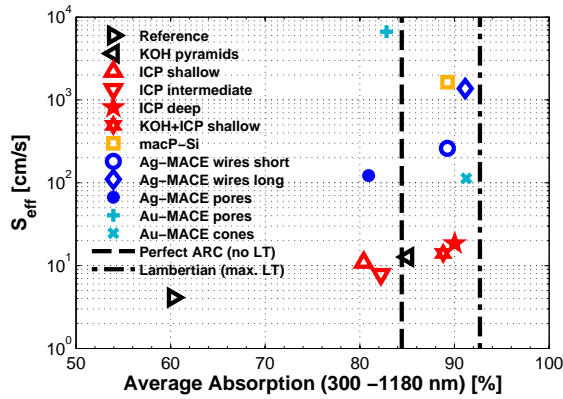


Figure 7.2: The plot shows an overview of measured lifetimes in correlation to the total absorptance integrated over the indicated spectral width.

demonstrates that the black etching methods may induce inherent lifetime limits that differ from one method to the other. Even though a small number of samples is presented, a slight tendency towards higher SRV with higher absorptance may be denoted within the group of ICP-RIE fabricated b-Si samples and within the Ag-MACE nanostructures, independently. However, the Au-MACE fabricated samples do not confirm this trend.

In general, the various black silicon types show excellent optical properties as lined out in sec. 5.3.2. Some ICP-RIE b-Si structured surfaces can even compete with common alkaline textures coated with well-suited [single-layer-]ARCs [90]. Since MACE fabricated NCs and NWs optically outperform the ICP structures, they can also compete with appropriately AR coated KOH textures.

The plot in fig. 7.2 may be compared qualitatively to the one in fig. 1.2. It was stated in sec. 1.1, that even in very thin wafers ($W \approx 25 \mu\text{m}$) SRVs below $\leq 125 - 25 \text{ cm/s}$ would suffice to be non-limiting to solar cell device performance if the bulk lifetime is in the range of $\approx 20 - 100 \mu\text{s}$, respectively (see fig. 1.1). Hence, the developed passivation scheme offers sufficiently low SRVs on all dry etched samples as well as on the Au-MACE NC and Ag-MACE NP b-Si surfaces. Now, consider that low SRV is of higher importance to obtain a high open circuit voltage, since V_{oc} saturates slower with decreasing S_{eff} than I_{sc} (see fig. 1.2). Therefore, SRVs as low as $S_{eff} \leq 10 \text{ cm/s}$ would be required to maximize the efficiency in the example given in sec. 1.2. This means that the absorption gain in the MACE samples would probably be over-compensated by the higher SRV, whereas such exceptionally low S_{eff} values may still be reached in the dry etched samples. It is important to note, that even though the absolute absorption would decrease in a thinner wafer,²¹ the solar cell efficiency would increase with decreasing wafer thickness for the ICP-RIE samples [90]. Simulations using an analytic solar cell model as performed by Kroll *et al.* showed that the optimal wafer thickness for the shallow and deep b-Si geometries lies below $W < 50 \mu\text{m}$ [90].

Conclusively, according to this experiment the ICP-RIE b-Si and the MACE NC structures have the potential to bring out high efficiency solar cells, which will still strongly depend on the type of solar cell junction and its implementation [105, 112, 128, 186]. The results are supported by different solar cell concepts presented in the literature, where the highest b-Si solar cell efficiency was reached for diffused emitters in dry etched b-Si ($\eta = 18.7\%$, [128]), closely followed by the MACE NP structures ($\eta = 18.2\%$, [112]). At the moment of writing, the highest reported efficiency for a hetero junction (a-Si on b-Si front) solar cell was $\eta = 17.2\%$ [105].

²¹ $A_{LLT,tot}(W=250\mu\text{m}) \approx 92.7\%$, vs. $A_{LLT,tot}(W=25\mu\text{m}) \approx 84.4\%$ for Lambertian light trapping (LLT) in double side structured Si wafers of thickness W , i.e. the $2n^2$ limit. Therefore, the overall absorption can not approach unity, as proposed in sec. 1.1.

Proper Cleaning of b-Si Surfaces

RCA cleaning has two important effects to obtain high lifetimes. First, the reduction of potential contaminants from the Si surface is essential (requirement (v)). As mentioned in sec. 3.2, the RCA procedure predominantly removes organic contaminants in SC1 and metallic ones in SC2 [80]. Second, a clean and high quality initial SiO_x has to be grown to enable high passivation performance of Al_2O_3 stacks. The importance of the initial SiO_x properties will be discussed in sec. 7.1.4. The herein developed RCA clean demonstrably reduced metallic contaminations at the interface²² and led to high charge carrier lifetimes on all presented ICP-RIE b-Si samples. All MACE processes required additional cleaning subsequent to the black etching step to remove the metal catalyst from the nanostructured surfaces. For Au removal I_2/KI solution or aqua-regia may be used [12,85], whereas Ag is effectively removed in concentrated HNO_3 [100]. If the catalyst is not removed properly, the samples suffer from a severe lifetime degradation. This was most probably the case for the Au-MACE NP sample, where rather high contents of Au and Ag were detected by ToF/SIMS (not shown). During Au-MACE fabrication of the NC structures a fibrous network develops, which also leads to elevated surface recombination. As mentioned, the SC1 step from the RCA cleaning sequence is sufficient to remove the layer [3] such that the lifetime may be almost fully recovered.

7.1.4 Microstructure of b-Si/ Al_2O_3 -Interfaces and the Passivation Mechanism

SiO_x Formation at Si/ Al_2O_3 -Interfaces and Importance to the Passivation Quality

The interfacial SiO_2 layer between the (b-)Si surface and the ALD- Al_2O_3 passivation layer was found to be of great importance to achieve a high level of surface passivation. Since the RCA cleaning sequence was applied without final HF dip, the initial SiO_x layer was grown in the wet chemical bath of SC2. Taking the SiO_x thickness into account as determined by optical ellipsometry mappings of RCA cleaned wafers (see figs. 7.3 and fig. A.5), it becomes clear, that this layer is prerequisite to an adequate surface passivation. Fig. 7.3(a) shows a very homogeneous SiO_x film on the front of the RCA cleaned wafer, whereas the SiO_x grown on the rear side (fig. 7.3(b)) exhibits three areas with distinct thicknesses. This growth behavior can be explained by the experimental conditions. The wafer is held by a sample holder in a beaker separating the wafer front by ≈ 5 mm from the beaker wall or an adjacent second wafer. At the rear where the SiO_x is especially thin (dark blue area), the holder rod is separated from the wafer at an equal distance of ≈ 5 mm, whereas the space between the rest of the wafer surface and the beaker wall is at least twice as large. An even more homogeneous SiO_x thickness is obtained for a SC2 step of 20 min duration. Interestingly, the total SiO_x thicknesses after 10 min and 20 min cleaning are comparable and exhibit the same pattern on the back (comp. figs. A.5 and A.6).

The slightly thinner SiO_x regions lead to improved lifetimes, which may be explained by a higher field effect passivation. A similar effect was shown for ALD deposited $\text{SiO}_2/\text{Al}_2\text{O}_3$ stacks on n-type c-Si [34].²³ Nevertheless, HF dipped wafers²⁴ (without initial SiO_x) exhibited lower lifetimes with a

²²measured by ToF/SIMS (not shown); see sec. 7.1.4.

²³Note, that the field effect passivation induced by negative fixed charges on n-type Si significantly differs from that on p-type Si, because in n-Si the majority charge carriers are repelled from the surface while the minorities are attracted.

²⁴Dingemans *et al.* reported that they obtained the lowest SRV and highest field effect on HF dipped samples [34].

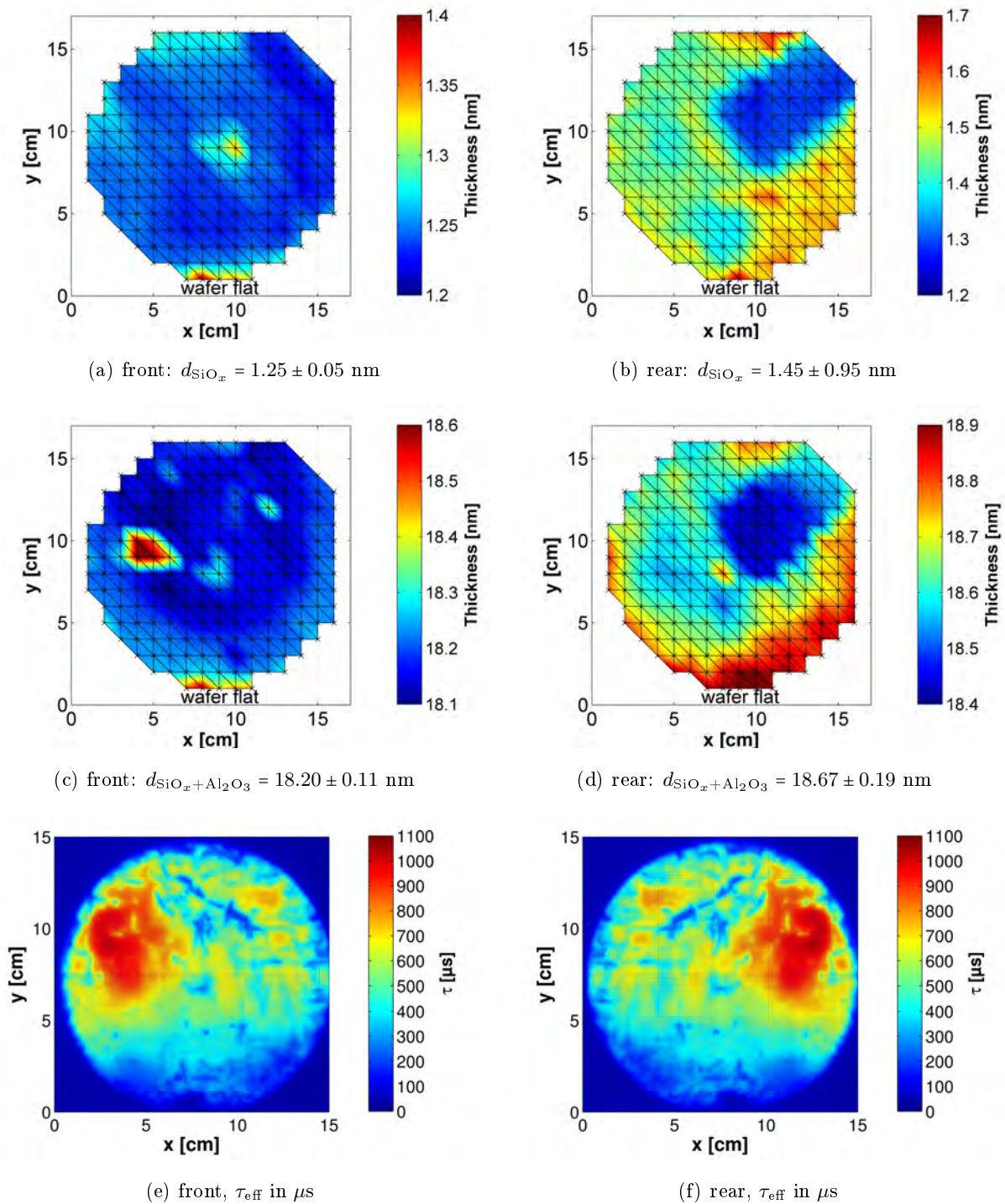


Figure 7.3: Ellipsometry mappings of the oxide (SiO_x) thickness grown during a **10 min** RCA SC2 cleaning step. The SiO_x is very homogeneous on the front (a) $d_{\text{min}} = 1.22 \text{ nm}$, $d_{\text{max}} = 1.90 \text{ nm}$, whereas on the rear (b) three regions are visible with thicknesses around 1.2 nm, 1.4 nm, and 1.6 nm. Nevertheless, the total span of the rear side is only 0.6 nm. After deposition of 150 cyc Al_2O_3 the oxide layer thickness on front (c) and rear (d) follows the original SiO_x patterns. Hence, a highly homogeneous Al_2O_3 layer thickness was deposited. Graphs (e) and (f) show lifetime maps of the same wafer as recorded by PL on front and rear, respectively. The highest lifetimes were measured where the SiO_x is thinnest. The thick red spot at the front side Al_2O_3 film (c) may stem from a dust flake either between the SiO_x and Al_2O_3 films or superficially present during the ellipsometry measurement. A direct influence on the lifetime at the same positions in (e) and (f) is not apparent, which speaks for the latter, whereas the triangular spot in the very center may correlate with the thickness variation in (a) or stem from a handling mark by the manufacturer. Higher lifetimes following the same pattern were achieved for samples that were not intermittently measured by ellipsometry (see figs. A.5 and A.6 in appendix A.6).

deteriorated homogeneity in this work, which may be explained by the insufficient DI water quality¹² and exposure of the bare Si–H surface to the ambient air. Hence, either the chemical purity of our solutions was not high enough to obtain sufficiently clean Si–H surfaces (see fig. 6.9 in sec. 6.1.3),²⁵ or fast re-oxidation during DI water rinsing leads to an inhomogeneous coverage with –OH groups [49], which may have an influence on initial growth of the ALD layer. Subsequently, inhomogeneous Al_2O_3 growth during the first ALD cycles with accordingly inhomogeneous and lower level passivation may result. Our results concerning Al_2O_3 growth investigated by XPS (see sec. 7.1.4, or ref. [107]) and ellipsometry (fig. A.2) on HF dipped substrates show that island growth appears to be very likely, which was also observed by Puurunen and Vandervorst for ALD- Al_2O_3 on HF treated c-Si [125]. In addition, the reproducibility was compromised, which may be explained by the absence of buffered HF in our experiments [79, and ref. 38 within]. To further increase the homogeneity of the SC2 SiO_x , a circulating laminar flow in (or stirring of) the RCA bath should be introduced. The author expects that better control of the SiO_x thickness and its influence on the lifetime should be gained, as both the bath’s temperature and the chemical’s distribution in the beaker would be homogenized. It would be very attractive to develop a SiO_2 ALD process to directly control the thickness of the interlayer as proposed in the work of Dingemans *et al.* [34].²⁶ The deposition of optimized ultra-thin ALD oxide stacks should enable the feasibility to fabricate hetero-junction devices on high quality ICP-RIE b-Si surfaces. Preliminary results on SIS²⁷ solar cells accompanying this work were published in [42, 114].

Microstructure and Chemical Composition of the (b-)Si/ SiO_2 / Al_2O_3 -Interface

The final SiO_2 thickness results from (further) oxidation during (the first cycles of) ALD and/or during the PDA treatment. In an accompanying study to this work, the micro-structural changes at unstructured (HF dipped) Si/ Al_2O_3 -interfaces upon thermal PDA were investigated in detail by XPS as a function of the deposited ALD cycle number [107]. During an in-situ annealing in the XPS chamber it was observed that the interfacial SiO_x thickness increased together with a strongly improved Si–O coordination. The measurements indicate a complete reaction of Si to SiO_2 at the Si/ Al_2O_3 -interface after PDA. It was found that a rather high amount of unbound –O (“excess O”) is present close to the interface within the first 1 nm of the Al_2O_3 films, which most probably stems from unreacted H_2O precursor and/or –OH groups, of which a non-negligible amount of excess O remained after annealing. Al is completely oxidized in the Al_2O_3 film already in the as-deposited state. Continued deposition led to near-stoichiometric Al_2O_3 growth (for $d_{\text{Al}_2\text{O}_3} \geq 5$ nm).

However, no XPS measurements were performed at b-Si interfaces. According to the TEM image contrast that is visible by eye in fig. 5.7, a thin interfacial SiO_2 is assumed to exist between the Si substrate and the Al_2O_3 passivation layer. HR-TEM EELS measurements of the chemical interface composition did not allow the conclusion that a SiO_2 layer is present on the b-Si needles. However, the image contrast may be interpreted as such, which is also visible in the unstructured sample, fig. 5.7.

²⁵Bare Si surfaces after HF dip exhibit chemically higher activity and are much more sensitive for contaminations [79].

²⁶Note, that XPS and AES (Auger electron spectroscopy) measurements of HF-dipped samples also suggest that atomic layer deposition of Al_2O_3 leads to a thin interfacial SiO_x [64, 77, 107].

²⁷Semiconductor Insulator Semiconductor

On the unstructured sample a thickness of $d_{\text{SiO}_2, \text{TEM}} = 1.58 \pm 0.23$ nm was measured, in accordance to the ellipsometry measurements. In comparison to the intermediate ICP b-Si structure the interfacial SiO₂ thickness might be slightly larger on curved surfaces.²⁸ If this is the case, the thicker SiO₂ may have contributed to the slightly lower lifetime in the b-Si sample. This effect might be easily adjusted by further optimizing the SC2 procedure to account for the b-Si geometry.

Unfortunately, the films quickly decomposed under the energetic electron beam before an adequate signal could be collected even if low TEM voltage of 80 keV was used. Hence, no clear evidence for the chemical fingerprint of an interfacial SiO₂ was evidenced.²⁹ This effect indicates just how unstable the films are if energy is deposited locally and might be related to the observed effect of thermal instability (i.e. “over-annealing”) of the films. Shortly after, the same difficulties were reported by Hoex *et al.*, who pointed out that a significant EELS signal could only be recorded if the primary electron beam with a very low current was scanned in parallel along the Si/Al₂O₃-interface for long integration times [63]. This procedure was intended herein,³⁰ but was not suitable on the roughly structured and 3-dimensionally curved b-Si/Al₂O₃-interfaces.

The initial microstructure of the b-Si interface was strongly modified during TEM imaging. The Al₂O₃ layer started to crystallize under the electron beam while the Si crystal was amorphized. One possible cause of this instability could be a high H content in the samples, which could not be directly proven by means of the available methods. However, the hypothesis is supported by the refractive index that increases with increasing purge time following the H₂O pulse (not shown), and is assumed to correlate with the film density as proposed in the literature [56]. It is also known from the literature, that effusion experiments and ERDA³¹ measurements exhibited rather high H contents ($c_{50^\circ\text{C}} \approx 13\%$; $c_{200^\circ\text{C}} \approx 3\%$) if the ALD-Al₂O₃ films were deposited at low temperature ($T_{\text{ALD}} < 200$ °C) [30]. Our films were deposited at optimal temperature for high lifetimes of $T_{\text{ALD}} = 180$ °C. It was also described by Dingemans *et al.*, that H originating from the water precursor for Al₂O₃ film growth, preferably diffuses into the near surface bulk of Si [28]. On the one hand, this hydrogenation contributes to the desired chemical surface passivation. On the other hand, very high H concentrations decrease the thermal stability of the samples [28]. Such thermal instability is reflected in the possibility of “over-annealing” a sample at too high temperatures or for too long annealing times and may also lead to blistering of thick layers [162]. The effect may also explain the shadow-like inhomogeneities in the underlying Si crystal structure at the intermediate b-Si/Al₂O₃-interface at the bottom of fig. 5.7(b). The regions are interpreted as Si crystal defects, which at such high density would clearly contribute to recombination. However, the absolute lifetime value in this intermediate b-Si structure was only a factor of two lower than in the reference (fig. 6.13). Furthermore, a deep b-Si nanostructure without such defect regions was presented in [114]. The b-Si sample was rather crystalline in the beginning. Unfortunately, it degraded faster during imaging than the reference. First, the faster degradation of

²⁸Due to the low image contrast difference, however, a solid measurement of the interfacial SiO₂ thickness was not carried out.

²⁹Note, that the black spots in fig. 5.8 resulted from a local dissociation of the lamella under the electron beam during beam adjustment.

³⁰before publication [63] appeared

³¹ERDA: elastic recoil detection analysis is an ion beam analysis method like Rutherford backscattering (RBS). In ERDA an ion beam of a slightly heavier species, e.g. Cl, is used to “knock” light atoms like hydrogen out of the investigated matrix material.

the crystal structure in the b-Si sample under the TEM beam could be an indication for a (slightly) higher damage previously present in the lattice. Second, it is possible that for geometry reasons a higher -H content diffused into the Si needles during PDA, possibly passivating a higher number of defects. This H may become volatile as the samples is locally heated and diffuses out (outgassing), causing the crystal lattice to relax by forming new defects. Even though there is no direct evidence, the author believes that the second mechanism should be more plausible.

The matrix composition of the near-surface b-Si bulk of the best intermediate structure was investigated by HR-TEM EDX. The measurements presented in fig. 5.8 were complemented by additional element maps recorded for C, N, S, and F to check for residues of the ICP-RIE plasma process. However, for all other tested elements only noise-signal was detected.³² Likewise, other attempts like EELS and energy-filtered (EF-TEM) imaging were used for elemental analysis, measuring no inhomogeneous distributions of any species other than the expected matrix-elements (Si, O, and Al). This indicates that (i) no plasma species were implanted at high concentrations into the surfaces during black etching, and (ii) residual surface contaminations were effectively removed in the RCA clean, if ever present in concentrations above the detection thresholds for EDX, EELS and EF-TEM prior to passivation. It was shown by ICP-MS³³ that non-negligible contamination levels are apparent on as processed ICP-RIE blackened wafers that may give rise to highly elevated surface recombination (see appendix A.7).³⁴ Hence, it can be concluded that the cleaning procedure efficiently worked for ICP-RIE b-Si.

Influence of the Field Effect and Chemical Passivation

The field effect passivation in Al₂O₃ on Si is claimed to be extraordinary strong due to a high number of negative fixed charges ($Q_{\text{fix}} \sim 10^{12} - 10^{13} \text{ cm}^{-2}$) that presumably build up at the SiO_x/Al₂O₃-interface. The gpc measurements by ellipsometry (fig. A.2(b)) indicate that the growth mode of our ALD-Al₂O₃ films can be categorized as substrate inhibited growth of Type 2,³⁵ which can be related to island growth [124, fig. 15; III.]. By XPS an initial linear decrease of the Si intensity led to the conclusion that the first mono-layer of Al₂O₃ closes after about 10 – 15 full ALD cycles [107], which is also in good agreement with the growth behavior observed by Puurunen *et al.* [125]. Furthermore, Hoex *et al.* reported that the field effect passivation scales with Q_{fix}^2 [64].

Fig. 6.5 shows a quadratic lifetime increase with the first 17 Al₂O₃ ALD cycles, which can be attributed to field effect passivation. Therefore, a linearly growing sub-monolayer of Al₂O₃ apparently already has a rather high and quadratically increasing passivating effect. With further Al₂O₃ deposition the lifetime follows a more linear trend which can be explained by chemical passivation due to a larger supply of -O and -H from the deposited film. After the linear increase for closed Al₂O₃ films, the lifetime finally goes into saturation after deposition of about 300 cyc (comp. fig. 6.4(a)). Hence, the

³²The detection limit is however rather high for EDX (usually $\sim 0.1\%$ for elements heavier than Na, [140])

³³Inductive Coupled Plasma Mass-Spectrometry

³⁴See also sec. 7.1.3.

³⁵Substrate inhibited growth is characterized by an increasing gpc with increasing number of cycles starting at a lower value than in the steady regime. In substrate inhibited growth of Type 2 the gpc goes through a maximum before settling to the constant value [124, fig. 15; III.]. Many references within [124] point out that for this growth mode island growth seems to occur.

negative fixed charges appear to build up at (or in the vicinity of) the SiO₂/Al₂O₃-interface and do not increase with increasing film thickness. Very similar observations were reported by Terlinden *et al.* for ultra-thin Al₂O₃ films on Si [154]. In the XPS study it was suggested that “in agreement with density functional theory calculations that revealed preferably negative charged states for O_i in Al₂O₃ [164]” the excess O may be a possible origin of the negative fixed charges [107].

A measurement of the fixed charge density on b-Si³⁶ by a contact-less capacitance voltage method exhibited a slightly (1.5×) larger Q_{fix} than on the flat reference (not shown), which might possibly be explained the larger surface area. However, no direct relation to the surface enhancement factors could be found. Furthermore, the data probably rather defective, since the automatic interpretation routine of the measurement apparatus (from SDI) did not account for the complex electric field distributions above the nanometric Si needles. Classical C-V measurements on MOS³⁷ structures were not available and would probably be complicated due to the necessary elaborate preparation of the MOS device on b-Si. Johnson *et al.* suggested that tetrahedrally coordinated Al sites in noncrystalline Al₂O₃ induce a net negative charge [77], which was recently confirmed via HR-EELS for atomically sharp Si/SiO₂/Al₂O₃-interfaces by Hoex *et al.* [63]. As mentioned, our HR-EELS measurements did not yield reliable results on b-Si due to fast lamella degradation and the curved interface geometry that made parallel scans along the Si/SiO₂/Al₂O₃ more or less impossible.

The fine white lines between the b-Si substrate and the dielectric layer (in the FIB cut SEM images of fig. 5.4(c)) could have several origins. One possible explanation would be a SiO₂ layer, which according to the TEM investigations (fig. 5.7(b)), however, has a thickness below the pixel resolution (7 nm/px) of the SEM image. The phenomenon might be a result of the high electric field intensity at the edge of the Si nanostructure that could lead to enhanced electron extraction probability or a deflection of the primary beam. Opposingly, it has to be mentioned, that the electron density underneath the Al₂O₃ layer should be strongly decreased due to negative charges at the interface. Note, that the Al₂O₃ layer did not charge up and appears rather dark in the image recorded with the IL detector.³⁸ Therefore, a pure charging effect of the sample due to primary electrons may be excluded. Furthermore, the effect was not observed for the SiN_x passivated samples under the same circumstances. SiN_x develops *positive* fixed charges [31]. Therefore, by speculation, the white line artifact may be related to the high amount of the *negative* fixed charges at the Si/SiO₂/Al₂O₃-interface. However, it can not be excluded that an imaging artifact causes the interface contrast. Hence, further investigations are necessary.

7.2 Recombination in Black Silicon

7.2.1 A Model to Distinguish Surface Enhancement from Damage³⁹

Due to their fabrication processes black silicon surfaces raise two challenges concerning their passivation feasibility. On the one hand, the surface area is greatly enhanced. On the other hand, defects

³⁶ $Q_{\text{fix,intm.}} = -(2.8 \pm 0.4) \cdot 10^{12} \text{ cm}^{-2}$.

³⁷Metal Oxide Semiconductor

³⁸In-Lense (IL) detector.

³⁹The model was published in [113, sec. 6].

at the surface or within the near-surface bulk might be introduced during black etching. As a result, strongly enhanced surface recombination rates are usually reported for black silicon surfaces.

To optimize a b-Si structure electronically, one must understand which of the two effects limits the lifetime. In practice, it is difficult to distinguish between the contributions of surface enhancement and elevated defect density (i.e. damage). The results of fig. 7.2 demonstrate that nanostructuring does not necessarily lead to a vast electronic degradation of the surface, even though the surface area may be greatly enhanced. To understand the reasons for the change in effective SRV, S_{eff} must be connected with its relevant parameters, namely the surface area enhancement and the surface defect density enhancement. From sec. 2.2.3 it is known, that S_{eff} is directly proportional to the defect density, which may scale with surface area in b-Si.

To understand the rather complex mechanisms of surface recombination in (nano)structured surfaces, the total number of apparent recombination active defects D_S must be taken into account, which is an essential parameter contributing to S_{eff} . Assume D_S includes the sum of surface-near and sub-surface defects that are *not screened* by field effect passivation and offer an energy level anywhere within the band gap. Therefore, D_S is explicitly not only the number of defects in the middle of the gap, as given by D_{it} , but D_S should be greater than D_{it} . Now, $D_{S,\text{nano}}$ is defined to include all such intrinsic and extrinsic defects (voids and impurities) due to black etching, independent of their exact origin. By further assuming that the unstructured sample exhibits the lowest number of surface defects $D_{S,\text{ref}}$ and possesses no additional “b-Si defects”, the number of defects induced by the black silicon process can be normalized:

$$\delta := \frac{D_{S,\text{nano}}}{D_{S,\text{ref}}} \quad (7.1)$$

According to eqn. (2.22) of sec. 2.2.3, the maximum SRV in low injection can simply be modeled as $S = v_{\text{th}}\sigma D_S$, where v_{th} and σ are the thermal velocity of diffusing charges ($\sim 10^7$ cm/s) and the according defect capture cross section ($\sim 10^{-15}$ cm²), respectively. It is further assumed, that all recombination active defects in the sample are located near the surface. Hence, they are contained in D_S , which corresponds to the earlier proposed assumption of an infinite bulk lifetime (eqn. (2.26)).⁴⁰ This leads to the known worst case approximation for S_{eff} with a relative error of less than 5%, as long as the recombination processes at the surface are not limited by minority charge carrier diffusion through the bulk [149]. The approximation introduced by Sproul is valid as long as $S_{\text{eff}} < \frac{D_a}{(4W)}$, with $D_a \approx 30$ cm²/s as the minority carrier diffusion constant (here, $W = 250$ $\mu\text{m} \Rightarrow S_{\text{eff}} \leq 300$ cm/s). The surface area of the nanostructures is taken into account by the enhancement factor $\gamma = A_{\text{nano}}/A_{\text{ref}}$,⁴¹ which was defined in eqn. (5.1). Following Hagedorn *et al.* [57], the SRV can be expressed by:

$$S_{\text{eff}} = \gamma \cdot v_{\text{th}}\sigma D_{S,\text{nano}} = \gamma \cdot v_{\text{th}}\sigma D_{S,\text{ref}} \cdot \delta \quad (7.2)$$

To evaluate the obtained surface passivation quality, the recombination in the nanostructured surfaces needs to be related to the reference sample:

$$\frac{S_{\text{nano}}}{S_{\text{ref}}} = \frac{A_{\text{nano}}}{A_{\text{ref}}} \cdot \frac{D_{S,\text{nano}}}{D_{S,\text{ref}}} = \gamma \cdot \delta \quad (7.3)$$

⁴⁰Here, the whole recombination rate is attributed to the surface.

⁴¹ A_{nano} is the true surface area of the nanostructure, while $A_{\text{ref}} \equiv 1$ is the planar footprint. Values for A_{nano} are given in tab. 7.1.

It is assumed that v_{th} and σ are identical in all samples.⁴² Thus, the effective lifetime, τ_{eff} , and the respective SRV, S_{eff} , scale linearly with the enhancement factor of the surface area γ and the ratio of recombination active surface defect states δ introduced by the black etching process. The experimental values of the ratio $S_{\text{nano}}/S_{\text{ref}}$ are listed in tab. 7.1. To separate the individual contributions of an enhanced surface area A_{nano} and additional surface damage, reflected in $D_{\text{S,nano}}$, an estimate of the surface area is required. However, as shown in sec. 5.1.1, accurate measurements of A_{nano} are rather difficult. A few different methods for this task were presented in sec. 5.1.1. Mostly only a lower bound for A_{nano} , is obtained which gives a lower limit to the true surface enhancement factor $\gamma_{\text{min}} \leq \gamma$. Correspondingly, the obtained value for the enhancement of the defect density can be considered as an upper limit to the true value $\delta_{\text{max}} \geq \delta$.

7.2.2 Analysis of the Origin of Recombination-Active Surface Defects in b-Si

The γ values were estimated as described in sec. 5.1.1 and are listed in tab. 7.1. This allowed to calculate the defect density enhancement factor δ_{max} of the different b-Si types or etching methods, which is analyzed with respect to the oob reference ($\delta_{\text{max}} \equiv 1$) and the KOH pyramids ($\delta_{\text{max}} = 1.8$). For the ICP-RIE method, δ_{max} is – within the error margins – of the same order of magnitude as the reference ($\delta_{\text{max}} \approx 1$) and appears to be independent of the etching time and pressure. The ICP deep and the ICP shallow b-Si surfaces have about the same δ_{max} but not the same surface enhancement factor γ_{min} . This suggests that the ICP-RIE process can be exploited to produce black silicon surfaces that are almost completely free of additional electronic (sub-)surface defects and supports the stated fulfillment of requirement (vi). This result seems to be in contradiction to the earlier argumentation of a possibly higher level of damage caused by faster plasma ions in the case of the deep b-Si process and to the findings of Schaefer and Lüdemann [134], who reported that cleaning Si by RIE in SF₆ usually does result in sub-surface damage. However, as mentioned in the discussion of requirements (iv) and (v), probably, the combination of the applied RCA cleaning and the thermal PDA treatment removed and/or cured a large fraction of plasma induced defects, respectively. The used annealing temperature for this experiment was $T_{\text{PDA}} = 385$ °C, which was optimal to activate the Al₂O₃ passivation. It was reported that annealing of the plasma treated samples under forming gas at $T_{\text{PDA}} \sim 350$ °C is well suited for the recovery of plasma damage [134]. Even though the Al₂O₃ activation was carried out in air, curing of defects was very probably supported by hydrogen diffusion from the Al₂O₃ film into the near-surface bulk as reported by Dingemans *et al.* [28]. In addition, the mentioned coordination of SiO₂ bonds reached a sufficiently good chemical passivation around $T_{\text{PDA}} = 400$ °C [107]. These results may partially explain, why the optimal PDA temperature was found at $T_{\text{PDA}} = 385$ °C, which on the other hand, should also be associated with the low deposition temperature of $T_{\text{ALD}} = 180$ °C [30]. Interestingly, the relative defect density δ_{max} of the superstructure (KOH + ICP shallow) is reduced after application of ICP-RIE etching on the KOH texture in comparison to KOH pyramids. In the plasma process the surface area is significantly enlarged, while the lifetime is reduced only slightly. The author speculates that the resulting “random” surface termination after ICP-RIE structuring is

⁴²This assumption inherits a possible error source as the capture cross sections of different defects may vastly differ. Therefore, in an enhanced recombination model, σ should be considered. Nevertheless, the factor was omitted because there were no measured σ values available for this work.

either more effectively passivated by Al_2O_3 than the KOH pyramid facets, or may have “(100)-like” properties. The argument is supported by the observations of Liang *et al.*, who found higher recombination rates on polished (111) terminated wafers than on (100) terminated ones after passivation with annealed thermal ALD- Al_2O_3 .

For the optimized MACE samples, δ_{max} is about a factor 5–10 higher than on the oob reference. This defect density enhancement appears to be mostly independent of the etching process including different catalysts (Ag-MACE NPs, Ag-MACE NWs (short and long), Au-MACE NCs) and independent of the laboratory (NREL, WSI, MLU).⁴³ Furthermore, $\delta_{\text{max,MACE}}$ does not significantly depend on the etching time and/or the length of the Ag-MACE NWs, even though the long NWs exhibit a factor of two larger δ_{max} . Note, however, that the estimation of the surface enhancement factor is especially challenging for this type of sample.⁴⁴ Altogether, these findings indicate that a certain optimum has been achieved. These optimization steps can be summarized as follows: First, the nanoporous/fibrous silicon network, which always occurs for MACE-like processes was completely removed during SC1 of the RCA cleaning procedure. Second, the SC1 step dramatically reduces the surface area and defect density and therefore eliminates the photo-luminescence of the fibrous layer [3]. It was also reported, that the lifetime could be increased by about one order of magnitude if SC1 was carried out after MACE and before Al_2O_3 deposition by plasma assisted ALD [3]. Hence, the process has beneficial effects on the MACE structures independent of the catalyst and the metal deposition technique, whereas the underlying crystalline morphology is not significantly altered by the cleaning procedure. Alternatively, dipping the MACE etched samples into KOH for 30 s may have a similar effect on the NW structures [100]. From FTIR measurements it was concluded by Algasinger *et al.* that after SC1 the b-Si has a similar surface termination like a planar c-Si wafer. Concerning the dangling bond density at the Si/SiO₂-interface, a Au-MACE NC-like sample exhibited about 3 times more defects than a planar reference [3], which is in agreement with the upper limit for the surface defect enhancement factor of $\delta_{\text{max}} \approx 5 - 10$, in this work. It is important to note that the optimization of the ALD- Al_2O_3 coating and the successive annealing step at 385 °C was carried out to best suit the ICP-RIE structures [119] and does not necessarily represent an optimum PDA condition for the other b-Si types, that may suffer from a completely different nature of defects. As was recently shown by Mews *et al.*, a-Si:H might be a much better surface coating than Al_2O_3 leading to minority carrier lifetime of about 1.3 ms, which is of the same order of magnitude as the ICP-RIE samples in this work [105].

The macP-Si samples have a significantly higher surface defect density of about $\delta_{\text{max}} \approx 200$. This high value is not completely unexpected since the doping level of the Si wafer is not adequate for the formation of macP-Si. It was chosen for comparability with the other b-Si methods. However, macP-Si growth on p-type Si is only stable for doping levels above 10 Ωcm [21]. Below this doping level, other growth regimes interfere and lead to a rather defect-rich, porous sub-surface structures of the macropores. N-type Si is better suited for this process. Ernst *et al.* obtained reasonably low SRVs in range of 25 $\text{cm/s} \leq S_{\text{eff}} \leq 75 \text{ cm/s}$ for 30 μm thick macroporous membranes [37,38]. This would yield similar values of $\delta_{\text{max}} \sim 3 - 9$ as determined for the MACE process.

⁴³The only exception is the Au-MACE NP sample, which was probably insufficiently cleaned as stated in sec. 7.1.3.

⁴⁴The γ values given in the literature widely deviate from 16 to 190 for NW structures of similar width and periodicity with lengths of 20 μm and 15 μm , respectively.

7.3 Optics of Conformally Coated Black Silicon Nanostructures⁴⁵

In this section, the relation between the different geometric features of the b-Si surfaces and the observed optical characteristics are subject to the discussion. By nanostructuring a Si wafer, the optical reflection losses can be greatly diminished. To understand this, one has to distinguish between two optical effects, as mentioned in sec. 2.1.3. First, a reduction of the refractive index discontinuity at the Si/air-interface leads to a low broad-band surface reflection and is therefore referred to as the anti-reflection (AR) effect. Second, strong scattering of light into oblique propagation angles leads to a high light trapping (LT) efficiency and therefore to a high absorption at the Si band edge. This phenomenon is referred to as the LT effect and predominantly influences the absorption in the NIR spectral range.

For the optical description of characteristic Si features with dimensions well above the wavelength of light (e.g. KOH pyramids), classic ray optics can be used. In contrast, smaller structures than the wavelength of light (like b-Si) require a wave-optical approach. This discussion focuses on the latter, i.e. the b-Si nanostructures. After deducing geometrically relevant factors, first, the AR properties (sec. 7.3.1) and second, the LT properties (sec. 7.3.2) of the samples operating in the wave optics regime are discussed.

To obtain the characteristic length scales of these samples, one dimensional height profiles were extracted from FIB cross sections. From the profiles, the peak-to-valley height, H , was measured and the lateral correlation length, L_c , was determined by fitting a Gaussian function to the one dimensional autocorrelation function of the profiles.⁴⁶ It was taken to be twice the standard deviation of the Gaussian and corresponds approximately to the lateral distance of adjacent peaks and valleys. The geometrical surface parameters (L_c and H) are listed in tab. 7.1 together with the average UV/VIS and NIR absorption, respectively. The latter is also listed as normalized to the Yablonovitch limit. From the cumulative height distribution, the depth profile of the silicon fraction, f , was estimated.⁴⁷ In dependence of the average side-wall profiles, this resulted in more or less “convex” or “concave” rising slopes as shown in fig. 7.4. The Au-MACE NCs and the ICP deep b-Si exhibit a concave depth profile. Their Si fractions increase very slowly at first ($f \leq 30\%$ at $H/2$) and fast towards the bottom of the nanostructures. The other structures exhibit a more convex slope with $f \geq 50\%$ at $H/2$. Note, that these geometrical parameters (L_c , H , and f) could only be extracted from single cross sections with widths of 5 – 10 μm . Therefore, the amount of statistical samples was limited and led to large statistical uncertainties for the geometrical data, especially in case of the correlation length.

7.3.1 Anti-Reflection Properties

The anti-reflection (AR) properties, i.e. the resulting absorption in the UV and VIS range ($300 \leq \lambda \leq 1000$ nm), are vastly different between the individual samples as indicated in tab. 7.1. Presumably, $A_{\text{UV,VIS}}$ is not linked to either one of the geometrical parameters alone. For example, the structures with the shortest and longest correlation lengths, namely the MACE NP and macP-Si samples,

⁴⁵The discussion of this section was in parts published in [119] and [113].

⁴⁶The data were computed by Matthias Kroll at the IAP (FSU Jena) and the results are used with his permission.

⁴⁷The profiles were normalized to the corresponding structure height, H .

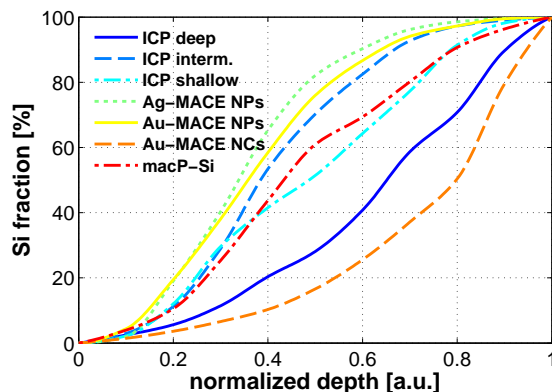


Figure 7.4: Depth profiles of the Si fraction, f , of some b-Si structures as extracted from FIB cross sections.⁴⁶

respectively, exhibit very similar AR properties. Some structures with medium correlation lengths perform significantly better than those, while others, e.g. the shallow and intermediate b-Si, perform significantly worse. The AR properties of the smallest structures result from the “moth-eye” effect [168], which is observed if the lateral feature size of the nanostructures is well below the wavelength of the incoming light. The incident wave then experiences an average refractive index that depends on the silicon volume fraction and makes the Si/air-interface appear rather smooth, which strongly reduces Fresnel reflections [146]. The efficiency of the gradient-index effect depends on the depth of the structure and the effective refractive index profile. Theoretically, the best performance is achieved with a quintic profile that has a continuous first and second derivative and a value of $f = 50\%$ at $H/2$ [146]. However, other profiles may also work well, even at a thickness of about half the incident wavelength, as long as the initial gradient is not too steep (see fig. 7.4). For structures with $L_c \ll \lambda$, the effective refractive index profile could be deduced from the Si volume fraction f by applying an effective medium mixing formula, as proposed by Brüggenmann [14]. Unfortunately, even the smallest of the investigated structures do not fulfill this criterion. Instead, the b-Si nanostructures exhibit some forward scattering in the NIR and most probably even stronger in the VIS and UV spectral region. This means that the structures might appear sub-wavelength from the air side, but not from the silicon side. Hence, the internal dynamics of the structures is far from plane-wave-like and simple effective medium theory is not applicable. Therefore, the effective refractive index profile not only depends on the Si volume fraction f , but also on the correlation length L_c and other geometrical properties, simultaneously. This behavior has been demonstrated by Boden and Bagnall [11], who investigated periodic arrays of Si moth-eye structures and found a strong dependence of the optical properties on the period of the arrays in the sub-wavelength regime. Therefore, it is not possible to quantitatively calculate refractive index profiles from the profiles of the Si fraction. Nevertheless, it is assumed that some qualitative similarities exist. Upon this assumption, it is still possible to develop a qualitative understanding of the AR properties of the different b-Si samples.

The Ag- and Au-MACE NP samples exhibit the shortest correlation lengths of $L_c \approx 30$ nm and 45 nm, respectively. Therefore, they are closest to a real effective medium. However, their rather convex shaped Si volume fraction has a large initial slope and might cause the relatively high residual reflectance of 3% – 4.5% [113]. The absorption spectra of both NP samples shown in fig. 5.15(a) are quite flat and depend only weakly on the wavelength. This indicates that the structure depths

($H \approx 550$ nm) are not the limiting parameter. Otherwise, a performance decrease with increasing wavelength would be expected. The latter is the case for the ICP shallow ($L_c \approx 100$ nm, $H = 590$ nm) and intermediate ($L_c \approx 115$ nm, $H = 550$ nm) b-Si samples and may result from their larger correlation lengths. The estimated correlation lengths of the NW samples are probably highly erroneous due to preparation issues of the cross sections (see fig. A.4 in sec. A.5 of the appendix). For the same reason the Si volume fraction could not be determined. Nevertheless, the author speculates that the rather narrow NWs may still operate close to an effective medium, which, combined with the large depths in the micrometer range probably leads to the very high and wavelength independent UV/VIS absorption. In addition, multiple scattering events may play a role for these structures. The NC structures are equally effective, which is most probably due to their highly concave Si volume depth profile f . Eventually, the NCs may have a more or less optimal correlation length of $L_x \approx 120$ nm, which is roughly in agreement with the findings of Boden and Bagnall [11]. It seems that larger correlation lengths ($L_c \gtrsim 150$ nm) lead to a deterioration of the AR performance even for nanostructures with large peak-to-valley heights H . The latter can be observed for the ICP deep b-Si and the macP-Si structure. The deep b-Si performs better, which may be explained either by the larger H , or the convex depth profile.

As mentioned in sec. 2.1.2, in a true Lambertian layer the light is multiply scattered and the absorption does not depend on the angle of incidence. The angular reflection dependence for non-perpendicular light injection is very robust for the ICP-RIE samples (fig. 5.12). The deep ICP structure is less affected, whereas the reflectance of the shallow structure increases for large incidence angles ($> 45^\circ$). Furthermore, it is expected that the NW samples should show an even higher angular robustness, while the other b-Si morphologies should lead to a similar behavior. The latter is supported by the observations of Huang *et al.* [70], who described improved broadband and quasi-omnidirectional AR properties of randomly distributed Si needles.

It is interesting to note, that the strong absorption dip in the UV region, which was observed for most samples at 370 nm, is associated with the direct band gap of Si. The feature can be interpreted as an indicator for the crystal quality of the sample's surface [3,6]. Since the penetration depth of UV light is very short (≤ 20 nm), the feature is rather surface sensitive. For example, the feature re-appeared in NC-like samples upon removal of the fibrous Si network layer by RCA SC1 [3]. The layer also led to a highly increased SRV, which was recovered in the same step. If this feature could be quantitatively related to the quantum efficiency (EQE or IQE), it may be a useful and easy-to-access indicator to monitor the b-Si surface quality optically.

7.3.2 Light Trapping Properties

The strong band edge absorption of the b-Si samples can be attributed to pronounced scattering at the surface nanostructures [89]. Upon the transition through the structured interface, a significant fraction of the incoming light is scattered into large propagation angles beyond the critical angle of (total) internal reflection. It then takes multiple round trips until the light scatters back into the loss cone and may leave the wafer. As a result the light becomes trapped inside the structure, which efficiently enhances the optical path length, and hence, the probability for absorption [89,114,174]. As mentioned in the previous section, the optically thicker medium offers a larger phase space. Therefore,

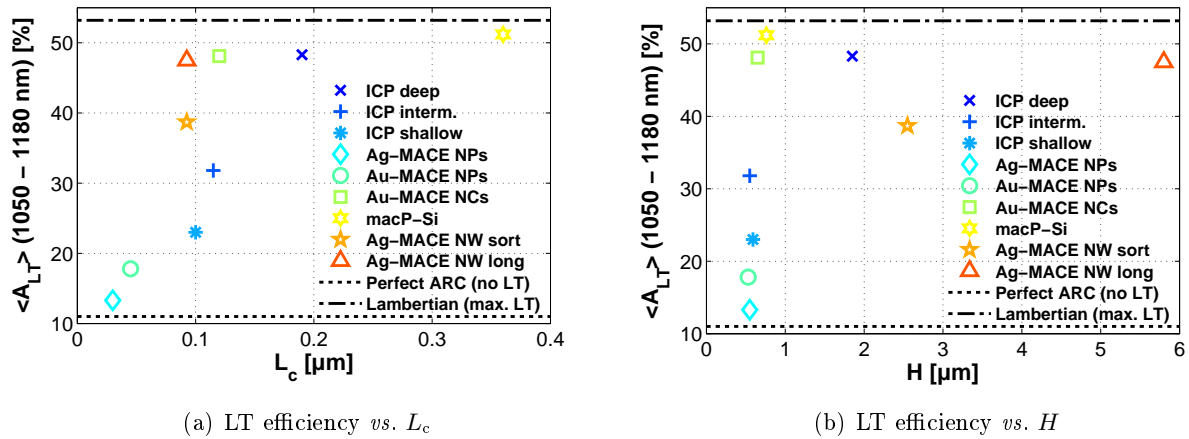


Figure 7.5: Average b-Si absorption in the light-trapping regime *vs.* the correlation length L_c (a) and the peak-to-valley height H (b).

the light is preferably scattered into the slab and not out of it, which leads to the high confinement of weakly absorbed light in the wafer [177]. In turn, the absorption edge for a b-Si wafer is red-shifted by about 90 nm in comparison to the calculated polished Si with perfect ARC but no LT (e.g. fig. 5.3.1).

As shown in fig. 7.5, the LT performance of the samples ($1050 \text{ nm} \leq \lambda \leq 1180 \text{ nm}$) covers the whole range from almost no LT in the case of the MACE NP samples ($A_{LT} \leq 17.8\%$) to nearly Lambertian light trapping ($A_{LT} = 53.2\%$) in the case of the macP-Si sample ($A_{LT} = 51.2\%$). Two general trends are visible in the presented data. First, structures with a large correlation length tend to exhibit a higher LT efficiency than structures with low correlation lengths L_c . Second, between samples with comparable L_c , the ones with higher light trapping absorption A_{LT} profit from a larger peak-to-valley height H . This observation stands in contrast to the electronic demand for low surface area enhancement and explains the described tendency of higher SRV with higher absorption in fig. 7.2. The latter effect is rather pronounced for the MACE NW samples. Due to their large depth, the NWs presumably facilitate multiple scattering, which leads to a better LT despite their low correlation length. This assumption is supported by the fact that true Lambertian surfaces provide multiple scattering events. Expanding the observation towards the ICP shallow and intermediate structures, which possess correlation lengths comparable to the NW samples, the effect is confirmed again. Hence, it can be assumed that the shallow and intermediate ICP-RIE and the MACE NP structures perform poorly because of the low depth ($H < 600 \text{ nm}$). Concentrating on sample pairs of one b-Si type with more or less identical peak-to-valley heights, it becomes obvious, that the LT efficiency strongly increases with increasing correlation length $L_c \lesssim 115 \text{ nm}$. Following this argumentation the ICP deep structure profits from both, the increased correlation length and the large depth. However, the Au-MACE NC sample performs significantly better than the ICP intermediate b-Si despite its comparable depth and only slightly increased correlation length. A possible explanation for this might be the difference in the depth profiles of the silicon material fraction and/or the side-wall angles of the structures as discussed in the previous section. Finally, the macP-Si structure, which exhibits the best LT performance also has the largest correlation length of the investigated samples. Even though it has a more or less convex structure and a moderate depth.

In this discussion, resonant effects, e.g. resonant Mie scattering, were not considered, although those also might occur if the size of an individual feature is in the order of the scaled wavelength. However, due to the stochastic nature of b-Si, it is likely that a small fraction of the features will be resonant at a given wavelength. However, the overall contribution should be small. Altogether, the results of investigated b-Si structures indicate that the correlation length is the key property for efficient light trapping. Structures with a correlation length significantly smaller than the scaled wavelength do not provide substantial scattering. On the other hand, a structure with a correlation length of the order of the scaled wavelength already performs close to the optimum even with a moderate depth of about twice the scaled wavelength. Structures with intermediate correlation lengths appear to provide some scattering which, in turn, seems to depend on the structure's depth and/or sidewall profile. Nevertheless, structures with very large peak-to-valley height and moderate correlation length, like the long NWs, can not keep up with the performance of a structure with a larger correlation length. It is important to note, that the AR efficiency strongly influences the LT efficiency, since only the light which had previously entered into the structure can be trapped.

Residual IR Absorption

Residual absorption below the band gap energy of Si (at $\lambda = 1200$ nm) was observed for almost all structured samples. This effect can mainly be attributed to free carrier absorption due to moderate boron doping of the wafers ($p \sim 3 \cdot 10^{15} - 1.4 \cdot 10^{16} \text{cm}^{-3}$). According to the model proposed by Green [54], the free carrier absorption coefficient at 1200 nm for those doping concentrations is in the range of $1.1 - 5.5 \cdot 10^{-2} \text{cm}^{-1}$. This is about the same order of magnitude as the intrinsic absorption coefficient of Si at this wavelength [54] and would require about 7 – 36 round trips in the 250 μm wafers. Therefore, the experimentally observed absorption-plateau above 1200 nm (not shown) is consistent with free carrier absorption enhanced by light trapping. The effect can be exploited to produce highly NIR/IR light absorbing b-Si [150]. It can not be excluded, however, that multi-phonon processes also play a non-negligible role [48].

Table 7.1: Overview of the passivated b-Si samples and references of the comparison series. Shown are the passivation quality (τ_{eff} , S_{eff}), and the surface enhancement and defect density enhancement factors γ and δ , respectively. Furthermore, the geometric surface parameters and optical performance indicators of the b-Si samples are listed with their overall optical absorption, the relative UV/VIS absorption, and the LT performance (absolute $\langle A_{\text{LT}} \rangle$, and relative to the Lambertian scatterer $\langle A_{\text{LLT}} \rangle$).

| Sample/ Structure | $\tau_{\text{eff}}^{[a]}$ [μs] | $S_{\text{eff,max}}^{[b]}$ [cm^2/s] | $\frac{S_{\text{nano}}[c]}{S_{\text{ref}}}$ [a.u.] | $\gamma_{\text{min}}^{[d]}$ [a.u.] | $\delta_{\text{max}}^{[e]}$ [a.u.] | $L_c^{[f]}$ [μm] | $H^{[g]}$ [μm] | $A_{\text{tot}}^{[h]}$ [% _{abs}] | $A_{\text{UV,VIS}}^{[i]}$ [% _{abs}] | $A_{\text{LT}}^{[j]}$ [% _{abs}] | $\frac{\langle A_{\text{LT}} \rangle [k]}{\langle A_{\text{LLT}} \rangle}$ [% _{rel}] |
|------------------------|--|--|---|---------------------------------------|---------------------------------------|----------------------------------|--------------------------------|---|--|--|---|
| unstructured reference | 3040 | 4.1 | 1 | 1 | 1 | – | – | 60.3 | 71.3 | 6.9 | 13.0 |
| KOH texture | 983 | 12.7 | 3.09 | 1.7 ± 1.7 | 1.8 ± 0.2 | – | – | 85.1 | 91.8 | 48.9 | 91.9 |
| ICP shallow | 1142 | 11.0 | 2.66 | $\approx 2 - 4$ | $\approx 0.9 - 1.3$ | 0.100 | 0.59 | 80.4 | 92.5 | 23.0 | 43.2 |
| ICP intermediate | 1597 | 7.8 | 1.90 | $\approx 2 - 4$ | $\approx 0.6 - 1.0$ | 0.115 | 0.55 | 82.2 | 92.6 | 31.8 | 59.8 |
| ICP deep | 677 | 18.5 | 4.49 | $\approx 5 - 10$ | $\approx 0.5 - 0.9$ | 0.190 | 1.85 | 90.0 | 97.9 | 48.3 | 90.8 |
| ICP superstructure | 891 | 14.0 | 3.41 | $\approx 3.4 - 7$ | $\approx 0.5 - 1.0$ | – | – | 88.8 | 96.0 | 51.0 | 95.9 |
| Au-MACE NCs | 111 | 113 | 27.5 | $\approx 3 - 6$ | $\approx 5.5 - 9$ | 0.120 | 0.65 | 91.3 | 99.4 | 48.1 | 90.4 |
| Ag-MACE NPs | 102 | 122 | 29.7 | $\approx 3 - 5$ | $\approx 6 - 10$ | 0.030 | 0.55 | 80.9 | 95.2 | 13.3 | 25.0 |
| Ag-MACE NWs (short) | 48 | 261 | 63.4 | $\approx 10 - 14$ | $\approx 4.5 - 6$ | $0.085 - 0.100$ | 2.55 | 89.3 | 99.2 | 38.7 | 72.7 |
| Ag-MACE NWs (long) | 9.1 | 1374* | 334 | $\approx 25 - 45$ | $\approx 7 - 13$ | $0.085 - 0.100$ | 5.80 | 91.1 | 99.4 | 47.5 | 89.3 |
| macP-Si | 7.6 | 1635* | 398 | ≈ 2 | ≈ 200 | 0.360 | 0.76 | 89.3 | 96.4 | 51.2 | 96.2 |
| perfect ARC (no LT) | – | – | – | – | – | – | – | 84.4 | 99.5 | 11.0 | 20.7 |
| Lambertian (max. LT) | – | – | – | – | – | – | – | 92.7 | 100 | 53.2 | 100 |

^[a] effective carrier lifetime at $\Delta n = 10^{15} \text{ cm}^{-3}$. The relative error is estimated to be up to 30%. Specific error values are given in tab. 6.1.

^[b] $S_{\text{eff}} \leq S_{\text{eff,max}} = W/2\tau_{\text{eff}}$ was calculated by eqn. (2.26), assuming a wafer thickness of $W = 250 \pm 25 \mu\text{m}$ and infinite bulk lifetime.

^[c] relative SRV enhancement of the structure normalized to the reference (see eqn. (7.3) on p. 93).

^[d] measured or conservatively estimated surface enhancement factor $\gamma_{\text{min}} \leq \gamma_{\text{true}} = A_{\text{nano}}/A_{\text{ref}}$. The relative error is estimated to be lower than 50%.

^[e] estimation of the maximum number of total recombination active defects which were introduced by black-etching, normalized to the reference: $\delta_{\text{max}} \geq \delta_{\text{max}} = D_{\text{S,nano}}/D_{\text{S,ref}}$. The true number of recombination active defects is expected to be inferior to δ_{max} . In accordance to error propagation from [d], the error of δ_{max} is estimated to be $\leq 40\%$.

^[f] lateral correlation length of the b-Si structures estimated from one dimensional FIB cuts as explained in sec. 7.3.

^[g] peak-to-valley height estimated from one dimensional FIB cuts as explained in sec. 7.3.

^[h] A_{tot} represents the total integrated absorption in the spectral range of $300 \text{ nm} \leq \lambda \leq 1180 \text{ nm}$.

^[i] $A_{\text{UV/VIS}}$ represents the total integrated absorption in the UV/VIS range ($300 \text{ nm} \leq \lambda \leq 1000 \text{ nm}$).

^[j] A_{LT} represents integrated absorption in the spectral range of $1050 \text{ nm} \leq \lambda \leq 1180 \text{ nm}$. Absorption in this spectral regime is mainly attained by light-trapping in the structures.

^[k] relative absorption: values of column [j] are re-normalized to the absolute absorption of $\langle A_{\text{LLT}} \rangle = 53.2\%$ of the Lambertian scatterer.

* These S_{eff} values may be influenced by either a deteriorated bulk lifetime, or could be limited due to minority carrier diffusion processes.

Chapter 8

Summary and Conclusions

8.1 Summary and Conclusions

This work presented an overview of the most common black silicon (b-Si) fabrication methods, their resulting surface morphologies, the concomitant optical response functions, and simultaneously, the feasibility to effectively passivate the b-Si nanostructures by conformal coatings with thermal ALD- Al_2O_3 and PECVD- SiN_x as well as the resulting interface microstructure. The investigated black etching methods were dry reactive ion etching in an inductive coupled plasma (ICP-RIE) under SF_6/O_2 atmosphere, which represents the main focus of this work, metal assisted chemical etching (MACE) with Ag and Au catalysts, and electrochemical etching of macroporous silicon (macP-Si) in low resistivity ($1 \Omega\text{cm}$) p-type material. It was shown, that for these ALD- Al_2O_3 passivated b-Si types no globally valid correlation of the optical and electronic surface properties exists. However, a tendency towards higher surface recombination velocity (SRV) with higher absorption was denoted within each b-Si method. The highest lifetimes of the groups differed by full orders of magnitude from ICP-RIE ($\approx 1 \text{ ms}$) over MACE ($\approx 0.1 \text{ ms}$) to macP-Si ($\approx 0.01 \text{ ms}$).

A model was proposed to differentiate between the contributions to b-Si surface recombination of the surface area enhancement and the defect density enhancement that resulted from black etching. Analysis of the different b-Si types revealed that: **(a)** The *(sub-)surface damage* introduced by the nanostructuring method must be minimized. The ICP-RIE method yielded virtually damage-free b-Si surfaces with defect densities as low as in the planar reference. As a result, the highest lifetime of 1.6 ms could be attained, which translated into an effective SRV of only $S_{\text{eff}} \leq 7.8 \text{ cm/s}$ for the ICP intermediate b-Si sample. The ICP b-Si samples even outperformed the alkaline textured substrates. However, by optimizing the post processing of the other b-Si types, similar results might be possible in the near future. **(b)** The *surface area enhancement* should be kept as low as possible. However, the nanostructure morphology must be designed for an optimal conjunction of anti-reflection (AR) and light trapping (LT) properties. The latter was best fulfilled for the Au-MACE nanocone structures, which exhibited the highest total absorption throughout the absorbing range of Si ($300 \text{ nm} \leq \lambda \leq 1180 \text{ nm}$) and captured 98.5% of the theoretically possible $2n^2$ limit of a bifacial Lambertian surface. Simultaneously, an effective SRV of $S_{\text{eff}} \leq 113 \text{ cm/s}$ was achieved, which, according to the solar cell device simulations by PC1D, is acceptable for high efficiency solar cell concepts.

Six requirements for the effective b-Si surface passivation were formulated, and could be positively evaluated for ALD- Al_2O_3 on the ICP-RIE b-Si samples. **(i)** The dielectric layer must be optimally suited to passivate unstructured and/or KOH textured Si surfaces, which was a given for ALD- Al_2O_3 prior to this work. **(ii)** The passivation stack needs to be applied absolutely conformal and cover the whole surface area. Obviously, high conformality was achieved for ALD- Al_2O_3 on all b-Si types including the extremely narrow Ag-MACE fabricated nanopore samples with lateral correlation lengths of $L_c \approx 30$ nm. PECVD SiN_x coatings on ICP deep b-Si did not fulfill this requirement. **(iii)** The application of the passivation scheme must not change the optical response function. ALD- Al_2O_3 layers with thicknesses up to $d_{\text{Al}_2\text{O}_3} \approx 50$ nm did not significantly influence the b-Si optics, while thinner layers ($d_{\text{Al}_2\text{O}_3} \approx 30$ nm) led to an additional AR effect in the blue spectral region. At the same time, the passivating effect saturated for layer thicknesses of $d_{\text{Al}_2\text{O}_3} \geq 30$ nm. Hence, a sufficiently large process window was found to enable effective b-Si surface passivation without afflicting the optical features. **(iv)** It is important to keep the process temperatures in an optimal corridor to avoid the possible in-diffusion of contaminants but enable post-deposition annealing of defects, simultaneously. It was found that both is possible by a combination of low temperature ALD deposition ($T_{\text{ALD}} = 180$ °C) and moderate post-deposition annealing temperature ($T_{\text{PDA}} \approx 385$ °C). **(v)** Since each b-Si method yields a slightly different sub-surface damage, the damage removal steps and the surface passivation layer have to be optimized for each b-Si type separately. **(vi)** Finally, the b-Si method must be tuned to result in virtually damage-free surfaces, as mentioned above. The results demonstrated that the ALD- Al_2O_3 passivation mechanism is truly strong enough to boost the lifetime of minority charge carriers in b-Si nanostructures toward the theoretical limit of Auger recombination, which according to Green is the most severe and therefore ultimate limitation to solar cell efficiency. Hence, ALD- Al_2O_3 offers a perfect combination for the passivation of b-Si surfaces. The developed optimal passivation scheme consists of three steps. **(I)** RCA cleaning with chemicals of sufficiently high purity, *first*, helped to reduce surface damage and contaminations to a minimum level. *Second*, the surface was conditioned with an optimally suited ultrathin and highly homogeneous SiO_x layer (optimally $d_{\text{SiO}_x} \leq 1.3$ nm). **(II)** The deposition of a thin (≈ 30 nm) and highly conformal Al_2O_3 passivation layer by thermal ALD provided all further prerequisites to an effective b-Si surface passivation. **(III)** The thermal activation of the passivation stack at adequately low post-deposition annealing (PDA) temperature was essential. It was found that the PDA treatment led to a high coordination of Si–O bonds and the formation of the field effect passivation. These processes are most probably supported by the saturation of dangling bonds by –H atoms provided by the Al_2O_3 layer. It appeared plausible that the PDA treatment helped to cure a rather large fraction of (sub-)surface damage in the b-Si surfaces.

The analysis and corresponding simulations of the optical properties of the different b-Si methods revealed that the light trapping (LT) performance primarily depends on the lateral correlation length, i.e. the lateral peak-to-valley distance of the b-Si features, whereby structures with a large correlation length tend to perform better. This trend was observed to hold at least for feature sizes up to those of the macroporous Si structure ($L_c \approx 360$ nm). Simultaneously, larger nanostructure heights, H , also appeared to be optically favorable, which stands in contrast to the electronic demand for low surface area enhancement and explains the described tendency of higher SRV with higher absorption. A good combination of both factors allowed almost Lambertian LT at moderate correlation lengths and

heights. The dependence of the anti-reflection (AR) performance on the geometrical surface properties of the b-Si surfaces was found to be more complicated. The depth profile of the Si volume fraction was found to be most important and should be of convex shape when traversing the air/Si-interface. However, a good combination of the correlation length and the peak-to-valley height appeared to be necessary to obtain effective forward scattering of light. It seemed that structures with correlation lengths around ≈ 100 nm perform best, if they exhibited either a convex Si depth profile or a sufficiently large structure depth H . Structures with larger correlation lengths suffered from increased back-scattering and structures with smaller correlation lengths tended to exhibit convex shaped effective index gradients. An important finding is that optically, the optimum overall performance can only be obtained if LT is achieved without affecting the AR properties. Consequently, the structures exhibiting the highest integrated absorption are not those with the best LT, but those with the best AR properties and some intermediate LT.

The height of the structures H is less critical for the optical properties and can be in the range of 500 nm to 5 μm without effecting neither the AR nor the scattering properties, significantly. However, the height H and the corresponding surface enhancement factor γ are strongly influencing the surface recombination velocity S_{eff} , and thus, the minority carrier lifetime. The analysis of the electronic properties of the different b-Si types revealed that the critical parameters are the (sub-)surface damage δ introduced by the nanostructuring method and the surface enhancement factor γ . It was shown that for the used passivation scheme, the ICP-RIE method leads to a surface damage comparable to that of the reference wafer. Hence, the surface enhancement factor γ , i.e., the height H is the dominant parameter limiting the minority carrier lifetime. Since the height H is not limiting to the optical properties, a combined electro-optic optimum is about $H \approx 500$ nm.

The achieved level of passivation on b-Si by the presented passivation scheme is rather high and comparable to the values produced in the literature. Therefore, the findings of this work will enable the fabrication of high efficiency b-Si solar cells in the near future.

8.2 Outlook

Besides the just solved passivation issue, on the way to fully integrated b-Si solar cells many more challenges have to be tackled. One of the first questions concerns the emitter formation. The classical high temperature diffusion processes for B or P violate the requirement for low temperature processing of b-Si. Furthermore, such processes behave very different on b-Si than they do on polished and/or pyramid-like textured substrates [112, 128, 142]. Therefore, alternatives such as hetero-junction (e.g. SIS, MIS or HIT)¹ concepts should be pursued. Next, the contact formation on the rough nanostructures also represents a challenging issue that could be resolved together with the emitter question by the approach of Zeigler *et al.* using b-Si as the passivated front texture on an interdigitated back-junction back-contact solar cell [186].

To fully exploit b-Si in solar cells, the junction should to be formed conformally around nanostructures. Therefore, the SIS, MIS, or HIT concepts are believed to gain the highest efficiencies on thin b-Si absorbers. However, at the moment, the deposition techniques for these materials do not allow highly conformal film deposition with precise control over the thickness and other important physical parameters, such as the work function and the optical absorptance of the junction forming layer. It was demonstrated that ALD of thin films is optimally suited to coat and passivate complex 3d nanostructured surfaces. Hence, it is possible to use this technology to build other electrically active layers for solar cell functionalization on substrates that are optimized for opto-electronic performance. Plasma enhanced (PE)ALD usually shows better passivation performance. Therefore, it would be advantageous if the process could be adjusted to conformally cover the b-Si surfaces. In addition, a variety of materials can be deposited by PEALD and ALD processes that would enable applications of b-Si in many more ways than only surface passivation in photovoltaic applications. Conceivably, advanced material design might enable the possibility to tailor the work function and barrier height to create an appropriate oxide for an optimized hetero-junction solar cell with an actual 3-dimensional emitter. The nanostructures could also be exploited for water splitting if coated by TiO_x . If anyway possible, an ALD process to deposit true a-Si:H layers or alternative materials with similar properties would be desirable. Such ALD composites would be able to tackle many of the mentioned challenges above and hetero-junction solar cells with extremely high V_{oc} and very high efficiencies should result. An extremely important topic of research on the way to the industrial implementation of b-Si solar cells will be the ICP-RIE fabrication of b-Si at elevated temperatures. SiO_xF_y evaporates (or decomposes) at temperatures above ≈ 0 °C [104]. Therefore, it is believed that b-Si etching at room temperature might not be possible. However, to achieve a reliable b-Si plasma process at room temperature is of enormous interest to the industry, because cryo-processes are much too expensive concerning cost of ownership. Power consumption due to cooling is a tremendous matter of expense in a high throughput process and devastating to the environment. Therefore, the topic should be pursued to make b-Si production feasible at an industrial scale.

A promising approach may be laser ablation of the Al_2O_3 passivation from b-Si surfaces, which is commonly used in the PV industry to locally open passivating layers. It was found that the process may result in well defined local openings with vanishing surface roughness on ICP-RIE samples (not

¹Semiconductor Insulator Semiconductor, Metal Insulator Semiconductor, or Hetero-junction with Intrinsic Thin layer concepts

shown). This way, it might be possible to contact the b-Si surfaces and/or to form locally highly doped emitters simultaneously.

A much more academic topic may consist of a more thorough investigation of the impact of field effect passivation by ALD- Al_2O_3 on b-Si surfaces. A deeper understanding of the passivation mechanism will be essential to further improve the interface quality and properties and may advance the understanding of the origin of field effect passivation, which up to this point has not been fully understood on unstructured surfaces either.

Last but not least it is to note that, unfortunately, in this work the light-trapping performance and passivation quality of the b-Si types on extremely thin wafers could not be investigated due to a lack of available substrates ($W \leq 50 \mu\text{m}$). According to the calculations of Kroll *et al.* a wafer thickness of $50 \mu\text{m}$ would yield an estimated solar cell efficiency of 24.5% and 23.8% for the deep and shallow b-Si structures, respectively if the bulk lifetime was $300 \mu\text{s}$ [90]. However, even though many concepts for thin wafer production are under development, thin Si material was not readily available at the time this work was carried out.

The combination of ultra-thin wafers with optimized b-Si surfaces that can be passivated by ALD- Al_2O_3 , e.g. in combination with an adequate emitter concept may ultimately lead to the predicted high efficiency b-Si solar cells to which this work has contributed a small, but essential step.

Bibliography

- [1] V. Afanas'ev, J. De Nijs, P. Balk, and A. Stesmans. Degradation of the thermal oxide of the si/sio₂/al system due to vacuum ultraviolet irradiation. *Journal of applied physics*, 78(11):6481–6490, 1995.
- [2] G. Agostinelli, A. Delabie, P. Vitanov, Z. Alexieva, H. Dekkers, S. D. Wolf, and G. Beaucarne. Very low surface recombination velocities on p-type silicon wafers passivated with a dielectric with fixed negative charge. *Sol. Energy Mater. Sol. Cells*, 90(18-19):3438, 2006.
- [3] M. Algasinger, F. Werner, S. Koynov, and R. Brendel. Improved black silicon for photovoltaic applications. *Advanced Energy Materials*, 3(8):1068–1074, 2013. article in press.
- [4] American Society for Testing and Materials (ASTM). Terrestrial reference spectra for photovoltaic performance evaluation. (online accessed: 2013-04-30), May 2011.
- [5] X. Ao, X. Tong, D. S. Kim, L. Zhang, M. Knez, F. Müller, S. He, and V. Schmidt. Black silicon with controllable macropore array for enhanced photoelectrochemical performance. *Appl. Phys. Lett.*, 101:111901, 2012.
- [6] D. E. Aspnes, A. A. Studna, and E. Kinsbron. Dielectric properties of heavily doped crystalline and amorphous silicon from 1.5 to 6.0 eV. *Phys. Rev. B*, 29:768–779, 1984.
- [7] P. Banerjee, W.-J. Le, K.-R. Bae, S. B. Lee, and G. W. Rubloff. Structural, electrical, and optical properties of atomic layer deposition Al-doped ZnO films. *Journal of Applied Physics*, 108:043504, 2010.
- [8] A. Bielawny, J. Üpping, P. T. Miclea, R. B. Wehrspohn, C. Rockstuhl, F. Lederer, M. Peters, L. Steidl, R. Zentel, S.-M. Lee, M. Knez, A. Lambertz, and R. Carius. 3D photonic crystal intermediate reflector for micromorph thin-film tandem solar cell. *physica status solidi (a)*, 205(12):2796–2810, November 2008.
- [9] A. Birner, R. Wehrspohn, U. Gösele, and K. Busch. Silicon-based photonic crystals. *Advanced Materials*, 13(6):377–388, 2001.
- [10] A. W. Blakers, A. Wang, A. M. Milne, J. Zhao, and M. A. Green. 22.8% efficient silicon solar cell. *Applied Physics Letters*, 55(13):1363–1365, 1989.
- [11] S. A. Boden and D. M. Bagnall. Tunable reflection minima of nanostructured antireflective surfaces. *Appl. Phys. Lett.*, 93:133108, 2008.
- [12] H. M. Branz, V. E. Yost, S. Ward, K. M. Jones, B. To, and P. Stradins. Nanostructured black silicon and the optical reflectance of graded-density surfaces. *Appl. Phys. Lett.*, 94:231121, 2009.
- [13] R. Brendel and M. Ernst. Macroporous Si as an absorber for thin-film solar cells. *physica status solidi (RRL)–Rapid Research Letters*, 4(1-2):40–42, 2010.
- [14] V. D. Bruggeman. Berechnung verschiedener physikalischer konstanten von heterogenen substanzen. i. dielektrizitätskonstanten und leitfähigkeiten der mischkörper aus isotropen substanzen. *Annalen der physik*, 416(7):636–664, 1935.
- [15] Cambridge Nanotech. Animated video on the surface reactions in Al₂O₃ ALD. <http://www.cambridgenanotech.com/ald-animation>.
- [16] Cambridge Nanotech. An introduction to principles and applications of atomic layer deposition. Presentation.
- [17] P. Campbell. Enhancement of light absorption from randomizing and geometric textures. *J. Opt. Soc. Am. B*, 10(12):2410, 1993.

- [18] P. Campbell and M. A. Gereen. Light trapping properties of pyramidally textured surfaces. *J Appl Phys*, 62(1):243, 1987.
- [19] Carl Roth GmbH + Co. KG. Flusssäure supra-qualität - ROTIPURAN [®] supra ~ 48%. [Online](#), (accessed: 31.07.2014), 2014.
- [20] Carl Roth GmbH + Co. KG. Flusssäure ultra-qualität - ROTIPURAN [®] ultra ~ 48%. [Online](#), (accessed: 31.07.2014), 2014.
- [21] J.-N. Chazalviel, F. Ozanam, N. Gabouze, S. Fellah, and R. Wehrspohn. Quantitative analysis of the morphology of macropores on low-doped p-si minimum resistivity. *Journal of the Electrochemical Society*, 149(10):C511–C520, 2002.
- [22] D. A. Clugston and P. A. Basore. PC1D version 5: 32-bit solar cell modeling on personal computers. In *Photovoltaic Specialists Conference, 1997., Conference Record of the Twenty-Sixth IEEE*, pages 207–210. IEEE, 1997. (Version 5.9).
- [23] H. Craighead, R. Howard, and D. Tennant. Textured thin-film si solar selective absorbers using reactive ion etching. *Applied Physics Letters*, 37(7):653–655, 1980.
- [24] C. Crouch, J. Carey, M. Shen, E. Mazur, and F. Génin. Infrared absorption by sulfur-doped silicon formed by femtosecond laser irradiation. *Appl. Phys. A*, 79:1635–1641, 2004.
- [25] A. Cuevas and D. Macdonald. Measuring and interpreting the lifetime of silicon wafers. *Solar Energy*, 76(1–3):255–262, 2003. .
- [26] H. Deckman, C. Roxlo, and E. Yablonovitch. Maximum statistical increase of optical absorption in textured semiconductor films. *Optics letters*, 8(9):491–493, 1983.
- [27] D. Dimova Malinovska, M. S. Vassileva, N. Tzenov, and M. Kamenova. Preparation of thin porous silicon layers by stain etching. *Thin Solid Films*, 297(1-2):9–12, 1997.
- [28] G. Dingemans, W. Beyer, M. C. M. van de Sanden, and W. M. M. Kessels. Hydrogen induced passivation of Si interfaces by Al₂O₃films and SiO₂/Al₂O₃stacks. *Appl. Phys. Lett.*, 97:152106, 2010.
- [29] G. Dingemans, A. Clark, J. A. van Delft, M. C. M. van de Sanden, and W. M. M. Kessels. Er³⁺ and si luminescence of ald er-doped Al₂O₃ films on si(100). *J. Appl. Phys.*, 109:113107, 2011.
- [30] G. Dingemans, F. Einsele, W. Beyer, M. C. M. van de Sanden, and W. M. M. Kessels. Influence of annealing and Al₂O₃ properties on the hydrogen-induced passivation of the Si/SiO₂ interface. *J. Appl. Phys.*, 111:093713, 2012.
- [31] G. Dingemans and E. Kessels. Status and prospects of Al₂O₃-based surface passivation schemes for silicon solar cells. *J. Vac. Sci. Technol. A*, 30(4):040802, 2012.
- [32] G. Dingemans and W. M. M. Kessels. Recent progress in the development and understanding of silicon surface passivation by aluminum oxide for photovoltaics. In *25th European Photovoltaic Solar Energy Conference Valencia, Spain*, volume 1083, 2010.
- [33] G. Dingemans, R. Seguin, P. Engelhart, M. C. M. van de Sanden, and W. M. M. Kessels. Silicon surface passivation by ultrathin Al₂O₃ films synthesized by thermal and plasma atomic layer deposition. *Phys. Status Solidi RRL*, 4(1-2):10, November 2010.
- [34] G. Dingemans, N. M. Terlinden, M. A. Verheijen, M. C. M. van de Sanden, and W. M. M. Kessels. Controlling the fixed charge and passivation properties of Si(100)/Al₂O₃ interfaces using ultrathin SiO₂ interlayers synthesized by atomic layer deposition. *J. Appl. Phys.*, 110:093715, 2011.
- [35] W. P. Dumke. Spontaneous radiative recombination in semiconductors. *Phys. Rev.*, 105(1):139, 1957.
- [36] S. J. Eisele, T. C. Röder, J. R. Köhler, and J. H. Werner. 18.9 *Appl. Phys. Lett.*, 95(13):133501, 2009.
- [37] M. Ernst and R. Brendel. Macroporous silicon solar cells with an epitaxial emitter. *IEEE Journal of Photovoltaics*, 3(2):723–729, 2013.
- [38] M. Ernst, R. Brendel, R. Ferré, and N.-P. Harder. Thin macroporous silicon heterojunction solar cells. *physica status solidi (RRL)–Rapid Research Letters*, 6:187–189, 2012.

- [39] M. Ernst, R. Brendel, R. Ferré, N.-P. Harder, and S. Kajari-Schröder. Macroporous silicon as an absorber for thin heterojunction solar cells. *Photovoltaic Specialists Conference (PVSC), 2012 38th IEEE*, 38:001040–001045, 2012.
- [40] P. M. Fahey, P. Griffin, and J. Plummer. Point defects and dopant diffusion in silicon. *Reviews of modern physics*, 61(2):289, 1989.
- [41] K. Fuchsels, A. Bingel, N. Kaiser, and A. Tünnermann. Transparent conductive oxides for nano-SIS solar cells. In *Proc. SPIE*, number 8065-0B in 8065, 2011.
- [42] K. Fuchsels, M. Kroll, T. Käsebier, M. Otto, T. Pertsch, E.-B. Kley, R. B. Wehrspohn, N. Kaiser, and A. Tünnermann. Black silicon photovoltaics. In R. B. Wehrspohn, editor, *Proc. SPIE*, number 8438-21 in 8438, 2012.
- [43] K. Fuchsels, M. Kroll, M. Otto, M. Steglich, A. Bingel, T. Käsebier, T. Pertsch, and A. Tünnermann. *Light trapping concepts for silicon solar cells*, chapter Black Silicon Photovoltaics, page (pending for publication). Wiley, 2014.
- [44] K. Fuchsels, U. Schulz, N. Kaiser, T. Käsebier, E.-B. Kley, and A. Tünnermann. Nanostructured SIS Solar cells. In R. B. Wehrspohn, editor, *Proc. SPIE*, number 7725-02 in 7725, 2010.
- [45] S. M. George. Atomic layer deposition: An overview. *Chemical Reviews*, 110:111–131, 2010.
- [46] B. Gesemann, A. Hackner, G. Müller, and R. Wehrspohn. Large scale fabrication of ordered silicon nanotip-arrays used for gas ionization in ion mobility spectrometers. *IEEE Transactions on Nanotechnology*, 10(1):50–52, 2010.
- [47] T. Gimpel, I. Höger, F. Falk, W. Schade, and S. Kontermann. Electron backscatter diffraction on femtosecond laser sulfur hyperdoped silicon. *Appl. Phys. Lett.*, 101:111911, 2012.
- [48] J. Gittleman, E. Sichel, H. Lehmann, and R. Widmer. Textured silicon: A selective absorber for solar thermal conversion. *Applied Physics Letters*, 35(10):742–744, 1979.
- [49] D. Graf, M. Grundner, R. Schulz, and L. Muhlhoff. Oxidation of hf-treated si wafer surfaces in air. *Journal of applied physics*, 68(10):5155–5161, 1990.
- [50] A. Graff. FEI TEM/STEM TITAN³ G2 60-300. (unpublished).
- [51] M. A. Green. Limits on the open-circuit voltage and efficiency of silicon solar cells imposed by intrinsic auger processes. *Electron Devices, IEEE Transactions on*, 31(5):671–678, 1984.
- [52] M. A. Green. Limiting efficiency of bulk and thin-film silicon solar cells in the presence of surface recombination. *Progress in Photovoltaics: Research and Applications*, 7(4):327–330, 1999.
- [53] M. A. Green. Lambertian light trapping in textured solar cells and light-emitting diodes: analytical solutions. *Prog. Photovoltaics Res. Appl.*, 10(4):235–241, 2002.
- [54] M. A. Green. Self-consistent optical parameters of intrinsic silicon at 300 k including temperature coefficients. *Sol. Energy Mater. Sol. Cells*, 92(11):1305–1310, 2008.
- [55] K. Grigoros, V.-M. Airaksinen, and S. Franssila. Coating of nanoporous membranes: atomic layer deposition versus sputtering. *Journal of Nanoscience and Nanotechnology*, 8:8, 2008.
- [56] M. D. Groner, F. H. Fabreguette, J. W. Elam, and S. M. George. Low-temperature Al₂O₃ atomic layer deposition. *Chem. Mater.*, 16:639, 2004.
- [57] K. Hagedorn, C. Forgacs, S. Collins, and S. Maldonado. Design considerations for nanowire heterojunctions in solar energy conversion/storage applications. *J. Phys. Chem. C*, 114:12010–12017, 2010.
- [58] M. Halbwx, T. Sarnet, P. Delaporte, M. Sentis, H. Etienne, F. Torregrosa, V. Vervisch, I. Perichaud, and S. Martinuzzi. Micro and nano-structuration of silicon by femtosecond laser: Application to silicon photovoltaic cells fabrication. *Thin Solid Films*, 516(20):6791–6795, 2008.
- [59] R. N. Hall. Electron-hole recombination in germanium. *Phys. Rev. Lett.*, 87:387, 1952.
- [60] L. Hemstreet. Electronic states of simple-transition-metal impurities in silicon. *Physical review B*, 15(2):834, 1977.
- [61] F. J. Henley. Kerf-free wafering: Technology overview and challenges for thin pv manufacturing. In *Photovoltaic Specialists Conference (PVSC), 2010 35th IEEE*, pages 001184–001192. IEEE, 2010.

- [62] R. Hezel and K. Jaeger. Low-temperature surface passivation of silicon for solar cells. *J. Electrochem. Soc.*, 136:518–523, 1989.
- [63] B. Hoex, M. Bosman, N. Nandakumar, and W. Kessels. C-si surface passivation by aluminium oxide studied with electron energy loss spectroscopy. *physica status solidi (RRL) - Rapid Research Letters*, 7:937–941, 2013.
- [64] B. Hoex, J. J. H. Gielis, M. C. M. van de Sanden, and W. M. M. Kessels. On the c-Si surface passivation mechanism by the negative-charge-dielectric Al_2O_3 . *J. Appl. Phys.*, 104:113703, 2008.
- [65] B. Hoex, S. B. S. Heil, E. Langereis, M. C. M. van de Sanden, and W. M. M. Kessels. Ultralow surface recombination of c-Si substrates passivated by plasma-assisted atomic layer deposited Al_2O_3 . *Appl Phys Lett*, 89(042112):042112, July 2006.
- [66] B. Hoex, J. Schmidt, R. Bock, P. P. Altermatt, M. C. M. van de Sanden, and W. M. M. Kessels. Excellent passivation of highly doped p-type si surfaces by the negative-charge-dielectric Al_2O_3 . *Applied Physics Letters*, 91:112107, 2007.
- [67] B. Hoex, M. C. M. van de Sanden, J. Schmidt, R. Brendel, and W. M. M. Kessels. Surface passivation of phosphorus-diffused n+-type emitters by plasma-assisted atomic-layer deposited Al_2O_3 . *Phys. Status Solidi RRL*, 6(1):4–6, 2012.
- [68] E. M. Honeywell. Product specifications for hydrofluoric acid (HF). [Online](#), (accessed: 31.07.2014), 2003.
- [69] P. Hoyer, M. Theuer, R. Beigang, and E.-B. Kley. Terahertz emission from black silicon. *Applied Physics Letters*, 93(091106):1–3, 2008.
- [70] Y.-F. Huang, S. Chattopadhyay, Y.-J. Jen, C.-Y. Peng, T.-A. Liu, Y.-K. Hsu, C.-L. Pan, H.-C. Lo, C.-H. Hsu, Y.-H. Chang, C.-S. Lee, K.-H. Chen, and L.-C. Chen. Improved broadband and quasi-omnidirectional anti-reflection properties with biomimetic silicon nanostructures. *Nat. Nanotechnol.*, 2:770–774, 2007.
- [71] Z. Huang, N. Geyer, P. Werner, J. de Boer, and U. Gösele. Metal-assisted chemical etching of silicon: A review. *Adv. Mater.*, 23:285–308, 2011.
- [72] D. Iencinella, E. Centurioni, R. Rizzoli, and F. Zignani. An optimized texturing process for silicon solar cell substrates using tmah. *Solar energy materials and solar cells*, 87(1):725–732, 2005.
- [73] Y. Inomata, K. Fukui, and K. Shirasawa. Surface texturing of large area multicrystalline silicon solar cells using reactive ion etching method. *Solar energy materials and solar cells*, 48(1):237–242, 1997.
- [74] E. P. Ivanova, J. Hasan, H. K. Webb, G. Gervinskis, S. Juodkazis, V. K. Truong, A. H. Wu, R. N. Lamb, V. A. Baulin, G. S. Watson, et al. Bactericidal activity of black silicon. *Nature Communications*, 4(2838):, 2013.
- [75] S. Jakschik, E. Erben, F. Benner, S. Kupke, I. Dirnstorfer, M. Rose, I. Endler, and T. Mikolajick. Dielectric backside passivation - improvements by dipole optimization. *Proceedings of the 26th EU PVSEC, Hamburg, Germany, 5–9 September*, 26:2252, 2011.
- [76] H. Jansen, M. de Boer, R. Legtenberg, and M. Elwenspoek. The black silicon method: a universal method for determining the parameter setting of a fluorine-based reactive ion etcher in deep silicon trench etching with profile control. *J. Micromech. Microeng.*, 5(2):115, 1995.
- [77] R. S. Johnson, G. Lucovsky, and I. Baumvol. Physical and electrical properties of noncrystalline Al_2O_3 prepared by remote plasma enhanced chemical vapor deposition. *Journal of vacuum science and technology A*, 19:1353–1360, 2001.
- [78] B. D. Johs, J. A. Woollam, C. M. Herzinger, J. N. Hilfiker, R. A. Synowicki, and C. L. Bungay. Overview of variable-angle spectroscopic ellipsometry (vase): II. advanced applications. In *Society of Photo-Optical Instrumentation Engineers (SPIE) Conference Series*, volume 1, pages 29–58, 1999.
- [79] W. Kern. The evolution of silicon wafer cleaning technology.pdf. *J. Electrochem. Soc.*, 137(6):1887–1892, 1990.
- [80] W. Kern and D. Puotinen. The rca-clean. *RCA Review*, 31:197, 1970.
- [81] M. J. Kerr and A. Cuevas. General parameterization of auger recombination in crystalline silicon. *Journal of Applied Physics*, 91(4):2473–2480, 2002.

- [82] S. Kühnhold, P. Saint-Cast, B. Kaffe, M. Hofmann, F. Colonna, and M. Zacharias. High-temperature degradation in plasma-enhanced chemical vapor deposition al_2o_3 surface passivation layers on crystalline silicon. *Journal of Applied Physics*, 116(5):054507, 2014.
- [83] M. Knez, K. Nielsch, and L. Niinistö. Synthesis and surface engineering of complex nanostructures by atomic layer deposition. *Adv. Mater.*, 19:3425, 2007.
- [84] S. Kontermann, A. L. Baumann, T. Gimpel, K. Guenther, A. Ruibys, U. Willer, and W. Schade. Structural and optical property tailoring of black silicon with fs-laser pulses. In *Mater. Res. Soc. Symp. Proc.*, volume 1405, 2012.
- [85] S. Koynov, M. S. Brandt, and M. Stutzmann. Black nonreflecting silicon surfaces for solar cells. *Appl. Phys. Lett.*, 88:203107, 2006.
- [86] S. Koynov, M. S. Brandt, and M. Stutzmann. Black multi-crystalline silicon solar cells. *pyhys. stat. sol. (RRL)*, 1:R53--R55, 2007.
- [87] S. Koynov, M. S. Brandt, and M. Stutzmann. Black thin film silicon. *J. Appl. Phys.*, 110:043537, 2011.
- [88] M. Kroll, T. Käsebier, M. Otto, and T. Pertsch. Rie black silicon for photovoltaic applications. *OSA meeting Optical Nanostructures and Advanced Materials for Photovoltaics (PV), Tucson, Arizona, USA*, 2013.
- [89] M. Kroll, T. Käsebier, M. Otto, R. Salzer, and R. Wehrspohn. Optical modeling of needle like silicon surfaces produced by an ICP-RIE process. In R. B. Wehrspohn, editor, *Proc. SPIE*, number 7725-05 in 7725, 2010.
- [90] M. Kroll, M. Otto, T. Käsebier, K. Füchsel, R. B. Wehrspohn, E.-B. Kley, A. Tünnermann, and T. Pertsch. Black silicon for solar cell applications. In R. B. Wehrspohn, editor, *Proc. SPIE*, number 8438-42 in 8438, 2012.
- [91] A. Langner, F. Müller, and U. Gösele. *Molecular- and Nano-Tubes*, chapter Macroporous Silicon, pages 431–460. Springer, 2011.
- [92] S.-M. Lee, G. Grass, G.-M. Kim, C. Dresbach, L. Zhang, U. Goesele, and M. Knez. Low-temperature ZnO atomic layer deposition on biotemplates: flexible photocatalytic ZnO structures from eggshell membranes. *Physical Chemistry Chemical Physics*, 11:3608–3614, March 2009.
- [93] V. Lehmann. The physics of macropore formation in low-doped n-type silicon. *J. Electrochem. Soc.*, 140:2836–2843, 1993.
- [94] V. Lehmann and H. Föll. Formation mechanism and properties of electrochemically etched trenches in n-type silicon. *Journal of The Electrochemical Society*, 137(2):653–659, 1990.
- [95] V. Lehmann and U. Gösele. Porous silicon formation: A quantum wire effect. *Appl. Phys. Lett.*, 56:856, 1991.
- [96] V. Lehmann and S. Rönnebeck. The physics of macropore formation in low-doped p-type silicon. *J. Electrochem. Soc.*, 146:2968–2975, 1999.
- [97] X. Li and P. W. Bohn. Metal-assisted chemical etching in hf/h₂o₂ produces porous silicon. *Appl. Phys. Lett.*, 77:2572, 2000.
- [98] X. Li, Y. Xiao, J. H. Bang, D. Lausch, S. Meyer, P.-T. Miclea, J.-Y. Jung, S. L. Schweizer, J.-H. Lee, and R. B. Wehrspohn. Upgraded silicon nanowires by metal-assisted etching of metallurgical silicon: A new route to nanostructured solar-grade silicon. *Adv. Mater.*, 25:3187–3191, 2013.
- [99] X. Li, Y. Xiao, C. Yan, K. Zhou, S. L. Schweizer, A. N. Sprafke, J.-H. Lee, and R. B. Wehrspohn. Influence of the mobility of Pt nanoparticles on the anisotropic etching properties of silicon. *ECS Solid State Lett.*, 2:P22–P24, 2013.
- [100] X. Li, Y. Xiao, K. Zhou, C. Yan, P. Wang, S. L. Schweizer, A. N. Sprafke, J.-H. Lee, and R. B. Wehrspohn. Towards maximal photoelectrochemical hydrogen evolution of si by applying tapered nanowire strcture. *Energy Environ. Sci.*, (pending for publication), 2013.
- [101] X. Liu, P. R. Coxon, M. Peters, B. Hoex, J. Cole, and D. Fray. Black silicon: fabrication methods, properties and solar energy applications. *Energy & Environmental Science*, (pending for publication), 2014.
- [102] D. Macdonald and L. Geerligs. Recombination activity of interstitial iron and other transition metal point defects in p-and n-type crystalline silicon. *Applied Physics Letters*, 85(18):4061–4063, 2004.

- [103] S. Matthias, F. Müller, J. Schilling, and U. Gösele. Pushing the limits of macroporous silicon etching. *Applied Physics A*, 80(7):1391–1396, 2005.
- [104] X. Mellhaoui, R. Dussart, T. Tillocher, P. Lefauchaux, P. Ranson, M. Boufnichel, and L. J. Overzetkroll. SiO_xF_y passivation layer in silicon cryoetching. *J. Appl. Phys.*, 98:104901, 2005.
- [105] M. Mews, C. Leendertz, M. Algasinger, S. Koynov, and L. Korte. Amorphous/crystalline silicon heterojunction solar cells with black silicon texture. *physica status solidi (RRL)-Rapid Research Letters*, 9999, 2014.
- [106] A. Montesdeoca-Santana, J. Ziegler, S. Lindekugel, E. Jiménez-Rodríguez, S. Keipert-Colberg, S. Müller, C. Krause, D. Borchert, and R. Guerrero-Lemus. A comparative study on different textured surfaces passivated with amorphous silicon. *Phys. Status Solidi C*, 8(3):747–750, 2011.
- [107] V. Naumann, M. Otto, C. Hagendorf, and R. B. Wehrspohn. Chemical and structural study of electrically passivating $\text{Al}_2\text{O}_3/\text{Si}$ interfaces prepared by atomic layer deposition. *J. Vac. Sci. Technol., A*, 30(4):04D106–04D106–6, 2012.
- [108] V. Naumann, M. Otto, R. B. Wehrspohn, M. Werner, and C. Hagendorf. Interface and material characterization of thin ALD- Al_2O_3 layers on crystalline silicon. *Energy Procedia*, 27:312–318, 2012.
- [109] K. Nishioka, T. Sueto, and N. Saito. Formation of antireflection nanostructure for silicon solar cells using catalysis of single nano-sized silver particle. *Applied Surface Science*, 255(23):9504–9507, 2009.
- [110] S. Nunomura, A. Minowa, H. Sai, and M. Kondo. Mie scattering enhanced near-infrared light response of thin-film silicon solar cells. *Applied Physics Letters*, 97(6):063507–063507, 2010.
- [111] I. Oh, J. Kye, and S. Hwang. Enhanced photochemical hydrogen production from silicon nanowire array photocathode. *Nano Lett.*, 12:298–302, 2012.
- [112] J. Oh, H.-C. Yuan, and H. M. Branz. An 18.2%-efficient black-silicon solar cell achieved through control of carrier recombination in nanostructures. *Nature Nanotechnology*, 7:743–748, 2012.
- [113] M. Otto, M. Algasinger, H. Branz, B. Gesemann, T. Gimpel, K. Fücksel, T. Käsebier, S. Kontermann, S. Koynov, X. Li, et al. Black silicon photovoltaics. *Advanced Optical Materials*, 3(2):147–164, February 2015.
- [114] M. Otto, M. Kroll, T. Käsebier, S.-M. Lee, M. Putkonen, R. Salzer, P. T. Miclea, and R. B. Wehrspohn. Conformal transparent conducting oxides on black silicon. *Adv. Mater.*, 22(44):5035–5038, 2010.
- [115] M. Otto, M. Kroll, T. Käsebier, R. Salzer, and R. Wehrspohn. Conformal Al_2O_3 coatings on black silicon by thermal ALD for surface passivation. In *Proceedings of the 2nd International Conference on Crystalline Silicon Photovoltaics (SiliconPV 2012)*, volume 27, pages 361–364, 2012.
- [116] M. Otto, M. Kroll, T. Käsebier, J. Ziegler, A. N. Sprafke, and R. Wehrspohn. Passivation of optically black silicon by atomic layer deposited Al_2O_3 . In *Proceedings of the 3rd International Conference on Crystalline Silicon Photovoltaics (SiliconPV 2013)*, volume 38, pages 862–865, 2013.
- [117] M. Otto, M. Kroll, T. Käsebier, X. Li, B. Gesemann, K. Fücksel, J. Ziegler, A. N. Sprafke, and R. Wehrspohn. Opto-electronic properties of different black silicon structures passivated by thermal ALD deposited Al_2O_3 . In *Proceedings of OSA: Optical Nanostructures and Advanced Materials for Photovoltaics*, pages PM1C–3. Optical Society of America, 2013.
- [118] M. Otto, M. Kroll, T. Käsebier, X. Li, B. Gesemann, K. Fücksel, J. Ziegler, A. N. Sprafke, and R. B. Wehrspohn. Passivation of different black silicon surfaces by ALD deposited Al_2O_3 . *IEEE Proceedings of the 39th PVSC conference, Tampa, FL, USA*, 39, accepted, 2013.
- [119] M. Otto, M. Kroll, T. Käsebier, R. Salzer, A. Tünnermann, and R. B. Wehrspohn. Extremely low surface recombination velocities in black silicon passivated by atomic layer deposition. *Appl. Phys. Lett.*, 100:191603, 2012.
- [120] J. H. Petermann, D. Zielke, J. Schmidt, F. Haase, E. G. Rojas, and R. Brendel. 19%-efficient and 43 μm -thick crystalline Si solar cell from layer transfer using porous silicon. *Progress in photovoltaics: research and applications*, 20:1–5, 2012.
- [121] P. Poodt. Spatial atomic layer deposition’s assembly line debut. http://avspublications.org/jvsta/spatial_atomic, 2012.

- [122] P. Poodt, A. Lankhorst, F. Roozeboom, K. Spee, D. Maas, and A. Vermeer. High-speed spatial atomic-layer deposition of aluminum oxide layers for solar cell passivation. *Advanced Materials*, 22:3564–3567, 2010.
- [123] R. L. Puurunen. Growth per cycle in atomic layer deposition: Real application examples of a theoretical model. *Chem. Vap. Deposition*, 9(6):327–332, 2003.
- [124] R. L. Puurunen. Surface chemistry of atomic layer deposition: A case study for the trimethylaluminum/water process. *J. Appl. Phys.*, 97:121301, 2005.
- [125] R. L. Puurunen and W. Vandervorst. Island growth as a growth mode in atomic layer deposition—A phenomenological model. *J. Appl. Phys.*, 96(12):7686–7695, 2004.
- [126] D. Redfield. Multiple-pass thin-film silicon solar cell. *Applied Physics Letters*, 25:647–648, 1974.
- [127] S. Rein. *Lifetime Spectroscopy: A Method of Defect Characterization in Silicon for Photovoltaic Applications*. Springer, 2005.
- [128] P. Repo, J. Benick, V. Vähänissi, J. Schön, G. von Gastrow, B. Steinhauser, M. C. Schubert, M. Hermle, and H. Savin. n-type black silicon solar cells. *Energy Procedia*, 38:866–871, 2013.
- [129] P. Repo, A. Haarahiltunen, L. Sainiemi, M. Yli-Koski, H. Talvitie, M. Schubert, and H. Savin. Effective passivation of black silicon surfaces by atomic layer deposition. *IEEE Journal of Photovoltaics*, 3(1):90–94, 2013.
- [130] A. Richter, J. Benick, M. Hermle, and S. W. Glunz. Reaction kinetics during the thermal activation of the silicon surface passivation with atomic layer deposited Al_2O_3 . *Applied Physics Letters*, 104(6):061606, 2014.
- [131] A. Richter, S. W. Glunz, F. Werner, J. Schmidt, and A. Cuevas. Improved quantitative description of Auger recombination in crystalline silicon. *Phys. Rev. B*, 86:165202, 2012.
- [132] P. Saint-Cast, D. Kania, R. Heller, S. Kuehnhold, M. Hofmann, J. Rentsch, and R. Preu. High-temperature stability of c-si surface passivation by thick PECVD Al_2O_3 with and without hydrogenated capping layers. *Applied Surface Science*, 258(21):8371–8376, 2012.
- [133] T. Sarnet, M. Halbwx, R. Torres, P. Delaporte, M. Sentis, S. Martinuzzi, V. Vervisch, F. Torregrosa, H. Etienne, L. Roux, and S. Bastide. Femtosecond laser for black silicon and photovoltaic cells. In T. Sarnet, M. Halbwx, R. Torres, P. Delaporte, M. Sentis, S. Martinuzzi, V. Vervisch, F. Torregrosa, H. Etienne, L. Roux, and S. Bastide, editors, *Proc. SPIE*, volume 6881, page 15, 2008.
- [134] S. Schaefer and R. Lüdemann. Low damage reactive ion etching for photovoltaic applications. *J. Vac. Sci. Technol., A*, 17(3):749, May/June 1999.
- [135] J. Schilling, F. Muller, S. Matthias, R. Wehrspohn, U. Gosele, and K. Busch. Three-dimensional photonic crystals based on macroporous silicon with modulated pore diameter. *Applied Physics Letters*, 78(9):1180–1182, 2001.
- [136] J. Schilling, V. Talalaev, A. Tonkikh, B. Fuhrmann, F. Heyroth, and M. Otto. Enhanced non-radiative recombination in the vicinity of plasma-etched side walls of luminescing si/ge-quantum dot structures. *Appl Phys Lett*, 103:161106, 2013.
- [137] J. Schmidt. *Untersuchungen zur Ladungsträgerrekombination an Oberflächen und im Volumen von kristallinen Silicium Solarzellen*. PhD thesis, Fachbereich Physik der Universität Hannover, 1998.
- [138] J. Schmidt, A. Merkle, R. Brendel, B. Hoex, M. C. M. van de Sanden, and W. M. M. Kessels. Surface passivation of high-efficiency silicon solar cells by atomic-layer-deposited Al_2O_3 . *Progress in Photovoltaics: Research and Applications*, 16:461–466, 2008.
- [139] M. Schnell, R. Ludemann, and S. Schaefer. Plasma surface texturization for multicrystalline silicon solar cells. In *Photovoltaic Specialists Conference, 2000. Conference Record of the Twenty-Eighth IEEE*, pages 367–370. IEEE, 2000.
- [140] M. Schwitzke. Rem/edx. [Online](#), (accessed: 16.08.2014).
- [141] SEMI PV Group. International technology roadmap for photovoltaic (itrpv) results 2012. www.itrpv.net, March 2013. Online; accessed 03.04.2013.
- [142] Z. Shen, B. Liu, Y. Xia, J. Liu, J. Liu, S. Zhong, and C. Li. Black silicon on emitter diminishes the lateral electric field and enhances the blue response of a solar cell by optimizing depletion region uniformity. *Scr. Mater.*, 68(3-4):199–202, FEB 2013.

- [143] W. Shockley and H. J. Queisser. Detailed balance limit of efficiency of pn junction solar cells. *J. Appl. Phys.*, 32(3):510, 1961.
- [144] W. Shockley and J. W. Read. Statistics of the recombinations of holes and electrons. *Phys. Rev. Lett.*, 87:835–842, 1952.
- [145] R. A. Sinton and A. Cuevas. Contactless determination of current–voltage characteristics and minority-carrier lifetimes in semiconductors from quasi-steady-state photoconductance data. *Applied Physics Letters*, 69(17):2510–2512, 1996.
- [146] W. H. Southwell. Gradient-index antireflection coatings. *Optics letters*, 8(11):584–586, 1983.
- [147] A. Sprafke, M. Otto, J. Ziegler, and R. B. Wehrspohn. Black silicon photovoltaics. *European Energy Innovation: Photonics*, Spring:26 – 27, 2013.
- [148] A. Sproul, M. Green, and A. Stephens. Accurate determination of minority carrier- and lattice scattering-mobility in silicon from photoconductance decay. *Journal of applied physics*, 72(9):4161–4171, 1992.
- [149] A. B. Sproul. Dimensionless solution of the equation describing the effect of surface recombination on carrier decay in semiconductors. *J. Appl. Phys.*, 76:2851, 1994.
- [150] M. Steglich, D. Lehr, S. Ratzsch, T. Käsebier, F. Schrempel, E.-B. Kley, and A. Tünnermann. An ultra-black silicon absorber. *Laser & Photonics Reviews*, 8(2):L13–L17, 2014.
- [151] M. Steglich, M. Zilk, F. Schrempel, A. Tünnermann, and E.-B. Kley. Improvement of ge-on-si photodiodes by black silicon light trapping. *Appl. Phys. Lett.*, 102:111110, 2013.
- [152] C. Striemer and P. Fauchet. Dynamic etching of silicon for broadband antireflection applications. *Applied physics letters*, 81(16):2980–2982, 2002.
- [153] T. Suntola and J. Anston. US-Patent: Method for producing compound thin films, 11 1977.
- [154] N. Terlinden, G. Dingemans, M. Van de Sanden, and W. Kessels. Role of field-effect on c-si surface passivation by ultrathin (2–20 nm) atomic layer deposited Al_2O_3 . *Applied Physics Letters*, 96(11):112101–112101, 2010.
- [155] The Nobel Prize in Physics. http://nobelprize.org/nobel_prizes/physics/laureates/1986/ (visited 09.10.2012), 1986.
- [156] T. Tiedje, E. Yablonovitch, G. D. Cody, and B. G. Brooks. Limiting efficiency in solar cells. *IEEE Trans. Electron Devices*, 31(5):711–716, May 1984.
- [157] T. Trupke, M. Green, P. Würfel, P. Altermatt, A. Wang, J. Zhao, and R. Corkish. Temperature dependence of the radiative recombination coefficient of intrinsic crystalline silicon. *Journal of applied physics*, 94(8):4930–4937, 2003.
- [158] L. Tsakalakos, J. Balch, J. Fronheiser, B. Korevaar, O. Sulima, and J. Rand. Silicon nanowire solar cells. *Applied Physics Letters*, 91:233117, 2007.
- [159] J. Üpping, A. Bielawny, S.-M. Lee, M. Knez, R. Carius, and R. B. Wehrspohn. Electric transport in 3D photonic crystal intermediate reflectors for micromorph thin-film tandem solar cells. *Proc. SPIE*, 7409:74090J, August 2009.
- [160] J. Üpping, R. Salzer, M. Otto, T. Beckers, L. Steidl, R. Zentel, R. Carius, and R. B. Wehrspohn. Transparent conductive oxide photonic crystals on textured substrates. *Photonics and Nanostructures–Fundamentals and Applications*, 9:31, 2011.
- [161] B. Vermang. *Aluminum oxide as negatively charged surface passivation for industrial crystalline silicon solar cells*. PhD thesis, Katholieke Universiteit Leuven, 2012.
- [162] B. Vermang, H. Goverde, A. Lorenz, A. Uruena, G. Vereecke, J. Meersschant, E. Cornagliotti, A. Rothschild, J. John, J. Poortmans, and R. Mertens. On the blistering of atomic layer deposited Al_2O_3 as si surface passivation. In *Proceedings of the 37th IEEE Photovoltaic Specialists Conference PVSC*, 3562–3567.
- [163] J. R. Wank, S. M. George, and A. W. Weimer. Nanocoating individual cohesive boron nitride particles in a fluidized bed by ALD. *Powder technology*, 142(1):59–69, 2004.
- [164] J. Weber, A. Janotti, and C. Van de Walle. Native defects in Al_2O_3 and their impact on iii-v/ Al_2O_3 metal-oxide-semiconductor-based devices. *Journal of Applied Physics*, 109(3):033715–033715, 2011.

- [165] R. B. Wehrspohn and J. Üpping. 3d photonic crystals for photon management in solar cells. *J. Opt.*, 14:024003, 2012.
- [166] F. Werner, B. Veith, D. Zielke, L. Kühnemund, C. Tegenkamp, M. Seibt, R. Brendel, and J. Schmidt. Electronic and chemical properties of the c-Si/Al₂O₃ interface. *Journal of Applied Physics*, 109:113701, 2011.
- [167] D. Williams and C. Carter. *Transmission Electron Microscopy: A Textbook for Materials Science*. Plenum Press, New York, 1996.
- [168] S. Wilson and M. Hutley. The optical properties of 'moth eye' antireflection surfaces. *Journal of Modern Optics*, 29(7):993–1009, 1982.
- [169] M. Wittmer and K. Tu. Low-temperature diffusion of dopant atoms in silicon during interfacial silicide formation. *Physical Review B*, 29(4):2010, 1984.
- [170] J. A. Woollam, B. Johs, C. M. Herzinger, J. Hilfiker, R. Synowicki, and C. L. Bungay. Overview of variable angle spectroscopic ellipsometry (vase), part i: basic theory and typical applications. *SPIE*, CR72:3–28, 1999.
- [171] J. A. Woollam Co. Inc. Ellipsometry solutions. [online](#), (accessed: 28.07.2014).
- [172] C. Wu, C. Crouch, L. Zhao, J. Carey, R. Younkin, J. Levinson, E. Mazur, R. Farrell, P. Gothoskar, and A. Karger. Near-unity below-band-gap absorption by microstructured silicon. *Applied Physics Letters*, 78(13):1850–1852, 2001.
- [173] Y. Xia, B. Liu, J. Liu, Z. Shen, and C. Li. A novel method to produce black silicon for solar cells. *Sol. Energy*, 85:1574–1578, 2011.
- [174] Yablonovitch. Statistical ray optics. *J. Opt. Soc. Am.*, 72(7):899, 1982.
- [175] E. Yablonovitch. Inhibited spontaneous emission in solid-state physics and electronics. *Phys. Rev. Lett.*, 58:2059–2062, May 1987.
- [176] E. Yablonovitch, D. L. Allara, C. C. Chang, T. Gmitter, and T. B. Bright. Unusually low surface-recombination velocity on silicon and germanium surfaces. *Phys. Rev. Lett.*, 57(2):249–252, 1986.
- [177] E. Yablonovitch and G. Cody. Intensity enhancement in textured optical sheets for solar cells. *IEEE Electron Devices Society*, 29:300, 1982.
- [178] A. Yamada, B. Sang, and M. Konagai. Atomic layer deposition of ZnO transparent conducting oxides. *Applied Surface Science*, 112:216–222, 1997.
- [179] Y. Yang, M. Green, A. Ho-Baillie, H. Kampwerth, S. Pillai, and H. Mehrvarz. Characterization of 2-d reflection pattern from textured front surfaces of silicon solar cells. *Solar Energy Materials and Solar Cells*, 115:42–51, 2013.
- [180] J. Yoo, I. Parm, U. Gangopadhyay, K. Kim, S. Dhungel, D. Mangalaraj, and J. Yi. Black silicon layer formation for application in solar cells. *Solar Energy Materials and Solar Cells*, 90(18-19):3085–3093, November 2006. 14th International Photovoltaic Science and Engineering Conference.
- [181] J. Yoo, G. Yu, and J. Yi. Black surface structures for crystalline silicon solar cells. *Mater. Sci. Eng., B*, 159-160:333–337, March 2009.
- [182] R. Younkin, J. E. Carey, E. Mazur, J. A. Levinson, and C. M. Friend. Infrared absorption by conical silicon microstructures made in a variety of background gases using femtosecond-laser pulses. *J. Appl. Phys.*, 93:2626–2629, 2003.
- [183] H.-C. Yuan, V. E. Yost, M. R. Page, P. Stradins, D. L. Meier, and H. M. Branz. Efficient black silicon solar cell with a density-graded nanoporous surface: Optical properties, performance limitations, and design rules. *Appl Phys Lett*, 95(123501):123501, 2009.
- [184] S. H. Zaidi, D. S. Ruby, and J. M. Gee. Characterization of random reactive ion etched-textured silicon solar cells. *IEEE T. Electron. Dev.*, 48(6):1200, 2001.
- [185] J. Zhao, A. Wang, P. Altermatt, and M. Green. Twenty-four percent efficient silicon solar cells with double layer antireflection coatings and reduced resistance loss. *Applied Physics Letters*, 66(26):3636–3638, 1995.

- [186] J. Ziegler, J. Haschke, T. Käsebier, L. Korte, A. N. Sprafke, and R. B. Wehrspohn. Influence of black silicon surfaces on the performance of back-contacted back silicon heterojunction solar cells. *Optics Express*, 22(S6):A1469–A1476, 2014.
- [187] J. Ziegler, M. Otto, A. N. Sprafke, and Ral. Activation of Al_2O_3 passivation layers on silicon by microwave annealing. *Applied Physics A*, 113:285–290, 2013.

List of the Author's Publications

As First Author

- M. Otto, M. Kroll, T. Käsebier, S.-M. Lee, M. Putkonen, R. Salzer, P. T. Miclea, and R. B. Wehrspohn, “Conformal Transparent Conducting Oxides on Black Silicon”, *Advanced Materials*, **22**(44), 5035 (2010). [114]
- M. Otto, M. Kroll, T. Käsebier, R. Salzer, A. Tünnermann, and R. B. Wehrspohn, “Extremely low surface recombination velocities in black silicon passivated by atomic layer deposition”, *Applied Physics Letters*, **100**, 191603 (2012). [119]
- M. Otto, M. Kroll, T. Käsebier, R. Salzer, and R.B. Wehrspohn, “Conformal Al₂O₃ Coatings on Black Silicon by Thermal ALD for Surface Passivation”, *Energy Procedia*, **27**, 361 (2012). [115]
- M. Otto, M. Kroll, T. Käsebier, J. Ziegler, A.N. Sprafke, and R.B. Wehrspohn, “Passivation of Optically Black Silicon by Atomic Layer Deposited Al₂O₃”, *Energy Procedia*, **38**, 862 (2013). [116]
- M. Otto, M. Kroll, T. Käsebier, X. Li, B. Gesemann, K. Fücksel, J. Ziegler, A. N. Sprafke, and R. B. Wehrspohn, “Passivation of different black silicon surfaces by ALD deposited Al₂O₃”, *Proceedings of PVSC IEEE*, **39**, H30 (350). [118]
- M. Otto, M. Kroll, T. Käsebier, X. Li, B. Gesemann, K. Fücksel, J. Ziegler, A. Sprafke, and R. B. Wehrspohn, “Opto-electronic properties of different black silicon structures passivated by thermal ALD deposited Al₂O₃”, *Proceedings of OSA: Optical Nanostructures and Advanced Materials for Photovoltaics*, **PM1C-3** (2013). [117]
- M. Otto, M. Algasinger, H. Branz, B. Gesemann, T. Gimpel, K. Fücksel, T. Käsebier, S. Kontermann, S. Koynov, X. Li, V. Naumann, J. Oh, A. N. Sprafke, J. Ziegler, M. Zilk, and R. B. Wehrspohn, “Black Silicon Photovoltaics”, *Advanced Optical Materials* **3**, 147–164 (2015). [113]

As Co-Author

- M. Kroll, T. Käsebier, M. Otto, R. Salzer, and R. Wehrspohn, “Optical modeling of needle like silicon surfaces produced by an ICP-RIE process”, *Proceedings of SPIE, Photonics for Solar Energy Systems III*, **7725**, 772505 (2010). [89]
- J. Üpping, R. Salzer, M. Otto, T. Beckers, L. Steidl, R. Zentel, R. Carius and R. B. Wehrspohn “Transparent conductive oxide photonic crystals on textured substrates”, *Photonics and Nanostructures - Fundamentals and Applications*, **9**(1), 31 (2011). [160]
- V. Naumann, M. Otto, R. B. Wehrspohn and C. Hagendorf, “Chemical and structural study of electrically passivating Al₂O₃/Si interfaces prepared by atomic layer deposition”, *Journal of Vacuum Science and Technology A*, **30**(4), 04D106 (2012). [107]

- V. Naumann, M. Otto, R. B. Wehrspohn, M. Werner and C. Hagendorf, “Interface and Material Characterization of Thin ALD- Al_2O_3 Layers on Crystalline Silicon”, *Energy Procedia*, **27**, 312 (2012). [108]
- M. Kroll, M. Otto, T. Käsebier, K. Füchsel, R. B. Wehrspohn, E.-B. Kley, A. Tünnermann, and T. Pertsch, “Black silicon for photovoltaic applications”, *Proceedings of SPIE, Photonics for Solar Energy Systems IV*, **8438**, 843817 (2012). [90]
- K. Füchsel, M. Kroll, T. Käsebier, M. Otto, T. Pertsch, E.-B. Kley, R. B. Wehrspohn, and A. Tünnermann, “Black silicon photovoltaics”, *Proceedings of SPIE, Photonics for Solar Energy Systems IV*, **8438**, 84380M (2012). [42]
- A. Sprafke, M. Otto, J. Ziegler, “Black Silicon Photovoltaics”, *European Energy Innovation, Photonics, Spring*, 26 (2013). [147]
- J. Ziegler, M. Otto, A. N. Sprafke, and R. B. Wehrspohn, “Activation of Al_2O_3 passivation layers on silicon by microwave annealing”, *Appl. Phys. A*, **113**, 285 (2013). [187]
- J. Schilling, V. Talalaev, A. Tonkikh, B. Fuhrmann, F. Heyroth, and M. Otto, “Enhanced non-radiative recombination in the vicinity of plasma-etched side walls of luminescing Si/Ge-quantum dot structures”, *Appl. Phys. Lett.*, **103**, 161106 (2013). [136]

Oral Presentations

- M. Otto et al., “Conformal Al doped ZnO on rough silicon surfaces” (DPG, Dresden, Germany, 2011)
- M. Otto et al., “Conformal Al doped ZnO on rough silicon surfaces” (DokDok, Naumburg, Germany, 2011)
- M. Otto et al., “Conformal Al_2O_3 coatings on black Si by thermal ALD for surface passivation” (DPG, Berlin, Germany, 2012)
- M. Otto et al., “Passivation of optically black silicon wafers by atomic layer deposited Al_2O_3 films” (OSA, Eindhoven, Netherlands, 2012)
- M. Otto et al., “Selective laser ablation of Al_2O_3 passivation layers from optically black silicon surfaces” (DPG, Regensburg, Germany, 2013)
- M. Otto et al., “Decent passivation of optically black silicon by atomic layer deposited Al_2O_3 ” (SiliconPV, Hameln, Germany, 2013)

List of Posters

- M. Otto et al., “Optimization of the electrical and optical properties of ALD-deposited TCOs on black silicon surfaces” (SPIE, Brussels, Belgium, 2010)
- M. Otto et al., “Conductive ZnO nanostructures for photovoltaic applications” (BALD, Hamburg, Germany, 2010)
- M. Otto et al., “Conformal ALD deposited Al doped ZnO on rough silicon surfaces” (PVSEC, Hamburg, Germany, 2011)
- M. Otto et al., “Optics of conformal Al_2O_3 coatings on b-Si by thermal ALD for surface passivation” (OSA, Austin, Tx, USA, 2011)

- M. Otto et al., “Conformal Al₂O₃ Coatings on Black Silicon by Thermal ALD for Surface Passivation” (SiliconPV, Leuven, Belgium, 2012)
- M. Otto et al., “Selective laser ablation of Al₂O₃ passivation layers from black Si surfaces” (SPIE, Brussels, Belgium, 2012)
- M. Otto et al., “Passivation of different black silicon surfaces by ALD deposited Al₂O₃” (PVSC, Tampa, FL, USA, 2013)

Appendix A

Appendix

A.1 The AM1.5G Spectrum

Sunlight arriving at the earth has to travel through the atmosphere before it may be captured by a solar cell at ground level. Direct traversal corresponds to an “air mass” of one. The Air Mass 1.5 Global spectrum with a 37° South facing tilt is defined by the “American Society for Testing and Materials (ASTM)” as a standardized “Terrestrial Reference Spectra for Photovoltaic Performance Evaluation” [4]. The irradiation intensity at the earth’s surface (at sea level) is shown in fig. A.1. The total intensity accounts for $\approx 1000 \text{ W/m}^2$. Herein, direct and circumferential sun light with a solid angle of $\pm 2.5^\circ$ as well as indirect light reflected from the earth’s surface and the atmosphere is included. About 2/3 of the available power from the total spectral range can be converted in a c-Si solar cell.

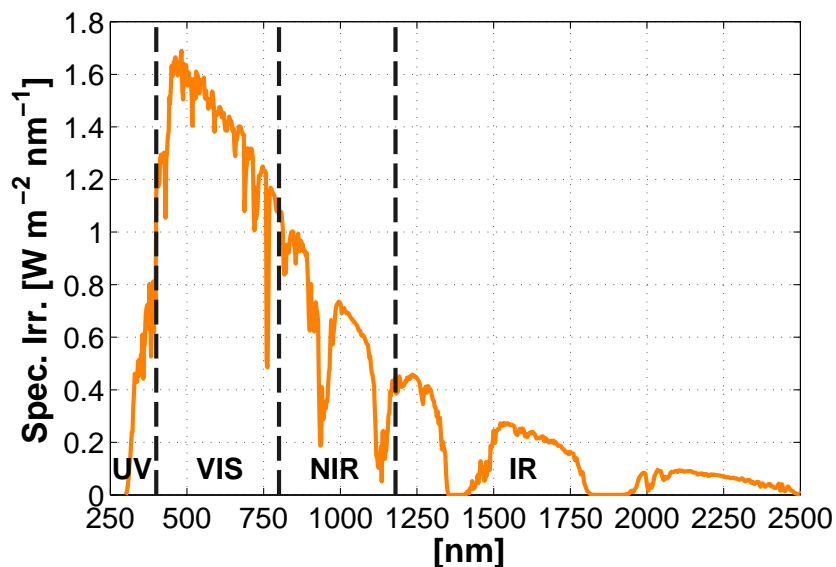


Figure A.1: The AM1.5G spectrum: “Terrestrial Reference Spectra for Photovoltaic Performance Evaluation” as defined by the ASTM shows the spectral solar irradiance at sea level. See text for further explanation.

Table A.1: Maximum short circuit current (I_{sc}) contained in the AM1.5G one sun solar spectrum for an optical absorptance of unity as well as a perfect IQE.

| spectrum | range | I_{sc} | |
|----------|-------------|-----------------------|-------|
| | [nm] | [mA/cm ²] | [%] |
| UV | 280 – 380 | 0.946 | 1.4 |
| VIS | 380 – 780 | 25.168 | 36.0 |
| NIR | 780 – 1180 | 19.562 | 28.4 |
| IR | 1180 – 4000 | 23.130 | 33.6 |
| total | 300 – 4000 | 68.805 | 100.0 |
| Si | 300 – 1180 | 45.675 | 66.4 |

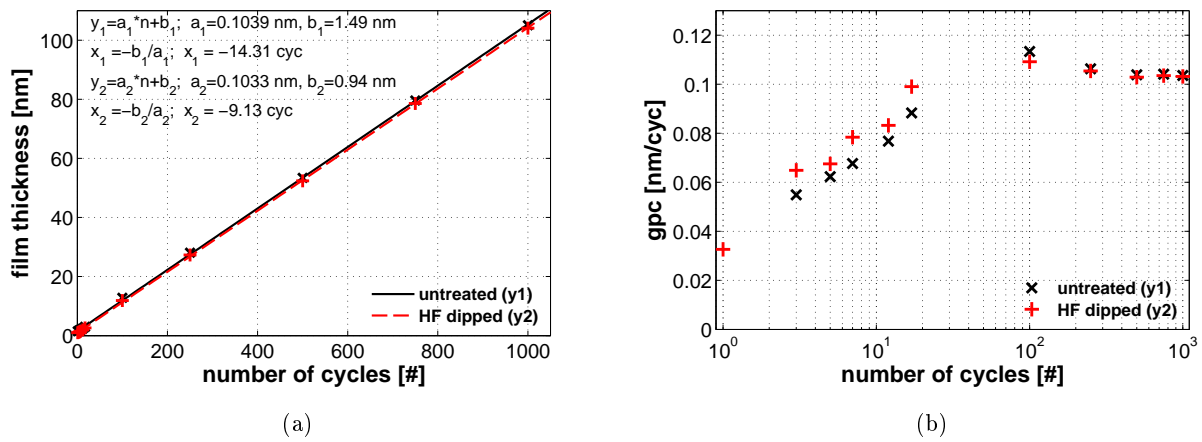


Figure A.2: Thickness and average gpc of Al_2O_3 on polished oob and HF-dipped Cz Si substrates. According to Puurunen the observed growth behavior can be categorized as substrate inhibited growth of Type 2, which is probably related to island growth [124, sec. III. fig. 15].

Table A.2: Typical ICP-RIE etching parameters of the 'standard' b-Si processes (IAP, FSU Jena).

| Process | SF_6/O_2 [sccm] | $p_{\text{ICP-RIE}}$ [Pa] | P_{CCP} [W] | V_{BIAS} [V] | P_{ICP} [W] | T [°C] | t [min] | h [nm] | w [nm] |
|---------|------------------------------------|------------------------------|-------------------------|--------------------------|-------------------------|-------------|--------------|-------------|-------------|
| shallow | 60/60 | 4 | 6 | -25 | 750 | -41 | 10 | 500 | 160 |
| interm. | 60/60 | 4 | 6 | -22 | 750 | -37 | 20 | 680 | 250 |
| deep | 60/60 | 2 | 2 | -22 | 750 | -47 | 10 | 1700 | 210 |

A.2 Growth Per Cycle

The gpc of Al_2O_3 was investigated on $-\text{H}$ and $-\text{OH}$ terminated polished Si surfaces and the results are shown in fig. A.2.

A.3 ICP-RIE b-Si Etching Parameters

A complete set of ICP-RIE Parameters is listed in table A.2.

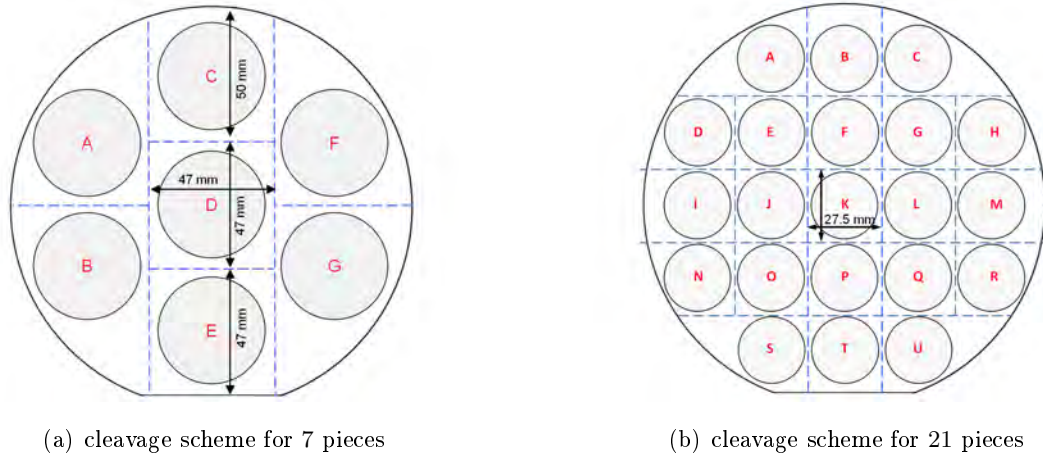


Figure A.3: For parameter variations, the wafers were cleaved into 7, or 21 pieces after the schemes shown in (a) and (b), respectively.

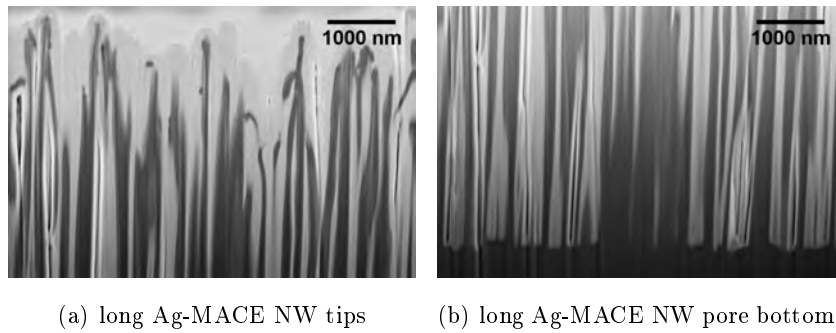


Figure A.4: FIB cut cross sections of the Al_2O_3 passivated long Ag-MACE b-Si NWs. Even though the exact film thickness could not be determined, the coating completely covers the surface of the nanostructures.

A.4 ALD Film Homogeneity and Wafer Cleavage Scheme

To facilitate a better comparison and for saving substrate material, many wafers were cleaved into 7 or 21 pieces as indicated in fig. A.3. On full wafers, the lifetime homogeneity was mapped by QSSPC along the same spots ($A = 1; \dots; U = 21$). The QSSPC probe (measurement coil) was placed inside the indicated circles.

A.5 ALD- Al_2O_3 on Ag MACE NW b-Si Structures

Concomitantly to fig. 5.10, the FIB cut cross sections of fig. A.4 show the Al_2O_3 passivated long b-Si NWs (Ag-MACE) at the tips and pore bottoms. The ALD- Al_2O_3 layer on the nanostructures appears to be highly conformal. However, as discussed in sec. 7.3, a reliable extraction of geometric parameters like the correlation length L_c and/or the depth profile of the Si volume fraction f was not possible because the nanowires partially bent during preparation and may stick together and/or cross the image plane.

A.6 Supplm. Info. on the Analysis of the Carrier Lifetime with Respect to the Homogeneity of the Interfacial SiO_x and ALD Films

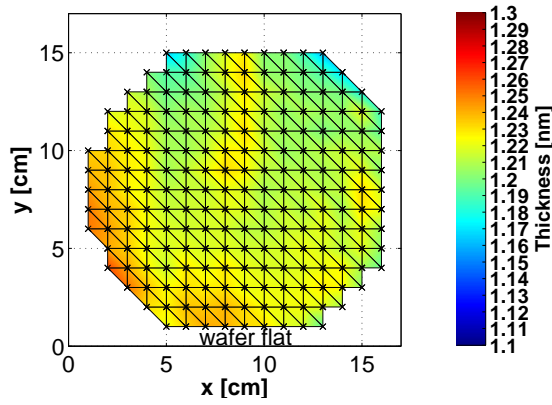
A.6.1 Intefacial SiO_x

The ellipsometry and photo-luminescence (PL) mappings of wafers that were RCA cleaned for 20 minutes are shown in fig. A.5. PL lifetime maps of similarly treated wafers, that were not analyzed intermittently by ellipsometry are shown in fig. A.6, accordingly. The data accompany the mappings of the SiO_2 thickness, the ALD- Al_2O_3 thickness, and the carrier lifetimes presented in fig. 7.3.

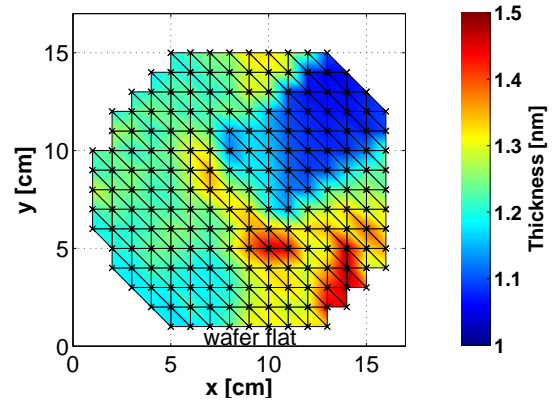
Ellipsometry mappings of the native oxide thickness on the front and rear side of a typical out-of-box wafer are shown in fig. A.7.

A.6.2 Influence of the Al_2O_3

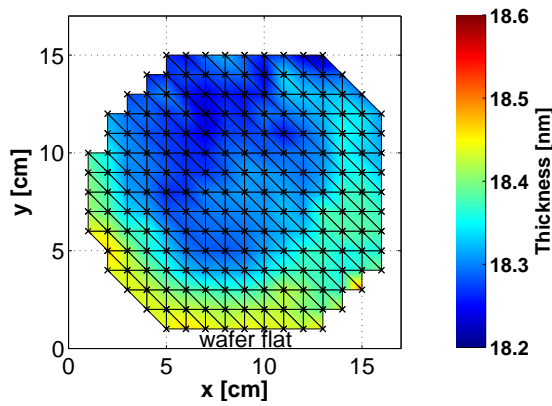
The achieved Al_2O_3 film homogeneity was demonstrated by mapping the film thickness of full 6" wafers and also became obvious in many other parameter series. Usually, the initial thickness variation of the underlying oxide ($\approx 2 \text{ nm} \pm 10\%$) dominates the standard deviation of the film and, hence, the uniformity increases with increasing film thickness (see fig. 3.4). Repeated deposition of 2000 cyc lead to the same lifetime pattern across all four out-of-box wafers (fig. 6.7). The three local maxima may be understood by the measurement pattern shown in fig. A.3(b) and were measured across the centered column of the wafer. Physically, this lifetime variation of up to 50% could be explained by two factors. First, it is assumed that the surfaces of the oob wafers were identically clean and entered the process with identically (in-)homogeneous SiO_x films, that could cause such a pattern. However, the highest lifetimes were measured along the vertical axes of the wafers, whereas ellipsometry mappings of the oxide (fig. A.7) showed a diagonal variation of the oxide thickness. Second, if the wafers were all cut from the same block, a slight doping inhomogeneity may be causing this lifetime undulation. The latter would be supported by the fact, that the highest lifetimes of $\approx 5 \text{ ms}$ and corresponding lowest SRVs of $S_{\text{eff}} \leq 2.3 \text{ cm/s}$ are extremely close to the intrinsic lifetime limit (Auger-Limit). Richter *et al.* experimentally determined an Auger-Limit of $S_{\text{eff}} \leq 4 \text{ cm/s}$ for a p-type wafer with a doping concentration of $1 \text{ } \Omega\text{cm}$ ($1.5 \cdot 10^{16} \text{ cm}^{-3}$, $W = 250 \text{ } \mu\text{m}$) [131]. Note, however, that a slight variation of the doping concentration of $+0.25 \text{ } \Omega\text{cm}$ would shift the Auger-Limit down to $\approx 2 \text{ cm/s}$ [131]. According to the provider's specifications of the used wafers, our results are well comparable to the results of Richter *et al.*, who deposited their Al_2O_3 films by plasma assisted ALD, which is known to yield a stronger passivation than thermal ALD. On the other hand, our films are rather thick and may offer a higher amount of H_2 , which plays an important role in terms of chemical passivation of dangling bonds [28, 130]. In addition, the layers constitute a very good barrier against out-diffusion of the passivating H_2 species [28]. Interestingly, no blistering was observed, which was reported to occur very likely in Al_2O_3 films with thicknesses over 10 nm [162]. Nevertheless, the occurrence of blisters can neither be fully ruled out, since the passivation level may stay adequately high [132]. It was observed in this work, that thicker Al_2O_3 films typically lead to higher carrier lifetimes, which can be explained by the chemical passivation component provided by the films.



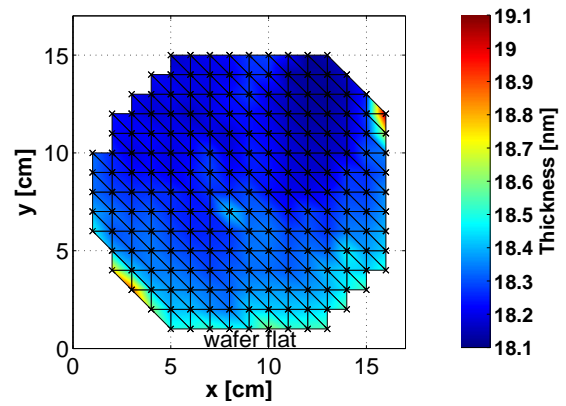
(a) front: $d_{\text{SiO}_x} = 1.22 \pm 0.02$ nm



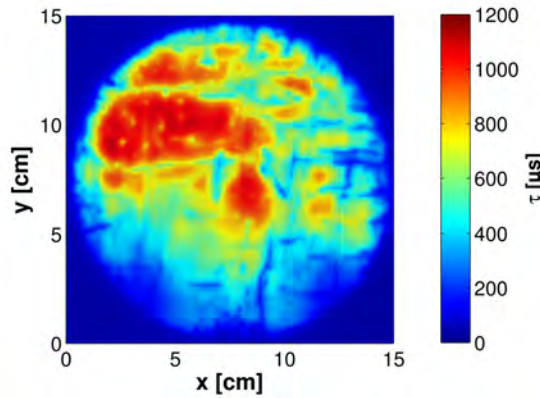
(b) rear: $d_{\text{SiO}_x} = 1.23 \pm 0.09$ nm



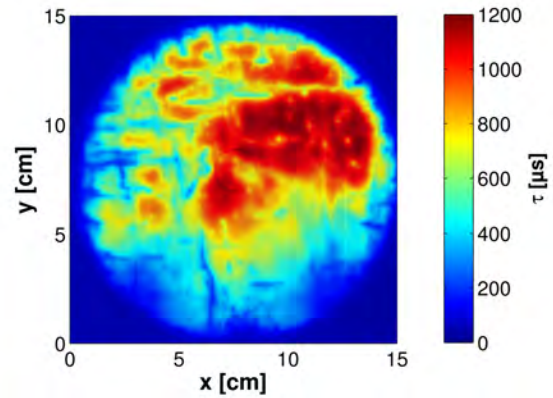
(c) front: $d_{\text{SiO}_x + \text{Al}_2\text{O}_3} = 18.34 \pm 0.07$ nm



(d) rear: $d_{\text{SiO}_x + \text{Al}_2\text{O}_3} = 18.31 \pm 0.15$ nm



(e) front, τ_{eff} in μs



(f) rear, τ_{eff} in μs

Figure A.5: Ellipsometry mappings of the oxide (SiO_x) thickness grown during a **20 min** RCA SC2 cleaning step. The SiO_x is extremely homogeneous on the front (a) $d_{\text{min}} = 1.16$ nm, $d_{\text{max}} = 1.26$ nm, whereas on the rear (b) three regions are visible with thicknesses around 1.1 nm, 1.25 nm, and 1.4 nm. The total span of the rear side is 0.42 nm. After deposition of 150 cyc Al_2O_3 the oxide layer thickness on front (c) and rear (d) follows the original SiO_x patterns. Hence, a highly homogeneous Al_2O_3 layer thickness was deposited. Graphs (e) and (f) show lifetime maps of the same wafer as recorded by PL on front and rear, respectively. The highest lifetimes were measured where the SiO_x is thinnest. Higher lifetimes following the same pattern were achieved for a sample that was not intermittently measured by ellipsometry.

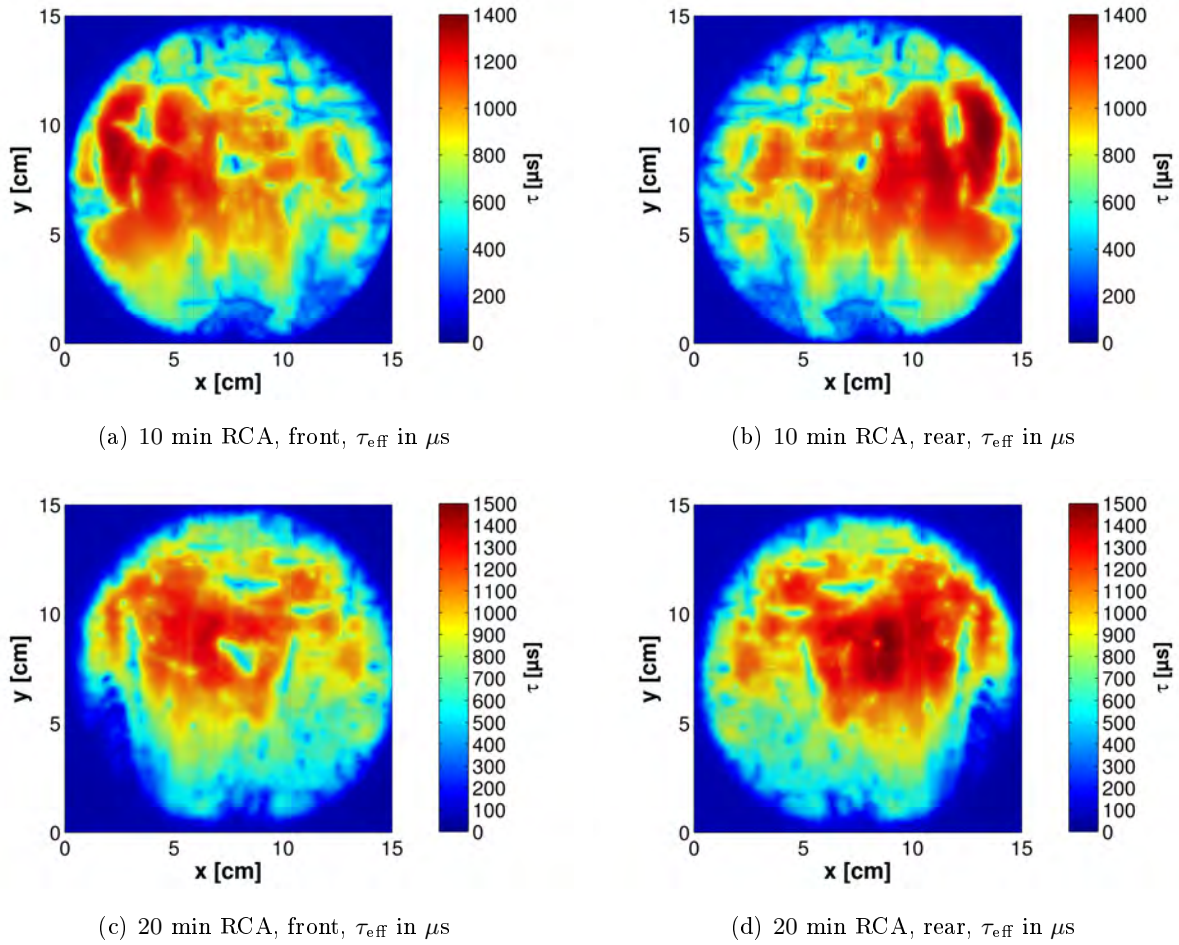


Figure A.6: The PL lifetime maps show wafers that were identically cleaned like the ones shown in figs. 7.3 and A.5. After the SC2 step 150 cycles Al_2O_3 were deposited directly and the samples were subsequently annealed without measuring the oxide thickness by ellipsometry. The highest lifetimes correlate with the thinnest RCA SiO_2 . The peak and average lifetimes are higher than in figs. 7.3 and A.5 because less sample handling was necessary.

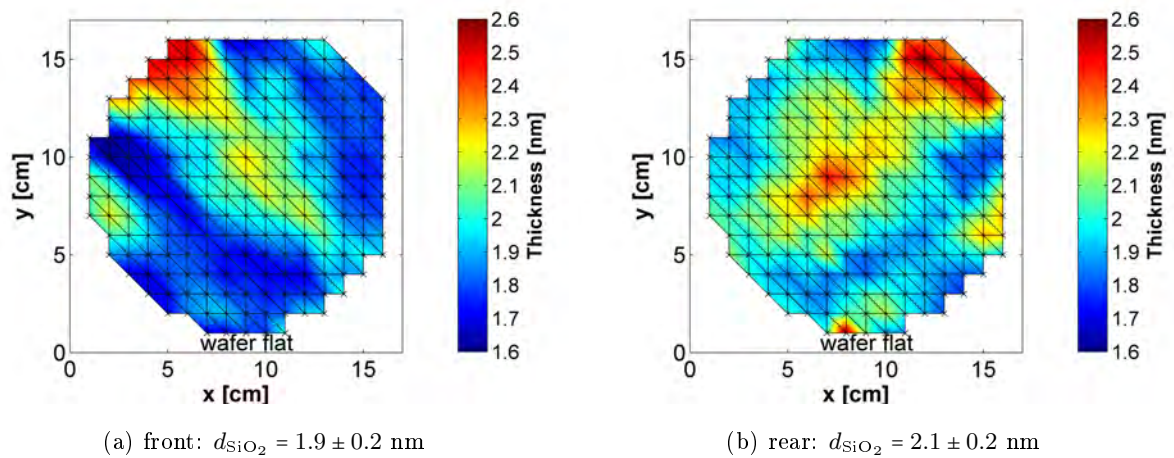


Figure A.7: Ellipsometry mapping of the "native" oxide thickness on an oob wafer. It appears clear that the oxide is symmetrically thicker on a diagonal line. The wafer was flipped over from front (a) to rear (b) along the y-axis while the wafer flat stayed on the bottom.

A.7 Chemical Analysis of Etching Residues on b-Si Surfaces by Inductive Coupled Plasma Mass-Spectrometry

Metal contaminations of ICP-RIE processed Cz Si surfaces were analyzed by Inductive Coupled Plasma Mass-Spectrometry (ICPMS). For this purpose full 6" wafers were bifacially nanostructured yielding the ICP shallow, intermediate, and deep b-Si types. In addition, one wafer was thinned down by means of a pure SF₆ plasma process in which a polished-like surface is maintained.

The wafers were dissolved layer-by-layer in acidic solutions in three steps during 30 min each. First, the samples were immersed in a mixture of HCl and HNO₃ to extract any superficial surface contaminations. Since neither acid attacks SiO_x, the oxide completely remained while superficial contaminations are dissolved in the acidic solution. In the second step, HF was used to dissolve the SiO_x layer from the wafer surfaces including possible contaminants. Here, crystalline Si acts as a natural etch stop. Finally, the surface-near Si bulk was dissolved by a mixture of HF and HNO₃. During this last step the b-Si structures completely vanished.

By ICPMS of the remaining solutions the concentrations of some selected metals could be determined.¹ The data are displayed in fig. A.8. On the surface, (first step/superficial contamination) the levels of Al, Cr, Fe, V, and Mn were elevated on the ICP-RIE treated Cz samples as compared to the out-of-box reference. All of these (transition) metals lead to recombination active defect states inside the forbidden band of Si and deteriorate the lifetime in c-Si for the indicated surface contamination levels. Especially the elevated Cr level of up to four orders above the reference was rather prominent. Cr is commonly used as a photo-lithographic hard-mask material but induces a shallow donor with extremely large capture cross sections (of $\sim 10^{-13}\text{cm}^2$) for electrons and holes [102]. The ICP-RIE chamber was used for different photo-lithographic processes, including the etching of Cr hard-masks and photo-resists. The concentrations peaked in the case of the shallow and deep structures, whereas they were lower on the intermediate and lowest on the thinned sample and appear to decrease for increasing etch time. This indicates that a cross contamination from the plasma chamber may remain on the wafer surface after ICP-RIE treatment.

The hypothesis is also supported by the results shown in fig. 6.13(a) of sec. 6.2.3, where a very good sample was prepared. A Cr mask was etched eight runs prior to that wafer. However, seven pure Si wafers were prepared with b-Si in the RIE etcher before the 8th wafer with the high lifetime. Unfortunately, the wafer-to-wafer reproducibility in ICP-RIE system is poor, which is most probably rooted in the reactor geometry. The installed electrode size is incongruous with the small chamber. Therefore, the etching behavior strongly depends on the chemistry residues on the reactor sidewalls. Unfortunately, even rather long cleaning sequences with pure O₂-plasma did not suffice to properly condition the etching chamber.

In the second step the interfacial SiO_x was dissolved in HF. The layer appears to host high levels of Cr and Al, as well as an elevated levels of K, Cu and Zn.

The third step indicated that elevated bulk concentrations of Cu, Cr, Mn, and Al were present. Furthermore, the dissolved amounts of Si of the different samples during step (3) as listed in tab. A.3 indicate the different etching rates on the plasma treated samples. One reason for the higher abrasion on b-Si samples is certainly the enlarged surface area. However, the mass loss of the thinned sample is almost as high as for the deep structure (≈ 2 orders of mag. higher than on the reference wafer). This suggests that the c-Si crystal may have been either strongly roughened or damaged in the ICP process, whereas the former can be ruled out by the optical appearance. QSSPC measurements of similar treated samples illustrated a strongly decreased lifetime after pure SF₆ etching and a decreasing trend with increased etching time, that could only in part be attributed to the reduction of the wafer thickness.

The samples were analyzed after plasma etching without applying additional RCA cleaning, Al₂O₃ deposition nor PDA. It appears probable that most of the superficial metal elements would become integrated into the

¹The concentrations of: Fe, Cu, Zn, Ni, Mg, Al, V, W, Ti, Na, Cr, Ca, Mn, K were measured.

Table A.3: Summary of ICPMS analyzed b-Si samples.

| Sample | RIE process gas | Dissolution of (#) in . . . | | | mass loss during step (3) [mg] |
|------------------|---------------------|-----------------------------|----------------------|---------------------|--------------------------------|
| | | (1) Surface | (2) SiO _x | (3) Bulk | |
| Reference | none | HCl/HNO ₃ | HF | HF/HNO ₃ | 1 |
| ICP shallow | SF ₆ /Ot | HCl/HNO ₃ | HF | HF/HNO ₃ | 24 |
| ICP intermediate | SF ₆ /Ot | HCl/HNO ₃ | HF | HF/HNO ₃ | 54 |
| ICP deep | SF ₆ /Ot | HCl/HNO ₃ | HF | HF/HNO ₃ | 91 |
| ICP thinned | SF ₆ | HCl/HNO ₃ | HF | HF/HNO ₃ | 72 |

Si/Al₂O₃ interface if no cleaning procedure would be applied, since Al₂O₃ is known to act as an effective out-diffusion barrier even for atomic H [28], which are the smallest and therefore most mobile atom species. After all, no W could be detected on any wafer, which also may be highly recombination active. The latter result shows that a clean chamber dedicated to only one process may allow to reduce surface contamination resulting from ICP-RIE processing. From this argument it can be concluded that there might still be potential to effectively passivate even deeper and more complex nanostructures if a lower contamination level could be achieved during the black etching step.

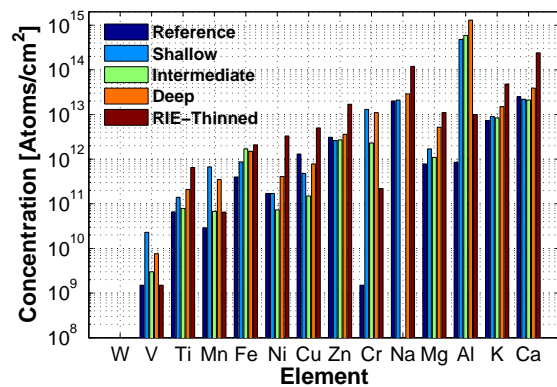
A.7.1 ALD Precursor Purity Investigated by ICPMS

In an additional experiment, the chemical analysis of the ALD H₂O precursor by ICPMS revealed elevated concentrations of Al, Mn, Fe, Ni, Zn, Na, and K after the water had been “stored” in the precursor bottle for several months. Most of these elements are known to be quite recombination active if diffused into the Si bulk or located at the Si surface. However, since the atomic species are only contained in a vapor pulse and are most probably oxidized, which makes them inert against surface reactions, the probability of including such contaminations from the precursors is considered rather low. In fact, Dingemans *et al.* reported that the passivation performance of Al₂O₃ films is not significantly influenced by the TMA purity level (semiconductor grade (99.999%) *vs.* solar grade (98%)) [31, 32]. Furthermore, the ALD manufacturer Cambridge Nanotechnology claimed that equivalently high passivation levels may be reached if beer is used instead of water [16].

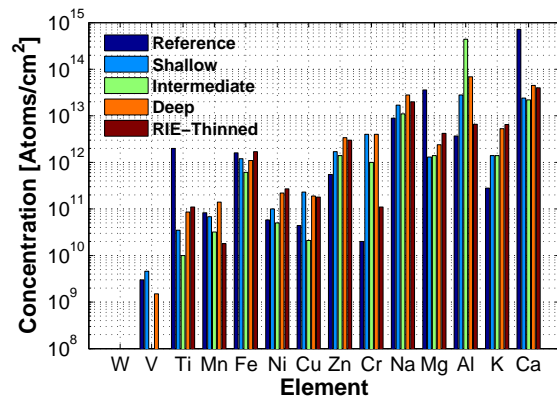
A.8 Discussion of Error Sources

A.8.1 Optics - Focused *vs.* Unfocused Beam Setup

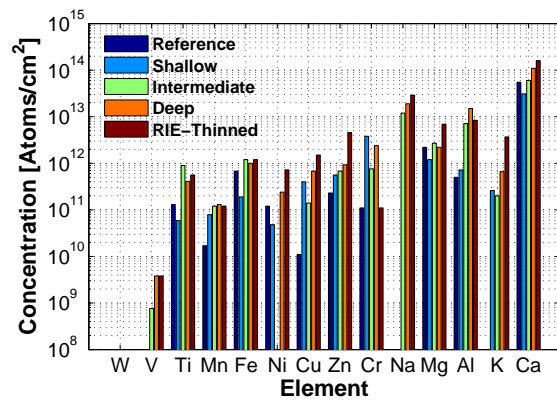
Concerning the optical absorption it is important to note, that the samples were measured with a focused light beam. The setup led to a slight overestimation of the reflectance, which was measured under an angle of incidence of 8° to capture the specular reflex inside integrating sphere. Possibly, the strong focus led to higher angles of incidence and therefore to slightly higher measured reflectance even from the b-Si surfaces. For some samples the optical measurements could be repeated with the unfocussed beam setup leading to lower reflectance values than previously measured as shown in fig. A.9. Throughout the whole UV/VIS spectral range, the reflectance is about 1% – 2% lower if probed with the unfocused beam. Nevertheless, the demonstrated trends and spectral response functions of the presented samples were not compromised because the error is of systematic nature. However, this result indicates that the absolute absorption of the b-Si samples is actually even stronger than presented.



(a) surface / dissolved in HCl:HNO₃



(b) SiO_x layer / dissolved in HF



(c) near-surface Si bulk / dissolved in HF:HNO₃

Figure A.8: The graphs show the elemental concentrations of the indicated metals at the surface (a), in the SiO_x layer (b), and in the near-surface Si bulk (c) as measured by ICPMS in plasma processed (black) Si wafers and an according untreated reference dissociated in the indicated acidic solutions, respectively. It is important to note, that the change of the elemental concentrations of two samples are considered significant, if the difference is close to/or larger than one order or magnitude.

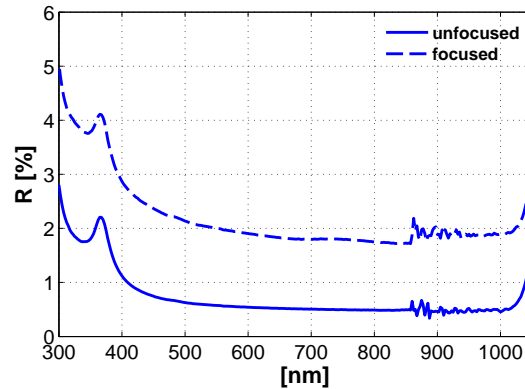


Figure A.9: Reflectance data measured with the unfocused light spot *vs.* data measured with the focused beam setup.

A.8.2 Discussion of Error Sources for the Lifetime Measured on b-Si Wafers

To compare the lifetimes of the different b-Si samples presented in sec. 6.3, the measurements with the highest τ_{eff} values at an injection level of $\Delta n = 10^{15} \text{ cm}^{-3}$ were used. The charge carrier lifetime is a very sensitive quantity which is easily negatively influenced by many factors (e.g. due to handling, etc.). The lifetimes of the wafers were measured at 21 positions by QSSPC. To exclude any negative process influences only the *highest three* values of each wafer were taken into account to calculate the error margins (see fig. A.10). In the group of four reference wafers, a run-to-run deviation is deduced to be at most 30%. Therefore, a reproducibility error of 30% can be assumed. To validate this premise, the run-to-run deviation was monitored on two KOH wafers, which turned out to be lower than 19%. On the one hand, this result indicates that the error estimation of less than 30% is reasonable. On the other hand, higher lifetime values are usually affected stronger by systematic errors than lower ones. This result is confirmed by a comparison of the two Ag-MACE handling references, which lead to a reproducibility error of 26.5% even though the processes and handling conditions were actually very distinct, as the samples were produced in different laboratories. Within single wafers, relative errors between 1% and 9% were calculated for all structures. The only exceptions are the MACE etched long NWs, the NCs, and the macP-Si sample, 14%, 36%, and 66%, respectively, due to technical aspects of the handling process. Thus, many results might be improved by further process optimization and by reducing handling issues.

The area integrated by the QSSPC probe clearly represents a statistically valid region of the nanostructures concerning both, their microscopical and macroscopical spatial homogeneity. Hence, it can be ruled out that local process variations in the structural geometry influence the lifetime results. An additional small error may arise from wafer thickness deviations as the samples may have been slightly thinned during black etching. However, the assumption of a thicker wafer base leads to an underestimation of the lifetime measured by QSSPC, that translated into an overestimation of the achievable SRV, $S_{\text{eff,max}} \leq \frac{W}{2 \cdot \tau_{\text{eff}}}$. Finally, the measured peak lifetime on each wafer represents at least an achievable value on the given surface structure and demonstrates the momentarily obtainable passivation quality of 300 cycles of thermal ALD deposited Al_2O_3 on the various b-Si types.

QSSPC

For a QSSPC measurement differences in wafer thickness and light-trapping have to be considered. If these quantities are entered correctly, very accurate lifetime measurements with errors smaller than 1 – 10 % can be determined in the range from 60 – 230 μs , respectively [145]. Lifetimes of $\tau_{\text{eff}} > 100 \mu\text{s}$ were measured in

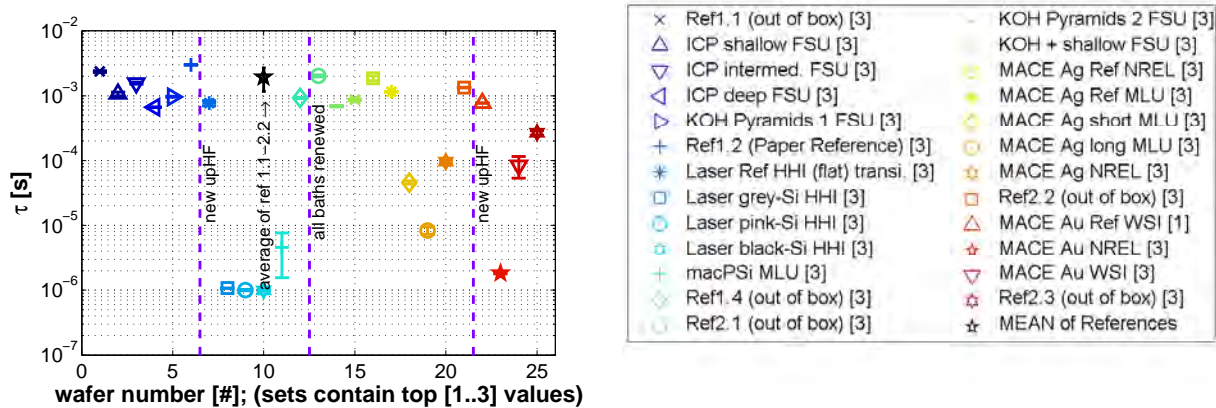


Figure A.10: Overview of the three highest available lifetime values from each processed sample set in the big b-Si passivation experiment series by chronological order. The samples entered the RCA cleaning sequence in the order they appear. Note, that several references were processed to monitor the potential purity of the cleaning solutions. The second reference processed after the ICP-RIE samples yielded a higher average lifetime than the reference prior to cleaning ICP-RIE b-Si. Hence, the cleaning power of the RCA was not deteriorated by the dry etched samples. Possibly, the lifetime increase may be understood by a lowered H_2O_2 concentration and accordingly thinner SiO_x formation on the second reference.

transient mode because here no estimation of the optical constant was necessary. As discussed earlier, wafer doping also influences the achievable lifetime due to the Auger effect. Especially the FZ wafers exhibited, however, a very low wafer-to-wafer deviation of the doping concentration, which was most probably of the same order of magnitude as the deviation within single wafers. Therefore, systematic errors due to variations in doping concentration are assumed to be very small.

The maximum achievable lifetime is influenced by three factors: (i) doping concentration in the wafer, (ii) the SiO_2 quality (i.e. the apparent defect density and due to the related influence on the field effect passivation) and (iii) the passivation quality of the annealed Al_2O_3 film (Q_{fix} , H_2 -content, Si-O bond coordination strength, -H content, etc.). Only the latter two could be properly controlled in this work, which may explain the large lifetime deviations of $\approx 30\%$. The doping level in FZ material was measured by QSSPC for a whole batch of 25 wafers and exhibited an extremely narrow standard deviation of $0.987 \pm 0.012 \Omega\text{cm}$. The values were calculated by the QSSPC software from the measured sheet resistance and manually determined wafer thickness. Therefore, the uncertainty slightly higher ($\approx 2\%$) due to a larger standard deviation of W . Therefore, the lifetime results shown in fig. 6.7 are impressively high, because the value exceeds the re-parametrized Auger-Limit.

A.8.3 ICP-RIE Process Stability

The ICP-RIE process was not perfectly stable over the time of the project. Basically, the structures were more or less equivalent but geometric surface details differed from time to time as a consequence of equipment modifications to the ICP-RIE etcher. The pore depths of the shallow and intermediate structure that were taken into account for the black silicon comparison (see fig. 5.5) were rather small ($\approx 300 \text{ nm}$) as compared to the initial ones shown in fig. 5.1. This might actually be a consequence of cooling issues during ICP-RIE processing and may have supported the extraordinary high lifetime results. Furthermore, the electrode size of the etching chamber did not exactly match the size of the chamber itself, which could also lead to certain process variations.

Acknowledgements / Danksagung

An erster Stelle möchte ich Herrn Prof. Dr. Ralf B. Wehrspohn dafür danken, mir diese Promotionsarbeit ermöglicht zu haben. Ich danke Ihnen für die große Freiheit, Ihre Unterstützung und Motivation. Ebenso danke ich meinen Gutachtern Prof. Dr. Roland Scheer und Prof. Dr. Mato Knez für die zur Verfügung gestellte Zeit diese Arbeit zu lesen und zu bewerten. Beim BMBF bedanke ich mich für die bereitgestellte Finanzierung des Projekts.

Weiter möchte ich allen Menschen danken, die dazu beigetragen haben, dass diese Arbeit gelungen ist.

Zuerst danke ich meinen Kollegen der Fachgruppe μ MD herzlich für die tolle Zeit, die stets angenehm lustige Atmosphäre und die gute Zusammenarbeit, was natürlich alle Sili-Nano Leute und die “Smarties” mit einschließt. Mein besonderer Dank gilt dabei Johannes Üpping. Danke, dass Du mich immer wieder motiviert und mir gezeigt hast, die Dinge auch mal anders zu sehen. Another special thanks goes to Xiaopeng Li. The time with you was especially funny and creative. I guess you are one of the most “crazy scientists” I know ;-). Johannes Ziegler und Alexander Spafke danke ich für die vielen Diskussionsrunden, durch die ich endlich gemerkt habe, wie viel ich schon gemacht und verstanden habe. Johannes Z., Alex, Xiaopeng und Johannes Y danke ich u.a. für die Korrekturen an dieser Arbeit. Bei meinen Bacheloranden und HiWis bedanke ich mich für die vielseitige Hilfe in der Probenpräparation und Datenaufnahme. Claudia Stehr, Susanne Wille und Hans Blaschek, sowie dem “Reinraumteam” des IZM danke ich für die tolle technische Unterstützung im Labor. Danke auch an Benjamin Gesemann, dass Du so oft schon eine praktische Lösung aus der Schublade gezogen hast, die einen Gang zur Werkstatt gänzlich überflüssig machte. Doreen Rawald und Sandra Seil danke ich für die gute Organisation. Ich danke Euch allen (auch nicht namentlich genannten) für Eure immer offenen Ohren und die Hilfe, wenn’s mal wieder gehakt oder geklemmt hat. Es war immer toll, so viele liebe Menschen um sich zu haben und diese Zeit mit Euch zu teilen.

Meinen Kollegen im Projekt PHIOBE Matthias Kroll, jetzt Zilk, Kevin Füchsel, Thomas Käsebier und Benjamin Höffling, sowie allen anderen Beteiligten danke ich ebenfalls für die tolle Zusammenarbeit und die vielen produktiven Treffen (v.a. in Jena). Besonders erwähnen möchte ich dabei Matthias. Von Dir habe ich in der ganzen Zeit am meisten über Optik gelernt. Danke, dass Du immer für noch eine Diskussionsrunde offen warst und so tatkräftig an den Papern mitgearbeitet hast. Vielen herzlichen Dank auch für die sehr gute Zusammenarbeit im experimentellen und theoretischen Bereich. Danke, dass Du geduldig so viele Messungen akribisch genau durchgeführt und mir die Daten und Simulationsdaten zur Verfügung gestellt hast. Thomas danke ich für die Herstellung der schwarzen Wafer und dafür, dass Du immer so zuverlässig und schnell geliefert hast. Nicht vergessen möchte ich meine Fraunhofer-Kollegen vom IWMH und CSP. U.a. danke ich Volker

Naumann für die ToF/SIMS und XPS Messungen sowie die vielen Stunden, die ich mit Dir gemeinsam im Reinraum verbringen durfte, ohne, dass es langweilig wurde. Andreas Graff, Paul T. Miclea, Roland Salzer und Rolf Herold sei respektive für die TEM und FIB Arbeiten gedankt. Marco Turek und Gruppe danke ich für die Möglichkeit die QSSPC und PL nutzen zu dürfen. Sylke Meyer und Stefanie Wahl danke ich für die ICPMS Messungen und unsere Diskussionen über die Verbesserung der Chemikalienqualität. Herzlichen Dank auch für die Unterstützung zur Verbesserung unserer Reinigungsprozedur, die u.a. durch Christian Hagedorf und seine Gruppe möglich war. I also thank Bart Vermang for the cleaning procedure carried out for a batch of wafers at imec. Marco Ernst vom ISFH danke ich für die SiN_x Beschichtungsversuche der b-Si Proben. Nicht zuletzt geht an dieser Stelle auch ein herzliches Dankeschön an meine neuen IWMH-Kollegen Manfred Fütting, Andreas Dockhorn und Martin Thonagel. Ohne Eure Unterstützung, und wenn ihr mir in den letzten Wochen der Schreibphase nicht den Rücken frei gehalten hättet, wäre diese Arbeit nicht mehr fertig geworden!

Meinen Freunden, die mich in diesem Lebensabschnitt (zeitweise) begleitet haben, und meiner Familie möchte ich Danke für das ganze "Drumherum" sagen. Diese Arbeit wäre mir nie möglich gewesen, wenn ihr nicht an mich geglaubt und mir immer wieder Mut gemacht hättet, dran zu bleiben. *Danke, dass ihr mir immer wieder die richtigen Fragen stellt.* Especially, I want to thank Maxine Starner once again, who fully read and spell-checked this work. Thank you for your time, your great effort and the suggestions that directly contributed to this work. I also thank you and Mark for the hospitality on my short stop-overs to the conferences and your everlasting friendship. Besonderer Dank gilt an dieser Stelle auch Christian Weiser und Armin Heyn für die effektive Motivation, die daraus resultierte, dass ihr mich in der Bibliothek begleitet habt. Tobias Hartmüller danke ich von Herzen für die psychologische Unterstützung am Telefon (= Andi Klamt möchte ich für die schöne Zeit in der Mensa und die kurzweiligen Gespräche danken. U.a. danke ich auch Christian Borschel für die Gastfreundschaft und die vielen Übernachtungen in Jena. Es war immer schön für kurze Zeit wieder Dein Mitbewohner sein zu dürfen. Natürlich möchte ich Anna-Lorena, Felix und Emiljan für die unbezahlbar schönen Alltagsmomente danken, die ihr mir immer wieder beschert habt. Danke, dass auf Eurer Couch immer ein Platz zum Ausruhen und ein Abendessen oder ein schneller Kaffee in guter Gesellschaft zur Verfügung stand. Benjamin möchte ich dafür danken, dass Du immer zur Stelle bist, wenn man dich braucht - egal wie voll Deine Woche schon ist. Anni Hagn danke ich für den tollen Schreib-Sommer und dafür, dass Du mich so annimmst, wie ich bin. Nicht zuletzt gilt mein besonderer Dank Mama und Papa, denen diese Arbeit gewidmet ist. Danke, dass ich bei Euch immer ein zu Hause habe.

Außerdem danke ich allen, die während dieser Zeit für mich gebetet haben. Gott hat ein offenes Ohr für Euch! Werdet nicht müde weiter zu glauben und zu beten! Vor allem danke ich Jesus für diese wunderbare Zeit. Deine Leitung durch den Heiligen Geist und der große Segen, den Du mir (und uns) jeden Tag zuteil werden lässt, steht über allen Dingen und macht das Leben immer wieder überraschend, interessant, spannend und herausfordernd aber vor allem superschön! Danke, dass Du die Natur und damit ihre Wissenschaft so wunderbar gemacht hast.

LOBE DEN HERRN MEINE SEELE UND VERGISS NICHT, WAS ER DIR GUTES GETAN HAT.

– PSALM 103, 2

Curriculum Vitae

Martin Otto

FG- μ MD
Heinrich-Damerow-Str. 4,
D-06120 Halle (Saale)

Persönliche Daten

Geburtsdatum: 20.05.1981,
Geburtsort: Kassel (Deutschland)

Ausbildung

- seit
November
2008* **Promotionsstudium** im Bereich Photovoltaik in der Arbeitsgruppe
von Prof. Dr. Ralf B. Wehrspohn an der Martin-Luther Universität Halle-Wittenberg
◊ Erstellung der Promotionsarbeit mit dem Titel “Effective Passivation of
Black Silicon Surfaces by Conformal Thermal ALD Deposited Al₂O₃ Layers”
[ALD: Atomic Layer Deposition]
- Oktober 2001
bis Juni 2008* **Physikstudium** an der Georg-August-Universität Göttingen
◊ Abschluss: **Diplom**
- 1992-2001* Jugenddorf-Christophorusschule Oberurff (CJD), Abschluss: **Abitur**

Eidesstattliche Erklärung / Declaration under Oath

Ich erkläre an Eides statt, dass ich die Arbeit selbstständig und ohne fremde Hilfe verfasst, keine anderen als die von mir angegebenen Quellen und Hilfsmittel benutzt und die den benutzten Werken wörtlich oder inhaltlich entnommenen Stellen als solche kenntlich gemacht habe.

I declare under penalty of perjury that this thesis is my own work entirely and has been written without any help from other people. I used only the sources mentioned and included all the citations correctly both in word or content.

Datum / Date

Unterschrift des Antragstellers /
Signature of the applicant